DOCTOR OF PHILOSOPHY

Multiscale modelling of cancer invasion

the role of dynamic fibre redistribution and matrix-degrading enzymes in tumour progression

Shuttleworth, Robyn

Award date:
2019

Multiscale modelling of cancer invasion:

the role of dynamic fibre redistribution and matrix-degrading enzymes in tumour progression

Robyn Shuttleworth

Mathematics

University of Dundee

This dissertation is submitted for the degree of

Doctor of Philosophy

October 2019

Contents

List of Figures

List of Tables

I would like to express my sincere gratitude to my supervisor, Dr. Dumitru Trucu, without whom I may never have pursued a PhD. It has been a privilege to study in the field of cancer research and I can safely say it has been the best, most challenging time of my academic career. I am grateful for the continued support and guidance provided by Dr. Trucu and I don't doubt this will continue into my future endeavours. I will always be grateful for the knowledge and research experience I have gained during my time here.

I would like to acknowledge all of the wonderful people I have met on my conference travels, sharing our PhD experiences with one another gave me new perspectives on my own and motivated me to become the best I could be. Also, a special thank you to my Aussie friend who helped me with the opportunity to present my work internationally that consequently led to many more conferences and workshops.

To all my family and friends who have listened to my ramblings for the past 4 years, you deserve the biggest thank you. You have always shown a keen interest in my work (even though you have not really had much idea what I'm talking about!) and it has meant everything to have your support. To my wonderful fiancé, you have put up with more than anyone else, you have always been so encouraging and supportive, and I'm so very happy to have had you by my side. Finally, to my colleague, best friend and part-time therapist, Arnina, you have made my last few years inexplicably easier, and undoubtedly more caffeine filled!

I would like to dedicate this thesis to my late best friend Tilda Hetrick. The most beautiful person inside and out, she was a wonderful friend and I cherish every moment we had together. We became friends through our love of maths and biology, and I can't help but think this is why I am where I am now.

Thank you sweets. Forever and always.

"We choose our own path. Our values and our actions, they define who we are."

I hereby declare that except where specific reference is made to the work of others, the contents of this dissertation are original and have not been submitted in whole or in part for consideration for any other degree or qualification in this, or any other university. This dissertation is my own work and contains nothing which is the outcome of work done in collaboration with others, except as specified in the text and Acknowledgements. This dissertation contains fewer than 65,000 words including appendices, bibliography, footnotes, tables and equations and has fewer than 150 figures.

Robyn Shuttleworth, October 2019

Certification

This is to certify that Robyn Shuttleworth has complied with all the requirements for the submission of this Doctor of Philosophy thesis to the University of Dundee.

Dr. Dumitru Trucu

Publications

1. R. Shuttleworth, and D. Trucu (2018), Two-scale Moving Boundary Dynamics of Cancer Invasion: Heterotypic Cell Populations Evolution in Heterogeneous ECM, *Cell Movement: Modeling and Applications*, (eds. N. E. Tarfulea and M. Stolarska), pp 1-26, Birkhauser, Springer Nature Switzerland, `http://dx.doi.org/10.1007/978-3-319-96842-1`

2. R. Shuttleworth, and D. Trucu (2019) Multiscale Modelling of Fibres Dynamics and Cell Adhesion within Moving Boundary Cancer Invasion, *Bulletin of Mathematical Biology*, `http://dx.doi.org/10.1007/s11538-019-00598-w`

3. R. Shuttleworth, and D. Trucu (2019), Multiscale dynamics of a heterotypic cancer cell population within a fibrous extracellular matrix, *Journal of Theoretical Biology* (39pp) *Submitted*, arXiv:1907.01092

4. R. Shuttleworth, D. Trucu (2019), Cell-scale degradation of peritumoural extracellular matrix fibre network and its role within tissue-scale cancer invasion, *Bulletin of Mathematical Biology*, (44pp) *Submitted*, arXiv:submit/2753201

Abstract

Recognised as one of the hallmarks of cancer, cancer invasion is a complex process involving the secretion of matrix-degrading enzymes that have the ability to degrade the surrounding extracellular matrix (ECM). Combined with cell proliferation and migration, and changes in cell-cell and cell-matrix adhesion, the tumour is able to spread into the surrounding tissue. The ECM constituents are favourably explored by the cancer cells during invasion, and in this context, of particular importance is the special contribution of ECM fibrous proteins components, such as collagen and fibronectin, which play an important part in cell proliferation and migration.

In this thesis we consider the two-scale dynamic cross-talk between the cancer cell population and a two-component ECM in the context of the proteolytic dynamics of matrix-degrading enzymes at the leading edge of a growing malignant tumour. We incorporate the two-scale dynamics of cells-ECM interactions by exploring key interlinked tissue-scale and cell-scale aspects contributing directly both to cell-adhesion and to the dynamic rearrangement and restructuring of the ECM fibres within the growing tumour. Finally, this bulk two-scale activity is embedded within a global multiscale moving boundary approach that also crucially accounts for an emerging multiscale dynamics of the matrix degrading enzyme proteolytic processes at the invasive edge of the tumour, which lead to peritumoural ECM degradation and results in changes of the tumour morphology and further cancer spread.

Chapter 1

Introduction

1.1 General Considerations

Cancer has become of increasing concern for the growing population over the past few decades, with one in two people now developing cancer in their lifetime. We are in a time where these statistics are at a standstill, and there has never been a greater need for cancer research and the development of new medicines. As research progresses, biological experiments are advancing and we are learning more about this deadly disease. Whilst knowledge of cancer processes are essential, new experiments and discoveries are opening doors involving more complex problems. Mathematics is bridging the gap between biology and the unknown and providing solutions to problems that, 20 years ago, were not thought possible. Cancer is known for its high mortality rates and is a disease that is particularly good at developing drug resistance and evasion techniques to current treatment strategies. By studying the biological composition of a patient's tumour and surrounding stroma it is possible to develop a predictive model of tumour growth.

Through mathematical modelling of cancer growth and spread we gain invalu-

able knowledge that will eventually contribute directly to a deeper understanding of tumour response to treatment therapies. This will bring nearer the perspective when clinical trials will be increasingly developed according to mathematical data predictions and patients will start being treated through these personalised treatment regimes, ultimately aimed at achieving improved perspectives for surviving cancer, one of the biggest killers in the world.

1.2 Biological Background

1.2.1 Introduction

Cancer invasion of tissue is a complicated, multiscale process which plays an essential role in tumour progression. The invasive nature of cancer cells was identified by Hanahan and Weinberg (2000, 2011) as being among a small number of *"hallmarks of cancer"*, which they considered to encompass the complexity of cancer development and progression. Specifically, Hanahan and Weinberg (2000) identified six hallmarks that separate a healthy cell from a cancerous cell, namely, the ability to: sustain proliferative signalling, to evade growth suppressors, to enable limitless replicative potential, to induce angiogenesis, the ability to resist cell death and the activation of invasion and metastasis. At some point during their development, primary tumour masses adopt the ability to detach cells that can then move out and invade surrounding tissue, allowing the cancerous cells to spread locally. This process, known as metastasis, allows new colonies of cancerous cells to form in distant sites of the body. This type of cancer invasion becomes especially deadly when cells gain access to the bloodstream or lymph nodes as they are no longer confined to the local space surrounding the primary tumour (Lodish et al., 2000). The most common site for breast cancer to metastasise is the bone; followed by the liver, brain

and lungs. Once a tumour has invaded the bone and these vital organs, it is fatal and can rarely be cured, only treated by various forms of cancer therapy such as surgical intervention, chemotherapy and radiation. These types of tumour are the cause of 90% of human cancer deaths (Sporn, 1996).

1.2.2 Basic properties of a tumour and surrounding tissue

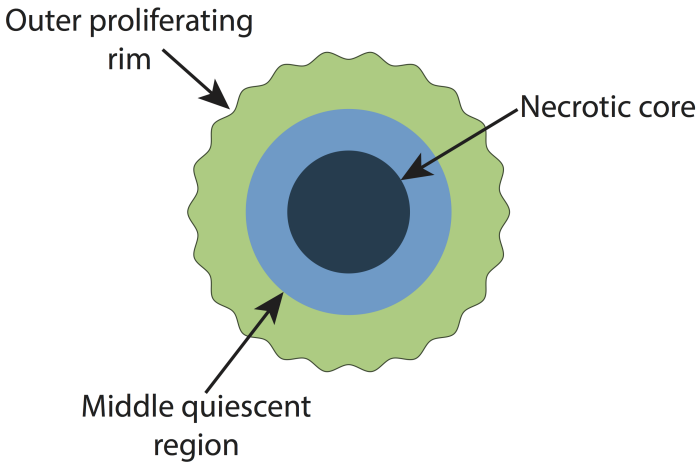

Figure 1.1: Basic composition of a spheroid tumour comprising of three layers: the inner necrotic core, a middle quiescent region and the outer proliferating rim.

A malignant tumour is a complex heterotypic community of cells, such as cancer cells, fibroblasts, stromal cells, macrophages, etc., and generally consists of three layers, schematically represented by the spheroid in Figure 1.1, which, in brief, are described as follows. The inner necrotic core of a malignant solid tumour is a dense region of "dead" cells, caused by the restricted access to any nutrients or oxygen. These cells arise as quiescent cells die. Quiescent cells form a thick region surrounding the necrotic core and can be either slowly growing or not growing at all. If a break occurs in the boundary of the tumour, these cells will take action and move to fill the gap, rebuilding the broken boundary. This final layer consists of proliferating cells that form a concentric shell on the exterior of the tumour and is the

region exposed to the highest level of nutrients and oxygen available, as well as being the region in which the majority of a tumour's invasive abilities manifest (Wallace and Guo, 2013). It is this region that will directly interact with the surrounding stroma and extracellular matrix (ECM).

The extracellular matrix is a key biological structure that provides not only support to surrounding cells and tissues, but also acts as a platform for cellular communication. This feature is of particular use to cancer cells, which take advantage of the molecular interactions mediated by various ECM components and favourably utilise these as means for achieving invasion of the surrounding tissue. Furthermore, the formation of the ECM is a vital process, particularly important in wound healing (Rozario and DeSimone, 2010), embryonic development (Xue and Jackson, 2015) and the metastasis of tumours.

The ECM is comprised of a variety of secreted proteins which can vary depending on the type of tissue or the location in which we are investigating. A main component of the ECM which provides structure and integrity is collagen, the most abundant protein in the human body, with collagens type I, II and III making up around 90% of the overall collagen present (Lodish et al., 2000). Complementing the rigidity of collagen is the protein elastin, which unlike collagen, provides a resilience and elasticity to the ECM, allowing it to be changed in shape. Elastin is one thousand times more flexible than collagens (Kristensen and Karsdal, 2016), hence it is a dominant component in tissues that require a high degree of flexibility, i.e, within the skin and lung tissue. Finally, moving away from the scaffolding structure of the ECM, there are other fibrous ECM components that provide functional qualities within the matrix. One such component is the glycoprotein fibronectin. Fibronectin contributes to cell migration, growth and proliferation, ensuring the normal functionality of healthy cells. It also plays a crucial role in cell adhesion, having the

ability to anchor cells to collagen and other components of the ECM.

1.2.3 Local Invasion of Tissue

Cancer invasion of the human body is a complex multiscale phenomenon that incorporates complicated cell-scale (micro-scale) molecular and individual cellular interactions that are intrinsically interlinked to emerging tissue-scale (macro-scale) collective heterotypic cell population dynamics. Recognised as one of the hallmarks of cancer (Hanahan and Weinberg, 2000, 2011), cancer invasion is a process that triggers and takes advantage of important changes in the behaviour of many molecular activities typical for a healthy cell, for example, gene mutations within cells stimulate the secretion of growth signals promoting enhanced cell proliferation, and this together with the secretion of proteolytic enzymes results in a fast spreading tumour capable of both matrix degradation and sustained tumour growth.

Degradation and reorganisation of the ECM

The local invasion of cancer is, in the first instance, stimulated by the secretion of matrix degrading enzymes (MDEs). There are several classes of MDEs, such as matrix metalloproteinases (MMPs) and the urokinase-type plasminogen activator (uPA), produced by cancer cells and these enzymes degrade and reshape the structure of the surrounding ECM. Collectively known as matrixins, MMPs are one of the main families of proteolytic enzymes which aid the metastasis of a tumour. There are currently 23 types of MMP that have been identified in the human body (Visse and Nagase, 2003). MMPs are substrate specific and can be either membrane bound (MT-MMPs), or can move freely in the stroma, each working on different components of the ECM ensuring a significant breakdown of the matrix (Brinckerhoff and Matrisian, 2002; Parsons et al., 1997). One particular MMP cascade employed dur-

ing the invasion of cancer is the MT1-MMP/MMP-2 system. This system contains freely diffusible MMP-2 molecules which are activated by the soluble membrane-tethered MT1-MMP, where the expression and over-production of MMP-2 indicates the level of malignancy in many forms of tumour (Dalberg et al., 2000). Figure 1.2 shows the MT1-MMP/MMP-2 invasion cascade. Stage 1 illustrates the MT1-MMPs (orange) tethered to the cancer cell mass (purple). When the membrane tethered MMPs come into contact with any surrounding collagen, indicated in the figure by (a), the MT1-MMPs will cleave the collagen into smaller pieces, labelled here by (b). Once into the stroma, MT1-MMPs recruit nearby proMMP-2 molecules (blue), and with the addition of cell adhesion molecules (yellow), denoted on the figure by (c), MT1-MMP will cleave proMMP-2 into activated MMP-2 (see Stage 2 of the figure). These activated MMP-2 molecules will then travel through the extracellular matrix, being indicated on the figure by (d). Finally, Stage 3 depicts the two processes of the activated MMP-2 molecules in that they degrade both the previously denatured collagen, denoted by (e), and the glycoprotein fibronectin (red arrows), labelled in the figure by (f), in order to create paths through which the cancer cells can advance.

Cellular adhesion

The invasive capabilities of a tumour gather their strength from a cascade of processes enabled by the cancer cells, which, besides abnormal secretion of matrix degrading enzymes, includes also enhanced proliferation and altered cellular adhesion abilities. Both cell-cell and cell-matrix adhesion play important roles in tumour progression, and changes to either of these contribute directly to the overall pattern of invasion (Behrens et al., 1989; Berrier and Yamada, 2007; Kawanishi et al., 1995; Todd et al., 2016). For example, a decrease in cell-cell adhesion allows the cells to detach from the primary tumour and invade further into the matrix, and this cou-

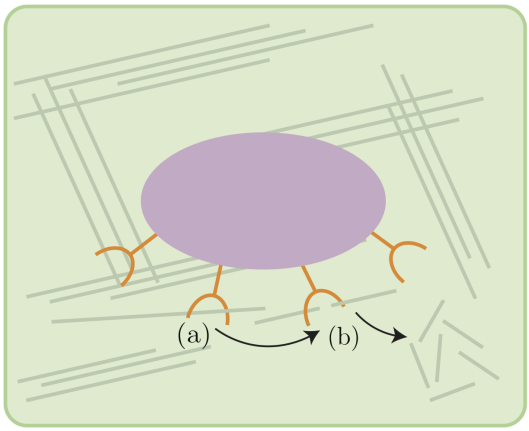

Stage 1

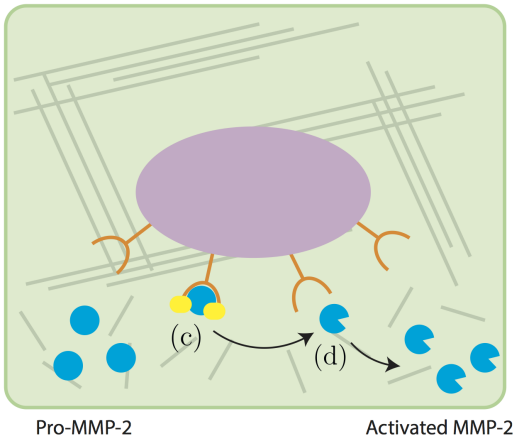

Stage 2

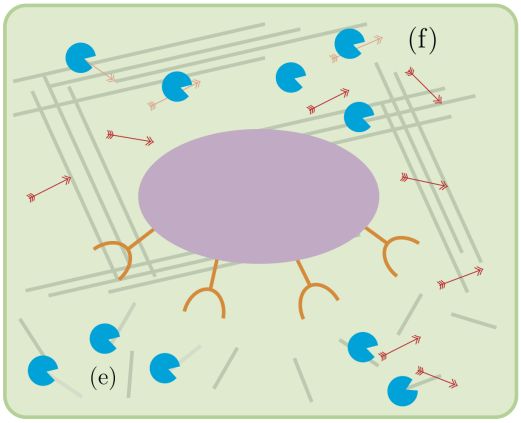

Stage 3

Figure 1.2: MT1-MMP/MMP-2 cascade.

pled with increased cell-matrix adhesion amplifies the tumours invasive capabilities and escalates the spread of cells (Cavallaro and Christofori, 2001).

In healthy cells, cell-cell adhesion is mediated by a family of specific molecules on the cell surface known as cell adhesion molecules (CAMs). Adhesion is dependent on the cell-cell signalling pathways that are formed due to the interactions between the distribution of calcium-sensing receptors and Ca^{2+} ions within the ECM. Essential for the formation of these pathways is a family of transmembrane glycoproteins, known as cadherins. These are calcium dependent adhesion molecules where in particular, the subfamily E-cadherins are responsible for binding with intra-cellular proteins, known as catenins, typically β-catenin, forming an E-cadherin/catenin complex. The recruitment of cadherins and β-catenin to the cell cytoskeleton is effectuated by intracellular calcium signalling (Ko et al., 2001). Evidence suggests that activation of calcium sensing receptors results in an increase of E-cadherins which in turn increases the binding of β-catenin (Hills et al., 2012). Any alteration to the function of β-catenin will result in the loss of ability of the E-cadherin to initiate cell-cell adhesion (Wijnhoven et al., 2000). The direct correlation between this calcium-based cell signalling mechanism and the regulation of E-cadherin and β-catenin was first discovered in colon carcinoma (Bhagavathula et al., 2007).

On the other hand, cell-matrix adhesion is regulated by the subfamily of calcium independent CAMs, known as integrins, that enable the cells to bind to different components of the ECM. Integrins link the cytoskeleton inside a cell to the ECM outside and this is aided by their ability to attach to a wide variety of ligands (Humphries et al., 2006). Additionally, integrins can bind to actin proteins within the cytoskeleton, aiding in cell migration by creating a leading and trailing edge to the cell, resulting in persistent migration in one direction (Delon and Brown, 2007; Moissoglu and Schwartz, 2006).

Tumour malignancy

As tumour malignancy increases, normal fibroblasts are subverted to promote tumour growth and are known as cancer-associated fibroblasts (CAFs) (Kalluri, 2016; Shiga et al., 2015). CAFs proliferate at a much higher rate than normal fibroblasts in healthy tissue (Erdogan et al., 2017). Biological evidence shows that CAFs induce tumour growth, metastasis, angiogenesis and resistance to chemotherapeutic treatments (Tao et al., 2017). Unlike normal fibroblasts, CAFs are specific to tumour cells and their microenvironment and possess the ability to change the structure and influence functions within the ECM (Jolly et al., 2016). Many *in vitro* experiments have shown that CAFs rearrange both collagen fibres and fibronectin, enabling a smooth invasion of the cancer cells (Erdogan et al., 2017; Fang et al., 2014; Gopal et al., 2017; Ioachim et al., 2002). The ability to reorganise fibrous proteins in the microenvironment is aided by the high secretion of collagen types I and II and fibronectin by the fibroblasts (Cirri and Chiarugi, 2011).

Moreover, to further increase the invasion potential of the tumour, cancer cells develop the ability to mutate into secondary cell sub-populations within the tumour (Loeb and Loeb, 2000) creating a heterotypic cell population. These mutated cells exhibit more aggressive traits than the primary cell population, often displaying higher proliferation rates, increased migrative activity and increased cell-matrix adhesion as well as decreased cell-cell adhesion. The development of cell mutations indicates an increase in tumour malignancy and is a further precursor to the metastasis of the cancer.

1.3 Mathematical Modelling of Cancer Invasion

1.3.1 Introduction

One of the earliest records of mathematics in biology dates back to the 12th Century with the Fibonacci series being used to describe the growing population of rabbits. It was not until centuries later that mathematics would be used to describe the biological processes involved in cancer invasion, the first of this dating back to the 1950's. However, it is only within the last 30 years that we have witnessed increasing focus on the mathematical modelling of cancer invasion, addressing various processes of cancer cells and their interactions with the surrounding environment.

With biological experiments advancing, there is an increasing need for more extensive modelling of the processes involved in cancer invasion. Biological and mathematical models of both *in vivo* and *in vitro* experiments have given us a deeper insight into many processes involved during tumour invasion. With an increase in the information that is available, the number of questions has also risen, calling for more complex mathematical models to describe the deeply convoluted systems that are being discovered. In this section we present a literature review of the approaches and evolving models used to describe the processes involved in several different aspects of cancer invasion.

1.3.2 Continuum and Individual-Based Models

In the past few decades there has been a lot of interest in the mathematical modelling of tumour invasion (Andasari et al., 2011; Anderson, 2005; Anderson et al., 2000; Bellamo et al., 2008; Chaplain et al., 2011, 2006; Gerisch and Chaplain, 2008; Peng et al., 2017; Ramis-Conde et al., 2008; Szymańska et al., 2009; Trucu et al., 2013). There are many mathematical models which investigate different aspects of cancer

invasion, particularly using insights from both *in vitro* and *in vivo* biological models. *In vivo* models present a higher potential for capturing the cancer growth and spread process, however it is difficult to visualise the individual steps of invasion. On the other hand, *in vitro* models are easier to construct and they enable us to control a lot of the experimental values we obtain, this allowing for easier quantitative analysis. One disadvantage to *in vitro* models however is the inability to see the global effect of invasion, i.e., *in vitro* models only contain a partial expression of the interactions between the cancer cells and the ECM (Katt et al., 2016) so we are unable to capture the full picture of cancer invasion. Great effort has been made to understand the interactions that are occurring during the invasion process, and the experiments, both *in vivo* and *in vitro* have helped to advance this knowledge.

Links between cell migration processes and the family of matrix degrading enzymes (MDEs) that are produced by the cancer cells have been discovered (Lu et al., 2011; Nabeshima et al., 2002), as well as links between cell migration and the structure of the extracellular matrix (He et al., 2016; Yamaguchi et al., 2005). There have been many attempts to model these interactions, using both continuum and discrete models, among these, we note here the ones concerning the secretion and transport of proteolytic enzymes such as uPAs and MMPs, with direct impact upon the degradation of ECM (Andasari et al., 2011; Chaplain and Lolas, 2005; Deakin and Chaplain, 2013; Peng et al., 2017; Trucu et al., 2013) as well as those exploring the direct effects of chemotaxis, proliferation and adhesion on tumour invasion (Bitsouni et al., 2017; Chauviere et al., 2007; Domschke et al., 2014; Gerisch and Chaplain, 2008; Painter, 2008; Ramis-Conde et al., 2008), all these aspects being of direct interest for us in the current investigation. Additionally, the heterogeneity of ECM has been investigated (Chauviere et al., 2007; Hillen et al., 2010; Painter, 2008) with results to show that the composition of the ECM is of vital importance to the

overall invasion of cancer. On the other hand, great focus has been placed on modelling the effects of cell-cell and cell-matrix adhesion (Anderson, 2005; Armstrong et al., 2006; Bitsouni et al., 2017; Domschke et al., 2014; Gerisch and Chaplain, 2008; Painter et al., 2010; Turner and Sherratt, 2002).

One of the first continuum approaches for modelling cell-cell adhesion was proposed in Armstrong et al. (2006) which considered the directed movement of cells in response to the adhesive forces made through cell binding. Moreover, the PDE model proposed in Anderson et al. (2000) describes the invasion of tissue by cancer cells considering three major components, namely, the tumour cells, tissue (extracellular matrix) and matrix degrading enzymes. There were two models proposed, the first being a continuum model which considered the tumour mass as a whole, while the second was an individual-based model focused on the invasive effects on the level of individual cells. The continuum model proposed there describes how the tumour cells respond to haptotactic effects produced within the ECM. It has been shown that the tumour cells will split into two groups, one driven by random migration, and the other spurred by haptotaxis. Furthermore, the individual-cell based model confirmed this behaviour and it is concluded that haptotaxis is important for cancer cell invasion.

The model proposed in Anderson et al. (2000) was used as a basis for the models in Gerisch and Chaplain (2008) where a continuum approach to cancer cell invasion was derived which accounts for both cell-cell and cell-matrix adhesion. These models used non-local approaches for both cell-cell and cell-matrix adhesion, introducing the notion of an adhesive flux and cell sensing radius, which was utilised to account for the adhesion bonds established by the cells both with their neighbouring cells as well as with the surrounding environment from their immediate proximity. Analytical investigations of these models were carried out in Chaplain et al. (2011), where a

system of nonlinear, non-local partial integro-differential equations describing the spatio-temporal dynamics of cancer invasion was considered. The behaviours of the cancer cell population under different adhesion regimes (corresponding to various cell-cell and cell-matrix adhesion coefficients) were explored.

There are several models which have previously focused on the components of the surrounding microenvironment of tumours and how these contribute to invasion (Perumpanani et al., 1998; Scianna and Preziosi, 2012). Chemotactic and haptotactic effects between cells and the fibrous environment of the ECM were considered in (Chauviere et al., 2007) where the following two scenarios were explored, namely that cancer cells will either try to gather in to high density regions of fibres or they will try to avoid these regions altogether.

A model describing the mesenchymal motion of cells in a fibre network was developed by Hillen (2006). Mesenchymal migration involves significant matrix remodelling, where the cell will leave a trail of aligned fibres along its path. Both mesoscopic (individual based) and macroscopic (population based) models were described, paving the way for modelling cell population migration and invasion on heterogenous orientated environments. This approach was continued by Painter (2008) using an individual-cell based model where two different forms of cell migration were investigated. Here it is shown that in terms of mesenchymal migration, the actions of both contact-guidance and ECM remodelling are sufficient processes for invasion to occur.

1.3.3 Multiscale Models

While, with few exceptions, most of the models reviewed above have been proposed at one individual scale and do not account for the multiscale nature of cancer invasion, cancer dynamics occurs in fact on many interlinked spatial scales, including

sub-cellular, cellular- and tissue- (organ) scales, Figure 1.3, with different but critical aspects of the invasion process occurring on each of these levels. Therefore, an integrated mathematical modelling across all of these scales is crucial in examining the full effects of cancer invasion (Deisboeck et al., 2011).

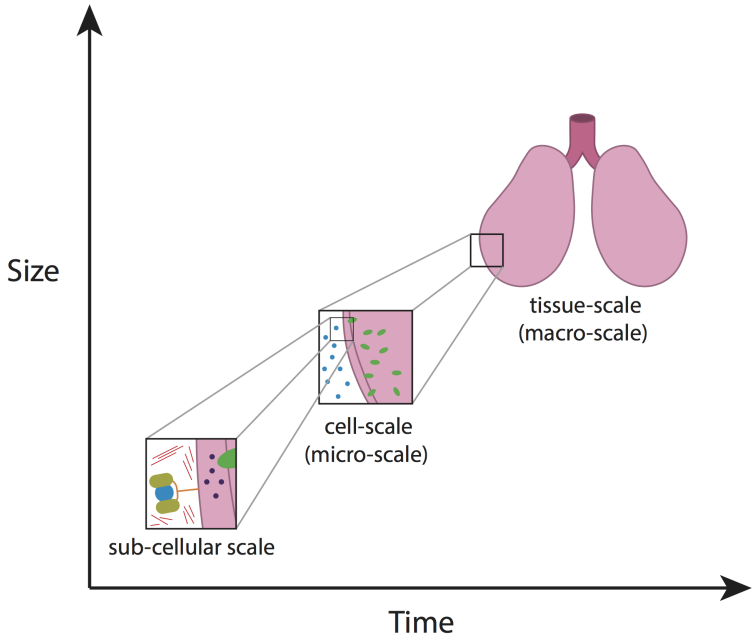

Figure 1.3: Schematic of macro-micro scales showing the largest scale, tissue-scale, to the smaller scales, cellular and sub-cellular.

With its dynamics ranging from molecular sub-cellular and cellular-scale to intercellular- and tissue-scale, the cancer invasion process has witnessed major modelling advances over the past 15 years (Anderson et al., 2007; Peng et al., 2017; Ramis-Conde et al., 2008; Trucu et al., 2013). Three different individual-cell based models were proposed in Anderson et al. (2007) to capture the invasion process at three spatial scales namely at extra-cellular, cellular and sub-cellular scales. Each model was developed to investigate a different stage of tumour invasion, namely, tumour initiation, growth and invasion. This type of single-cell based modelling allowed for heterogeneity to be explored in both the tumour and the surround-

ing microenvironment. However, while recognised by most previous works that a combination of information from different scales would pave the way for a better understanding of cancer invasion, the naturally interlinked multiscale dynamics of this process was for the first time addressed in a genuinely spatially multiscale fashion in Trucu et al. (2013), where a novel multiscale moving boundary model was developed by exploring the double feedback link between tissue-scale tumour dynamics and the tumour invasive edge cell-scale matrix degrading enzymes (MDEs) activity. In that multiscale model, while the tissue-scale macro-dynamics of cancer cells induces the source for the leading edge cell-scale molecular micro-dynamics of MDEs, in turn, through its proteolytic activity, this molecular micro-dynamics causes significant changes in the structure of the ECM in the peritumoural region that ultimately translates in a tissue-scale relocation of the tumour boundary. Later on, that model was adapted in Peng et al. (2017) to capture the influence within the tumour invasion process of the proteolytic dynamics of urokinase-plasminogen activator (uPA) system, exploring various scenarios for ECM degradation and proliferation of cancer cells. These multiscale models have a common focus on exploring the evolution of a tumour whose importance is justified by clinical considerations, namely that it is not necessarily the overall size but the morphology of the tumour that creates huge surgical challenges. This is mainly due to the deficiencies in all current imaging techniques, which are only able to capture between 65% and 90% of the tumour, enabling the real possibility of not resecting the true extent of the tumour during the surgical process by leaving behind small but complicated leading-edge tumour morphological patterns that are not captured by the imaging, which subsequently lead to an aggressive tumour relapse.

1.4 Thesis Outline

The main aim of this thesis is to better understand the processes of local cancer invasion within the extracellular matrix and explore the crucial interactions between cancer cells and the surrounding tissue using an integrated multiscale model that incorporates both tissue- and cell-level activities. To that end, we develop the moving boundary multiscale model first introduced in Trucu et al. (2013) to further investigate both tissue- and cell-level activities by considering the following:

- the introduction of cell adhesion, namely cell-cell and cell-matrix adhesion to a heterotypic cell population consisting of two sub-populations, where the second cell population arises due to mutations from the primary cell population,
- the development of a two-phase ECM structure, containing a fibres component and a non-fibres component, incorporating the new cell-ECM interactions within the tumour region that will contribute to both cell adhesion and the rearrangement of the ECM fibres,
- the inclusion of a heterotypic cancer cell population within the new two-phase ECM multiscale model,
- and the peritumoural cell-scale fibre degradation by the MDEs.

To that end, in Chapter 2 we will discuss the mechanisms involved during local cancer invasion, specifically cellular adhesion and matrix degradation. We will build on the multiscale moving boundary framework proposed in Trucu et al. (2013) by developing the modelling of the tissue-scale dynamics to include cell-cell and cell-matrix adhesion concerning a heterotypic cancer cell population. We will consider two cancer cell sub-populations, namely a primary tumour cell distribution and a second cancer cell sub-population that arises due to mutations from the primary

tumour cells and exhibits higher malignancy. We intend to explore the multiscale moving boundary dynamics of this heterotypic tumour cell population in the presence of cell-adhesion at the tissue-scale and matrix degrading enzyme molecular processes considered at cell-scale. Using computational simulations we will examine the effects of different levels of adhesion and matrix remodelling on the invasion of cancer cells.

In order to gain a deeper understanding of the tumour invasion process, we pay special attention to the interacting dynamics between the cancer cell population and various constituents of the the surrounding tumour microenvironment. Consequently, Chapter 3 considers the key role that ECM plays within the human body tissue, providing not only structure and support to surrounding cells, but also acting as a platform for cells communication and spatial movement. There are several other vital structures within the ECM, however we are going to focus primarily on fibrous proteins, such as fibronectin and collagen. These fibres are key players in the function of healthy cells, contributing to many essential processes such as cell migration, differentiation, migration and proliferation. They also play a crucial role in tumour progression with the ability to anchor cells to other components of the ECM. We will consider the two-scale dynamic cross-talk between cancer cells and a two component ECM (consisting of both a fibre and a non-fibre phase). To that end, we plan to incorporate the interlinked two-scale dynamics of cells-ECM interactions within the tumour support that contributes simultaneously both to cell-adhesion and to the dynamic rearrangement and restructuring of the ECM fibres. Furthermore, this will be embedded within a novel global multiscale moving boundary approach for the invading cancer cell population, which will incorporate two multiscale sub-frameworks that share the same macro-scale dynamics while exhibiting two independent in nature micro-dynamics that are separately linked through double feedback links to the

macro-scale tumour activity. The overall modelling framework will be accompanied by computational results that will explore the impact on cancer invasion patterns of different levels of cell adhesion in conjunction with the continuous ECM fibres rearrangement.

As considered in the first instance in Chapter 2, as a tumour increases in malignancy, the cancer cells adopt the ability to mutate into secondary cell subpopulations giving rise to a heterotypic tumour. This new cell subpopulation often carries higher invasive qualities and permits a quicker spread of the tumour. Therefore, building upon the multiscale modelling framework for cancer invasion within a fibrous ECM introduced in Chapter 3, in Chapter 4 we consider the process of local invasion by a heterotypic tumour consisting of two cancer cell populations mixed within a two-phase ECM. To that end, we will address the double feedback link between the tissue-scale cancer dynamics and the cell-scale molecular processes through the development of a two-part modelling framework that crucially incorporates the multiscale dynamic redistribution of oriented fibres occurring within a two-phase extra-cellular matrix and combines this with the multiscale leading edge dynamics exploring key matrix-degrading enzymes molecular processes along the tumour interface that drive the movement of the cancer boundary. The modelling framework will be accompanied by computational results that explore the effects of the underlying fibre network on the overall pattern of cancer invasion.

Finally, in Chapter 5, we look to further integrate the novel two-part multiscale model developed in Chapter 3 by incorporating the two independent micro-scales at the invasive edge of the tumour, namely, the fibres and MDEs boundary micro-processes. Specifically, this will be considering the degradation of micro-fibres to be not only a macroscopic interaction within the tumour region, but also a microscopic interaction dependent on the density and orientation of MDEs, specifically MMP-2,

on the tumour interface. We will consider the secretion of MMPs to be enhanced by the underlying fibre density, in addition to a fibre dependent anisotropic type diffusion of MMPs at the tumour boundary. These qualities combined with the microscopic degradation of micro-fibres will ensure the development of a further integrated multiscale model, whereby the two micro-scale systems are connected via a double feedback loop whilst embedded within the global multi-scale moving boundary model developed in Chapter 3.

Chapter 2

Heterotypic cell populations evolution in heterogeneous ECM

Aims and Novelty: This chapter opens the stage for the investigation of local tumour invasion by expanding on the moving boundary multiscale model initially introduced in Trucu et al. (2013). To that end, we investigate tumour morphology within a heterogeneous ECM by considering the effects of cell adhesion, namely cell-cell and cell-matrix adhesion of a heterotypic cell population.

2.1 Introduction

In recent years there have been many approaches taken to model the local invasion of cancer, in particular, three major players of cancer invasion are commonly chosen to be modelled, namely, the cancer cells, extracellular matrix, and MDEs. However, due to the highly complex nature of the process of tumour invasion, it is becoming increasingly difficult to justify the modelling of the interactions between each of these components at only one scale, for example, the MDEs contribute to interactions confined to the molecular scale, whilst the tumour itself can be modelled within

a continuous tissue-level scale. Hence, a multiscale moving boundary method of tumour invasion was proposed in Trucu et al. (2013) using three scale modelling; macro-scale occurring at the tissue level, micro-scale occurring at a cellular level and a naturally arising third scale which is used to characterise the invasive boundary of the tumour. We propose a model which builds on this original framework to incorporate the adhesive nature of cancer cells (Domschke et al., 2014) with both themselves and the surrounding microenvironment.

In this chapter we will explore the progression of a heterotypic cell population consisting of two cell sub-populations and the effects of both cell-cell and cell-matrix adhesion during tumour invasion. The content of this chapter has been explored and discussed in full in the publication Shuttleworth and Trucu (2018).

2.2 The Multiscale Modelling Approach

We will now briefly describe the multiscale framework initially introduced in Trucu et al. (2013) for modelling cancer cell invasion and then develop the macroscopic dynamics to incorporate cell-adhesion and a heterotypic tumour population. The multiscale framework developed in Trucu et al. (2013) considers detailed interactions taking place at the cellular- and tissue-scales alongside the linking between these different scales.

Within a maximal environmental tissue cube Y, at initial time t_0, $\Omega(t_0)$ represents the snapshot of the tumour domain where, at any spatio-temporal node $(x,t) \in \Omega(t) \times [0,T]$, the combined distributions of cancer cells $c_1(x,t)$ and $c_2(x,t)$ exercise their dynamics, with c_1 and c_2 representing the sub-populations 1 (primary tumour cells) and 2 (representing mutated cells), and their combined vector being denoted by $\mathbf{c}(x,t) = [c_1(x,t), c_2(x,t)]^T$. The tumour cell populations exercise their activity within a supporting density of ECM that is denoted here with $v(x,t)$, and

for compact notation, we will consider the combined vector of cancer cells, c_1, c_2 and ECM, v, defined as

$$\mathbf{u}(x,t) := (c_1(x,t), c_2(x,t), v(x,t))^T.$$

The spatial considerations play an important role in this model. We assume that the concentration of MDEs occupy a negligible amount of space within the tissue scale tumour, and similar to the approach in Domschke et al. (2014), we shall define the *volume fraction of occupied space* as

$$\rho(x,t) \equiv \rho(\mathbf{u}(x,t)) := \vartheta_v v(x,t) + \vartheta_c \sum_{n=1}^{2} c_n(x,t)$$

where ϑ_v, ϑ_c represent the fractions of physical space occupied by the ECM and cancer cells, respectively. However, while for the purpose of this work, at the tissue scales (macro-scale) we consider only cancer cells and ECM, the crucial activity of the MDEs and their dynamics is described at cell-scale (micro-scale) by accounting for spatial dynamics of proteolytic processes that occur along the invasive edge of the tumour. In the following Sections we will describe in detail the model, where we will take the same approach as in Trucu et al. (2013) and begin with a nondimensionalised model.

2.2.1 Macro-scale Dynamics

The dynamics of the two cell populations are similar in flavour. In the presence of a logistic proliferation law, per unit time, the primary tumour cells $c_1(x,t)$ are assumed to exercise spatial movement that is a combined effect of local brownian movement (approximated here through diffusion) and cell adhesion, and lose some of the cell population through certain levels of mutation towards a second more motile

and aggressive population $c_2(x,t)$. Once mutations have started occurring, under the presence of a logistic proliferation law, population c_2 begin its own dynamics, and so per unit time, this is also experiencing a spatial redistribution dictated by a local brownian movement (approximated again through diffusion) and cell adhesion. Therefore, mathematically, the dynamics can be recast as

$$\begin{aligned}
\tfrac{\partial c_1}{\partial t} &= \underbrace{\nabla\cdot[D_1\nabla c_1]}_{\text{random motility}} - \underbrace{\nabla\cdot[c_1\mathcal{A}(t,x,\mathbf{u}(\cdot,t))]}_{\text{adhesion}} + \underbrace{\mu_1 c_1(1-\rho(\mathbf{u}))^+}_{\text{proliferation}} - \underbrace{M_1(\mathbf{u},t)c_1}_{\text{mutation}} \\
\tfrac{\partial c_2}{\partial t} &= \underbrace{\nabla\cdot[D_2\nabla c_2]}_{\text{random motility}} - \underbrace{\nabla\cdot[c_2\mathcal{A}(t,x,\mathbf{u}(\cdot,t))]}_{\text{adhesion}} + \underbrace{\mu_2 c_2(1-\rho(\mathbf{u}))^+}_{\text{proliferation}} + \underbrace{M_1(\mathbf{u},t)c_1}_{\text{mutation}}
\end{aligned} \tag{2.1}$$

where: D_n, $n=1,2$ are the non-negative diffusion coefficients; $\mathcal{A}_n(x,t,\mathbf{u}(\cdot,t))$ is the non-local term accounting for cell adhesion incorporating both cell-cell and cell-matrix adhesion; μ_n describes the proliferation coefficient, here; and the final term M_1 describes the mutation from $c_1(x,t)$. To account for the physical space available and avoid overcrowding, we adopt here the proliferation term $(1-\rho(\mathbf{u}))^+ := \max\{0, 1-\rho(\mathbf{u})\}$ introduced in Gerisch and Chaplain (2008). Furthermore, the non-local term $\mathcal{A}_n(x,t,\mathbf{u}(\cdot,t))$, known as the adhesive flux, has a form of the type proposed in Gerisch and Chaplain (2008); Domschke et al. (2014), and is given as

$$\mathcal{A}_n(x,t,\mathbf{u}(\cdot,t)) = \frac{1}{R}\int\limits_{\mathbf{B}((0,0),R)} n(y)\cdot\mathcal{K}(||y||_2)\cdot g_n(\mathbf{u}(x+y,t),t)\chi_{\Omega(t)}(x+y)\,dy, \tag{2.2}$$

where $n=1,2$. This describes the motion of cells due to both cell-cell and cell matrix adhesion, which occurs as a result of the forces produced when adhesion bonds are both produced and broken. Here $R>0$ is the *sensing radius* of cell-cell and cell matrix interactions, $\mathbf{B}(0,R)\subset\mathbb{R}^2$ denotes the usual ball centred at zero and of radius R, and $\chi_{\Omega(t)}(\cdot)$ represents the characteristic function of $\Omega(t)$. At any time instance t, for any $x\in\Omega(t)$, the set $x+\mathbf{B}(0,R)$ is known as the *sensing region*

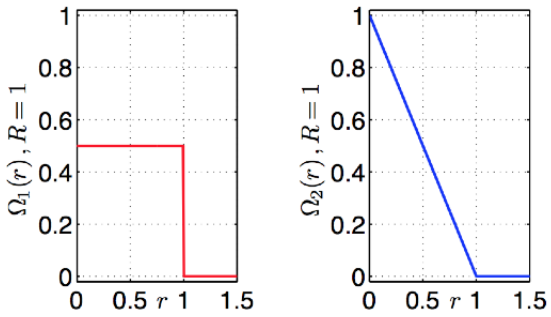

Figure 2.1: The kernel in red is shown for a 1-D example, $\mathcal{K}_1(r) = \frac{1}{2R}$, and the kernel in blue is shown for a 2-D example, $\mathcal{K}_2(r) = \frac{1}{R}\left(1 - \frac{r}{R}\right)$.

on which all the cells distributed at x, interact and form or break adhesion bonds with the cells located at $y \in \mathbf{B}(x, R) \cap \Omega(t)$. Further, $n(y)$ denotes the unit vector pointing from x to $x + y$, which is given by

$$n(y) := \begin{cases} y/||y||_2 & \text{if} \quad y \in \mathbf{B}(0, R) \setminus \{(0, 0)\}, \\ (0, 0) & \text{otherwise.} \end{cases} \tag{2.3}$$

where $|| \cdot ||_2$ is the l^2 norm as defined in (Yosida, 1980).

To describe the way the adhesion velocity of $\mathcal{A}_n(x, t, \mathbf{u}(\cdot, t))$ is influenced by the spatial distribution of the cell populations and ECM within the sensing region $\mathbf{B}(x, R)$, we use the radially dependent spatial kernel $\mathcal{K}(||y||_2)$. Examples of different kernels can be seen in Figure 2.1. The first kernel is an example of a step-like function in 1-dimension and the second kernel would give a cone-like shape in 2-dimensions. We shall use the spatial kernel defined by Gerisch and Chaplain (2008),

$$\mathcal{K}(r) := \frac{3}{\pi R^2}\left(1 - \frac{r}{R}\right), \tag{2.4}$$

this implies that for points in the sensing region x, as the distance r from x increases, the influence on adhesion-driven migration decreases, this can be seen schematically

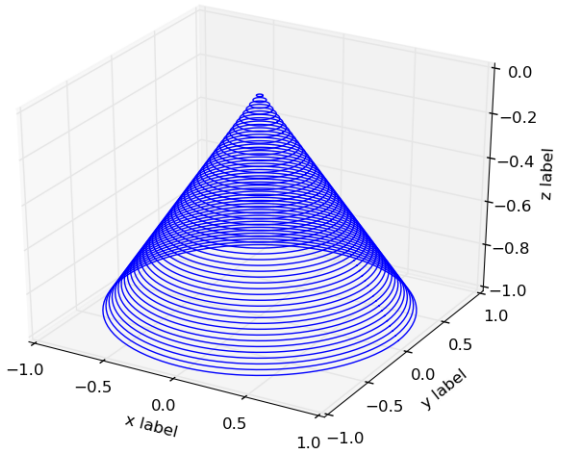

Figure 2.2: Plot of the 3D representation of the kernel given in equation (2.4).

in Figure 2.2. The adhesion function $\mathbf{g}(\mathbf{u}(x+y,t),t)$ is the vector of concentrations $\mathbf{u}$ at time t and at the point $x+y$. This non-local term explores the velocity of the cancer cells due to cell-cell and cell-matrix adhesion, sampled over the sensing region at x. That is, the adhesion velocity of the cells at x is in the direction at which the cells can form the most bonds both among themselves and with components of the ECM within the sensing region around x. Here, $g_n(\mathbf{u}(x+y,t),t)$, $n=1,2$ denotes the n-th component of

$$\mathbf{g}(t,\mathbf{u}) = [\mathbf{S}_{cc}\mathbf{c} + \mathbf{S}_{cv}v] \cdot (1-\rho(\mathbf{u}))^{+}, \tag{2.5}$$

and represents the cell-cell and cell-matrix adhesion properties for population n, which are explicitly enabled via the associated cell-cell and cell-matrix adhesion matrices, $\mathbf{S}_{cc}$, $\mathbf{S}_{cv} \in \mathbb{R}^{2,2}$, given by

$$\mathbf{S}_{cc} = \begin{bmatrix} S_{c_1,c_1} & S_{c_1,c_2} \\ S_{c_2,c_1} & S_{c_2,c_2} \end{bmatrix} \quad \text{and} \quad \mathbf{S}_{cv} = \begin{bmatrix} S_{c_1,v} & 0 \\ 0 & S_{c_2,v} \end{bmatrix}.$$

Furthermore, the overcrowding of the cell population and ECM is avoided through the term $(1 - \rho(\mathbf{u}))^+$, which ensures that if a point in the domain is already overcrowded (with cells and/or ECM), then that space point does not contribute towards biasing the tumour cells migration due to adhesion.

As a tumour becomes increasingly malignant, it can obtain the ability to mutate to a more aggressive form of cancer cell. For this reason, $M_1(\mathbf{u}, t)$ represents the mutation rate from population c_1 to population c_2. This mutation term is modelled as in Andasari et al. (2011); Domschke et al. (2014), namely

$$M_1(\mathbf{u}, t) = \delta_m H(t - t_{1,2}) \cdot H(v(x, t) - v_{\min}),$$

where $H(\cdot)$ denotes the usual Heaviside function and explore the fact that mutations from the primary tumour occur at a rate $\delta_m > 0$ after a certain time $t_{1,2}$ and in the presence of a minimal level $v_{\min}$ of ECM.

Within the tissue level, we must account for the activity of the surrounding environment of the tumour; the extracellular matrix. Per unit time, the ECM exhibits degradation in the presence of cancer cells, along with a general remodelling of itself. Thus, this dynamics can be described mathematically as

$$\frac{\partial v}{\partial t} = \underbrace{-\gamma \mathbf{c} v}_{\text{degradation}} + \underbrace{\mu_3 (1 - \rho(\mathbf{u}))^+}_{\text{ECM remodelling}}, \tag{2.6}$$

where: γ is the degradation coefficient multiplied by the current cancer cell distributions, and μ_3 is the remodelling constant, here the matrix remodelling is controlled by the volume filling factor $(1-\rho(\mathbf{u}))^+$. Biological evidence suggests that the remod-

elling of the ECM is not only an essential role of development and wound healing, but also in the development of cancer, contributing to processes such as metastasis and tumour cell invasion (Cox and Erler, 2011).

The macroscopic processes described in (2.1) and (2.6) have the initial conditions

$$\begin{aligned} c_1(x,0) &= c^0_{1_{\Omega(0)}}(x), \quad x \in \Omega(0), \\ c_2(x,0) &= c^0_{2_{\Omega(0)}}(x), \quad x \in \Omega(0), \\ v(x,0) &= v^0_{\Omega(0)}(x), \quad x \in \Omega(0), \end{aligned}$$

as well as zero Neumann and micro-scale moving boundary conditions defined in the following Section.

2.2.2 Top-down tissue- to cell-scale link and the resulting microscopic dynamics.

As discussed previously, cancer cell invasion is a multiscale process in which the micro-dynamics of the matrix degrading enzymes (MDEs) are responsible for the degradation of the ECM. The macroscopic processes defined by the equations (2.1) and (2.6) give rise to a micro-scale dynamics occurring along the invasive edge of the tumour, which, in turn, causes the macro-scale boundary of the tumour to advance further into the healthy tissue, as schematically illustrated in Figure 2.3.

Following a series of topological requirements as detailed in Trucu et al. (2013), at any given time t_0, for the maximal tissue cube $Y \subset \mathbb{R}^N$ (which includes the growing tumour $\Omega(t_0)$) we select the coarsest uniform decomposition of Y into the union of ϵY-sized dyadic cubes with the property that from this dyadic decomposition of Y taken together with the family of all *half-way shifted* dyadic cubes (as defined in Trucu et al. (2013)), a subfamily of over-lapping cubes $\{\epsilon Y\}_{\epsilon Y \in \mathcal{P}}$ can be extracted

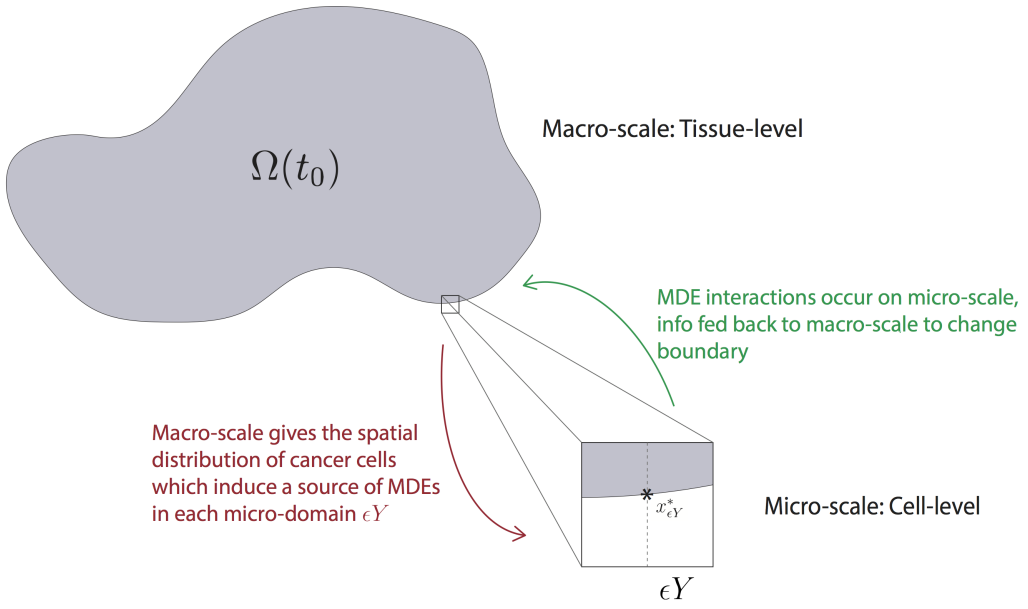

Figure 2.3: Schematic of macro-micro interactions.

with the following two key characteristics:

(1) each cube $\epsilon Y \in \mathcal{P}$ conveys a neighbourhood for $\epsilon Y \cap \partial\Omega(t_0)$ with both the part inside the tumour $\epsilon Y \cap \Omega(t_0)$ and the part outside the tumour $\epsilon Y \setminus \Omega(t_0)$ having their interior as connected sets;

(2) $\{\epsilon Y\}_{\epsilon Y \in \mathcal{P}}$ provides a complete covering of the boundary $\partial\Omega(t)$.

On this bundle of covering boundary micro-domains $\{\epsilon Y\}_{\epsilon Y} \in \mathcal{P}$, which is schematically illustrated in Figure 2.4, in the presence of the MDEs source induced from the macro-scale (as detailed in Trucu et al. (2013)), the MDEs micro-dynamics is then explored. The MDEs, such as matrix metalloproteinases (MMPs) of type 2, are produced within the cancer cells and distributed on the outer proliferating rim of the tumour, with their activity occurring within the area directly surrounding the tumour. Specifically, during a time interval $[t_0, t_0 + \Delta t]$, the cancer cells arriving within the outer proliferating rim of the tumour secrete these MDEs giving rise to a

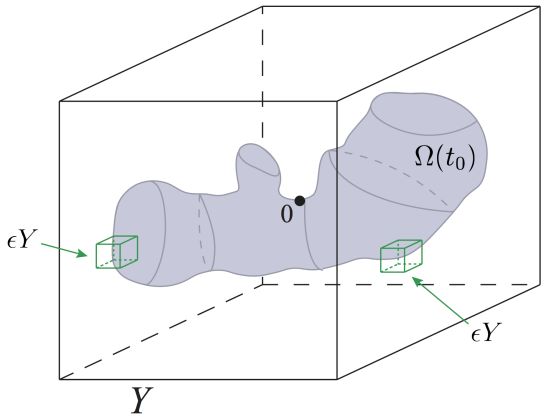

(a) Spatial domain of tumour

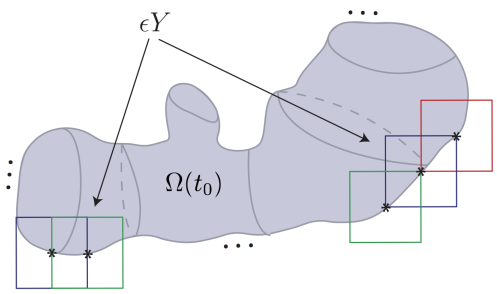

(b) Boundary tracking with overlapping micro-domains

Figure 2.4: Schematic diagrams showing in (a) the spatial cubic region Y centred at the origin in $\mathbb{R}^3$. The solid red lines represent the family of macroscopic ϵY cubes placed on the boundary of the tumour $\partial\Omega(t_0)$, and the pale green region represents the mass of cancer cells $\Omega(t_0)$. The appropriately chosen bundle $\{\epsilon Y\}_{\epsilon Y \in \mathcal{P}}$ of micro-domains introduced in Trucu et al. (2013) that covers the boundary $\partial\Omega(t_0)$ are shown in red and the corresponding half-way shifted cubes are illustrated by blue dashed lines.

source of such proteolytic enzymes that then exercise a cross-interface transport process within a cell-scale (micro-scale) size neighbourhood of $\partial\Omega(t_0)$, this way getting to interact directly and as a consequence significantly alter the ECM density that it meets in the peritumoural region. Thus, while assuming that we have no source for the cell-scale dynamics being formed outside $\Omega(t_0)$, at each instance $\tau \in [0, \Delta t]$ of the micro-dynamics and at each given micro-scale point $y \in \epsilon Y \cap \Omega(t_0)$ the source of MDEs is arising as a collective contribution of the cells from the outer proliferating rim that is located within a given distance $\delta > 0$ with respect to y. Therefore,

denoting the source by $f_{\epsilon Y}(y,\tau)$, this is mathematically formulated as

$$1.\quad f_{\epsilon Y}(y,\tau) = \frac{\int_{\mathbf{B}(y,\delta)\cap\Omega(t_0)} \alpha_1 c_1(x,t_0+\tau) + \alpha_2 c_2(x,t_0+\tau)dx}{\lambda(\mathbf{B}(y,\delta)\cap\Omega(t_0))}, \qquad y \in \epsilon Y \cap \Omega(t_0),$$

$$2.\quad f_{\epsilon Y}(y,\tau) = 0, \quad y \in \epsilon Y \setminus \big(\Omega(t_0) + \{z \in Y |\ ||z||_2 < \gamma\}\big), \tag{2.7}$$

where $\lambda(\cdot)$ is the standard Lebesgue measure on $\mathbb{R}^2$ (Yosida, 1980), $\mathbf{B}(y,\delta) := \{\xi \in Y |\ ||y-\xi||_\infty \leq \gamma\}$, α_i, $i = 1,2$ are MDEs secretion rates by each of the two cell sub-populations, and γ is a small parameter enabling us to capture a sharp but smooth decay to 0 of the MDEs source immediately outside the tumour boundary.

Finally, as the $\epsilon-$size neighbourhood of $\partial\Omega(t_0)$ given by the bundle of half-way overlapping micro-cubes ϵY enables a decoupling of the micro-dynamics on individual ϵYs, in the presence of the source (2.7), we assume in this work that the MDEs are simply locally diffusing. Hence, denoting the density for MDEs by $m(y,\tau)$, in each ϵY the micro-dynamics exercised by the MDEs is described by:

$$\frac{\partial m}{\partial \tau} = \underbrace{\Delta m}_{\text{diffusion}} + \underbrace{f_{\epsilon Y}(y,\tau)}_{\text{source term}}, \qquad y \in \epsilon Y,\ \tau \in [0,\Delta t]. \tag{2.8}$$

with zero initial conditions and zero Neumann boundary conditions.

Macroscopic boundary movement induced by micro-scale. During the micro-dynamics, the MDEs present in the peritumoural region interact with the ECM captured by each ϵY cube on the boundary of the tumour. Within each micro-domain ϵY, the degradation of the ECM is dependent on the pattern of the front of the advancing spatial distribution of MDEs in $\epsilon Y \setminus \Omega(t_0)$ that have been secreted by the cancer cells. This pattern of the degradation defines a movement

direction, $\eta_{\epsilon Y}$, and displacement magnitude, $\xi_{\epsilon Y}$, for the progression of the tumour boundary. This activity is the driving force behind the relocation of the boundary midpoints $x^*_{\epsilon Y}$ which are translated to the movement of the tumour boundary at macro-scale. As illustrated schematically in Figure 2.5, this choreographic movement of the tumour boundary captured by the micro-domain ϵY is represented back at macro-scale through the relocation of the tumour boundary midpoint $x^*_{\epsilon Y}$, which is located at the intersection of $\partial\Omega(t_0) \cap \epsilon Y$ with the median of ϵY perpendicular to the side of ϵY inside the cancer region, this being chosen as the inner most point in this intersection with respect to the cancer region.

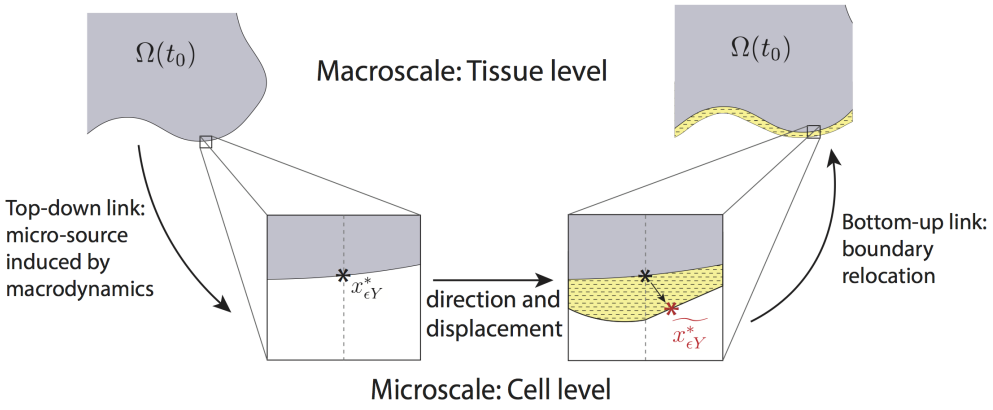

Figure 2.5: Schematic of one macro-micro stage in the multiscale process. The projected ϵY cube from macro- to micro-scale with boundary point reallocation occurring through the micro dynamics and the new relocated boundary position projected back into the macroscopic scale at the tissue level.

Thus, proceeding as detailed in Trucu et al. (2013), an appropriate uniform dyadic decomposition $\{\mathcal{D}_j\}_{j=1,p_{\epsilon Y}}$, with $p_{\epsilon Y} := 2^{k_{\epsilon Y}}$ is chosen for ϵY. Since the pattern of degradation is ultimately given by the part of the level set of significant MDEs peaks that are transported at the largest possible distance from the tumour interface $\epsilon Y \cap \Omega(t_0)$ within the peritumoural region $\epsilon Y \setminus \Omega(t_0)$, as discussed in Trucu et al. (2013), by denoting the barycentre of each D_j by y_j, the movement direction

$\eta_{\epsilon Y}$ and displacement magnitude $\xi_{\epsilon Y}$ of each boundary midpoint $x^*_{\epsilon Y}$ are represented mathematically as

$$\eta_{\epsilon Y} = x^*_{\epsilon Y} + \nu \sum_{l \in \mathcal{J}^*} \left(\int_{\mathcal{D}_j} m(y, \tau_f)\ dy \right) \overrightarrow{x^*_{\epsilon Y} y^*_j}$$

and

$$\xi_{\epsilon Y} = \sum_{l \in \mathcal{J}^*} \frac{\int_{\mathcal{D}_j} m(y, \tau_f)\ dy}{\sum_{l \in \mathcal{I}^*_\delta} \int_{\mathcal{D}_j} m(y, \tau_f)\ dy} |\overrightarrow{x^*_{\epsilon Y} y^*_j}|.$$

where $\mathcal{J}^*$ is the family of indices of the dyadic cubes which track only the most advanced frontier formed by the significant peaks at the tip of the progressing front of the MDEs (i.e., situated at the furthest away distance from the $x^*_{\epsilon Y}$) within the micro-domain ϵY.

Although a movement direction and displacement have been derived for each $x^*_{\epsilon Y}$, movement will only occur if the ECM degradation is of a certain local strength. The strength of this local ECM degradation is explored through the transitional probability q^* defined in Trucu et al. (2013) and it is a quantification of the amount of MDE in $\epsilon Y \setminus \Omega(t_0)$ relative to the total amount of MDE in the micro domain ϵY. Therefore the midpoint $x^*_{\epsilon Y}$ will only move to a new spatial position if and only if $q^*(x^*_{\epsilon Y}) := q^*(\epsilon Y \setminus \Omega(t_0))$ exceeds a certain threshold $\omega_{\epsilon Y} \in (0, 1)$ that captures local peritumoural tissue characteristics. Hence, we find that the new invasive boundary $\partial\Omega(t_0 + \Delta t)$ will be an interpolation of the new locations for the points that exercised the movement and those boundary points $x^*_{\epsilon Y}$ that did not move. The invasion process will continue on the newly expanded domain $\Omega(t_0 + \Delta t)$ with a new set of macro-micro stage dynamics on the next multiscale time step $[t_0 + \Delta t, t_0 + 2\Delta t]$. The initial conditions on the expanded domain $\Omega(t_0 + \Delta t)$ are determined by the solutions at the final time of the previous invasion step, as detailed in Trucu et al.

(2013), namely,

$$c_{n_{\Omega(t_0+\Delta t)}}(x, t_0+\Delta t) = c_{n_{\Omega(t_0)}}(x, t_0+\Delta t)(\chi_{\Omega(t_0)\bigcup_{\epsilon Y\in\mathcal{P}}\epsilon Y} * \psi_\gamma) \tag{2.9}$$
$$v_{\Omega(t_0+\Delta t)}(x, t_0+\Delta t) = v_{\Omega(t_0)}(x, t_0+\Delta t)(\chi_{\Omega(t_0)\bigcup_{\epsilon Y\in\mathcal{P}}\epsilon Y} * \psi_\gamma + \chi_{Y\setminus\Omega(t_0)\bigcup_{\epsilon Y\in\mathcal{P}}\epsilon Y} * \psi_\gamma)$$

where $n = 1, 2$ denotes the cancer cell subpopulations c_1 and c_2 and $\chi_{\Omega(t_0)\bigcup_{\epsilon Y\in\mathcal{P}}\epsilon Y} * \psi_\gamma$ and $\chi_{Y\setminus\Omega(t_0)\bigcup_{\epsilon Y\in\mathcal{P}}\epsilon Y} * \psi_\gamma$ are the characteristic functions corresponding to the sets $\Omega(t_0)\bigcup_{\epsilon Y\in\mathcal{P}_\epsilon}\epsilon Y$ and $Y\setminus\Omega(t_0)\bigcup_{\epsilon Y\in\mathcal{P}_\epsilon}\epsilon Y$, and choosing $\gamma \ll \frac{\epsilon}{3}$, $\psi_\gamma : \mathbb{R}^N \to \mathbb{R}_+$ is constructed as a smooth compact support function with $\text{supp}(\psi_\gamma) = \{z \in \mathbb{R}^N |\ ||z||_2 \leq \gamma\}$. That is the standard mollifier defined in Trucu et al. (2013), and described in Appendix C.1.

2.2.3 Summary of the Global Multiscale Model

At each stage of the invasion process, the macro-scale dynamics govern the spatial distributions of both cancer cell populations and the ECM density. The initial distribution of cancer cells $\Omega(t_0)$ induce a source of MDEs (2.7) on the boundary at each micro-domain ϵY. The microscopic dynamics induce a change in the boundary position and this movement is then translated back into the macro-scale, where the new spatial positions of the boundary $\widetilde{x^*_{\epsilon Y}}$ are interpolated with the spatial positions that could not be moved and a new invading edge in obtained as illustrated in Figures 2.3 and 2.5. The next macro-micro stage will then proceed using the solution (2.9) from the previous step as the new initial conditions and invasion will continue. Once the invasion process has advanced, mutations will begin to occur between cell populations. The mutated population c_2 carries a higher malignancy than population c_1, thus it secretes a higher volume of MDEs, which in turn will allow the second population to advance quicker.

2.3 Numerical approaches and simulations

The numerical scheme developed for the multiscale model described above is organised on similar structure as the multiscale computational framework introduced in full details in Trucu et al. (2013), incorporating two big components corresponding to the macro- and micro-scales processes involved, namely: (1) a finite differences based macro-solver that addresses the macro-dynamics; and (2) a finite element micro-solver exploring the micro-dynamics that is based on a standard approach involving bilinear shape functions on a squared mesh for each micro-domain (detailed in Appendix B.1). While the micro-solver with finite element is precisely the one used in Trucu et al. (2013), the macro-solver however required further development of the finite difference scheme to accommodate the second population c_2 and incorporate the contribution of the non-local adhesion fluxes $\mathcal{A}_n$ within the right hand side spatial operator $\nabla \cdot [\nabla c_n - c_n \mathcal{A}_n(x, t, \mathbf{u}(\cdot, t))]$ appearing in the dynamics of both cell sub-populations, c_1 and c_2.

In the following subsection, we will address the all the new developments required by the macro-dynamics. We start by focussing first on the special treatment for the spatial discretisation of the adhesion fluxes $\mathcal{A}_n$, and then we will proceed with the discretisation of the rest of the terms involved in the spatial operator $\nabla \cdot [\nabla c_n - c_n \mathcal{A}_n(x, t, \mathbf{u}(\cdot, t))]$ which will eventually complete the spatial discretisation. Finally, to complete the scheme, for the time-marching, we use a standard trapezoidal-based predictor-corrector method in time.

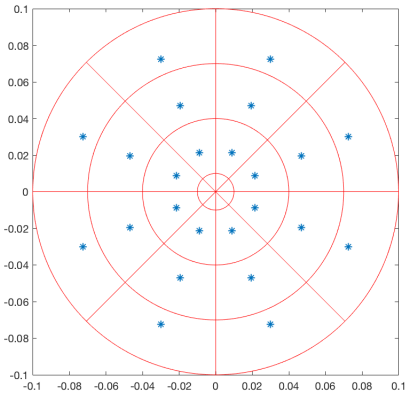

Figure 2.6: Sensing region $\mathbf{B}(x, R)$ approximated by the annulus radial sectors with the barycentre $\mathbf{b}_{\mathcal{S}_l}$ associated to each sector $\mathcal{S}_l$ highlighted with a blue dot.

2.3.1 Brief description of the discretisation of the right hand side spatial operator in the macro-solver

As already mentioned above, an important aspect within the macroscopic part of our solver is the numerical approach for the adhesive fluxes $\mathcal{A}_n$ (that explores the effects of cell-cell and cell-matrix adhesion of population c_n), which involves off-grid computations and we address these as follows. We decompose the sensing region $\mathbf{B}(x, R)$ in $s2^m$ annulus radial sectors $\mathcal{S}_1, \ldots, \mathcal{S}_{2^m}$ (obtained by intersecting s annuli with 2^m uniform radial sectors of $\mathbf{B}(x, R)$, as shown in Figure 2.6, with the radius of the central circle taken small enough so that this is neglected in the subsequent computation steps). Then, for each $\mathcal{S}_l$, we evaluate the total population c_1, total population c_2, and the total ECM mass distributed on $\mathcal{S}_l$ that are given by

$$\omega_{\mathcal{S}_l,c_1}(t) := \frac{1}{\lambda(\mathcal{S}_l)} \int_{\mathcal{S}_l} c_1(x,t)dx, \quad \omega_{\mathcal{S}_l,c_2}(t) := \frac{1}{\lambda(\mathcal{S}_l)} \int_{\mathcal{S}_l} c_2(x,t)dx, \tag{2.10}$$
$$\text{and} \quad \omega_{\mathcal{S}_l,v}(t) := \frac{1}{\lambda(\mathcal{S}_l)} \int_{\mathcal{S}_l} v(x,t)dx,$$

respectively. For implementation, for each sector $\mathcal{S}_l$, we consider first the associated centroid denoted by $\mathbf{b}_{\mathcal{S}_l}$, and we approximate these mean-values on $\mathcal{S}_l$ simply through the values of each of these three functions at the centroid $\mathbf{b}_{\mathcal{S}_l}$, namely as: $c_1(\mathbf{b}_{\mathcal{S}_l}, t)$, $c_2(\mathbf{b}_{\mathcal{S}_l}, t)$ and $v(\mathbf{b}_{\mathcal{S}_l}, t)$. These values are obtained by involving Delaunay triangulation on the macroscopic mesh for the points within the sensing region $\mathbf{B}(0, R)$ to identify the on-grid triangle ΔABC and the associated the barycentre coordinates $\beta_A, \beta_B, \beta_C \in [0, 1]$ (with $\beta_A + \beta_B + \beta_C = 1$) for the off-grid centroids $\mathbf{b}_{\mathcal{S}_l}$. These barycentre coordinates are then used to approximate the value of the three functions simply as

$$
\begin{aligned}
c_1(\mathbf{b}_{\mathcal{S}_l}, t) &\simeq \beta_A c_1(A, t) + \beta_B c_1(B, t) + \beta_C c_1(C, t),\\
c_2(\mathbf{b}_{\mathcal{S}_l}, t) &\simeq \beta_A c_2(A, t) + \beta_B c_2(B, t) + \beta_C c_2(C, t),\\
v(\mathbf{b}_{\mathcal{S}_l}, t) &\simeq \beta_A v(A, t) + \beta_B v(B, t) + \beta_C v(C, t).
\end{aligned}
$$

Finally, using $\mathbf{b}_{\mathcal{S}_l}$ for the barycenter of $\mathcal{S}_l$, $\forall l = 1, \ldots, s2^m$ and evaluating the unit vector $\mathbf{n}(\mathbf{b}_{\mathcal{S}_l}) := \frac{\mathbf{b}_{\mathcal{S}_l} - x}{\|\mathbf{b}_{\mathcal{S}_l} - x\|_2}$, the adhesion flux $\mathcal{A}_n$, $n = 1, 2$, is approximated by

$$
\mathcal{A}_n(x, t, \mathbf{u}(\cdot, t)) = \sum_{\substack{l=1 \\ \mathbf{b}_{\mathcal{S}_l} \cap \Omega(t_0) \neq \emptyset}}^{s2^m} \frac{\lambda(\mathcal{S}_l)}{R} \mathbf{n}(\mathbf{b}_{\mathcal{S}_l}) \cdot \mathcal{K}(\mathbf{b}_{\mathcal{S}_l}) g_n(\tilde{\mathbf{u}}(\mathbf{b}_{\mathcal{S}_l}, t))
$$

where

$$
\tilde{\mathbf{u}}(\mathbf{b}_{\mathcal{S}_l}, t) := [\omega_{\mathcal{S}_l, c_1}(t), \omega_{\mathcal{S}_l, c_2}(t), \omega_{\mathcal{S}_l, v}(t)]^T
$$

and

$$
g_n(\tilde{\mathbf{u}}(\mathbf{b}_{\mathcal{S}_l}, t)) = [\mathbf{S}_{cc}[\omega_{\mathcal{S}_l, c_1}(t), \omega_{\mathcal{S}_l, c_2}(t)]^T + \mathbf{S}_{cv}\omega_{\mathcal{S}_l, v}(t)] \cdot (1 - \rho(\tilde{\mathbf{u}}(\mathbf{b}_{\mathcal{S}_l}, t)))^+
$$

For the actual implementation, we discretise the entire domain Y by considering a uniform spatial mesh of fixed size $h > 0$, i.e., $\Delta x = \Delta y = h$ as well as the time

interval $[t_0, t_0+\Delta t]$ into k uniformly distributed time steps, i.e., $\delta_\tau = \frac{\Delta t}{k}$. In order to approximate the reaction-diffusion equations (2.1), we develop a predictor-corrector in time scheme; whilst the term $\nabla \cdot [\nabla c_n - c_n \mathcal{A}_n(x, t, \mathbf{u}(\cdot, t))]$ will be approximated through a second-order mid-point rule (LeVeque, 2007) as detailed below.

In brief, for any time step of index $p = 0, ..., k$ and for the spatial nodes (i, j), where $i = 1, ..., q,\ j = 1, ..., q$ are the indices for the $x-$ and y-direction, respectively, and considering Neumann zero boundary conditions, we introduce the midpoint approximations as:

$$\begin{cases} c^p_{n,i,j+\frac{1}{2}} := \frac{c^p_{n,i,j}+c^p_{n,i,j+1}}{2} \\ c^p_{n,i,j-\frac{1}{2}} := \frac{c^p_{n,i,j}+c^p_{n,i,j-1}}{2} \\ c^p_{n,i+\frac{1}{2},j} := \frac{c^p_{n,i,j}+c^p_{n,i+1,j}}{2} \\ c^p_{n,i-\frac{1}{2},j} := \frac{c^p_{n,i,j}+c^p_{n,i-1,j}}{2} \end{cases} \quad \text{and} \quad \begin{cases} \mathcal{A}^p_{n,i,j+\frac{1}{2}} := \frac{\mathcal{A}^p_{n,i,j}+\mathcal{A}^p_{n,i,j+1}}{2} \\ \mathcal{A}^p_{n,i,j-\frac{1}{2}} := \frac{\mathcal{A}^p_{n,i,j}+\mathcal{A}^p_{n,i,j-1}}{2} \\ \mathcal{A}^p_{n,i+\frac{1}{2},j} := \frac{\mathcal{A}^p_{n,i,j}+\mathcal{A}^p_{n,i+1,j}}{2} \\ \mathcal{A}^p_{n,i-\frac{1}{2},j} := \frac{\mathcal{A}^p_{n,i,j}+\mathcal{A}^p_{n,i-1,j}}{2} \end{cases}$$

We also have the following notation for the central differences:

$$\begin{cases} [c_{n,y}]^p_{i,j+\frac{1}{2}} := \frac{c^p_{n,i,j+1}-c^p_{n,i,j}}{\Delta y} \\ [c_{n,y}]^p_{i,j-\frac{1}{2}} := \frac{c^p_{n,i,j}-c^p_{n,i,j-1}}{\Delta y} \\ [c_{n,x}]^p_{i+\frac{1}{2},j} := \frac{c^p_{n,i+1,j}-c^p_{n,i,j}}{\Delta x} \\ [c_{n,x}]^p_{i-\frac{1}{2},j} := \frac{c^p_{n,i,j}-c^p_{n,i-1,j}}{\Delta x} \end{cases}$$

Using this notation, the approximation for (ignoring the constant parameters at the moment) $\nabla \cdot [\nabla c_n - c_n \mathcal{A}_n(x, t, \mathbf{u}(\cdot, t))]$ in (2.1) is as follows:

$$\nabla \cdot [\nabla c_n - c_n \mathcal{A}_n(x,t,\mathbf{u}(\cdot,t))] = \operatorname{div}[\nabla c_n - c_n \mathcal{A}_n(x,t,\mathbf{u}(\cdot,t))]^p_{i,j}$$
$$\simeq \frac{[c_{n,x}]^p_{i+\frac{1}{2},j} - [c_{n,x}]^p_{i-\frac{1}{2},j} - c^p_{n,i+\frac{1}{2},j} \cdot \mathcal{A}^p_{n,i+\frac{1}{2},j} + c^p_{n,i-\frac{1}{2},j} \cdot \mathcal{A}^p_{n,i-\frac{1}{2},j}}{\Delta x}$$
$$+ \frac{[c_{n,y}]^p_{i,j+\frac{1}{2}} - [c_{n,y}]^p_{i,j-\frac{1}{2}} - c^p_{n,i,j+\frac{1}{2}} \cdot \mathcal{A}^p_{n,i,j+\frac{1}{2}} + c^p_{n,i,j-\frac{1}{2}} \cdot \mathcal{A}^p_{n,i,j-\frac{1}{2}}}{\Delta y} \tag{2.11}$$

For the time discretisation of equation (2.6), following Trucu et al. (2013), we have used a predictor-corrector method, where the predictor is given by a second-order Adams-Bashforth scheme and the corrector uses a second-order trapezoidal approximation (LeVeque, 2007).

2.3.2 Simulations in two spatial dimensions

To explore numerically multiscale model of cancer invasion given in (2.1)-(2.8), we consider region $Y := [0,4] \times [0,4]$ discretised uniformly with macroscopic spatial step size $h = 0.03125$, while the time step is taken here as $\delta_\tau = 10^{-3}$. Assuming that initially population c_2 has no distribution and population c_1 occupies a region $\Omega(0) := \mathbf{B}((2,2), 0.5)$ positioned at the centre of the domain Y. The initial condition for cancer cell population c_1 is taken as in Trucu et al. (2013) and is given by

$$c_1(x,0) = 0.5 \left(\exp\left(-\frac{||x-(2,2)||_2^2}{0.03} \right) - \exp(-28.125) \right) \left(\chi_{\mathbf{B}((2,2),0.5-\gamma)} * \psi_\gamma \right),$$

where ψ_γ is the mollifier defined in Trucu et al. (2013) with $\gamma << \frac{\Delta x}{3}$. Population c_2 initially has zero density, so $c_2(x,0) = 0$ and we assume a heterogeneous distribution for the initial ECM density based on the initial condition proposed in Domschke et al.

(2014) and given by

$$v(x,0) = \min\left\{h(x_1,x_2), \frac{1-\vartheta_c c(0,x)}{\vartheta_v}\right\}, \tag{2.12}$$

where

$$h(x_1,x_2) = \frac{1}{2} + \frac{1}{2}\sin(\zeta x_1 x_2)^3 \cdot \sin\left(\zeta\frac{x_2}{x_1}\right), \tag{2.13}$$

with

$$(x_1,x_2) = \frac{1}{3}(x+1.5) \ \in [0,1]^2 \text{ for } x \in Y, \quad \zeta = 7\pi.$$

Here we consider the volume fraction of cells and ECM to be $\vartheta_c \in [\frac{\pi}{6}, 1]$ and $\vartheta_v \in [0, \frac{5\pi}{6}]$. The initial condition for MDEs is $m(x,0) = 0.5c_1(x,0)$, however since this closely resembles the profile of the cancer cell distribution, we shall not present the simulation results of MDE concentration. The initial conditions of the combined cell populations and ECM density can be seen in Figure 2.7.

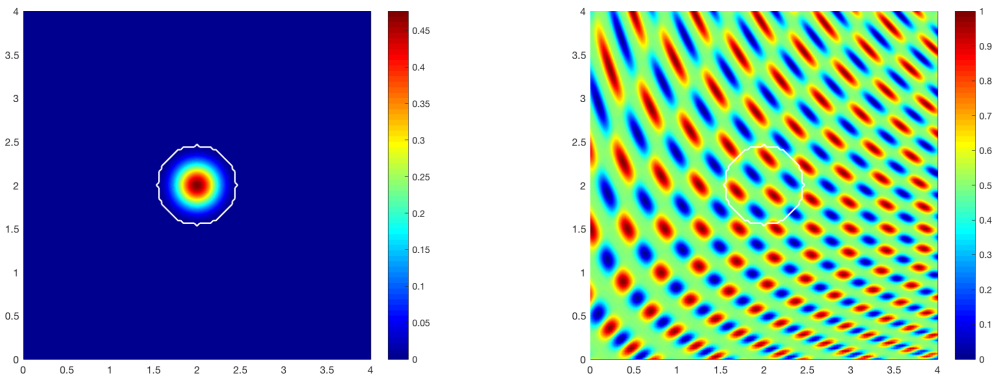

(a) Initial cancer distribution **(b)** Initial ECM density

Figure 2.7: Initial conditions showing the distribution of cancer cells (a), and the density of ECM (b) with the invasive boundary of the tumour represented by the white contour.

Throughout these simulations, unless otherwise stated, we use the following parameter set for the non-dimensionalised system of equations (2.1) and (2.6), which

were estimated based on those used in Domschke et al. (2014), namely:

$$\Sigma_p: \quad \begin{array}{lllll} D_1 = 10^{-3}, & D_2 = 10^{-3}, & \gamma = 2, & t_{1,2} = 10, & \alpha_1 = 1 \quad \alpha_2 = 1.5 \\ \mu_1 = 0.25, & \mu_2 = 0.25, & \mu_3 = 0, & v_{\min} = 0.3 & \delta = 0.3 \end{array}$$

We also have here the adhesive strengths matrices $\mathbf{S}_{cc}$ and $\mathbf{S}_{cv}$ given by

$$\mathbf{S}_{cc} = \begin{pmatrix} 0.5 & 0 \\ 0 & 0.3 \end{pmatrix} \quad \text{and} \quad \mathbf{S}_{cv} = \begin{pmatrix} 0.3 & 0 \\ 0 & 0.6 \end{pmatrix}. \tag{2.14}$$

Initially, we have no cross-adhesion occurring, so $S_{c_1,c_2} = 0 = S_{c_2,c_1}$. All model simulations in this thesis have been performed using MATLAB® (MATLAB, 2017).

Figure 2.9 gives simulations using the initial conditions and parameter set Σ_p as stated above. They are shown at stages $25\Delta t$, $50\Delta t$ and $75\Delta t$. Here, we also show the simulations at stage $10\Delta t$, Figure 2.8, the stage at which mutations occur. By this stage, population c_1 has degraded and lowered the density of the ECM in which the initial cancer distribution was placed. The threshold on which mutations can occur, δ, is higher than the resulting density of ECM, thus when mutations occur, they only take place on the outer edge of the tumour, where $\delta > 0$, as the ECM density is too low inside to support the mutations. The white contour shows the proliferating boundary of the tumour, which, at this stage has consistently expanded outwards into the ECM. Due to the initial conditions of the ECM, there are patches of high and low density areas throughout the domain. These patches vary in distance and size from one another, which reflects a non-symmetric microenvironment for the cells. The pattern of the advancing front of the tumour loosely follows this pattern of ECM. Where there are dense patches of low density we see slower cancer progression; this is because there is a lower overall density of matrix for the cells to adhere.

After 25 macro-micro stages, $25\Delta t$, population c_1 and c_2 are both increasing in density, with population c_1 changing shape as the cells continue to mutate. As the

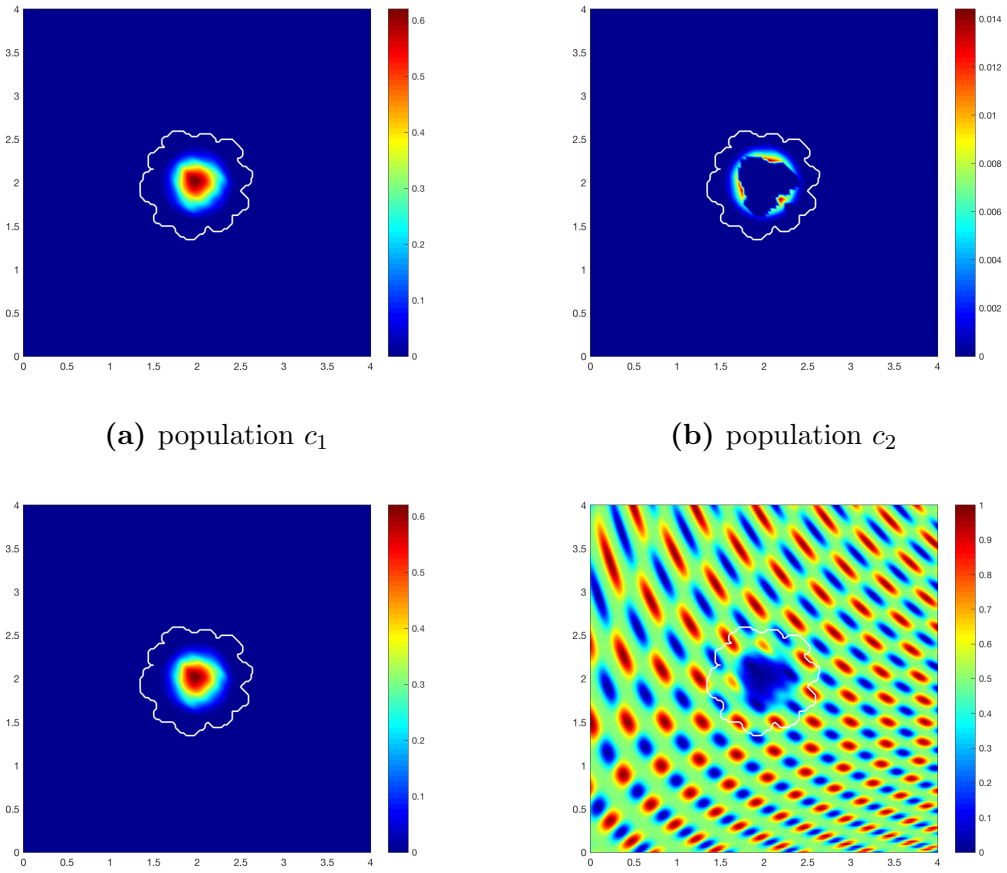

(a) population c_1 **(b)** population c_2

(c) combined populations **(d)** ECM density

Figure 2.8: Simulation results of model at stage $10\Delta t$ when the mutations from population c_1 start to occur.

tumour spreads, a larger region of ECM is degraded, which is shown in the plot for ECM.

As the cancer continues to invade, a wider region of the ECM is destroyed and the proliferating edge of the tumour continues to reach outwards, see stages $50\Delta t$ and $75\Delta t$ in Figure 2.9. The invasive edge of the tumour loosely follows the pattern of ECM at each stage, and small islands start to appear over low density patches of ECM. These islands have zero ECM density and hence cause the cancer cells to be slow to invade as there is an insufficient level of ECM for which the cells can

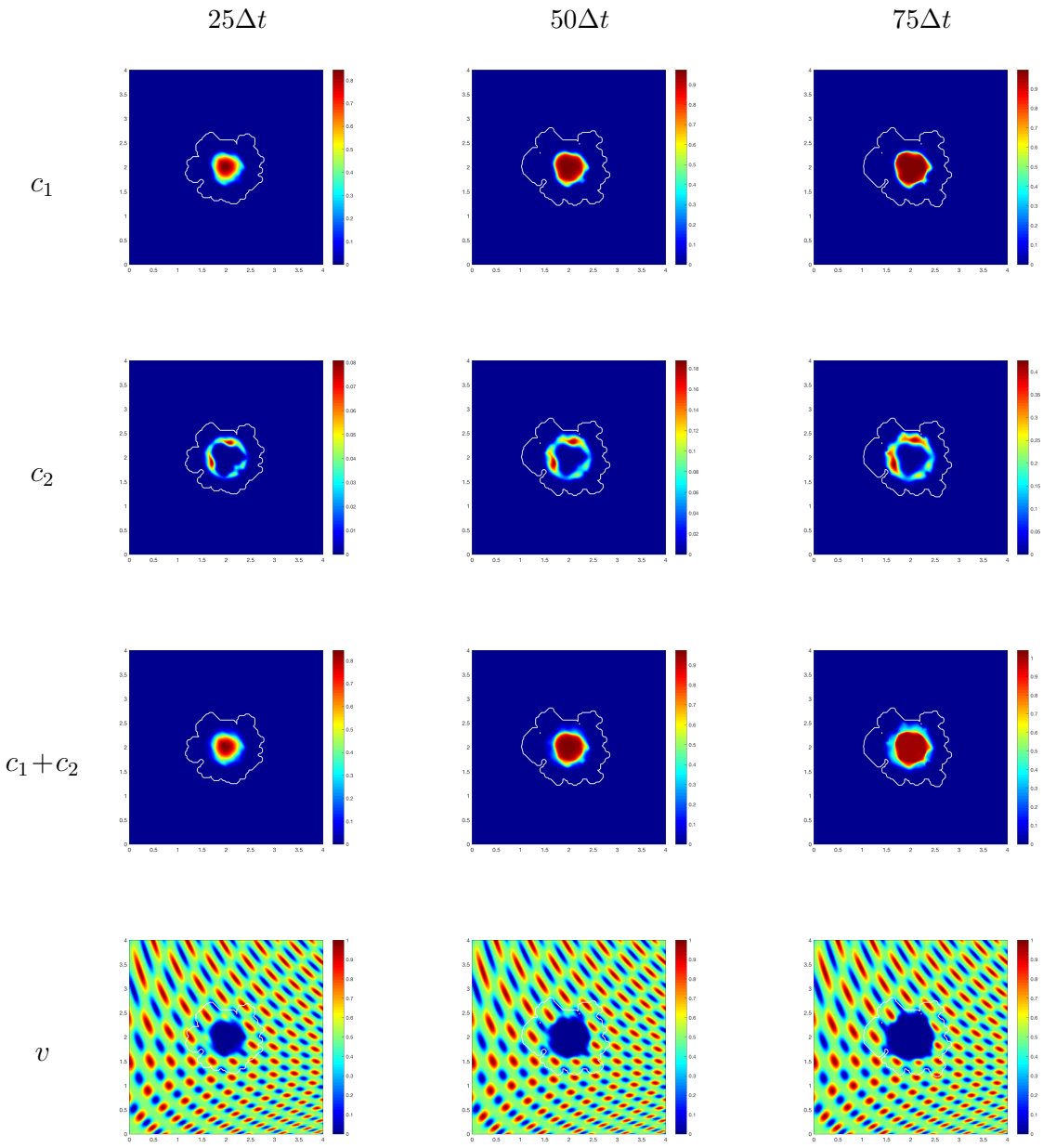

Figure 2.9: Simulation results of model using the parameter set Σ_p and adhesion matrices (2.14). Plots of both cancer populations c_1 and c_2, as well as the combined cancer distributions and the ECM densities at stages $25\Delta t$, $50\Delta t$, and $75\Delta t$.

adhere. This pattern of the boundary is due to the multiscale nature of the invasion process, where the macro-dynamics govern the source of the MDEs on the invading

edge and then movement of the boundary is determined in each boundary cube ϵY by the resulting micro-dynamics. The MDEs produced by the cancer cells can only degrade locally; this becoming apparent from the resulting ECM plots.

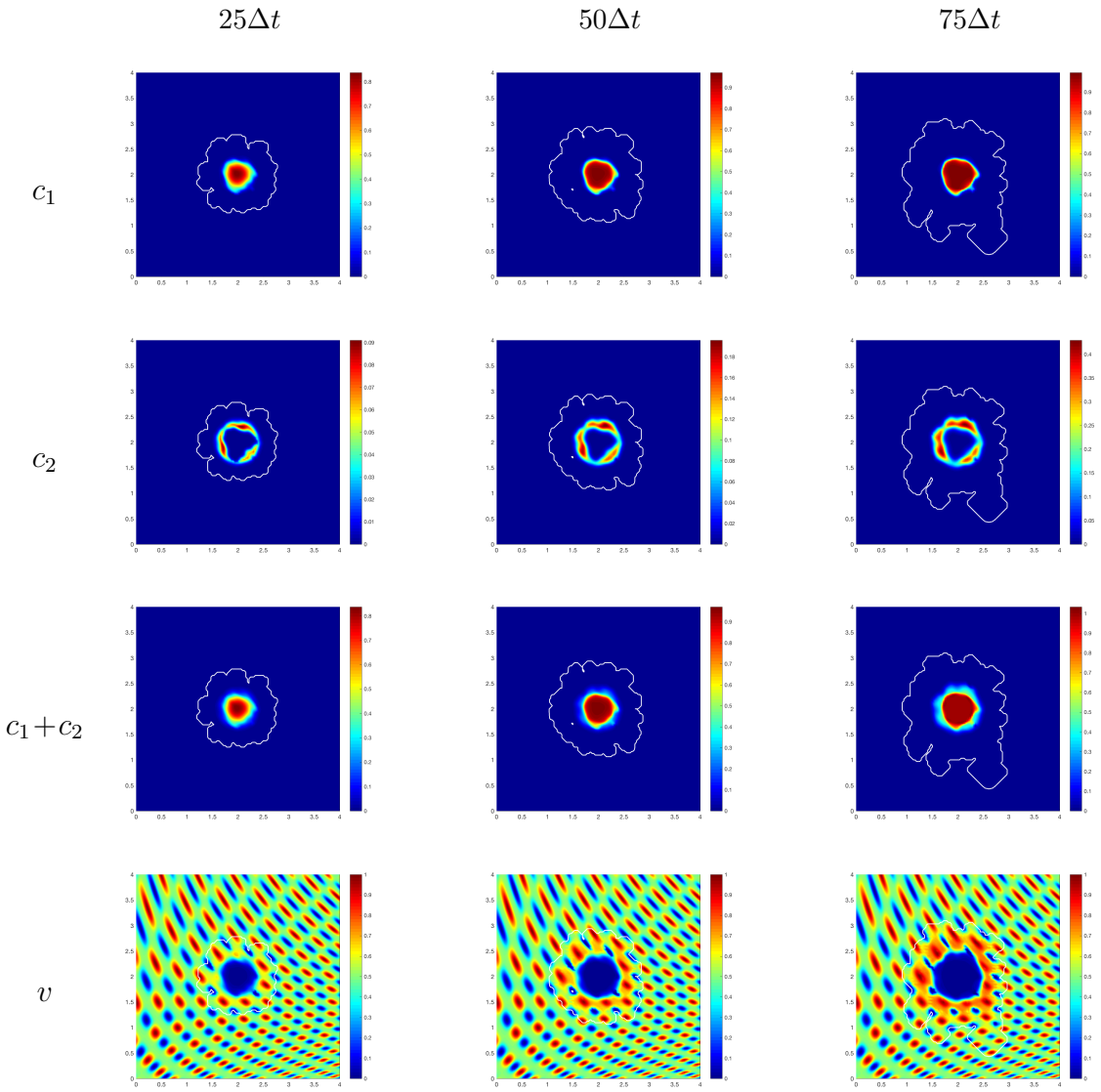

Figure 2.10: Simulation results of model using the parameter set Σ_p and adhesion matrices (2.14) with ECM remodelling introduced, $\mu_3 = 0.04$. Plots of both cancer populations c_1 and c_2, as well as the combined cancer distributions and the ECM densities at stages $25\Delta t$, $50\Delta t$, and $75\Delta t$.

We now want to consider the effect of matrix remodelling on the progression of

cancer. Figure 2.10 shows simulations again using the parameter set Σ_p, but this time with the ECM remodelling rate μ_3 being increased from 0 to 0.04. Here we see that the spread of cancer is ultimately covering a larger area than in the absence of remodelling, Figure 2.9. Population c_2 displays a much larger spread of density surrounding population c_1 than in the absence of ECM remodelling. The increased density of ECM surrounding the cells gives more opportunity for adherence and opens a greater number of pathways in which the cells can invade.

The boundary of the cancer is following the pattern of the ECM more consistently than in Figure 2.9, this is due to the higher density of the remodelled ECM allowing for stronger adhesive qualities between the cancer cells and ECM. We can again see the invasion briefly halted at patches of lower density, but this is for a shorter period than before, with the islands being fully invaded by the later stages.

Figure 2.11 gives simulations where the cell-matrix adhesion between cancer cell population c_1 and the ECM, $S_{c_1,v}$, has been increased from 0.3 to 0.5 and the cell-matrix adhesion between cell population c_2 and the ECM, $S_{c_2,v}$, has been decreased from 0.6 to 0.5, i.e., the adhesion rate between the cells and matrix are equal for both populations. The proliferating edge of the tumour is lobular in the way it follows the pattern of the ECM, much like the simulations in Figure 2.9, with protrusions pushing out in the direction of high density areas of the matrix. Although the cell-matrix adhesion term is now equal for both populations, the S_{c_1,c_1} and S_{c_2,c_2} have remained the same, thus we do not see a great change in the profile of the levels of cancer cell densities of the main body of the tumour itself, but we instead see a difference in the pattern of the invading edge of the tumour, due to the further spread of the lower levels of these densities closer to the invasive edge of the tumour. The increase in adhesion between population c_1 and the matrix sees the invading boundary stick closer to the main body of the tumour, particularly to population

c_2.

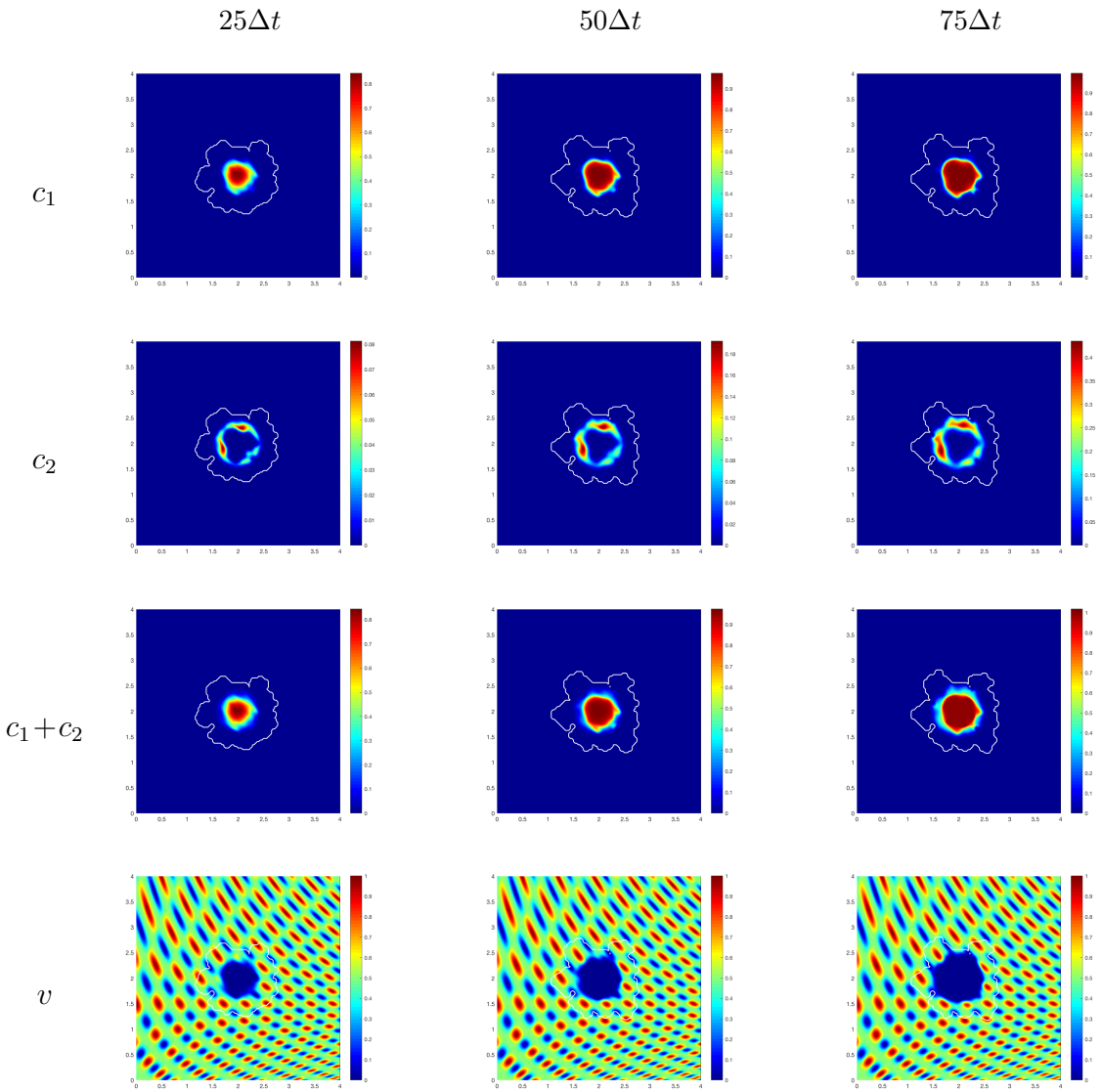

Figure 2.11: Simulation results of model using the parameter set Σ_p and cell-matrix adhesion terms $S_{c_1,v} = 0.5 = S_{c_2,v}$. Plots of both cancer populations c_1 and c_2, as well as the combined cancer distributions and the ECM densities at stages $25\Delta t$, $50\Delta t$, and $75\Delta t$.

Finally, we investigate the effects of cell-cell adhesion and in particular cross-adhesion. Cross-adhesion is when different cancer cell populations adhere to one another. Here we set $S_{c_1,c_2} = S_{c_2,c_1}$ as both populations will have the same rate

of adherence to each other. We look at the case using parameter set Σ_p and the adhesion matrices

$$\mathbf{S}_{cc} = \begin{pmatrix} 0.5 & 0.5 \\ 0.5 & 0.3 \end{pmatrix} \quad \text{and} \quad \mathbf{S}_{cv} = \begin{pmatrix} 0.3 & 0 \\ 0 & 0.6 \end{pmatrix}, \tag{2.15}$$

Our simulations in this case, shown in Figure 2.12, exhibit the same general morphology of the tumour boundary as in results with no cross-adhesion present, mainly due to the fact that in this work both cancer cell population are assumed to degrade the ECM at the same rate. However, the difference with respect to the no cross-adhesion case is emphasized by the spatial distribution of the two cancer cell populations within the main body of the tumour. Population c_1 remains consistent with results computed in Figure 2.9, however population c_2 exhibits different behaviour. We can distinguish now two higher density patches of c_2 densities which do not spread away from the significantly high levels of c_1 cell density and rather build up in their immediate proximity. Combining the cell populations now gives an increasingly contained spread of the tumour. This result is to be expected because the cells are now more inclined to stick together, rather than invade outwards, and although the adherence between cell populations has increased, their adhesion towards the matrix has stayed the same, hence we observe no difference in the movement of the boundary. This difference is also consistent with the other no cross-adhesion cases considered in Figs. 2.10 and 2.11.

2.3.3 Sensitivity to Initial Conditions

To address sensitivity with respect to initial data, we present and discuss here the results of four different sets of initial conditions for the ECM that are induced (2.12) with (2.13) by function h given in (2.16), which are gradually convergent towards the

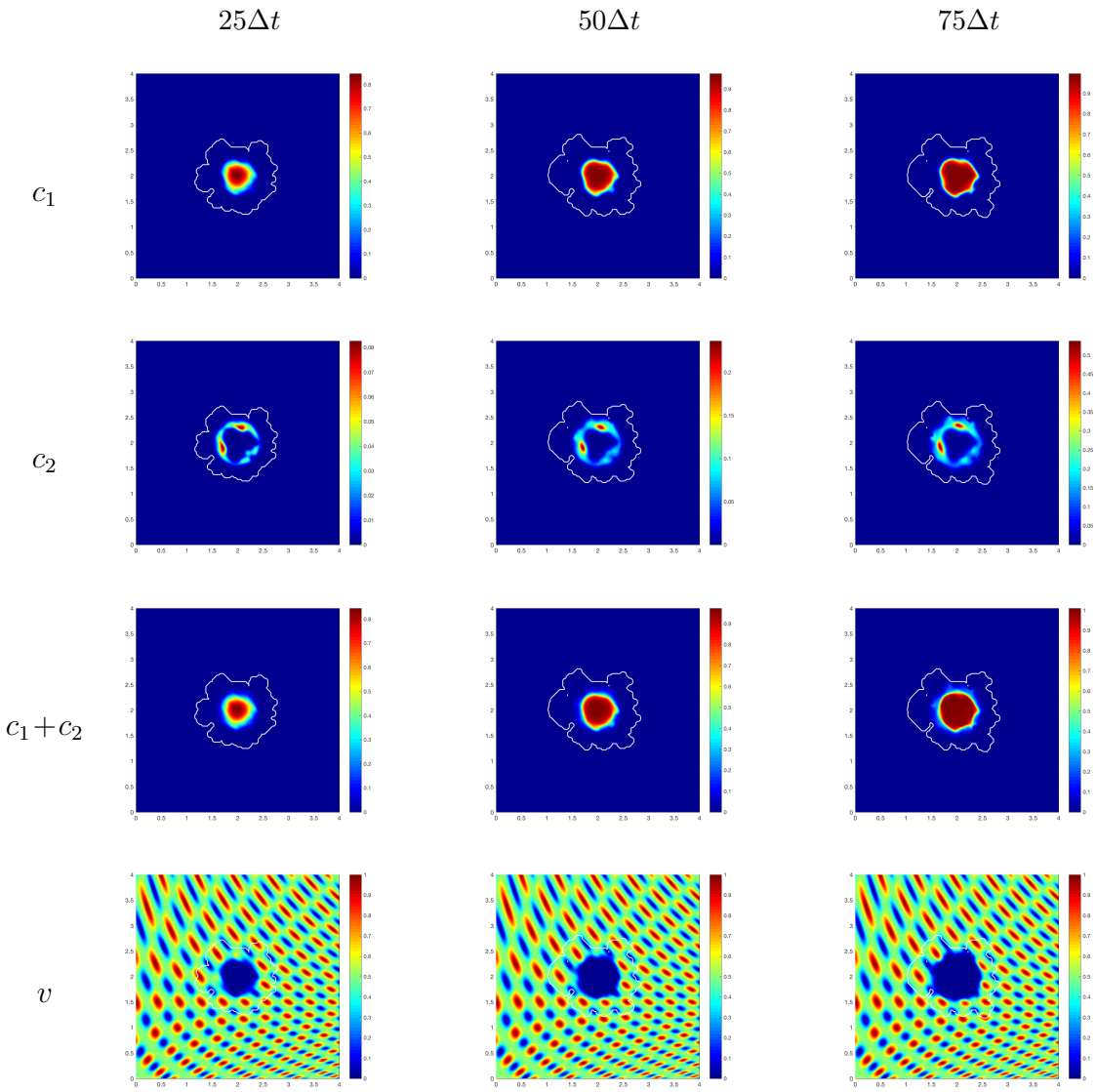

Figure 2.12: Simulation results of model using the parameter set Σ_p and adhesion matrices (2.15) which consider the inclusion of cross adhesion between cell subpopulations. Plots of both cancer populations c_1 and c_2, as well as the combined cancer distributions and the ECM densities at stages $25\Delta t$, $50\Delta t$, and $75\Delta t$.

case of homogeneous ECM. Figure 2.13(a) illustrates a homogenous ECM induced in (2.12) by the limit case for h that we obtain as $n \to \infty$, namely $h(x_1, x_2) = \frac{1}{2}$. Figure 2.13(b) and 2.13(c) use the initial condition (2.12), where the equation for

$h(x_1, x_2)$ is changed to

$$h(x_1, x_2) = \frac{1}{2} + \frac{1}{2^n} \sin(\zeta x_1 x_2)^3 \cdot \sin(\zeta \frac{x_2}{x_1}), \tag{2.16}$$

with $n = 3, 5$ for Figure 2.13(b) and 2.13(c), respectively. Using this form effectively flattens down the high density regions of the heterogeneous ECM, making it progressively closer to a homogeneous case, who exhibits a symmetric growth. Finally, Figure 2.13(d) shows the simulations using the initial conditions (2.12) with (2.13), as in Figure 2.9. The main body of the tumour remains similar from each initial condition of ECM as all coefficients remain the same as in the no cross-adhesion case shown in Figure 2.9. The differences between the invading boundaries are clearly visible, ranging from a symmetric expansion of the boundary for homogeneous initial conditions to a fingering leading edge for heterogeneous conditions. We conclude that as the initial condition for the ECM becomes increasingly heterogeneous, the proliferating edge of the tumour becomes consistently more lobular in its invasion.

2.4 Discussion

We have presented a multiscale moving boundary model which builds on previous framework proposed by Trucu et al. (2013) by exploring adhesive dynamics (Domschke et al., 2014) between a heterogeneous cancer cell population and the surrounding microenvironment. This considers both the macro-scale dynamics of two cancer cell sub-populations within the ECM and their influence on the micro-scale MDEs molecular dynamics occurring at the cell-scale along the invasive edge of the tumour. This macro-micro top-down link is given here via the source of MDEs that are secreted by the cancer cells from both c_1 and c_2 sub-populations arriving within the outer proliferating rim of the tumour. In turn, the micro-dynamics occurring

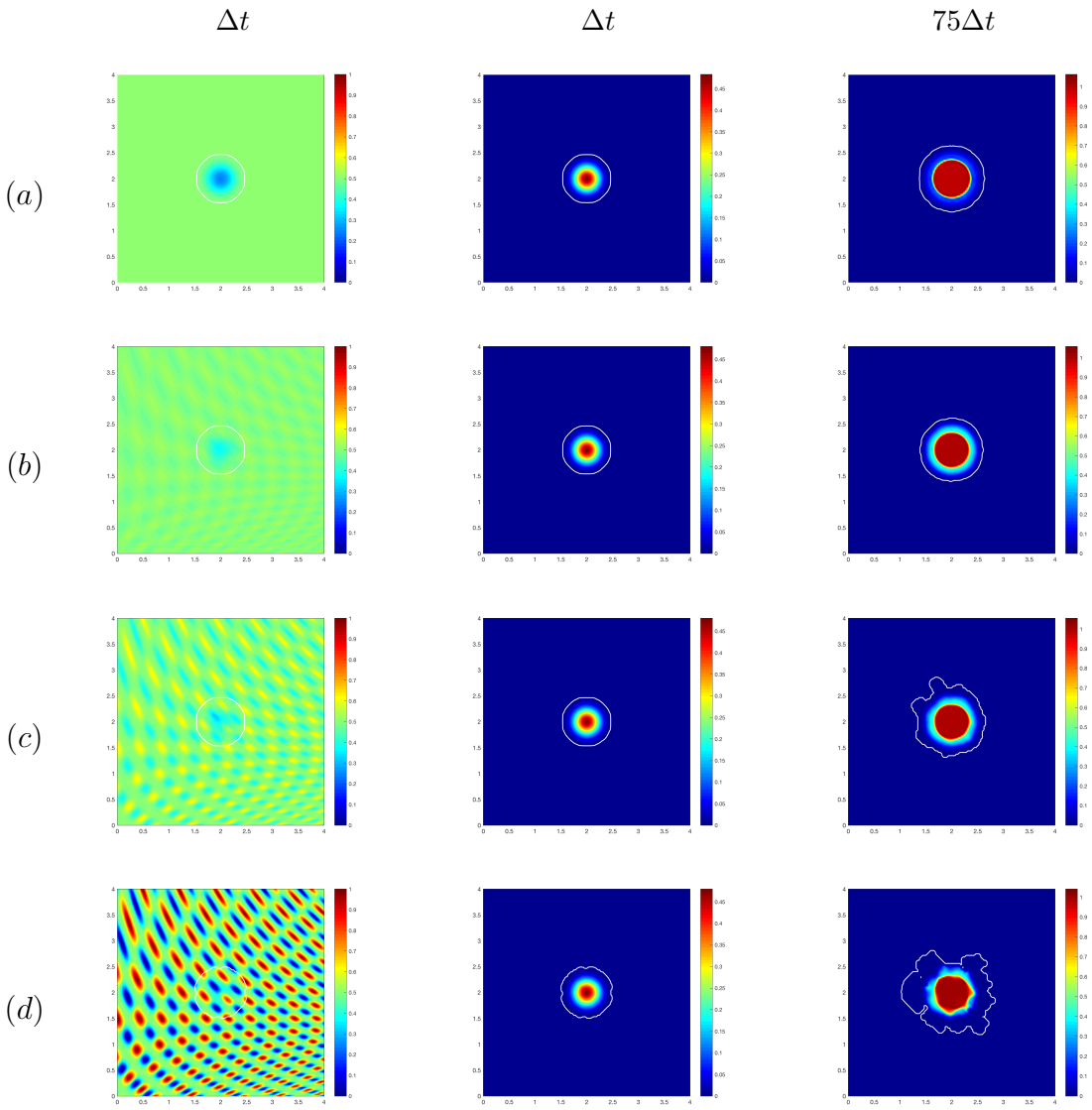

Figure 2.13: Simulation results showing different initial conditions for the ECM. Plots showing ECM and the combined cancer distribution at their initial stage Δt, and the tumour at final stage $75\Delta t$.

on the cell-scale enables a micro-macro feedback in the form of a bottom-up link by providing the movement direction and displacement magnitude of the tumour boundary.

In contrast with results from the previous framework proposed in Trucu et al. (2013) (which only included a local haptotactic term and no cell adhesion), here

we have shown that the inclusion of cell-cell and cell-matrix adhesion changes the way in which the cancer progresses. The computational results presented in this chapter have shown that the initial tumour region exercises greater movement than in the absence of adhesive qualities. We then incorporate another cell population and further explore the interactions between both cancer cell populations and their microenvironment. We have shown that in the presence of ECM remodelling, there is a greater spread of cancer cells as there is more opportunity for adherence which allows the cells to move. Increased cell-matrix adhesion, in particular between c_1 and v, has shown that a change in cell-matrix adhesion will not necessarily change the main body of the tumour, but it induces a change in the invading boundary, becoming very lobular when following the pattern of the ECM. Adding cross-adhesion to these models has shown how the different cell populations mix with one another and exhibits a denser region of population c_2 which remain in the proximity of highest regions of c_1 density. Finally, we investigated the effects of varying initial conditions of ECM, starting with a homogeneous distribution and becoming increasingly heterogenous. We have concluded that as the initial ECM distribution increases in heterogeneity, the proliferating boundary of the tumour becomes more lobular.

To gain further understanding of how cancer cells invade, focus must be placed on the surrounding microenvironment. The extracellular matrix is made from many different components, most of which play a vital role in cancer invasion. The main component of the ECM is collagen, particularly collagen type I which provides the matrix with its structure and flexibility. Investigations into the mesenchymal motion of tumour cells (Chauviere et al., 2007; Hillen, 2006; Painter, 2008), shows that the difference between *undirected* and *directed* fibres is of high importance. Undirected fibres are symmetrical along their axes and their direction is identical at both ends, an example of this type of fibre would be collagen in the human body. Un-

like undirected fibres, directed fibres are unsymmetrical and can be distinguished at both ends. Recent work considering fibres by Wang et al. (2008), focussed on directed fibres, have highlighted differences between directed and undirected fibres using a one-dimensional model. The addition of fibres, directed or undirected, into the multiscale model would greatly change the pattern of invasion. Several other components of the ECM such as fibronectin, laminin and a variety of different MMPs are also vital in tumour invasion and a greater mathematical understanding of these would allow for an overall better understanding of cancer progression.

Chapter 3

Dynamic fibre redistribution and cell adhesion

Aims and Novelty: In this chapter we consider the new concept of a heterogeneous two-phase ECM consisting of a fibres and non-fibres component. We introduce a second micro-scale to the moving boundary multiscale model introduced in Chapter 2 to consider a completely novel underlying fibre network and explore both the influence of the fibres on the macroscopic cancer dynamics as well as cancer cell-induced microscopic fibre rearrangement.

3.1 Introduction

One of the first steps of invasion is the degradation and remodelling of the surrounding extracellular matrix where a major part of this process is the reorganisation of the strong collagen fibrils present in the ECM by the cancer cells. Redistribution of this key structural component of the ECM permits the cells a route of invasion that is tailored to their specific needs, typically towards areas that are going to further the growth and spread of the tumour, leading the cells to spread into areas of free

physical space, or towards areas which hold an abundance of resources.

In this chapter we will highlight the significance of the fibrous structure of the invading tumour and explore not only the influence of these fibres within the macroscopic cancer cell dynamics, but also capture their microscopic rearrangement. To this end, we consider the two-scale fibres dynamics in the context of the multiscale moving boundary invasion process as formulated in Trucu et al. (2013), leading this way to a novel multiscale moving boundary framework, with two simultaneous but different in nature micro-dynamic processes that are each connected through two double feedback loops to a shared tissue-scale cancer macro-dynamics.

The content of this chapter has been explored and discussed in full in the publication Shuttleworth and Trucu (2019c).

3.2 The Novel Multiscale Modelling Framework

Building on the multiscale moving boundary framework initially introduced in Trucu et al. (2013) and taken forward in Chapter 2, in the following we describe the novel modelling platform for cancer invasion. Besides the underlying tumour invasive edge two-scale proteolytic activity of the matrix degrading enzymes considered in Trucu et al. (2013), the new modelling framework will now incorporate and explore the multiscale ECM fibre dynamics within the bulk of the invading tumour, accounting in a double feedback loop for their microscopic rearrangement as well as their macroscale effect on cancer cell movement.

Let us denote the support of the locally invading tumour by $\Omega(t)$ and assume that this evolves within a maximal environmental tissue cube $Y \in \mathbb{R}^N$, with $N = 2, 3$, which is centred at the origin of the space. In this context, at any tissue-scale spatio-temporal node $(x, t) \in \Omega(t) \times [0, T]$, we consider the tumour as being a dynamic mixture consisting of a cancer cell distribution $c(x, t)$ combined with a

cumulative extracellular matrix density $v(x,t) := F(x,t) + l(x,t)$ whose multiphase configuration (F, l) will be detailed in Sections 3.3-3.3.1.

3.2.1 The multiscale moving boundary perspective

While postponing for the moment the precise details of the macro-dynamics (leaving this to be fully introduced and explored in Section 3.3.2), since the novel modelling platform that we develop here builds on the initial multiscale moving boundary framework proposed in Trucu et al. (2013), let us start by devoting this entire section to briefly revisiting and summarising the main features of the general two-scale moving boundary approach. In this context, let us express for the moment the tissue-scale tumour macro-dynamics on the the evolving $\Omega(t)$ in the form of the following pseudo-differential operator equation

$$\mathcal{T}(c, F, l) = \mathbf{0} \tag{3.1}$$

where $\mathcal{T}(\cdot, \cdot, \cdot)$ denotes an appropriately derived reaction-diffusion-taxis operator whose precise form will be completely defined in Section 3.3.2. Furthermore, as detailed in Trucu et al. (2013), the key multiscale role played by the tumour invasive proteolytic enzymes processes in cancer invasion is captured here in a multiscale moving boundary approach where the link between the tumour macro-dynamics (3.1) and the cell-scale leading edge proteolytic molecular micro-dynamics is captured via a double feedback loop. This double feedback loop is realised via a *top-down* and a *bottom-up* link which is detailed below.

The top-down link. As discussed previously, cancer invasion is a multiscale process in which the matrix-degrading enzymes (MDEs), such as matrix metalloproteinases (MMP) which are secreted by the cancer cells from within the outer

proliferation rim of the tumour, are responsible for the degradation of the peritumoural ECM, enabling further tumour expansion. Thus, adopting the terminology and framework developed in Trucu et al. (2013), this tumour invasive edge molecular micro-dynamics, which occurs within a cell-scale neighbourhood of the tumour interface $\partial\Omega(t)$, can be explored on an appropriately constructed bundle of $\epsilon-$size *half-way overlapping micro-domains* $\{\epsilon Y\}_{\epsilon Y\in\mathcal{P}}$ satisfying some naturally arising topological requirements. These requirements ensure that each ϵY *"sits on the interface"* and captures relevant parts of both inside and outside regions of the tumour where the proteolytic activity takes place (as detailed in Chapter 2, while for complete details we refer the reader to Trucu et al. (2013)). This allows us to decouple this leading-edge proteolytic activity in a bundle of corresponding MDE micro-processes occurring on each ϵY. In this context, a source of MDEs arises at each $y \in \epsilon Y \cap \Omega(t_0)$ as a collective contribution of all the cells that (subject to macro-dynamics (3.1)) arrive within the outer proliferating rim at a spatial distance from y smaller than a certain radius $\gamma > 0$ (representing the maximal thickness of the outer proliferating rim). Thus, the source of MDEs that is this way induced by the macro-dynamics at the micro-scale on each ϵY realises a significant *top-down link* that can be mathematically expressed as

$$\begin{aligned} &1.\quad g_{\epsilon Y}(y,\tau) = \frac{\int\limits_{\mathbf{B}(y,\gamma)\cap\Omega(t_0)} \alpha_1 c(x,t_0+\tau)dx}{\lambda(\mathbf{B}(y,\gamma)\cap\Omega(t_0))}, \quad y\in\epsilon Y\cap\Omega(t_0), \\ &2.\quad g_{\epsilon Y}(y,\tau) = 0, \quad y\in\epsilon Y\setminus\big(\Omega(t_0)+\{y\in Y|\ ||y||_2<\gamma\}\big), \end{aligned} \tag{3.2}$$

where $\mathbf{B}(y,\gamma) := \{\xi \in Y \mid \parallel y-\xi \parallel_\infty \leq \gamma\}$ and α_1 is an MDE secreting rate for the cancer cell population. In the presence of this source, a cross interface MDEs transport takes place. As in this Chapter we only consider the micro-dynamics of a

single class of MDEs, such as MMPs, this simply results in a diffusion type transport over the entire ϵY micro-domain, and so denoting the MDE molecular density by $m(y,\tau)$, this can be mathematically formulated as

$$\frac{\partial m}{\partial \tau} = D_m \Delta m + g_{\epsilon Y}(y,\tau), \qquad y \in \epsilon Y,\ \tau \in [0, \Delta t], \tag{3.3}$$

The bottom-up link. During the micro-dynamics (3.3), the MDEs transported across the interface in the peritumoural region interact with ECM distribution that they meet in the immediate tumour proximity outside the cancer region within each boundary micro-domain ϵY. On each micro-domain ϵY, provided that a sufficient amount of MDEs have been transported across the cancer invading edge enclosed in this micro-domain, it is the pattern of the front of the advancing spatial distribution of MDEs that characterises the way in which the ECM is locally degraded. As introduced and described in Trucu et al. (2013), within each ϵY, the pattern of degradation of ECM caused by the significant levels of the advancing front of MDEs give rise to a direction $\eta_{\epsilon Y}$ and displacement magnitude $\xi_{\epsilon Y}$ (detailed previously in Chapter 2), which determine the cancer boundary movement characteristics represented back at macro-scale through the movement of the appropriately defined boundary mid-points $x^*_{\epsilon Y}$ to their new spatial positions $\widetilde{x^*_{\epsilon Y}}$. Thus, over a given time perspective $[t_0, t_0 + \Delta t]$, the *bottom-up link* of the interaction between the proteolytic tumour invasive edge micro-dynamics and macro-scale is realised through the macro-scale boundary movement characteristics that are provided by the micro-scale MDEs activity, leading to the expansion of the tumour boundary $\Omega(t_0)$ to an enhanced domain $\Omega(t_0 + \Delta t)$ where the multiscale dynamics is continued as described in Chapter 2.

3.3 The multiscale and multi-component structure of the ECM

To gain a deeper understanding of the invasion process, in this chapter we pay special attention to the ECM structure within the overall multiscale dynamics. While in previous multiscale approaches (such as those proposed in Peng et al. (2017); Trucu et al. (2013)) the ECM has been considered as a *"well mixed"* matrix distribution, with no individual components taken in to consideration, in the following we account for the structure of the ECM by regarding this as a two-component media. The first ECM component that we distinguish accounts for all significant ECM fibres such as collagen fibres or fibronectin fibrils. This will be denoted by $F(x,t)$ and will simply be referred to as the *fibres* component. Finally, the second ECM component that we distinguish consists of the rest of ECM constituents bundled together. This will be referred to as the *non-fibres* component and will be denoted by $l(x,t)$.

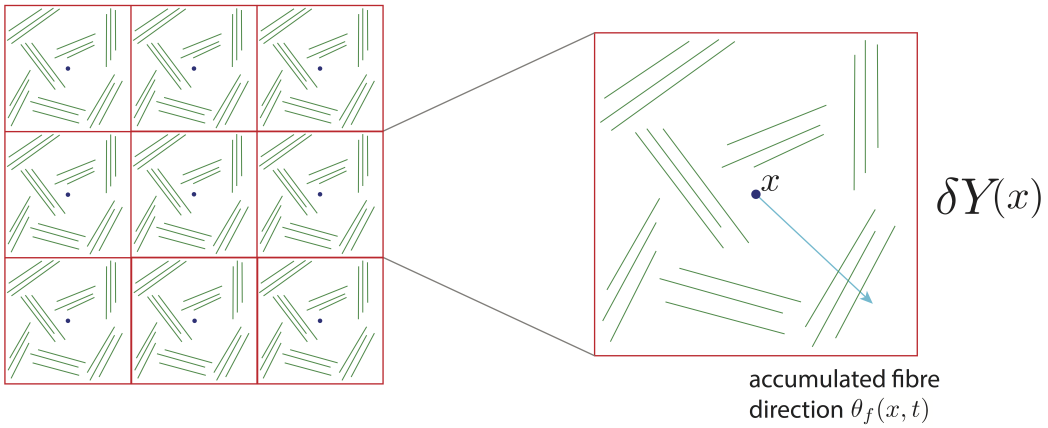

Figure 3.1: Schematic showing copies of δYcube on the grid with micro-fibres distribution in green and their induced macroscopic direction $\theta_f(x,t)$ in pale blue.

While from the tissue-scale (macro-scale) stand point the fibres are regarded as a continuous distribution at any $x \in Y$, from the cell-scale (micro-scale) point of

view, a specific micro-structure can be in fact distinguished as a mass-distribution of the ECM micro-fibres $f(z,t)$ that are spatially distributed on a small micro-domain of micro-scale size $\delta > 0$ centred at any macroscopic point $x \in Y$, namely on $\delta Y(x) := \delta Y + x$.

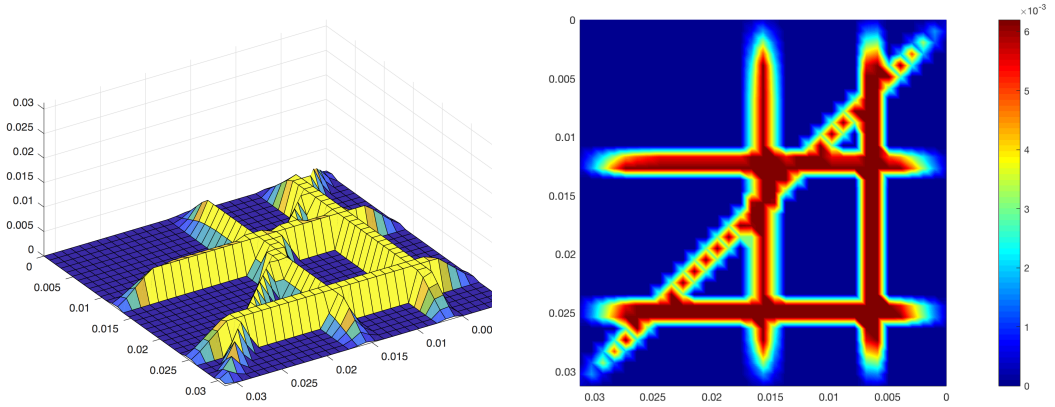

(a) Graph of micro-fibre distribution on $\delta Y(x)$

(b) 2D color plot of the micro-fibre distribution on $\delta Y(x)$

Figure 3.2: Micro-fibre distribution on $\delta Y(x)$.

In this context, as we will detail below, the microscopic mass-distribution of ECM micro-fibres will be able to supply important macro-scale fibre characteristics, both in terms of their associated *macroscopic fibre orientation* $\theta_f(x,t)$ and *magnitude* $F(x,t)$, which will be introduced in Section 3.3.1. Figure 3.1 illustrates such micro-fibres distribution in micro-domains $\delta Y(x)$, $x \in \Omega(t)$. A concrete example of such micro-scale fibres pattern is then proposed in Figure 3.2, this being given as

$$f(z,t) := \sum_{j \in J} \psi_{h_j}(z)(\chi_{(\delta-\gamma)Y(x)} * \psi_\gamma)(z) \tag{3.4}$$

where $\{\psi_{h_j}\}_{j\in J}$ are smooth compact support functions of the form

$$\psi_{h_j} : \delta Y(x) \to \mathbb{R}$$

which, at every $z := (z_1, z_2) \in \delta Y(x)$, are given by:

$$\psi_{h_j}(z_1, z_2) := \begin{cases} C_{h_j} e^{-\frac{1}{r_{\text{fib}}^2 - (h_j(z_2) - z_1)^2}}, & \text{if } z_1 \in [h_j(z_2) - r_{\text{fib}}, h_j(z_2) + r_{\text{fib}}], \\ 0, & \text{if } z_1 \notin [h_j(z_2) - r_{\text{fib}}, h_j(z_2) + r_{\text{fib}}]. \end{cases} \tag{3.5}$$

with $r_{\text{fib}} > 0$ being the width of the micro-fibres and C_{h_j} being constants that determine the maximum hight of ψ_{h_j} along the smooth paths $\{h_j\}_{j\in J}$ in $\delta Y(x)$ given by a combination of five distinctive micro-fibres patterns that are defined along the following smooth paths $\{h_j\}_{j\in J}$:

$$h_1 : z_1 = z_2; \quad h_2 : z_1 = \frac{1}{2}; \quad h_3 : z_1 = \frac{1}{5}; \quad h_4 : z_2 = \frac{2}{5}; \quad \text{and} \quad h_5 : z_2 = \frac{4}{5}.$$

Finally, $\chi_{(\delta-\gamma)Y(x)}(\cdot)$ represents the characteristic function of the cubic micro-domain $(\delta - \gamma)Y(x)$ centred at x and of size $(\delta - \gamma)$, with $\gamma > 0$ a small enough radius, while ψ_γ is the standard mollifier that is smoothing out this characteristic function to a smooth compact support function on δY, $\psi_\gamma : \mathbb{R}^N \to \mathbb{R}_+$ (which was used also in Trucu et al. (2013)) is defined as usual, namely

$$\psi_\gamma(x) := \frac{1}{\gamma^N} \psi\big(\frac{x}{\gamma}\big),$$

where ψ is the smooth compact support function given by

$$\psi(x) := \begin{cases} \frac{exp\frac{1}{\|x\|_2^2 - 1}}{\int\limits_{\mathbf{B}(0,1)} exp\frac{1}{\|z\|_2^2 - 1} dz}, & if \quad x \in \mathbf{B}(0,1), \\ 0, & if \quad x \notin \mathbf{B}(0,1). \end{cases}$$

Furthermore, as we will discuss in the following, while the fibre micro-structure will be dynamically rearranged at micro-scale by the incoming flux of cancer cell population, their *"on the fly"* updated revolving orientation $\theta_f(x,t)$ and magnitude $F(x,t)$ will be involved in the dynamics at macro-scale.

3.3.1 Macroscale fibres orientation and magnitude induced by the ECM micro-fibres spatial distribution at microscale: derivation and well-posedness

On every micro-domain $\delta Y(x)$ centred at a macro-point $x \in \Omega(t)$, at a given time instance $t \in [0,T]$, the spatial distribution of the micro-fibres $f(z,t)$ on $\delta Y(x)$ naturally provides a cumulative revolving orientation of these with respect to the barycentre x, and to derive this we proceed as follows.

Considering an arbitrary dyadic decomposition $\{\mathcal{D}_j\}_{j\in\mathcal{J}_n}$ of size $\delta 2^{-n}$ for the micro-domain $\delta Y(x)$, let us denote by z_j the barycentre of each dyadic cube $\mathcal{D}_j$. Then, for any $j \in \mathcal{J}_n$, the mass of micro-fibres distributed on $\mathcal{D}_j$ will influence the overall revolving fibre orientation on $\delta Y(x)$ through its contribution in direction of the position vector $\overrightarrow{x\ z_j} := z_j - x$ in accordance with its weight relative standing with respect to the micro-fibre mass distributed on all other $\mathcal{D}_j$ covering $\delta Y(x)$. Therefore, the overall *revolving micro-fibres orientation on* $\delta Y(x)$ *associated with*

the dyadic decomposition $\{\mathcal{D}_j\}_{j\in\mathcal{J}_n}$ is given by:

$$\begin{aligned}
\theta^n_{f,\delta Y(x)}(x,t): &= \sum_{j\in\mathcal{J}_n} \frac{\int_{\mathcal{D}_j} f(\zeta,t)d\zeta}{\sum\limits_{j\in\mathcal{J}_n}\int\limits_{\mathcal{D}_j} f(\zeta,t)\ d\zeta}\overrightarrow{x\,z_j} \\
&= \sum_{j\in\mathcal{J}_n} \frac{\int\limits_{\mathcal{D}_j} f(\zeta,t)d\zeta}{\int\limits_{\delta Y(x)} f(\zeta,t)d\zeta}\overrightarrow{x\,z_j} \\
&= \frac{\sum\limits_{j\in\mathcal{J}_n}\Big(\frac{1}{\lambda(\mathcal{D}_j)}\int\limits_{\mathcal{D}_j} f(\zeta,t)d\zeta\Big)\lambda(\mathcal{D}_j)\overrightarrow{x\,z_j}}{\int\limits_{\delta Y(x)} f(\zeta,t)d\zeta} \\
&= \frac{\int\limits_{\delta Y(x)}\Big[\sum\limits_{j\in\mathcal{J}_n}\Big(\frac{1}{\lambda(\mathcal{D}_j)}\int\limits_{\mathcal{D}_j} f(\zeta,t)d\zeta\Big)\chi_{\mathcal{D}_j}(z)\overrightarrow{x\,z_j}\Big]dz}{\int\limits_{\delta Y(x)} f(\zeta,t)d\zeta} \\
&= \frac{\int\limits_{\delta Y(x)}\Big[\sum\limits_{j\in\mathcal{J}_n}\Big(\frac{1}{\lambda(\mathcal{D}_j)}\int\limits_{\mathcal{D}_l} f(\zeta,t)d\zeta\Big)\chi_{\mathcal{D}_j}(z)(z_j-x)\Big]dz}{\int\limits_{\delta Y(x)} f(\zeta,t)d\zeta}
\end{aligned} \tag{3.6}$$

where $\lambda(\cdot)$ is the usual Lebesgue measure and $\chi_{\mathcal{D}_l}(\cdot)$ is the characteristic function of the dyadic cube D_l. Thus, for any $n\in\mathbb{N}^*$ denoting the numerator function

$$g_n(z) := \sum_{j\in\mathcal{J}_n}\left(\frac{1}{\lambda(\mathcal{D}_j)}\int\limits_{\mathcal{D}_j} f(\zeta,t)\ d\zeta\right)\chi_{\mathcal{D}_j}(z)(z_j-x), \tag{3.7}$$

let's observe immediately that $\{g_n\}_{n\in\mathbb{N}^*}$ is actually a sequence of vector-valued simple functions that is convergent to $f(z,t)(z-x)$ and that its associated sequence of integrals converges to the Bochner Intergal of $f(z,t)(z-x)$ on $\delta Y(x)$ with respect to $\lambda(\cdot)$ (Yosida, 1980), namely

$$\int\limits_{\delta Y(x)} f(z,t)(z-x)dz := \lim_{n\to\infty}\int\limits_{\delta Y(x)} g_n(z)dz. \tag{3.8}$$

Hence, from (3.6)-(3.8), we obtain that the sequence of revolving $\{\theta^n_f(x,t)\}_{n\in\mathbb{N}^*}$ fibres orientations associated to the entire family of dyadic decompositions $\{\{D_j\}_{j\in\mathcal{J}_n}\}_{n\in\mathbb{N}^*}$ is convergent to the unique *revolving barycentral micro-fibres orientation on* $\delta Y(x)$

denoted by $\theta_{f,\delta Y(x)}(x,t)$ and given by

$$\begin{aligned}
\theta_{f,\delta Y(x)}(x,t) &:= \lim_{n\to\infty} \theta^n_{f,\delta Y(x)}(x,t) \\
&= \lim_{n\to\infty} \frac{\int_{\delta Y(x)} \Big[\sum_{j\in\mathcal{J}_n} \Big(\frac{1}{\lambda(\mathcal{D}_j)} \int_{\mathcal{D}_j} f(\zeta,t)d\zeta \Big)(z_j - x)\chi_{\mathcal{D}_j}(z) \Big] dz}{\int_{\delta Y(x)} f(\zeta,t)d\zeta} \\
&= \frac{\lim_{n\to\infty} \int_{\delta Y(x)} g_n(z)dz}{\int_{\delta Y(x)} f(\zeta,t)d\zeta} \\
&= \frac{\int_{\delta Y(x)} f(z,t)(z-x)dz}{\int_{\delta Y(x)} f(\zeta,t)d\zeta} \\
&= \frac{\int_{\delta Y(x)} f(z,t)(z-x)dz}{\int_{\delta Y(x)} f(z,t)dz},
\end{aligned} \tag{3.9}$$

which is actually precisely the *Bochner-mean-value* of the position vectors function $\delta Y(x) \ni z \mapsto z - x \in \mathbb{R}^N$ with respect to the measure $f(x,t)\lambda(\cdot)$ that is induced by the micro-fibres distribution.

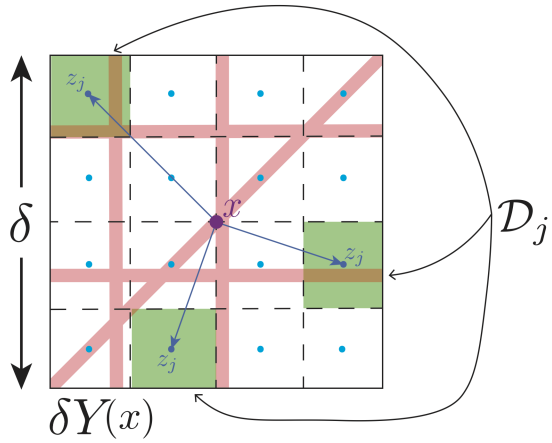

Figure 3.3: Schematic of the fibre micro-domain $\delta Y(x)$ decomposed into dyadic cubes shown in green, $\mathcal{D}_j$, with associated barycentre z_j in cyan. The position vectors are shown in dark blue.

Therefore, denoting by $\theta_f(x,t)$ *the macroscopic fibres orientation* at (x,t) induced by the *revolving barycentral micro-fibres orientation* on $\delta Y(x)$, we have that

this is given by

$$\theta_{_f}(x,t) := \frac{1}{\lambda(\delta Y(x))} \int\limits_{\delta Y(x)} f(z,t)dz \cdot \frac{\theta_{_{f,\delta Y(x)}}(x,t)}{\parallel \theta_{_{f,\delta Y(x)}}(x,t) \parallel_{_2}}. \tag{3.10}$$

Finally, the macroscopic representation of the ECM fibres distributed at (x,t) is denoted by $F(x,t)$ and is given by the Euclidean magnitude of $\theta_{_f}(x,t)$, namely:

$$F(x,t) :=\parallel \theta_{_f}(x,t) \parallel_{_2}, \tag{3.11}$$

and so using now (3.10), from (3.11) we obtain that

$$\begin{aligned} F(x,t): &= \parallel \theta_{_f}(x,t) \parallel_{_2} \\ &= \parallel \tfrac{1}{\lambda(\delta Y(x))} \int\limits_{\delta Y(x)} f(z,t)dz \cdot \tfrac{\theta_{_{f,\delta Y(x)}}(x,t)}{\|\theta_{_{f,\delta Y(x)}}(x,t)\|_{_2}} \parallel_{_2} \\ &= \tfrac{1}{\lambda(\delta Y(x))} \int\limits_{\delta Y(x)} f(z,t)dz \cdot \tfrac{\|\theta_{_{f,\delta Y(x)}}(x,t)\|_{_2}}{\|\theta_{_{f,\delta Y(x)}}(x,t)\|_{_2}} \\ &= \tfrac{1}{\lambda(\delta Y(x))} \int\limits_{\delta Y(x)} f(z,t)dz, \end{aligned} \tag{3.12}$$

which is precisely the mean-value of the micro-fibres distributed on $\delta Y(x)$. Therefore, *the macroscopic fibres orientation* at (x,t) induced by the *revolving barycentral micro-fibres orientation on* $\delta Y(x)$ has its magnitude given by the mean-value of the micro-fibres on $\delta Y(x)$, and since in (3.6)-(3.9) we have ensured the well-posedness of $\theta_{_{f,\delta Y(x)}}(x,t)$, from (3.10)-(3.12), we obtain that $\theta_{_f}(x,t)$ and $F(x,t)$ are also well-posed.

With all these preparations, we are now in the position to describe the tumour macro-dynamics, which will be detailed in full in the next section.

3.3.2 Tumour macro-dynamics

To explore mathematically the macro-scale coupled dynamics exercised by the cancer cells mixed with the ECM, for notation convenience, let's first gather the macroscopic distributions of cancer and the two ECM phases considered here in the three-dimensional vector

$$\mathbf{u}(x,t) := (c(x,t), F(x,t), l(x,t))^T,$$

and let's denote tumour's volume fraction of occupied space by

$$\rho(\mathbf{u}) \equiv \rho(\mathbf{u}(x,t)) := \vartheta_v(F(x,t) + l(x,t)) + \vartheta_c c(x,t), \tag{3.13}$$

with ϑ_v representing physical space occupied by the fibre and non-fibre phases of the ECM taken together and ϑ_c being the fraction of physical space occupied by the cancer cell population c.

Therefore, focusing first upon the cancer cell population, per unit time, under the presence of a proliferation law, its spatial dynamics is not only due to random motility (approximated mathematically by diffusion), but this is also crucially influenced by a combination of cell adhesion processes that include cell-cell adhesion and cell-matrix adhesion, with cell-matrix adhesion exhibiting distinctive characteristics in relation to the two ECM phases (namely: the fibres and non-fibres components). Hence, assuming here a logistic proliferation law, the dynamics of the cancer cell population can be mathematically represented as

$$\frac{\partial c}{\partial t} = \nabla \cdot [D_1 \nabla c - c\mathcal{A}(x,t,\mathbf{u}(\cdot,t),\theta_f(\cdot,t))] + \mu_1 c(1-\rho(\mathbf{u}))^+, \tag{3.14}$$

where: D_1 and μ_1 are non-negative diffusion and proliferation rates, respectively, while $\mathcal{A}(x,t,\mathbf{u}(\cdot,t),\theta_f(\cdot,t))$ represents a non-local constitutive flux term accounting

for the critically important cell-adhesion processes that influence directly the spatial tumour movement, whose precise form will be explored as follows.

While generally adopting a similar perspective to the one in Armstrong et al. (2006); Domschke et al. (2014); Gerisch and Chaplain (2008) concerning cell-cell adhesion and cell-ECM-non-fibres substrate, here we move beyond the context considered in those works by accounting for the crucial role played by the cell-fibres adhesive interaction. Thus, within a sensing radius R, at a given time t and spatial location x, the adhesive flux associated to the cancer cells distributed at (x,t) will account for not only the adhesive interactions with the other cancer cells and ECM non-fibres phase distributed on $\mathbf{B}(x,R)$, but this will also appropriately consider and cumulate the adhesive interaction arising between cancer cells and the oriented ECM fibres, resulting in the following novel non-local adhesion flux term:

$$\mathcal{A}(x,t,\mathbf{u}(\cdot,t),\theta_{_f}(\cdot,t)) = \frac{1}{R}\int_{\mathbf{B}(0,R)} \mathcal{K}(\|\,y\,\|_2)\big(n(y)(\mathbf{S}_{_{cc}}c(x+y,t)+\mathbf{S}_{_{cl}}l(x+y,t)) + \hat{n}(y)\;\mathbf{S}_{_{cF}}F(x+y,t)\big)(1-\rho(\mathbf{u}))^{+} \tag{3.15}$$

The influence on adhesive interactions of the distance from the spatial location x is accounted for through the radial kernel $\mathcal{K}(\cdot)$ which explores the decreasing influence on adhesion-driven migration as the distance from $x+y$ to x within the sensing region $\mathbf{B}(x,r)$ increases and is taken here to be:

$$\mathcal{K}(r) := \frac{2\pi R^2}{3}\left(1-\frac{r}{2R}\right). \tag{3.16}$$

While $n(\cdot)$ represents the usual unit radial vector given by

$$n(y) := \begin{cases} y/||y||_2 & \text{if } y \in \mathbf{B}(0,R) \setminus \{0\}, \\ (0,0) & \text{if } y = (0,0), \end{cases} \tag{3.17}$$

along which we consider the cell-cell and cell-ECM-non-fibres adhesion bonds established between the cancer cells distributed at x and the cells and non-fibre ECM phase distributed at $x+y$ with strengths $\mathbf{S}_{cc}$ and $\mathbf{S}_{cl}$, respectively. Specifically, while $\mathbf{S}_{cl}$ is considered here to be constant, as biological evidence discussed in Gu et al. (2014); Hofer et al. (2000) suggests that, in direct correlation to collagen levels, it is the high level of extracellular Ca^{2+} ions rather than the sole production and presence of intracellular Ca^{2+} that enables strong and stable adhesive bonds between cells, hence directly impacting the strength of cell-cell adhesion, we therefore assume that $\mathbf{S}_{cc}$ is dependent on the collagen density, smoothly ranging between 0 and a Ca^{2+}-saturation level $S_{\max}$, this being taken here of the form

$$\mathbf{S}_{cc}(x,t) := S_{\max} e^{\left(1-\frac{1}{1-(1-l(x,t))^2}\right)}. \tag{3.18}$$

Finally, the last term in (3.15) considers the crucially important adhesive interactions between the cancer cells distributed at x and the oriented fibres distributed on $\mathbf{B}(x,R)$. In this context, while the strength of this interaction is proportional to the macro-scale amount of fibres $F(\cdot,t)$ distributed at $x+y$, and, as illustrated in Figure 3.4, the orientation $\theta_f(\cdot,t)$ of these fibres biases the direction of these adhesive interactions in the direction of the vector $\hat{n}(\cdot)$ defined by

$$\hat{n}(y) := \begin{cases} \frac{y+\theta_f(x+y)}{||y+\theta_f(x+y)||_2}, & \text{if } (y+\theta_f(x+y)) \neq (0,0), \\ (0,0) \in \mathbb{R}^2, & \text{otherwise.} \end{cases} \tag{3.19}$$

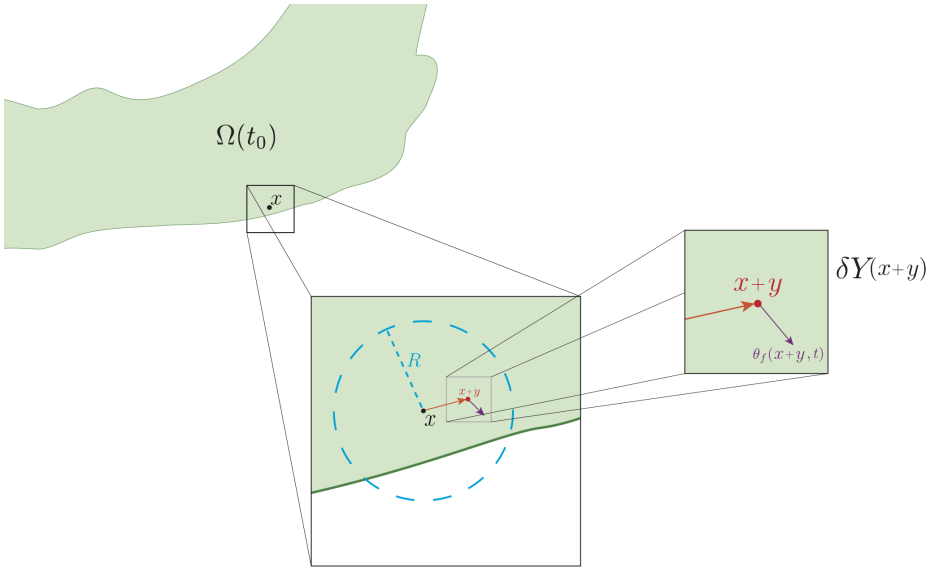

Figure 3.4: Schematic to describe the process of the new cell-fibre adhesion term which includes the distribution of fibres. It shows the ball $B(x, R)$ centred at x and of radius R, the point $x + y$ with the direction vector $n(y)$ in orange, and the fibre orientation $\theta_f(x + y, t)$ in purple.

Further, per unit time, the fibres distribution are simply degraded by the cancer cells at macroscale, and so the dynamics of their macroscopic dynamics is simply governed by

$$\frac{dF}{dt} = -\gamma_1 cF, \tag{3.20}$$

where γ_1 describes the rate of degradation. This macroscopic degradation of fibres is feed back to the micro-fibres $f(\cdot, t)$ on the micro-domains $\delta Y(x)$ as a factor which will lower their microscopic height accordingly. To complete the description of the macroscopic system, the non-fibre ECM is simply degraded by the cancer cells, and so its dynamics can be mathematically formulated as

$$\frac{dl}{dt} = -\gamma_2 cl, \tag{3.21}$$

where γ_2 describes the rate of degradation.

3.3.3 Microscopic fibre rearrangement induced by the macro-dynamics

As the cancer cells invade, they push the fibres in the direction they are travelling, thereby influencing the ECM fibres by their own directive movement. Thus, in addition to the macroscale fibre degradation (explored in (3.20)), during the tumour dynamics, at any instance in time t and spatial location $x \in \Omega(t)$, the cancer cell population are also pushing and realigning the fibres, causing a microscale spatial rearrangement of the micro-fibres distributed on $\delta Y(x)$. Specifically, this micro-fibres rearrangement is triggered by the macro-scale spatial flux of migratory cancer cells, namely by

$$\mathcal{F}(x,t) = D_1 \nabla c(x,t) - c(x,t)\mathcal{A}(x,t,\mathbf{u}(\cdot,t),\theta_{_f}(\cdot,t)). \tag{3.22}$$

Under the influence of the flux $\mathcal{F}(x,t)$ the fibre rearrangement vector $r(\delta Y(x),t)$ arises as a weighted sum between the flux of cancer cells ($\mathcal{F}(x,t)$) incoming at position (x,t) and the oriented fibres ($\theta_{_f}(x,t)$) at that position, given as

$$r(\delta Y(x),t) := \omega(x,t)\mathcal{F}(x,t) + (1-\omega(x,t))\theta_f(x,t). \tag{3.23}$$

The weight is chosen to capture the fact that the impact of the flow is proportional to the relative mass of cells versus cells and fibres existing at that position (i.e., the mass fraction of cells within the mixture of cells and fibres), expressed as

$$\omega(x,t) = \frac{c(x,t)}{c(x,t)+F(x,t)}. \tag{3.24}$$

Note that $(1-\omega(x,t))$ represents the relative mass of fibres versus cells and fibres. In this context, denoting the barycentric position vector of any micro-scale position

$z \in \delta Y(x)$ by

$$x_{\text{dir}}(z) = \overrightarrow{x\,z},$$

let's observe that this microscale fibres rearrangement will be exercised provided that the micro-fibres $f(z,t)$ would not have already reached a certain maximum level $f_{\max}$ (when the micro fibre distribution would be very "stiff" and the cancer cells would struggle to move through those micro-locations) and that their movement magnitude will be affected by the micro-fibre saturation fraction

$$f^* = \frac{f(z,t)}{f_{\max}} \tag{3.25}$$

combined with size of the micro-scale position defect with respect to $r(\delta Y(x),t)$ that is given simply by

$$||r(\delta Y(x)) - x_{\text{dir}}(z)||_2.$$

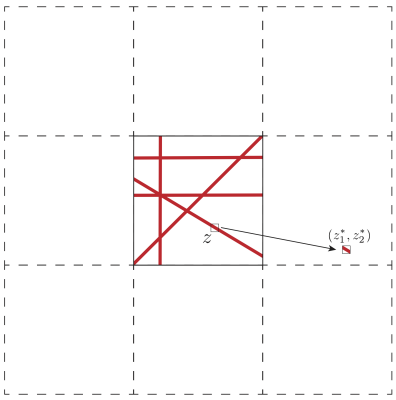

(a) Relocation micro-fibre distributions in $\delta Y(x)$ within its neighbouring micro-domains

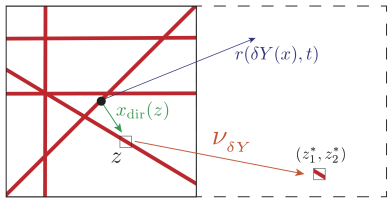

(b) Enlarged version of δY cube illustrating the components required for relocation

Figure 3.5: Schematics to describe the process of reallocation of fibre distribution in each δY cube.

Therefore, under the action of the rearrangement flux $r(\delta Y(x),t)$, the micro-fibres distributed at z will attempt to exercise their movement in the direction of

the resulting vector $x_{\text{dir}}(z) + r(\delta Y(x),t)$, and so their relocation to the corresponding position within neighbouring micro-domain will be given by the vector-valued function:

$$\nu_{\delta Y(x)}(z,t) = (x_{\text{dir}}(z) + r(\delta Y(x),t)) \cdot \frac{f(z,t)(f_{\max} - f(z,t))}{f^* + ||r(\delta Y(x)) - x_{\text{dir}}(z)||_2} \cdot \chi_{\{f(\cdot,t)>0\}} \quad (3.26)$$

where $\chi_{\{f(\cdot,t)>0\}}$ represents the usual characteristic function of the micro-fibres support set $\{f(\cdot,t) > 0\} := \{z \in \delta Y(x) | \, f(z,t) > 0\}$. Finally, the movement of the micro-fibres distributed at z to the newly attempted location z^* given by

$$z^* := z + \nu_{\delta Y(x)}(z,t)$$

is exercised in accordance with the space available at the new position z^*. Thus, this is explored here through the movement probability

$$p_{move} := \max\left(0, \frac{f_{\max} - f(z^*,t)}{f_{\max}}\right)$$

which enables only an amount of $p_{move} f(z,t)$ of micro-fibres to be transported to position z^* (as illustrated in Figure 3.5), while the rest of $(1 - p_{move}) f(z,t)$ remains at z.

3.3.4 Schematic summary of global multi-scale model

In this model, there are two interconnected multi-scale systems, each with their own distinct cell-scale micro-dynamics, but both of them sharing the same macro-scale cancer dynamics at the tissue scale, being linked to this through two double feedback loops, as illustrated in Figure 3.6. The macro-scale dynamics governs the spatial

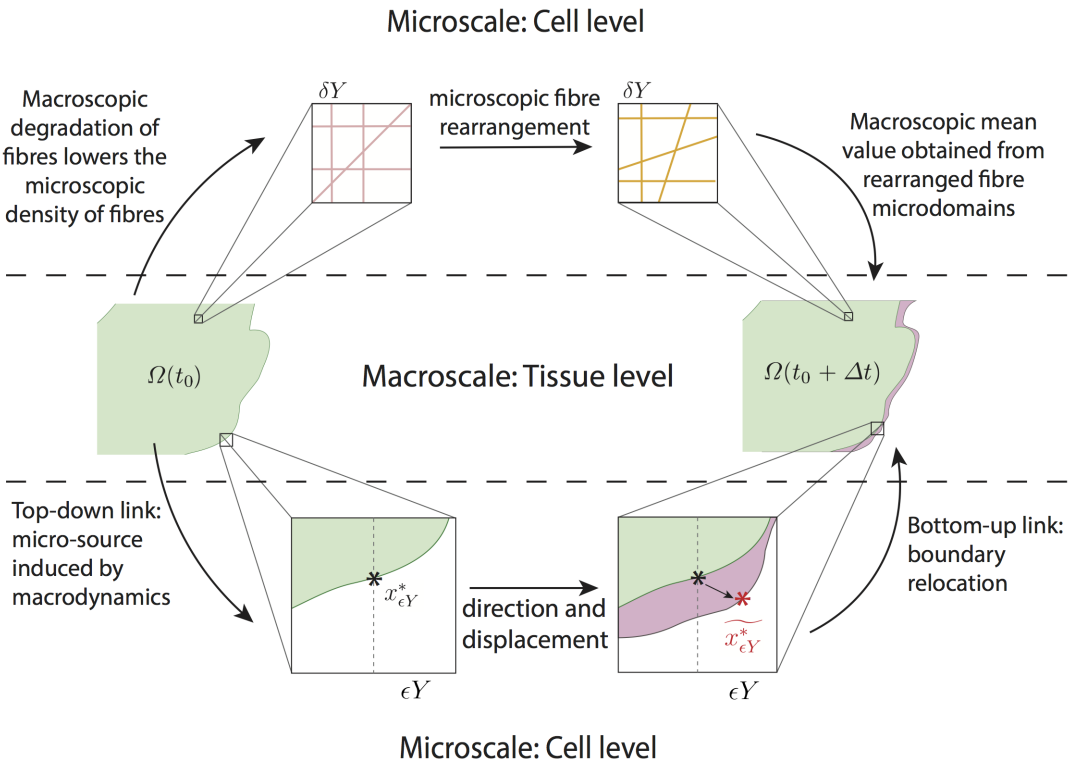

Figure 3.6: Schematic summary of global multi-scale model.

distribution of both the invading cancer cells and the fibrous and non-fibrous density components of the ECM, and is given by the following non-local coupled system:

$$\frac{\partial c}{\partial t} = \nabla \cdot [D_1 \nabla c - c\mathcal{A}(x, t, \mathbf{u}(\cdot, t), \theta_f(\cdot, t))] + \mu_1 c(1 - \rho(\mathbf{u}))^+, \tag{3.27a}$$

$$\frac{dF}{dt} = -\gamma_1 cF, \tag{3.27b}$$

$$\frac{dl}{dt} = -\gamma_2 cl. \tag{3.27c}$$

Occurring on the cell-scale, the micro-scale part of the first multiscale system controls the dynamic redistribution of microscopic fibres within the entire cancer region. On each micro-domain $\delta Y(x)$, the realignment of the existing micro-fibres is trig-

gered by the spatial flux of cancer cells from the macro-scale and this is realised by weighted action of this over the oriented macroscopic fibres distribution that they meet at x. Once all fibre micro-domains within the cancer region have undergone redistribution, a new macroscopic fibre orientation and mean value per each $\delta Y(x)$ is obtained and that in its turn will have its effect in the important cell-adhesion behaviour that the cancer exhibits at macro-scale. Finally, in the second multi-scale system, the spatial distribution of cancer cells induces a source of MDEs on the boundary at the micro-scale level. In return, the leading edge proteolytic micro-dynamics of MDEs instigates a change in the position of the tissue-scale tumour boundary that corresponds to the pattern of the peritumoural ECM degradation, enabling this way the invasion process to continue on the expanding domain.

3.4 Numerical Approach: Key Points of the Implementation

Building on the numerical multiscale platform initially introduced in Trucu et al. (2013), the implementation of the novel multiscale moving boundary model that we proposed in this work required a number of new major computational steps, which will be detailed in the next three subsections. These include a special treatment for several computational aspects, such as those concerned with: macro-scale computations on the expanding tumour; the macro-scale adhesion term; and a new predictor-corrector scheme for the cancer dynamics equation (3.27a).

Finally, the approach for the cross-interface proteolytic micro-dynamics on each tumour boundary micro-domain ϵY follow precisely the steps described in Trucu et al. (2013), involving a finite element scheme using bilinear shape functions and square elements, reason for which we do not include that here.

3.4.1 Macro-scale computations on the expanding tumour domain

While considering a uniform spatial mesh of size $\Delta x = \Delta y = h$ for the maximal cube Y, recorded on a square grid $\{(x_i, x_j)\}_{i,j=1...M}$, with $M := length(Y)/h + 1$, the actual macroscopic computation will be performed exclusively on the expanding tumour $\Omega(t_0)$ over every macro-micro time interval $[t_0, t_0 + \Delta t]$ as will be detailed in the following. Specifically, to explore this, let us first denote by $\mathcal{I}(\cdot,\cdot) : \{1, ..., M\} \times \{1, ..., M\} \to \{0, 1\}$ the *on-grid cancer indicator* function given as usual by

$$\mathcal{I}(i,j) := \begin{cases} 1 & \text{if } (x_i, x_j) \in \Omega(t_0), \\ 0 & \text{if } (x_i, x_j) \notin \Omega(t_0), \end{cases} \tag{3.28}$$

Further, let's observe that the *on-grid closest neighbour indicator* functions

$$I_{x,+1}(\cdot,\cdot)\,, I_{x,-1}(\cdot,\cdot), I_{y,+1}(\cdot,\cdot)\,, I_{y,-1}(\cdot,\cdot) \colon \{2, ..., M-1\} \times \{2, ..., M-1\} \to \{0, 1\},$$

defined by

$$\begin{aligned} I_{x,\pm1}(i,j) &:= |\mathcal{I}(i,j) - \mathcal{I}(i, j \pm 1)| \cdot \mathcal{I}(i,j), \\ I_{y,\pm1}(i,j) &:= |\mathcal{I}(i \pm 1, j) - \mathcal{I}(i,j)| \cdot \mathcal{I}(i,j), \end{aligned} \tag{3.29}$$

enable us to detect *on-the-fly* the grid positions immediately outside the cancer boundary as the points of non-zero value along each spatial direction, given by the union of preimages $I^{-1}_{x,-1}(\{1\}) \cup I^{-1}_{x,+1}(\{1\})$ and $I^{-1}_{y,-1}(\{1\}) \cup I^{-1}_{y,+1}(\{1\})$ for x- and y-direction, respectively.

Over each macroscale time perspective $[t_0, t_0+\Delta t]$ the overall macroscopic scheme for (3.27) involves the method of lines coupled with a novel predictor-corrector method for time marching (whose main steps will be detailed in the next subsection),

the discretisation of the spatial operators appearing in the right-hand side of (3.27a) is based on central differences and midpoint approximations. For this, considering a uniform discretisation $\{t_p\}_{p=0\ldots k}$ of $[t_0, t_0 + \Delta t]$, of time step $\delta t > 0$, let's denote by $c^p_{i,j}$, $\mathcal{A}^p_{i,j}$, $F^p_{i,j}$, $l^p_{i,j}$ the discretised values of $c, \mathcal{A}, F, l$ at $((x_i, x_j), t_p)$, respectively. Thus, at any spatial node $(x_i, x_j) \in \Omega(t_0)$, the no-flux across the moving boundary dynamics is accounted for via the indicators (3.28)-(3.29) on the expanding spatial mesh, and results into the midpoint approximations

$$\begin{aligned} c^p_{i,j\pm\frac{1}{2}} &:= \tfrac{c^p_{i,j}+[I_{x,\pm1}(i,j)c^p_{i,j}+\mathcal{I}(i,j\pm1)c^p_{i,j\pm1}]}{2}, \\ c^p_{i\pm\frac{1}{2},j} &:= \tfrac{c^p_{i,j}+[I_{y,\pm1}(i,j)c^p_{i,j}+\mathcal{I}(i\pm1,j)c^p_{i\pm1,j}]}{2}, \end{aligned} \tag{3.30}$$

and

$$\begin{aligned} \mathcal{A}^p_{i,j\pm\frac{1}{2}} &:= \tfrac{\mathcal{A}^p_{i,j}+[I_{x,\pm1}(i,j)\mathcal{A}^p_{i,j}+\mathcal{I}(i,j\pm1)\mathcal{A}^p_{i,j\pm1}]}{2}, \\ \mathcal{A}^p_{i\pm\frac{1}{2},j} &:= \tfrac{\mathcal{A}^p_{i,j}+[I_{y,\pm1}(i,j)\mathcal{A}^p_{i,j}+\mathcal{I}(i\pm1,j)\mathcal{A}^p_{i\pm1,j}]}{2}, \end{aligned} \tag{3.31}$$

while the central differences for c at the virtual nodes $(i, j \pm \frac{1}{2})$ and $(i \pm \frac{1}{2}, j)$ are given by

$$\begin{aligned} [c_x]^p_{i,j+\frac{1}{2}} &:= \tfrac{[I_{x,+1}(i,j)c_{i,j}+\mathcal{I}(i,j+1)c_{i,j+1}]-c_{i,j}}{\Delta y}, \\ [c_x]^p_{i,j-\frac{1}{2}} &:= \tfrac{c_{i,j}-[I_{x,-1}(i,j)c_{i,j}+\mathcal{I}(i,j-1)c_{i,j-1}]}{\Delta y}, \\ [c_y]^p_{i+\frac{1}{2},j} &:= \tfrac{[I_{y,+1}(i,j)c_{i,j}+\mathcal{I}(i+1,j)c_{i+1,j}]-c_{i,j}}{\Delta x}, \\ [c_y]^p_{i-\frac{1}{2},j} &:= \tfrac{c_{i,j}-[I_{y,-1}(i,j)c_{i,j}+\mathcal{I}(i-1,j)c_{i-1,j}]}{\Delta x}. \end{aligned} \tag{3.32}$$

Therefore, the approximation for the term $\nabla \cdot [D_1 \nabla c - c\mathcal{A}(t, x, \mathbf{u}(\cdot, t), \theta_f(\cdot, t))]$ in

(3.27a) is obtained as

$$
\begin{aligned}
&(\nabla \cdot [D_1 \nabla c - c\mathcal{A}(x,t,\mathbf{u}(\cdot,t),\theta_f(\cdot,t))])^p_{i,j} \\
&\qquad \simeq \frac{D_1([c_x]^p_{i,j+\frac{1}{2}} - [c_x]^p_{i,j-\frac{1}{2}}) - c^p_{i,j+\frac{1}{2}} \cdot \mathcal{A}^p_{i,j+\frac{1}{2}} + c^p_{i,j-\frac{1}{2}} \cdot \mathcal{A}^p_{i,j-\frac{1}{2}}}{\Delta x} \\
&\qquad\quad + \frac{D_1([c_y]^p_{i+\frac{1}{2},j} - [c_y]^p_{i-\frac{1}{2},j}) - c^p_{i+\frac{1}{2},j} \cdot \mathcal{A}^p_{i+\frac{1}{2},j} + c^p_{i-\frac{1}{2},j} \cdot \mathcal{A}^p_{i-\frac{1}{2},j}}{\Delta y},
\end{aligned}
\tag{3.33}
$$

and so, denoting by $\mathcal{F}^p_{i,j}$ the discretised value of the flux $\mathcal{F}(\cdot,\cdot)$ at the spatio-temporal node $((x_i,x_j),t_p)$, the spatio-temporal discretisation of $\nabla\cdot\mathcal{F} := \nabla\cdot[D_1\nabla c - c\mathcal{A}(x,t,\mathbf{u}(\cdot,t),\theta_f(\cdot,t))]$ given in (3.33) can therefore be equivalently expressed in a compact form as

$$
(\nabla \cdot \mathcal{F})^p_{i,j} \simeq \frac{\mathcal{F}^p_{i,j+\frac{1}{2}} - \mathcal{F}^p_{i,j-\frac{1}{2}}}{\Delta x} + \frac{\mathcal{F}^p_{i+\frac{1}{2},j} - \mathcal{F}^p_{i-\frac{1}{2},j}}{\Delta y} \tag{3.34}
$$

where $\mathcal{F}^p_{i,j\pm\frac{1}{2}} := D_1[c_x]^p_{i,j\pm\frac{1}{2}} - c^p_{i,j\pm\frac{1}{2}} \cdot \mathcal{A}^p_{i,j\pm\frac{1}{2}}$ and $\mathcal{F}^p_{i\pm\frac{1}{2},j} := D_1[c_y]^p_{i\pm\frac{1}{2},j} - c^p_{i\pm\frac{1}{2},j} \cdot \mathcal{A}^p_{i\pm\frac{1}{2},j}$.

3.4.2 Adhesive flux computation

As already mentioned above, an important aspect within the macroscopic part of our solver is the numerical approach addressing the adhesive flux $\mathcal{A}(x,t,\mathbf{u}(\cdot,t),\theta_f(\cdot,t))$, which explores the effects of cell-cell, cell-ECM-non-fibre and cell-fibre adhesion of cancer cell population. Although to a certain extent we adopt a similar approach to the one that we previously proposed in Chapter 2 and detailed in Shuttleworth and Trucu (2018) (for a similar macro-scale invasion context but in the absence of fibre dynamics), the numerical approximation for the non-local term $\mathcal{A}(x,t,\mathbf{u}(\cdot,t),\theta_f(\cdot,t))$ involves a series of off-grid computations on a new decomposition of the sensing region, developing further the approach introduced in Section 2.3.1 in Chapter 2 and adapting that to the new context of the current macro-model. For completeness, we

detail this here as follows. Thus, at a given spatio-temporal node $((x_i, x_j), t_p)$, we decompose the sensing region $\mathbf{B}((x_i, x_j), R)$ in

$$q := \sum_{i=1}^{s} 2^{m+(i-1)} \text{ annulus radial sectors } \mathcal{S}_1, \ldots, \mathcal{S}_{q,}$$

which are obtained by intersecting each annulus $i \in \{1, ..., s\}$ annuli with a corre-

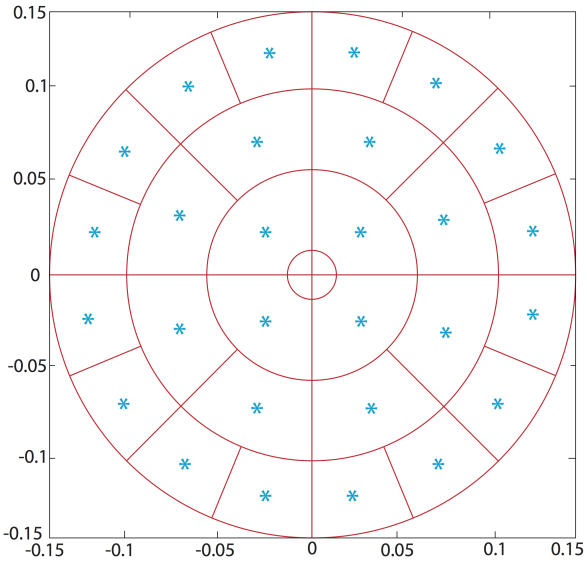

Figure 3.7: Sensing region $\mathbf{B}(x, R)$ approximated by the annulus radial sectors with the barycentre $\mathbf{b}_{\mathcal{S}_\nu}$ associated to each sector $\mathcal{S}_\nu$ highlighted with a blue star.

sponding number of $2^{m+(i-1)}$ uniformly distributed radial sectors of $\mathbf{B}((x_i, x_j), R)$, as shown in Figure 3.7, while considering the remaining central circle to be of a computationally negligible radius. Then, using a standard barycentric interpolation approach for approximating the off-grid values, $\forall \nu \in \{1, \ldots, q\}$, on each annulus sector S_ν, we calculate the mean-values of all the macro-scale densities of cancer cells $c(\cdot, t_p)$, ECM non-fibres component $l(\cdot, t_p)$, macroscopic ECM fibres $F(\cdot, t_p)$

and their associated directions $\theta_f(\cdot, t_p)$, namely:

$$W^p_{\mathcal{S}_\nu,c} := \tfrac{1}{\lambda(\mathcal{S}_\nu)} \int\limits_{\mathcal{S}_\nu} c(\xi, t_p)\, d\xi, \qquad W^p_{\mathcal{S}_\nu,l} := \tfrac{1}{\lambda(\mathcal{S}_\nu)} \int\limits_{\mathcal{S}_\nu} l(\xi, t_p)\, d\xi,$$

$$W^p_{\mathcal{S}_\nu,F} := \tfrac{1}{\lambda(\mathcal{S}_\nu)} \int\limits_{\mathcal{S}_k} F(\xi, t_p)\, d\xi, \quad \text{and} \quad W^p_{\mathcal{S}_\nu,\theta_f} := \tfrac{1}{\lambda(\mathcal{S}_\nu)} \int\limits_{\mathcal{S}_\nu} \theta_f(\xi, t_p)\, d\xi,$$

respectively. Further, $\forall \nu \in \{1, \ldots, q\}$, denoting by $\mathbf{b}_{\mathcal{S}_\nu}$ the barycenter of $\mathcal{S}_\nu$, this enable us to evaluate the unit vector denoted by $\mathbf{n}_\nu$ that points from the centre of the sensing region to $\mathbf{b}_{\mathcal{S}_\nu}$, i.e.,

$$\mathbf{n}_\nu := \frac{\mathbf{b}_{\mathcal{S}_\nu} - (x_i, x_j)}{\| \mathbf{b}_{\mathcal{S}_\nu} - (x_i, x_j) \|_2},$$

as well as the corresponding macroscopic vector accounting for the influence of the cumulative mean-value direction of the fibres on $\mathcal{S}_\nu$, namely

$$\widehat{\mathbf{n}}^p_\nu := \frac{\mathbf{n}_\nu + W^p_{\mathcal{S}_\nu,\theta_f}}{\| \mathbf{n}_\nu + W^p_{\mathcal{S}_\nu,\theta_f} \|_2},$$

Thus, finally, the approximation of the adhesion flux $\mathcal{A}(x, t, \mathbf{u}(\cdot, t), \theta_f(\cdot, t))$ at the spatio-temporal node $((x_i, x_j), t_p)$, is denoted by $\mathcal{A}^p_{i,j}$ and is given by

$$\mathcal{A}^p_{i,j} = \frac{1}{R} \sum_{\substack{\nu=1 \\ \mathbf{b}_{\mathcal{S}_\nu} \in \Omega(t_0)}}^{q} \mathcal{K}(\mathbf{b}_{\mathcal{S}_\nu})[\mathbf{n}_\nu \cdot (\mathbf{S}_{cc} W^p_{\mathcal{S}_\nu,c} + \mathbf{S}_{cl} W^p_{\mathcal{S}_\nu,l}) + \widehat{\mathbf{n}}^p_\nu \cdot \mathbf{S}_{cF} W^p_{\mathcal{S}_\nu,F}](1 - \rho(\mathbf{u}^p_{\mathbf{b}_{\mathcal{S}_\nu}}))^+ \lambda(\mathcal{S}_\nu), \tag{3.35}$$

where, $\forall \nu \in \{1, \ldots, q\}$, denoting $\mathbf{u}^p_{\mathbf{b}_{\mathcal{S}_\nu}} := [W^p_{\mathcal{S}_\nu,c}, W^p_{\mathcal{S}_\nu,l}, W^p_{\mathcal{S}_\nu,F}]^T$, we have that $\rho(\mathbf{u}^p_{\mathbf{b}_{\mathcal{S}_\nu}})$ is volume fraction defined in (3.13) that corresponds to the discrete vector $\mathbf{u}^p_{\mathbf{b}_{\mathcal{S}_\nu}}$.

3.4.3 Time-marching: the predictor-corrector step

For the time discretisation of equation (3.27a), we develop a novel predictor-corrector scheme involving a non-local trapezoidal corrector. For this, let us denote by $H(\cdot,\cdot,\cdot)$ the right-hand side spatial operator of (3.27a), which is defined as follows. At any instance in time and any corresponding triplet $(\overline{\mathcal{F}}, \overline{c}, \overline{\mathbf{u}})$ of given spatially discretised values for the flux $\mathcal{F}$, the cell population c, and the tumour vector $\mathbf{u}$, by ignoring for simplicity the time notation we have that H is given by

$$H(\overline{\mathcal{F}}_{i,j}, \overline{c}_{i,j}, \overline{\mathbf{u}}_{i,j}) := (\nabla \cdot \overline{\mathcal{F}})_{i,j} + \mu_1 \overline{c}_{i,j}(1 - \rho(\overline{\mathbf{u}}_{i,j})), \tag{3.36}$$

where the spatial discretisation $(\nabla \cdot \overline{\mathcal{F}})_{i,j}$ is given here still by (3.34) but applied to the spatial flux $\overline{\mathcal{F}}$, and $\rho(\overline{\mathbf{u}}_{i,j})$ is simply the volume fraction defined in (3.13) evaluated for the discrete vector $\overline{\mathbf{u}}_{i,j} := [\overline{c}_{i,j}, \overline{F}_{i,j}, \overline{l}_{i,j}]$, $\forall i,j = 1...M$. In this context, on the time interval $[t_p, t_{p+1}]$, we first predict *on-the-fly* values for c at $t_{p+\frac{1}{2}}$, namely

$$\tilde{c}_{i,j}^{p+\frac{1}{2}} = c_{i,j}^{p} + \frac{\delta t}{2} H(\mathcal{F}_{i,j}^{p}, c_{i,j}^{p}, \mathbf{u}_{i,j}^{p}). \tag{3.37}$$

where $\mathbf{u}_{i,j}^{p} := [c_{i,j}^{p}, F_{i,j}^{p}, l_{i,j}^{p}]$, $\forall i,j = 1...M$. Further, using these predicted values $\tilde{c}^{p+\frac{1}{2}}$, we calculate the corresponding predicted flux at $t_{p+\frac{1}{2}}$, namely $\tilde{\mathcal{F}}^{p+\frac{1}{2}}$, and then we construct a non-local corrector that involves the average of the flux at the active neighbouring spatial locations

$$\{(x_i, x_{j\pm1}), (x_{i\pm1}, x_j), (x_{i\pm1}, x_{j-1}), (x_{i\pm1}, x_{j+1})\} \cap \Omega(t_0). \tag{3.38}$$

Thus, denoting by $\mathcal{N}$ the set of indices corresponding to these active locations, we have that the corrector flux is calculated as

$$\mathcal{F}_{i,j}^{*p+\frac{1}{2}} = \frac{1}{card(\mathcal{N})} \sum_{(\sigma,\zeta)\in\mathcal{N}} \tilde{\mathcal{F}}_{\sigma,\zeta}^{p+\frac{1}{2}}, \tag{3.39}$$

ultimately enabling us to use the trapezoidal approximation to obtain the corrected value for c at $t_{p+\frac{1}{2}}$ as

$$c_{i,j}^{p+\frac{1}{2}} = c_{i,j}^{p} + \frac{\delta t}{4}\big[H(\mathcal{F}_{i,j}^{p}, c_{i,j}^{p}, \mathbf{u}_{i,j}^{p}) + H(\mathcal{F}_{i,j}^{*p+\frac{1}{2}}, \tilde{c}_{i,j}^{p+\frac{1}{2}}, \tilde{\mathbf{u}}_{i,j}^{p+\frac{1}{2}})\big] \tag{3.40}$$

where $\tilde{\mathbf{u}}_{i,j}^{p+\frac{1}{2}} := [\tilde{c}_{i,j}^{p+\frac{1}{2}}, F_{i,j}^{p}, l_{i,j}^{p}]$, $\forall i,j = 1...M$. Finally, we use the average

$$\bar{c}_{i,j}^{p+\frac{1}{2}} := \frac{c_{i,j}^{p} + c_{i,j}^{p+\frac{1}{2}}}{2} \tag{3.41}$$

to re-evaluate the flux at $t_{p+\frac{1}{2}}$, namely $\mathcal{F}^{p+\frac{1}{2}}$ (corresponding to the average values $\bar{c}^{p+\frac{1}{2}}$) and then to initiate the predictor-corrector steps described above on this new time interval $[t_{p+\frac{1}{2}}, t_{p+1}]$. Thus, following the predictor step, we first obtain the predicted values at at t_{p+1}, namely

$$\tilde{c}_{i,j}^{p+1} = \bar{c}_{i,j}^{p+\frac{1}{2}} + \frac{\delta t}{2} H(\mathcal{F}_{i,j}^{p+\frac{1}{2}}, \bar{c}_{i,j}^{p+\frac{1}{2}}, \bar{\mathbf{u}}_{i,j}^{p+\frac{1}{2}}) \tag{3.42}$$

where $\bar{\mathbf{u}}_{i,j}^{p+\frac{1}{2}} := [\bar{c}_{i,j}^{p+\frac{1}{2}}, F_{i,j}^{p}, l_{i,j}^{p}]$, $\forall i,j = 1...M$. Finally, we correct these values at t_{p+1} with the same non-local trapezoidal-type corrector as described in (3.40), here involving the corrector flux calculated as average of the predicted flux values $\tilde{\mathcal{F}}^{p+1}$ (corresponding to the predicted values $\tilde{c}^{p+1}$) at the active neighbouring locations

given in (3.38), namely

$$\mathcal{F}_{i,j}^{*p+1} = \frac{1}{card(\mathcal{N})} \sum_{(\sigma,\zeta)\in\mathcal{N}} \tilde{\mathcal{F}}_{\sigma,\zeta}^{p+1}. \tag{3.43}$$

Thus, this last corrector step gives us ultimately the values that we accept at t_{p+1}, namely

$$c_{i,j}^{p+1} = \bar{c}_{i,j}^{p+1} + \frac{\delta t}{4}\big[H(\mathcal{F}_{i,j}^{p+\frac{1}{2}}, \bar{c}_{i,j}^{p+\frac{1}{2}}, \bar{\mathbf{u}}_{i,j}^{p+\frac{1}{2}}) + H(\mathcal{F}_{i,j}^{*p+1}, \tilde{c}_{i,j}^{p+1}, \tilde{\mathbf{u}}_{i,j}^{p+1})\big] \tag{3.44}$$

where $\tilde{\mathbf{u}}_{i,j}^{p+1} := [\tilde{c}_{i,j}^{p+1}, F_{i,j}^{p}, l_{i,j}^{p}]$, $\forall i,j = 1...M$.

Lastly, for the discretisation of (3.27b) and (3.27c), we follow the same predictor-corrector method as the one used in Trucu et al. (2013), where the corrector part uses simply a second-order trapezoidal scheme on $[t_p, t_{p+1}]$.

3.5 Computational Simulations and Results

To illustrate our model, we consider the region $Y := [0,4] \times [0,4]$ and we start our dynamics by adopting here the same initial condition for c as in Trucu et al. (2013), namely

$$c(x,0) = 0.5\left(\exp\left(-\frac{||x-(2,2)||_2^2}{0.03}\right) - \exp(-28.125)\right)\left(\chi_{\mathbf{B}((2,2),0.5-\gamma)} * \psi_\gamma\right), \tag{3.45}$$

where ψ_γ is the standard mollifier detailed in Appendix C.1 that acts within a radius $\gamma << \frac{\Delta x}{3}$ from $\partial\mathbf{B}((2,2),0.5-\gamma)$ to smooth out the characteristic function $\chi_{\mathbf{B}((2,2),0.5-\gamma)}$. Thus, initially, the cancer cell population occupies the region $\Omega(0) = \mathbf{B}((2,2),0.5)$ positioned in the centre of Y.

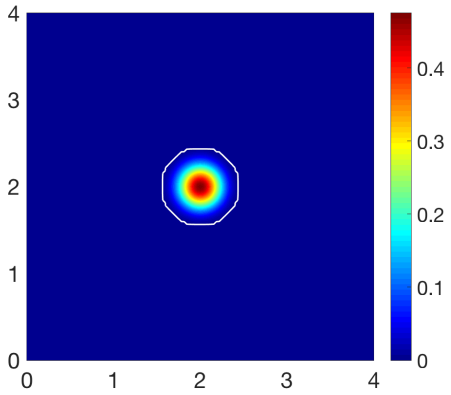

(a) initial cancer distribution

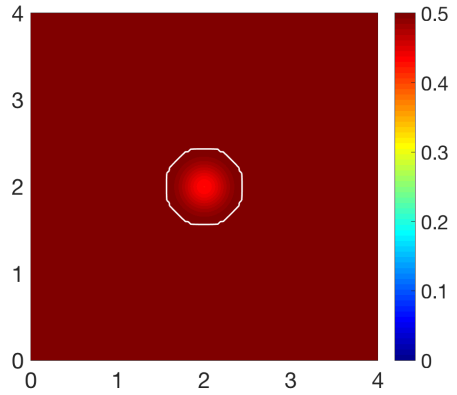

(b) initial ECM density: $F(\cdot, 0) + l(\cdot, 0)$

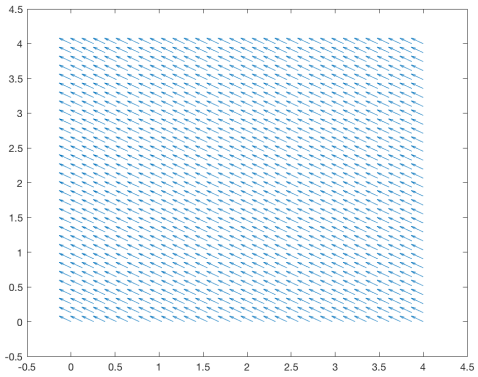

(c) initial macro-scale fibres vector field

Figure 3.8: Initial conditions showing the distribution of cancer cells (a), the homogeneous density of ECM (b) with the invasive boundary of the tumour represented by the white contour, and the initial macroscopic fibre orientations per each micro-domain represented by a vector field (c). These vectors have been magnified from the usual size of the domain for better representation.

Initial condition for the ECM fibre component. For the initial distribution of the ECM fibre phase, we consider first a generic micro-domain centred at 0 of cell-scale size $\delta = h$, namely δY, and using the microscopic patterns of fibres defined in (3.5) and illustrated in Figure 3.2, we replicate and centre this micro-fibre distribution in the cell-scale neighbourhood of any spatial location (x_i, x_j) in the discretisation of Y on the corresponding micro-domain $\delta Y(x_i, x_j) := \delta Y + (x_i, x_j)$.

The maximal height of the micro-fibres considered here is appropriately calibrated uniformly across all micro-domains is so that the resulting macroscopic distribution of fibres $F(x,\cdot)$ represents a percentage $p = 0.2$, of the mean density of the non-fibrous ECM phase. Therefore at initial time $t_0 = 0$, all fibre micro-domains $\delta Y(x_i, x_j)$ support identical distributions of micro-fibres, $\forall i, j = 1...M$ and as a consequence, every fibre orientation $\theta_f((x_i, x_j), 0)$ exhibits the same initial orientation and magnitude, as shown in Figure 3.8c.

Finally, for the non-fibre ECM component, we consider both a homogeneous and a heterogeneous scenario, which will be detailed below.

3.5.1 Homogeneous non-fibre ECM component

The initial distribution of the non-fibre ECM component, $l(x, 0)$, will be in the first instance taken as the homogenous distribution, namely as $l(x, 0) = \min\{0.5, 1 - c(x, 0)\}$. The initial conditions of the cell population $c(x, 0)$ given in (3.45), the full ECM density $v(x, 0) = l(x, 0) + F(x, 0)$, and the resulting initial fibre orientations $\theta_f(x, 0)$ can be seen in Figure 3.8. Using the parameter set Σ_1, Table 3.1, and the following adhesive strength coefficients for cell-cell adhesion, cell-fibre adhesion and cell-non-fibre ECM adhesion,

$$\mathbf{S}_{max} = 0.5, \qquad \mathbf{S}_{cF} = 0.1 \qquad \text{and} \quad \mathbf{S}_{cl} = 0.01, \tag{3.46}$$

respectively, in Figure 3.9 we show the computational results at macro-micro stage $20\Delta t$ for the evolution of: the cancer cell population in subfigure 3.9a; the full ECM density in subfigure 3.9b; the macro-scale fibre magnitude in subfigure 3.9c; the vector field of oriented fibres at two different resolutions, namely, coarsened twice and coarsened fourfold in subfigures 3.9d and 3.9f, respectively; and a 3D plot of the macroscopic oriented fibres in 3.9e.

Table 3.1: *The parameters in* Σ_1

Parameter	Value	Description	Reference
D_1	3.5×10^{-4}	diffusion coeff. for cell population c_1	Domschke et al. (2014)
D_m	10^{-3}	diffusion coeff. for MDEs	Estimated
μ_1	0.25	proliferation coeff. for cell population c_1	Domschke et al. (2014)
γ_1	2	non-fibrous ECM degradation coeff.	Shuttleworth and Trucu (2019c)
γ_2	1.5	macroscopic fibre degradation coeff.	Peng et al. (2017)
α_1	1	MDE secretion rate of c_1	Estimated
R	0.15	sensing radius	Shuttleworth and Trucu (2019c)
r_{fib}	0.0016	width of micro-fibres	Shuttleworth and Trucu (2019c)
$f_{\max}$	0.6360	max. micro-density of fibres	Shuttleworth and Trucu (2019c)
p	0.15-0.2	percentage of non-fibrous ECM	Estimated
h	0.03125	macro-scale spatial discretisation size	Trucu et al. (2013)
ϵ	0.0625	size of micro-domain ϵY	Trucu et al. (2013)
δ	0.03125	size of micro-domain δY	Shuttleworth and Trucu (2019c)

Comparing with the initial distributions of cancer cells and ECM displayed in Figure 3.8, the main body of the tumour is increasing in size, whilst decreasing in overall density, spreading the initial distribution outwards and creating a plateau of cancer cells, as shown in subfigure 3.9a. While in the absence of fibres the boundary of the tumour was expanding isotropically in the case of homogenous ECM, as shown in Shuttleworth and Trucu (2018); Trucu et al. (2013), a different situation we witness here in the case of homogeneous non-fibre ECM as the presence of the oriented fibres phase of ECM is now taken into consideration. Specifically, the cancer cell invasion becomes anisotropic, leading to lobular patterns and having the fibres reaching outwards in the boundary regions of faster tumour progression. This behaviour is clarified by the fibre vector plot 3.9d where the orientations of the redistributed fibres can be seen to point in the direction of this lobule on the invasive edge. The orientation of the fibres is strongly affected during their rearrangement, with their behaviour dependent on the initial macroscopic density of fibres and

the spatial flux of the cancer cells. This flux carries a higher weight than the distribution of fibres and thus the cells ultimately have governance over the direction of realignment. Finally, Alongside the fibre realignment, the cancer cells also degrade the fibres, this leading to a low density central region of fibres 3.9c.

As the simulation continue to stage $40\Delta t$, the initial main body of the tumour (consisting of a high density region of cells in the centre of Y) is spreading out, following the initial orientation of the fibres, giving rise to lobular progression pattern for the cell population in this direction, as shown in Figure 3.10a. The boundary of the tumour has undergone minor changes with respect to stage $20\Delta t$ shown in Figure 3.9, the main tumour dynamics occurring mainly on the central cluster of cells. The non-fibrous part of the ECM is further degraded under the presence of cancer cells 3.10b, and the fibres are being pushed to the boundary of the tumour 3.10c, creating a larger region of low density ECM.

3.5.2 Heterogeneous non-fibrous ECM component

We now introduce an initially heterogeneous non-fibre ECM component. Whilst maintaining the same initial conditions for $c(x, 0)$ specified in (3.45) as well as for the initial distributions of ECM micro-fibres (illustrated in Figure 3.2), the heterogeneity of the non-fibre ECM phase will be structured in a similar manner to Domschke et al. (2014); Shuttleworth and Trucu (2018) using the initial condition

$$l(x, 0) = \min\left\{h(x_1, x_2), 1 - c(x, 0)\right\}, \tag{3.47}$$

where

$$h(x_1, x_2) = \frac{1}{2} + \frac{1}{4}\sin(\zeta x_1 x_2)^3 \cdot \sin(\zeta \frac{x_2}{x_1}),$$
$$(x_1, x_2) = \frac{1}{3}(x + 1.5) \ \in [0,1]^2 \text{ for } x \in Y, \quad \zeta = 7\pi.$$

These initial conditions can be seen in Figure 3.11.

Computational results at stage $20\Delta t$ are shown in Figure 3.12, using the initial conditions shown in Figure 3.11 and the parameter set Σ_1 with the adhesive terms (3.46). Due to the initial distribution of the non-fibrous component of the matrix, there are patches of high and low density areas, and regions of high tumour density correspond to the areas of high degradation of fibres and the surrounding non-fibre ECM 3.12b. The proliferating edge of the tumour is expanding in a lobular fashion, reaching out to the high density patches and encasing the low density regions in the process, as the higher ECM density equates to increased opportunity for cell-adhesion. This is the natural direction in which the tumour cells try to invade, pushing out from its centre and into the surrounding matrix, and causing the tumour to encircle itself with a region of higher magnitude fibres, as shown in 3.12c-3.12f. The macroscopic orientation of the fibres is refashioned 3.12d as the cancer cells have rearranged and degraded the fibres, leading to significant changes in the fibre orientations and magnitude patterns near the boundary of the tumour with respect to their initial state, and causing them both to increase their magnitude and to point generally toward the the fast invading regions of the cancer boundary. While the fibre are being pushed and rearranged by the cancer cells outwards, away from the main body of the tumour, in regions of high cancer density, these are degraded, as evidenced by the low distribution of fibres in the centre of the tumour, presented in subfigures 3.12c-3.12f.

Figure 3.13 illustrates simulations plotted at stage $40\Delta t$. The main body of the tumour is beginning to form new high distribution regions within the highly degraded patch of ECM, as shown in 3.13a-3.13b. This build up of cells is due to increasingly higher magnitudes for rearranged fibres with invasion favourable orientations, which result into a significantly higher effect of cell-fibre adhesion leading to increased transport of cells towards those areas. Islands are forming within the boundary of the tumour away from the primary tumour mass due to low ECM density in those regions, which result in weak levels of both cell-non-fibre ECM and cell-fibre adhesion, and as a consequence the cells take longer time to advance upon these regions. As shown in Figures 3.13c-3.13f, the fibres persevere in surrounding the tumour, with their oriented fibres on the central part of the tumour (corresponding to regions of very high cancer cell density) continuing to be strongly degraded and dominated in their direction by the flow $\mathcal{F}$. Again, high density regions of ECM fibres equates to more opportunities for cell-fibre adhesion, thus creating a preferential direction of invasion. The cancer cells are rearranging the fibres to follow this direction, allowing them an easier route of invasion. As shown in Figure 3.13c, by the gathering of fibre distributions away from the tumour centre, it is evident that the cancer cells are pushing the fibres outwards to the boundary of the tumour and in the direction of the invasion front, as found also in Pinner and Sahai (2008) .

3.5.3 Increased cell-fibre adhesion within the heterogeneous non-fibre ECM phase scenario

As we explore the effect of the heterogeneous two phase ECM, it is important to consider the relation between the tumour progression and increased cell-fibre adhesion. By increasing cell-fibre adhesion, we expect the cancer cells to advance further into their surrounding environment. For that, we double the cell-fibre adhesion,

taking $\mathbf{S}_{cF} = 0.2$, while maintaining the same initial conditions (i.e., for cancer cell population, those given in (3.45); for fibre ECM phase, those defined in (3.5) and illustrated in Figure 3.2; and for heterogeneous non-fibrous ECM, those given in (4.20)) along with the parameters defined in the parameter set Σ_1 and the cell-cell and cell-ECM-non-fibres adhesion as stated in (3.46). The computational results shown for this situation in Figures 3.14 and 3.15, show that the fibres now have more influence over the route of invasion and its pattern, presenting a leading edge with a highly lobular structure. There are small islands present in high density regions of the ECM, suggesting the density is simply too high and first requires more degradation before the cells can completely engulf this area. The overall degradation of the matrix has remained centralised to the central part of the tumour as before. Similar to the previous cases considered here, the cancer cells have rearranged the fibres also in this situation, strongly degrading the fibres in the regions with very high cancer density 3.14c, whilst the magnitude and orientation of the fibres situated closer to the tumour periphery have been altered and are positioned similar to the case where cell-fibre adhesion $\mathbf{S}_{cF} = 0.1$, pointing clearly outwards in boundary regions of increased invasive behaviour.

Figure 3.15 displays computations at stage $40\Delta t$. An important difference between Figures 3.14a and 3.15a is observed within the main body of the tumour. When the cell-fibre adhesion coefficient is increased, the central part of the tumour has an overall higher distribution, and is being pulled in different directions, as illustrated by the three areas of increased cell distribution. Shown in Figure 3.15d, the fibre orientations have been realigned, and in boundary regions of faster invasion the cumulative fibres direction tends to become almost perpendicular to the fibres from the peritumoural region. The cancer cells attempt to align the fibres with their own directional preference, i.e., outwards from the centre and towards the higher

density regions of ECM where they have increased opportunity for adherence. The cells continue to pursue this goal, as evidenced in Figure 3.15b where we see the leading edge advancing on the higher density areas of ECM. From our simulations, we noted that an increase in cell-fibre adhesion causes a larger overall invasion of the tumour, suggesting that the fibres presence plays an important role in the invasion of cancer.

3.6 Sensitivity to initial fibre distributions

To address sensitivity to the initial conditions of the model, we present and discuss the results of four different initial fibre distributions under both a homogeneous and heterogeneous non-fibre ECM. By first considering a homogeneous non-fibre-ECM phase, $l(0,t) = 0.5$, we construct the initial distributions of fibres by varying the percentage of the mean density of the non-fibrous ECM phase, namely, $p = 0.05, 0.1, 0.15, 0.2$. As we increase the percentage of the non-fibre ECM phase, the fibrous part of the matrix has a progressively larger influence on cell movement. This behaviour is expected due to their involvement within the cellular adhesion process, with increased fibre distribution causing a higher affinity for cell-fibre adhesion.

The main body of the tumour remains symmetrical in the presence of a low initial fibre distribution $p = 0.05$, Figure 3.16a. The macroscopic fibre directions undergo little change here, continuing to exhibit the same direction throughout the domain, Figure 3.18a. As we increase the distribution of fibres, $p = 0.1$, the previous symmetry is lost, Figure 3.16b, and there is a small gathering of cells in the direction of fibres, Figure 3.18b. Continuing on, $p = 0.15$, there is a larger region of cells forming in the direction of fibres and an increase in the size of tumour boundary, Figure 3.16c. Finally, Figures 3.16d displays results in which the initial fibre distribution is increased to $p = 0.2$. Here, the main body of the tumour has

changed in shape, elongated in the direction of fibres and showing several regions of high cell distribution. The boundary of the tumour has progressed and has become irregular in shape with protrusions in the macroscopic direction of fibres, Figure 3.18d. In the presence of a homogeneous non-fibre ECM phase, the differences in the invading boundaries are clearly visible, ranging from a symmetric leading edge in low initial fibre distribution to a fingering boundary in high initial fibre distribution.

To compliment these simulations we investigate the same cases of initial fibre distributions as above coupled with a heterogeneous non-fibre ECM phase (4.20). Figures 3.19 and 3.20 display computations at stage $40\Delta t$ of both the cancer cell population and macroscopic fibre distribution, respectively, and Figure 3.21 gives the macroscopic fibre directions associated with each case. Similar to in the presence of a homogeneous non-fibre ECM phase, as the initial fibre distribution is increased, we see the formation of a larger tumour. The most prominent difference is witnessed by the case $p = 0.2$, Figure 3.19d and 3.21d. Here the tumour boundary is covering a larger area and exhibiting a lobular pattern on the leading edge. This behaviour is due to both the heterogeneous pattern of non-fibre ECM and increased initial fibre distributions. Overall, these simulations conclude that a higher initial distribution of fibres coupled with either a homogeneous or heterogeneous non-fibre ECM phase results in a more aggressive tumour.

3.7 Discussion

We have presented a novel multi-scale moving boundary model which builds on previous framework first developed in Trucu et al. (2013). This multiscale model is developed to explore the adhesive dynamics of a cancer cell population within a two-phase heterogeneous ECM and its impact over the overall invasion pattern during cancer growth and spread within the surrounding human body tissue. The ECM

is considered here as being a mixture of two constitutive phases, namely a fibre and non-fibre phase. We pay a special attention to the fibre phase, whose multiscale dynamics is explored and modelled in an integrated two-scale spatio-temporal fashion, with the cell-scale micro-dynamics being connected to the tissue-scale tumour dynamic through an emerging double feedback loop. To that end, we developed a novel multiscale model that explores on one hand the way the fibre micro-dynamics translates into the macro-scale level fibre dynamics (by providing *on-the-fly* at tissue-scale a spatially-distributed vector field of oriented macroscopic fibre that have direct influence within the tumour progression) and, on the other hand, the way in which the tissue-scale cancer cell population dynamics causes not only fibres degradation at macro-scale but also fibres rearrangement at microscale. Finally, the new multiscale model is embedded within the multiscale moving boundary framework exploring the leading edge proteolytic activity of matrix degrading enzymes introduced in Trucu et al. (2013). Thus, we ultimately obtain a novel multi-scale modelling framework that combines two multiscale sub-systems that contribute to and share the same macro-dynamics, but have separate micro-scale processes that are simultaneously connected to the macro-dynamics through two independent feedback loops, with one of them addressing the cell-scale activity involved in the rearrangement of micro-fibres within the bulk of the tumour, and the second one exploring the proteolytic activity within a cell-scale neighbourhood of the tumour boundary.

At the tissue scale, in order to explore the influence of the ECM fibre phase within the tissue-scale dynamics, besides the usual adhesion terms considered in Domschke et al. (2014); Gerisch and Chaplain (2008) concerning cell-cell and cell-ECM-non-fibre adhesion, we derived and introduce a new non-local term in the macroscopic equation (3.27a) for tumour cell population that accounts for the cell-fibres adhesion. This new term, explores the critical influence that the macroscopic

fibre vector field has over the direction of cellular adhesion in the macro-dynamics. Moreover, as this vector field of oriented ECM fibres is induced from the micro-scale distribution of micro-fibres, a novel *bottom-up* feedback link between cell- and tissue-scale dynamics has this way been identified and explored mathematically.

Further, while the cancer cells degrade both the ECM non-fibre and the ECM fibre components at macro-scale, it was important to observe that the cancer cell flux $\mathcal{F}$ given in (3.22) causes the rearrangement of the micro-fibres at micro-scale. To understand this, at any given macro-scale position $x \in \Omega(t)$ we explored this macro-micro interacting link on appropriately small cubic micro-domains centred at x, namely $\delta Y(x)$, where the distribution of the micro-fibres $f(z,t)$ (with $z \in \delta Y(x)$) induces naturally the fibre magnitude $F(x,t)$ and orientation $\theta_{_f}(x,t)$, and whose rigorous derivation and well-posedness was ensured in Section 3.3.1. Futhermore, while getting balanced by the initial macro-scale orientation of the existing fibres (induced from the distribution of the microfibres on $\delta Y(x)$, the macro-scale spatial flux $\mathcal{F}$ acts uniformly on the existing distribution of micro-fibres on any micro-domain $\delta Y(x)$, causing the micro-fibres initially distributed on $\delta Y(x)$ to be redistributed and rearranged in the resulting fibres relocation direction given in (3.26). This fibres relocation direction was obtained as the contribution of the flux $\mathcal{F}(x,t)$ and the fibre vector field $\theta_f(x,t)$ that are weighted in accordance to the amount of cancer cells transported at (x,t) and the magnitude of fibre that they meet at (x,t), respectively. Finally, this relocation is accomplished to the extent in which the local microscopic conditions permit, these being explored here through an appropriately defined movement probability. This way, a top down link was established between the macro-dynamics and the dynamics fibres rearrangement at micro-scale.

To address this new multiscale modelling platform computationally, we extended significantly the computational framework introduced in Trucu et al. (2013) by

bringing in the implementation of the interlinked two-scale fibre dynamics. To that end, besides the computational approach based on barycentric interpolation that the micro-scale fibres relocation process has required, the macro-solver needed several extension to accommodate the new modelling. To that end, alongside the formulation of a new approach to computing on the moving tumour domain, we proposed a new off-grid barycentric interpolation approach to calculate the new adhesion term, and finally we developed a novel non-local predictor-corrector numerical scheme to address the challenging macro-scale computational conditions created through the presence of a multiphase ECM that crucially includes the multiscale dynamics of the oriented fibres.

Using this multiscale computational approach for the proposed model, we were able to simulate the multiscale nature of cancer invasion by exploring the link between the macroscopic spatial distribution and orientation of cancer cells and the matrix, and the microscopic rearrangement of fibres and micro-dynamics of MDEs that occur on the proliferating edge of the tumour. Overall, we considered the invasion of a cancer cell population within both homogenous and heterogeneous non-fibrous ECM phase, investigating the macro-scale dynamics of the cancer population and macroscopic densities of the ECM components, whilst considering their influence on both the micro-scale MDEs molecular dynamics occurring at the cell-scale along the invasive edge and also the microscopic fibre movement occurring within the boundary of the tumour. Finally, it is worth remarking at this stage that even in the homogeneous non-fibre ECM, the ECM as a whole will not be homogeneous, due to the presence of the oriented fibres that already lead to a constitutive heterogeneous ECM.

The simulations presented in this Chapter have some similarities with previous work. We note a general lobular, fingering pattern for the progression of tumour

boundary, aspect that was observed also in Peng et al. (2017); Trucu et al. (2013) in the case of heterogeneous ECM. There is a noticeable increase in this behaviour when the coefficient of cell-fibre adhesion is increased, suggesting the microscopic fibres play a key role in the invasion process, aiding in the local progression of the tumour. It is shown throughout all simulations that, while being degraded by the cancer cells, the fibres are being pushed outwards from the centre of the domain towards the boundary (Pinner and Sahai, 2008). This behaviour is known for amoeboid cell types, and particularly occurs in a loose/soft matrix (Krakhmal et al., 2015), which is reminiscent of our model as the cancer cells flux rearranges the fibres continuously at micro-scale. We can conclude from our simulations that a heterogeneous ECM non-fibrous phase permits for an increase in tumour progression compared to an initial homogeneous distribution. It is clear that the ECM fibres play an important role during invasion, with an increase in cell-fibre adhesion displaying a larger overall region of invasion. This is in line with recent biological experiments that suggest the organisation of fibronectin fibrils promotes directional cancer migration (Erdogan et al., 2017).

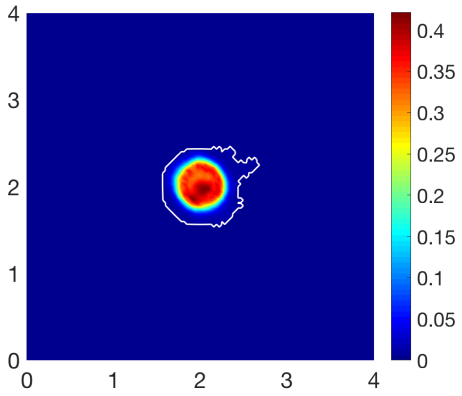

(a) Cancer cell population

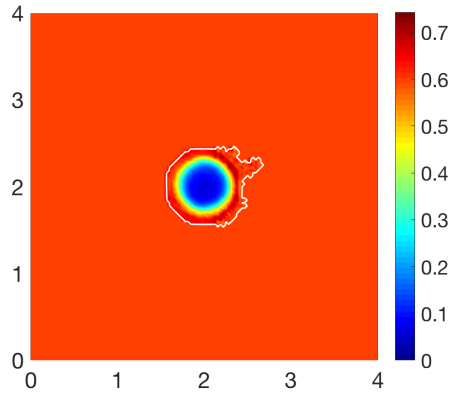

(b) Matrix distribution

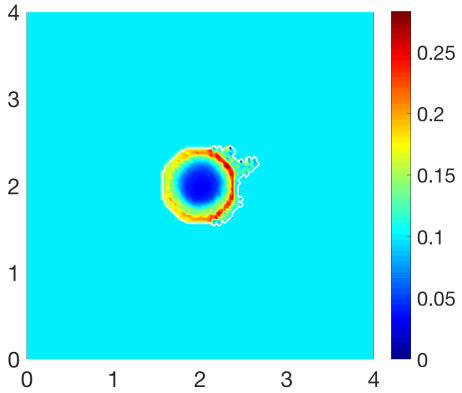

(c) Macroscopic fibre density

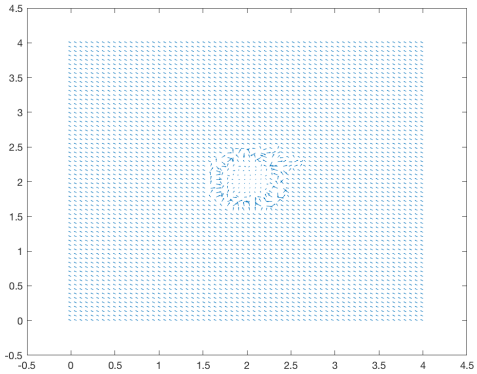

(d) Fibre orientation - coarsened 2 fold

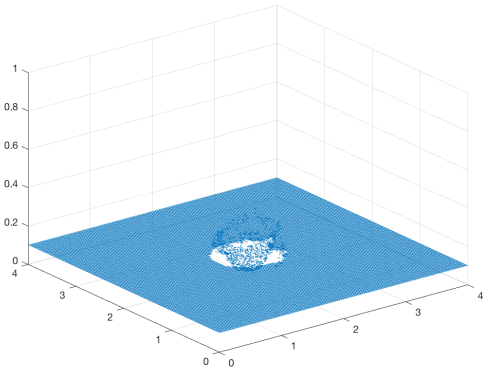

(e) 3D fibre vector field

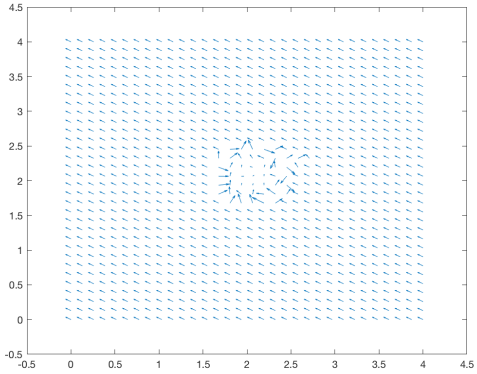

(f) Fibre orientation - coarsened 4 fold

Figure 3.9: Simulations at stage $20\Delta t$ with a both a homogeneous non-fibres ECM phase and a homogenous distribution of the fibre component with parameter set Σ_1.

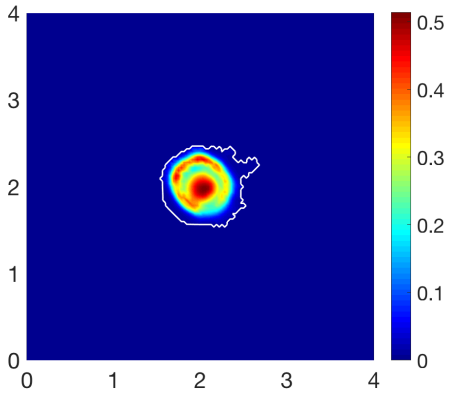

(a) Cancer cell population

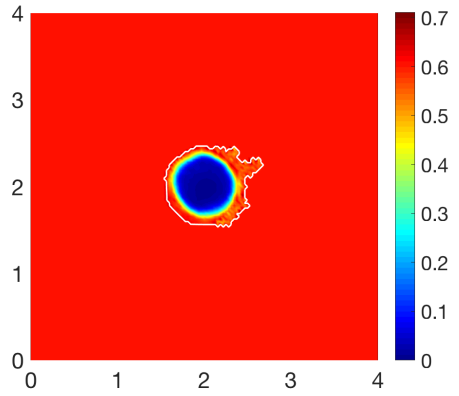

(b) Matrix distribution

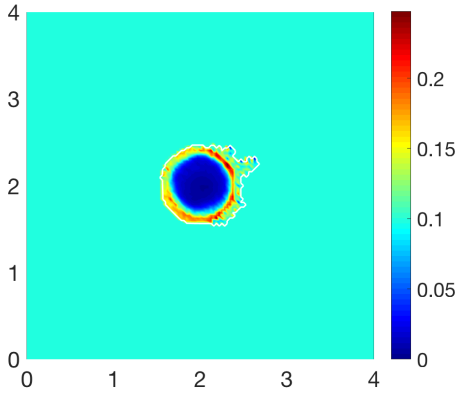

(c) Macroscopic fibre density

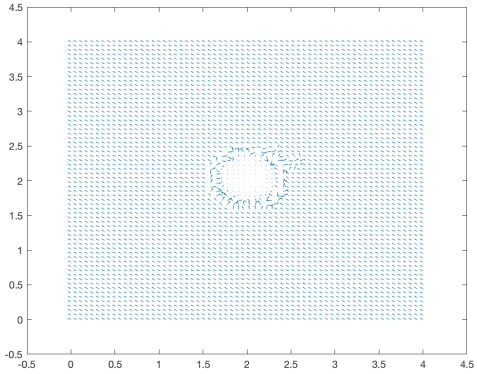

(d) Fibre orientation - coarsened 2 fold

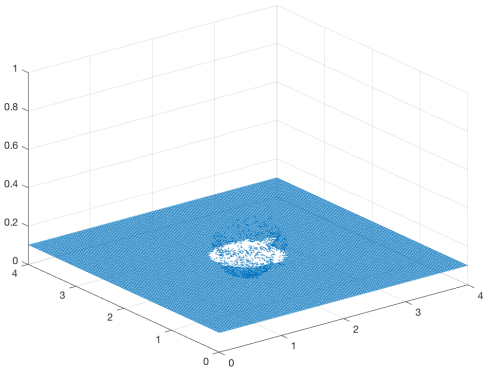

(e) 3D fibre vector field

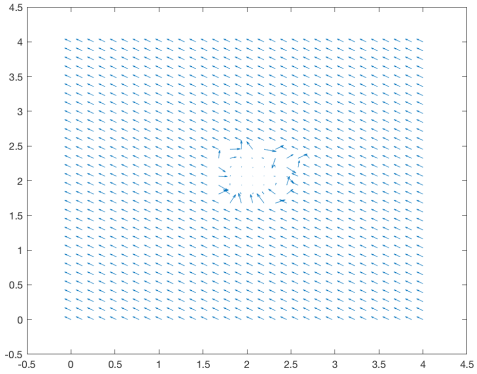

(f) Fibre orientation - coarsened 4 fold

Figure 3.10: Simulations at stage $40\Delta t$ with a both a homogeneous non-fibres ECM phase and a homogenous distribution of the fibre component with parameter set Σ_1.

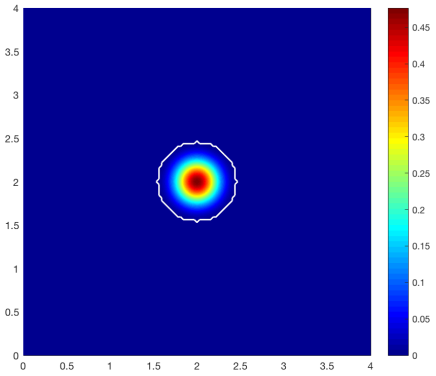

(a) initial cancer distribution

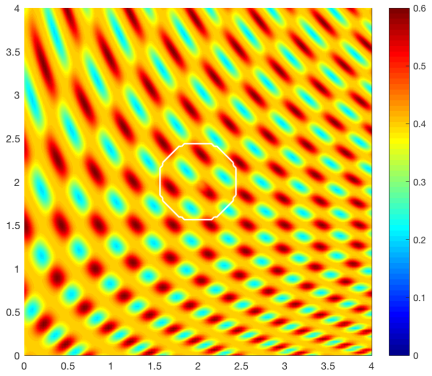

(b) Initial ECM density

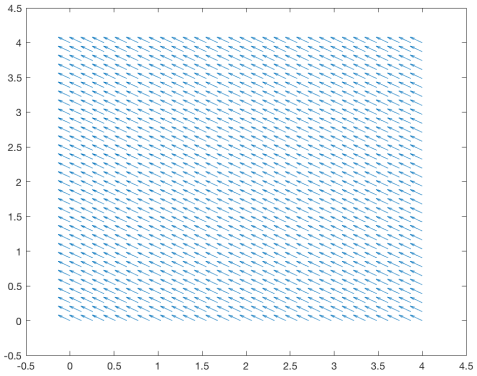

(c) Initial vector field of fibre directions

Figure 3.11: Initial conditions showing the distribution of cancer cells (a), the heterogeneous density of ECM (b) with the invasive boundary of the tumour represented by the white contour, and the initial macroscopic fibre orientations per each micro-domain represented by a vector field (c). These vectors have been magnified from the usual size of the domain for better representation.

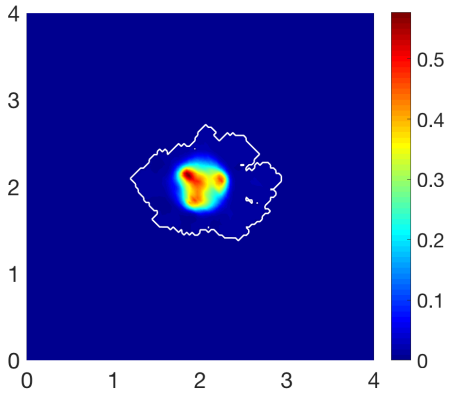

(a) Cancer cell population

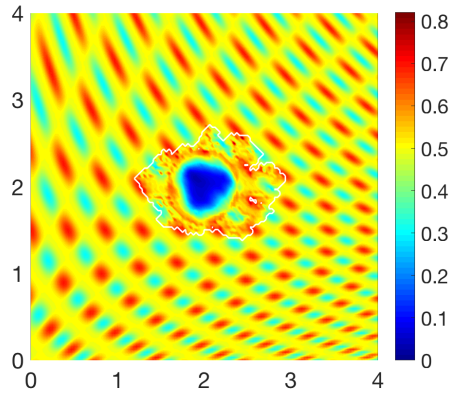

(b) Matrix distribution

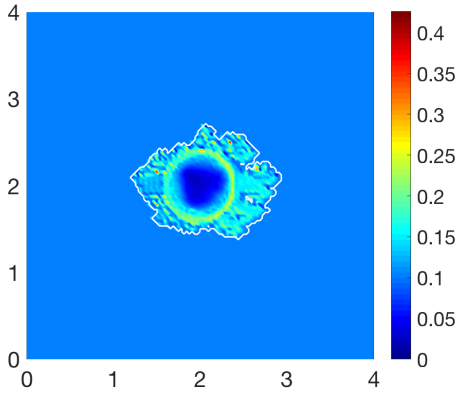

(c) Fibre magnitude density

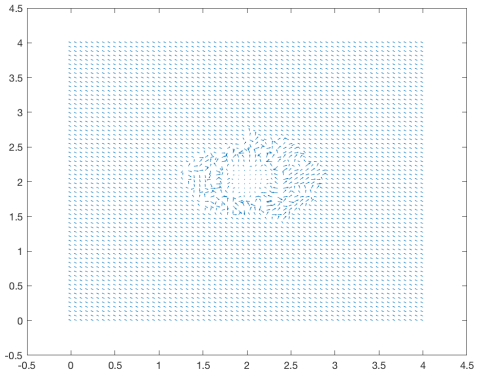

(d) Fibre vector field - coarsened 2 fold

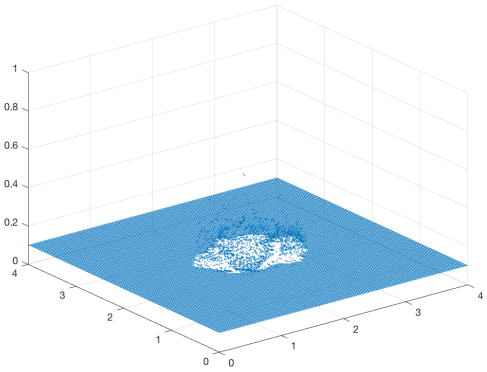

(e) 3D fibre vector field

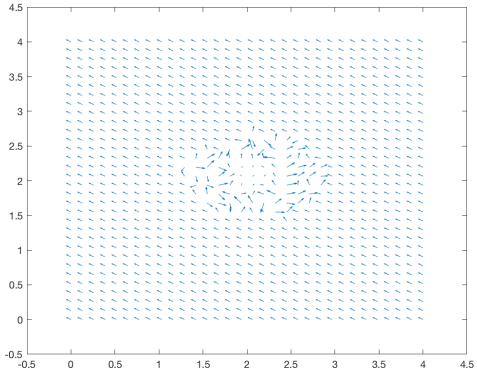

(f) Fibre vector field - coarsened 4 fold

Figure 3.12: Simulations at stage $20\Delta t$ with a heterogeneous non-fibres ECM phase and a homogenous distribution of the fibre component with parameter set Σ_1.

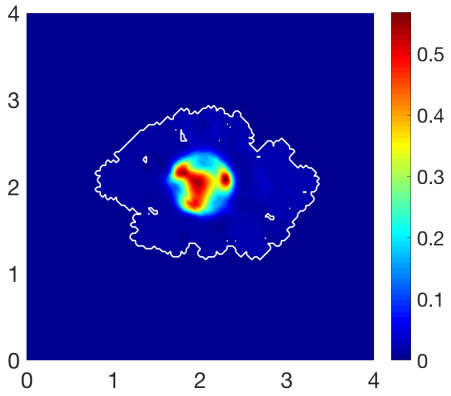

(a) Cancer cell population

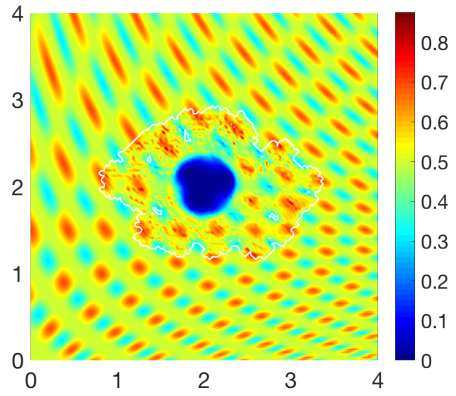

(b) Matrix distribution

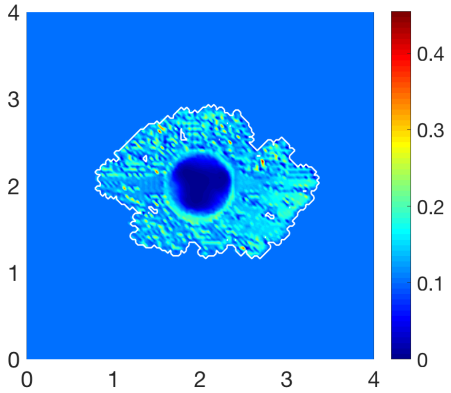

(c) Macroscopic Fibre density

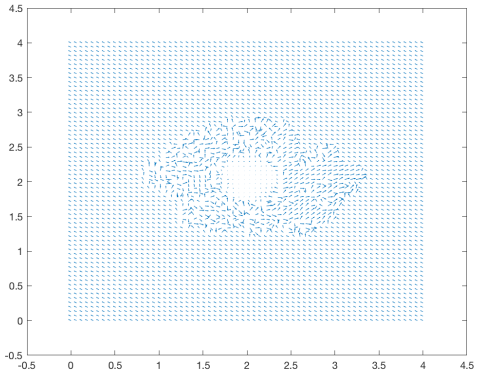

(d) Fibre orientation - coarsened 2 fold

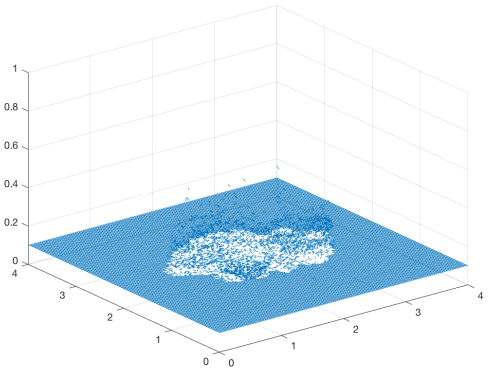

(e) 3D fibre vector field

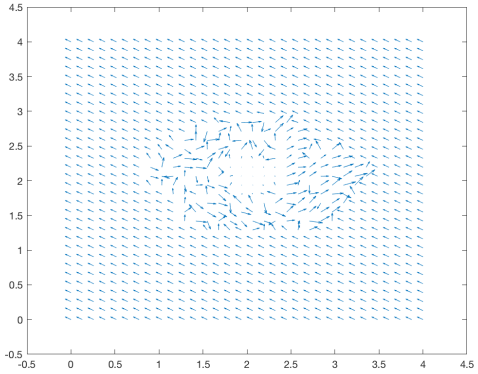

(f) Fibre orientation - coarsened 4 fold

Figure 3.13: Simulations at stage $40\Delta t$ with a heterogeneous non-fibres ECM phase and a homogenous distribution of the fibre component with parameter set Σ_1.

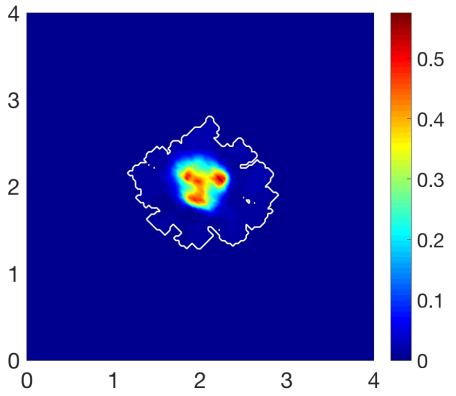

(a) Cancer cell population

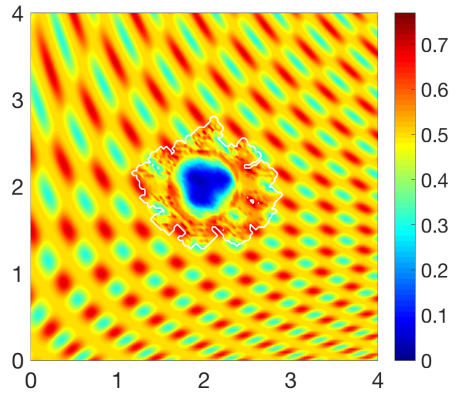

(b) Matrix distribution

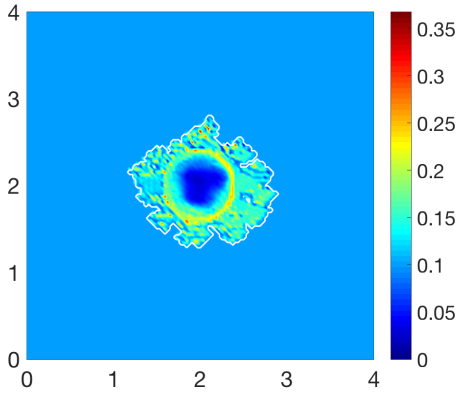

(c) Macroscopic fibre density

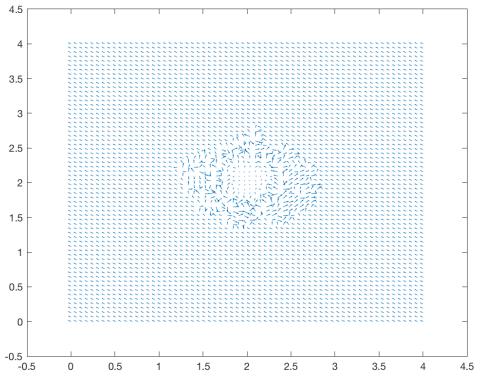

(d) Fibre orientation - coarsened 2 fold

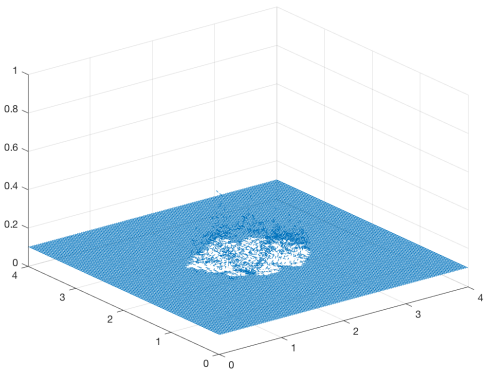

(e) 3D fibre vector field

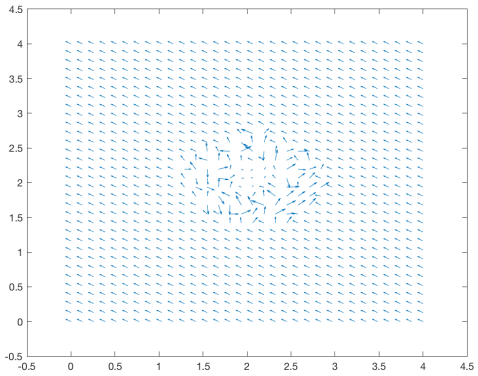

(f) Fibre orientation - coarsened 4 fold

Figure 3.14: Simulations at stage $20\Delta t$ with a heterogeneous non-fibres ECM phase and a homogenous distribution of the fibre component with parameter set Σ_1 and an increased cell-fibre adhesion coefficient.

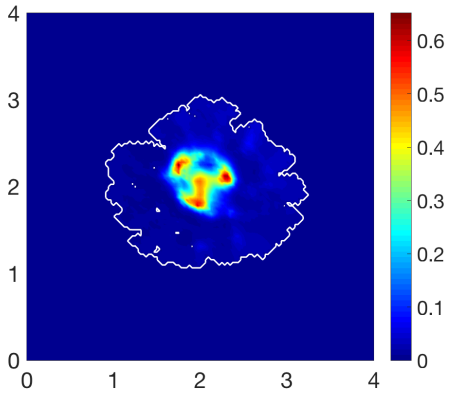

(a) Cancer cell population

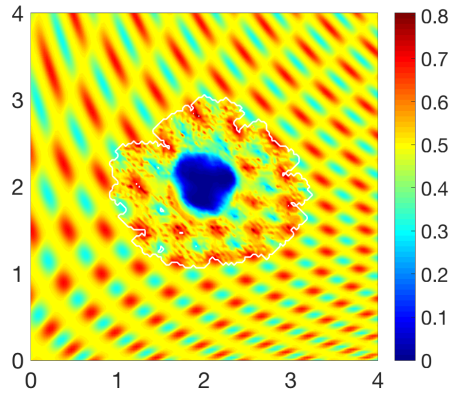

(b) Matrix distribution

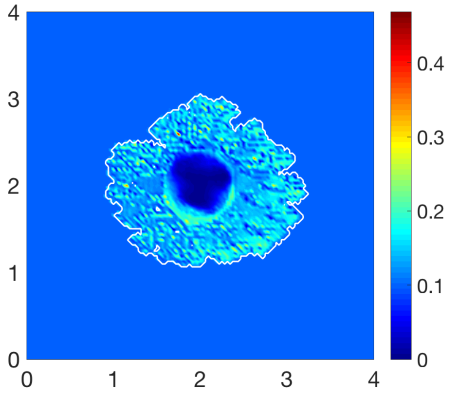

(c) Macroscopic fibre density

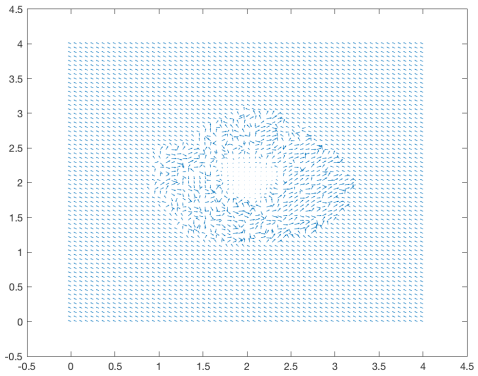

(d) Fibre orientation - coarsened 2 fold

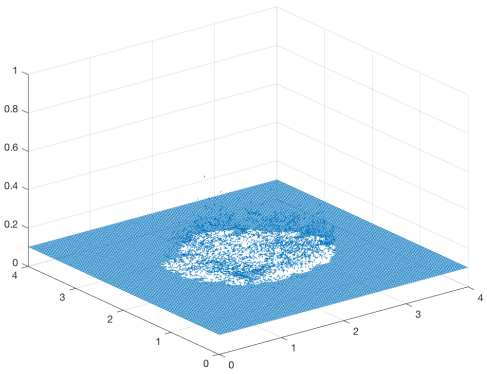

(e) 3D fibre vector field

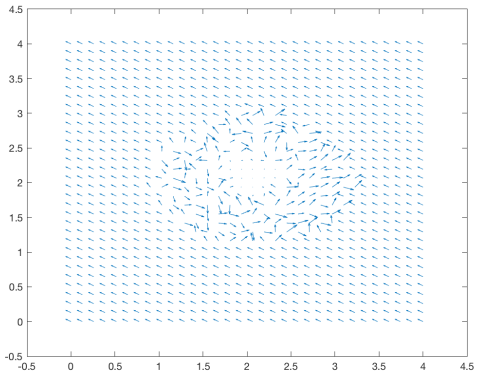

(f) Fibre orientation - coarsened 4 fold

Figure 3.15: Simulations at stage $40\Delta t$ with a heterogeneous non-fibres ECM phase and a homogenous distribution of the fibre component with parameter set Σ_1 and an increased cell-fibre adhesion coefficient.

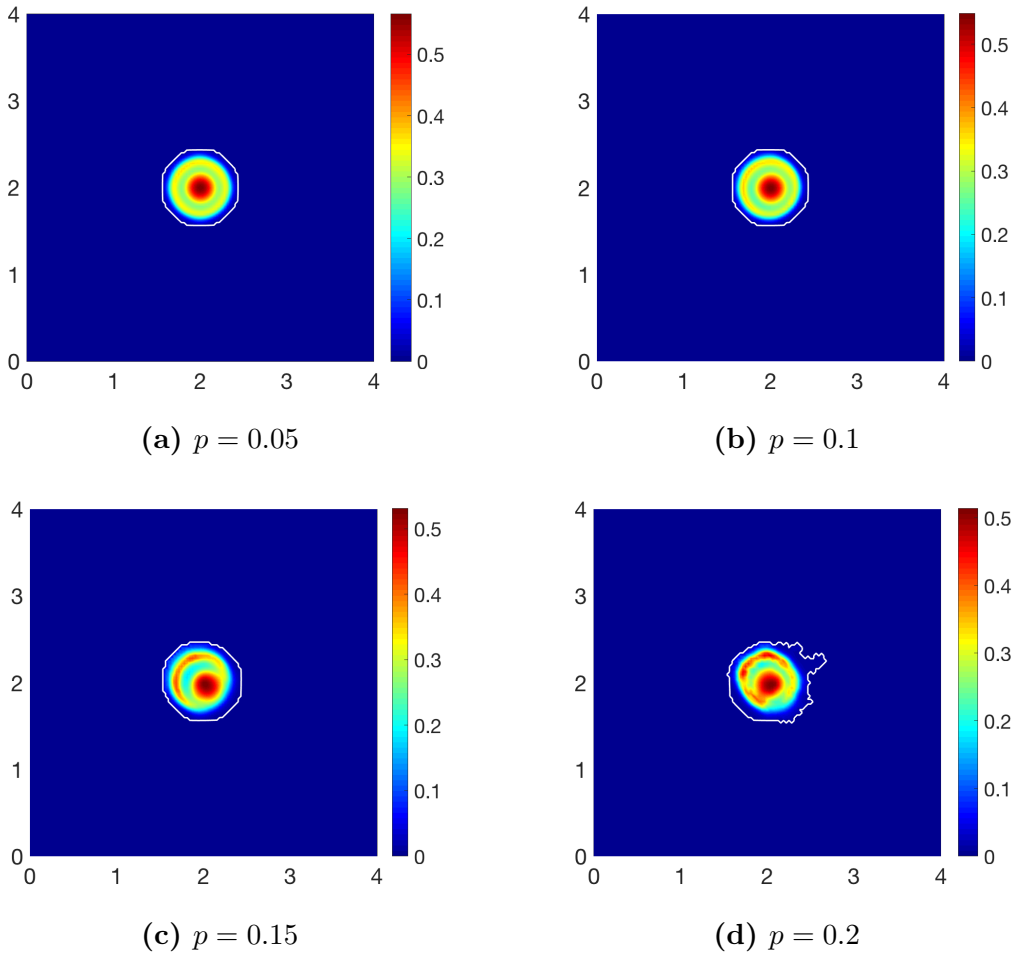

(a) $p = 0.05$ **(b)** $p = 0.1$

(c) $p = 0.15$ **(d)** $p = 0.2$

Figure 3.16: Simulation results of cancer cell distributions at stage $40\Delta t$ using different percentages of the mean density value of the homogeneous non-fibres ECM phase, (a) $p = 0.05$, (b) $p = 0.1$, (c) $p = 0.15$ and (d) $p = 0.2$.

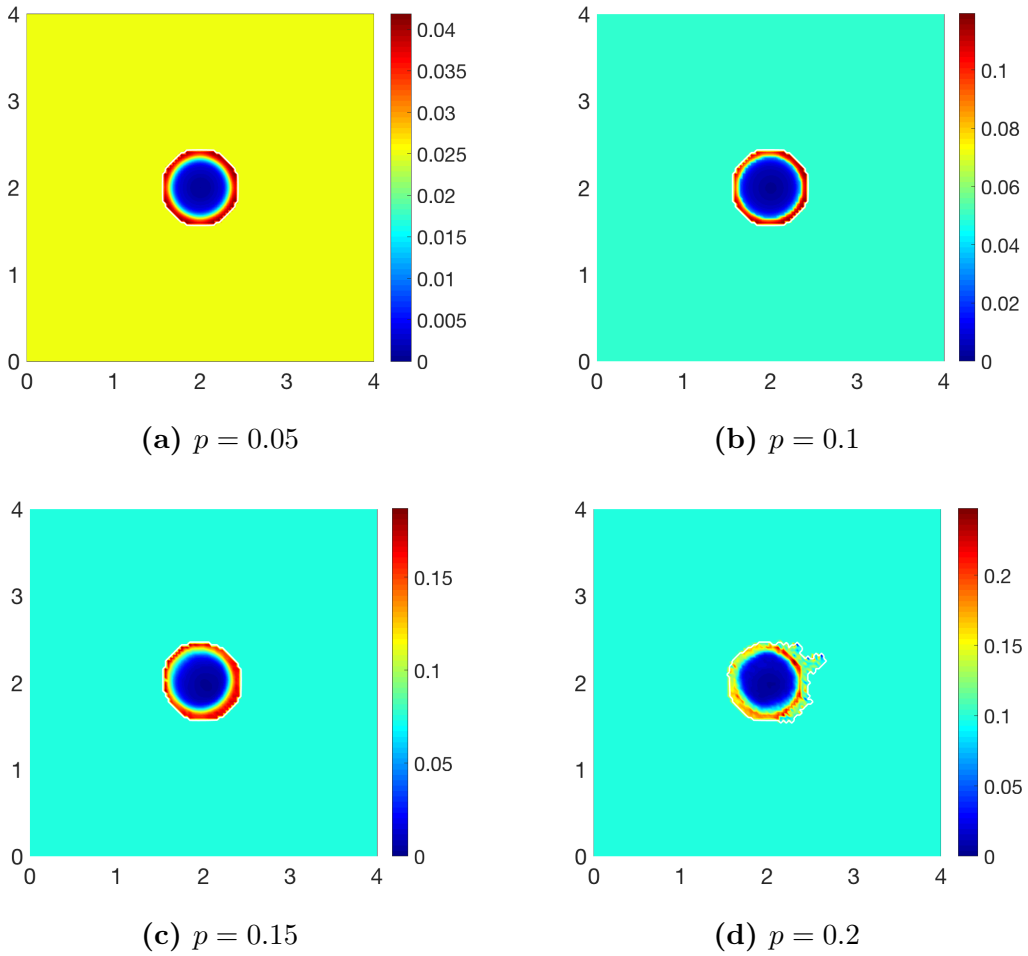

(a) $p = 0.05$ **(b)** $p = 0.1$

(c) $p = 0.15$ **(d)** $p = 0.2$

Figure 3.17: Simulation results of fibre density at stage $40\Delta t$ using different percentages of the mean density value of the homogeneous non-fibres ECM phase, (a) $p = 0.05$, (b) $p = 0.1$, (c) $p = 0.15$ and (d) $p = 0.2$.

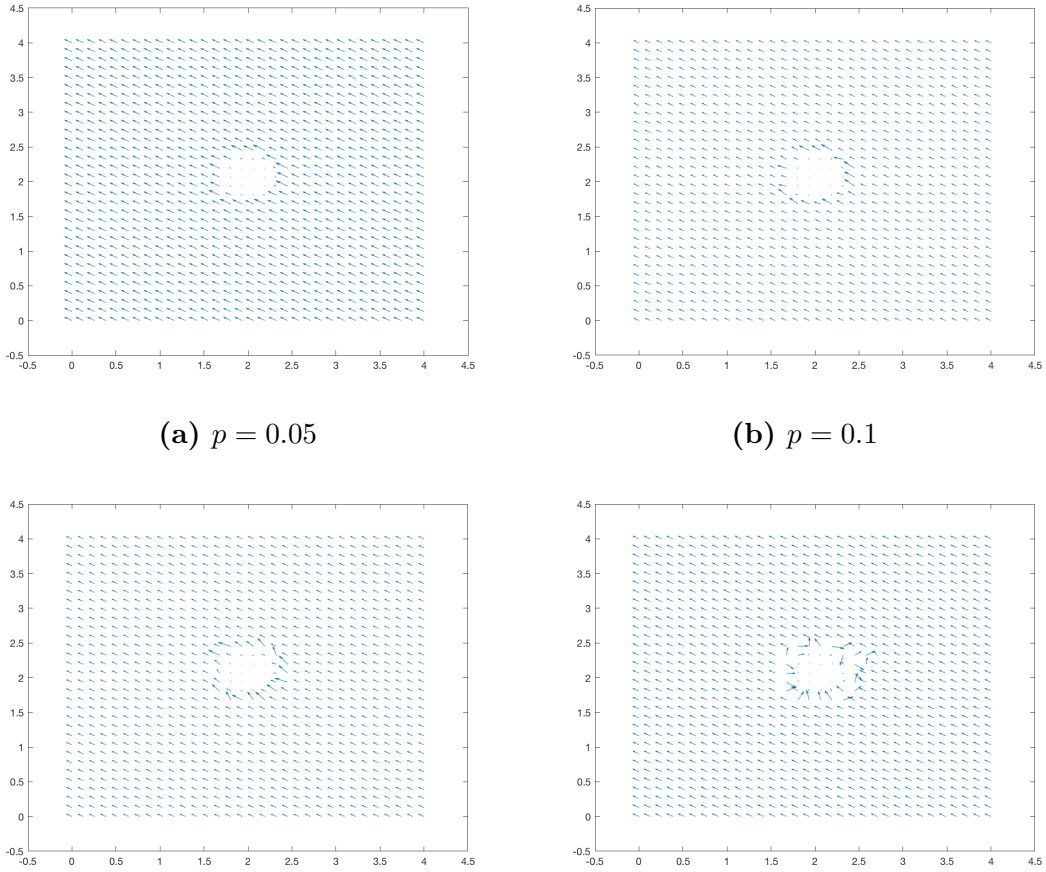

(a) $p = 0.05$ **(b)** $p = 0.1$

(c) $p = 0.15$ **(d)** $p = 0.2$

Figure 3.18: Vector plots of the macroscopic orientation of fibres - coarsened 4 fold at stage $40\Delta t$, using different percentages of the mean density value of the homogeneous non-fibres ECM phase, (a) $p = 0.05$, (b) $p = 0.1$, (c) $p = 0.15$ and (d) $p = 0.2$.

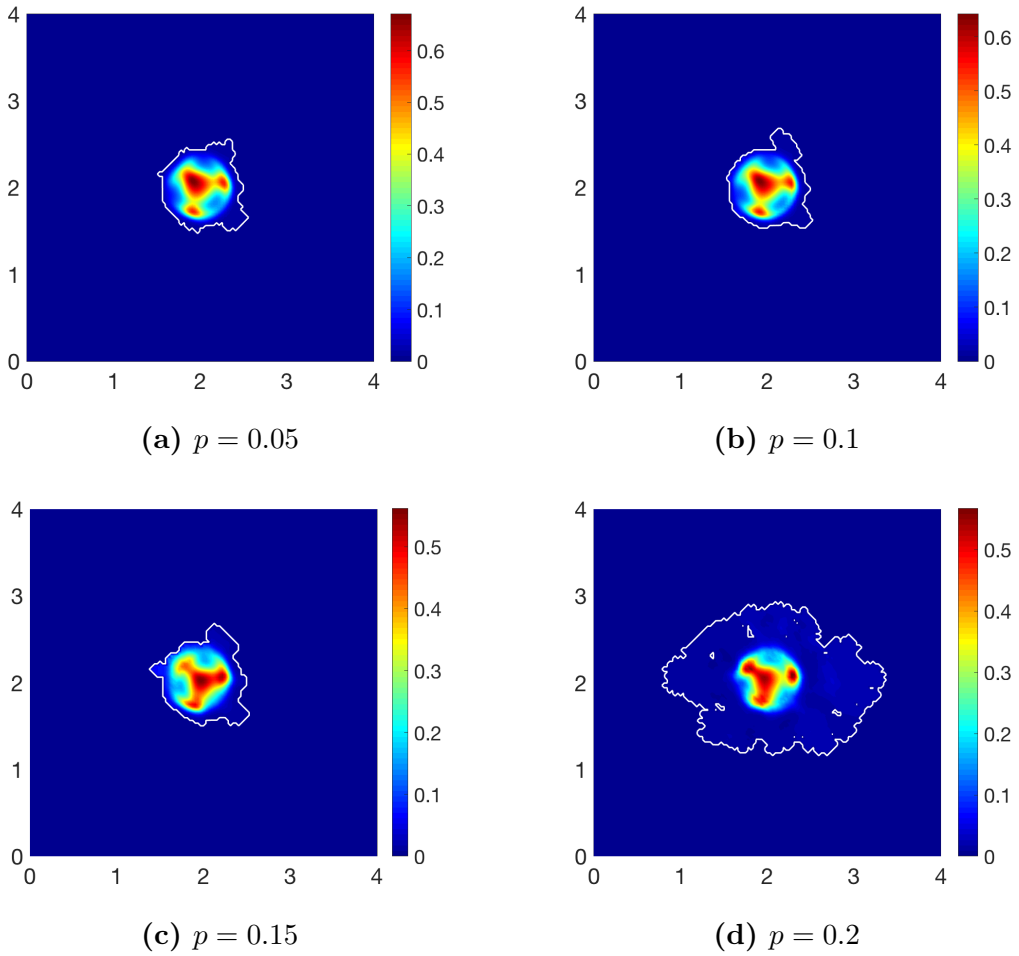

(a) $p = 0.05$ **(b)** $p = 0.1$

(c) $p = 0.15$ **(d)** $p = 0.2$

Figure 3.19: Simulation results of cancer cell distributions at stage $40\Delta t$ using different percentages of the mean density value of the heterogeneous non-fibres ECM phase, (a) $p = 0.05$, (b) $p = 0.1$, (c) $p = 0.15$ and (d) $p = 0.2$.

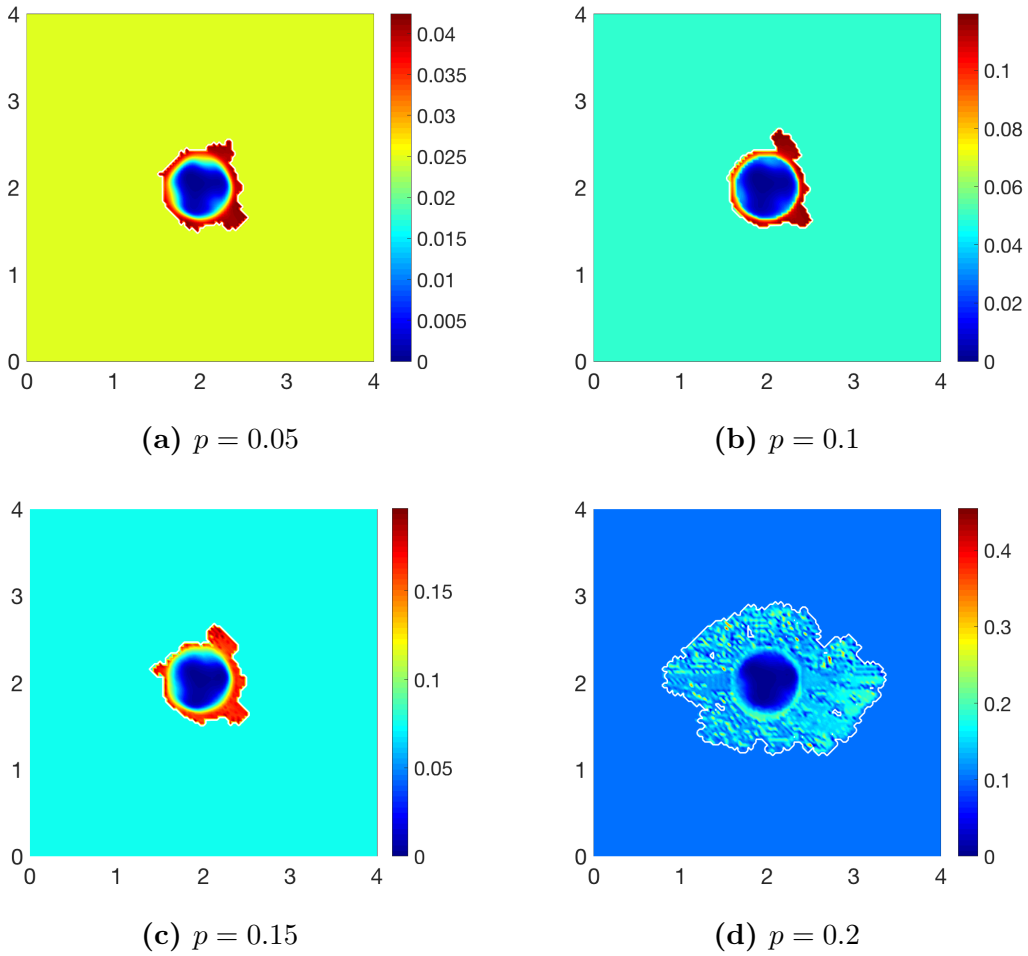

(a) $p = 0.05$ **(b)** $p = 0.1$

(c) $p = 0.15$ **(d)** $p = 0.2$

Figure 3.20: Simulation results of fibre density at stage $40\Delta t$ using different percentages of the mean density value of the heterogeneous non-fibres ECM phase, (a) $p = 0.05$, (b) $p = 0.1$, (c) $p = 0.15$ and (d) $p = 0.2$.

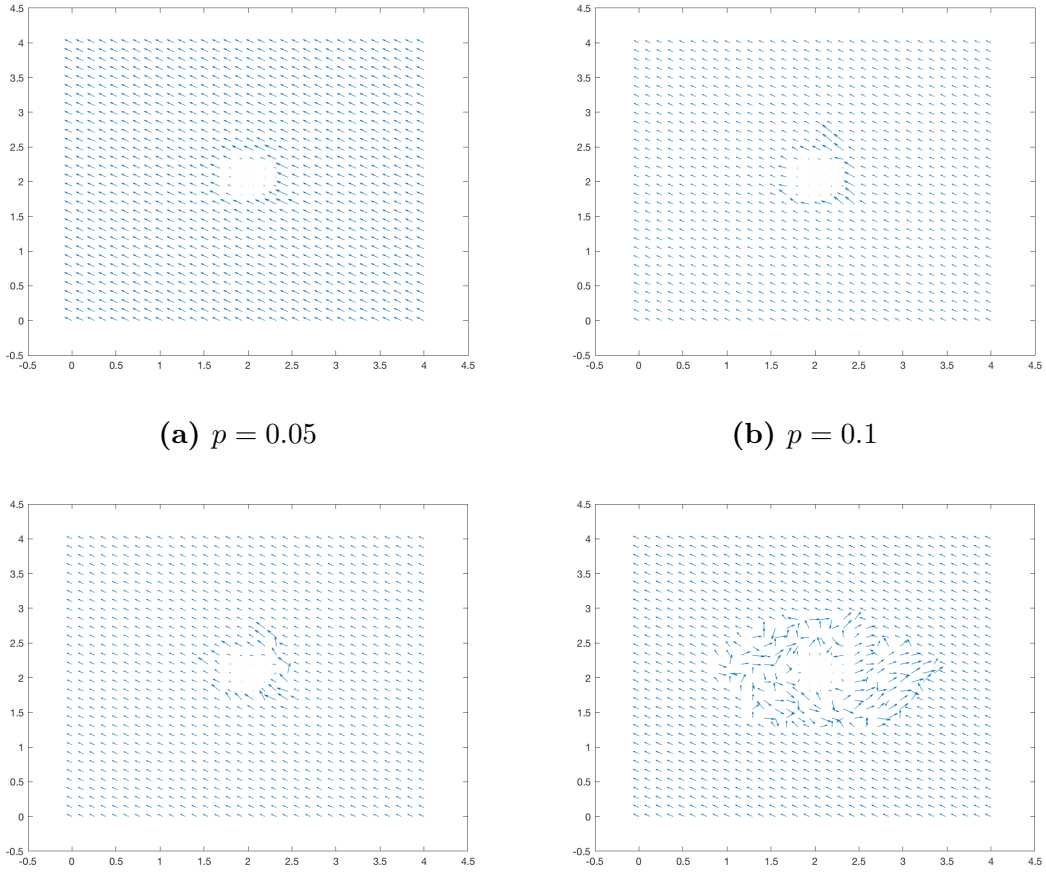

(a) $p = 0.05$ **(b)** $p = 0.1$

(c) $p = 0.15$ **(d)** $p = 0.2$

Figure 3.21: Vector plots of the macroscopic orientation of fibres - coarsened 4 fold at stage $40\Delta t$, using different percentages of the mean density value of the heterogeneous non-fibres ECM phase, (a) $p = 0.05$, (b) $p = 0.1$, (c) $p = 0.15$ and (d) $p = 0.2$.

Chapter 4

Multiscale dynamics of a heterotypic cancer cell population within a fibrous extracellular matrix

Aims and novelty: In this Chapter we extend the multiscale framework developed to include the underlying fibre structure introduced in Chapter 3 to investigate tumour invasion of a heterotypic cancer cell population consisting of two cancer cell sub-populations.

4.1 Introduction

During the invasion process a tumour can become increasingly malignant, whereby the primary cancer cell population acquires the ability to mutate giving rise to a secondary sub-population of cancer cells that exhibits more aggressive invasion

qualities, including: faster random motility, increased proliferation, and changes in cell-cell and cell-matrix adhesion properties enabling an acceleration of local cancer invasion. Biological experiments have revealed that increased stromal collagen density promotes tumour formation and results in tumours exhibiting a more invasive phenotype (Provenzano et al., 2008). In addition, it has been demonstrated that local invasion is further accelerated by collagen reorganisation (Provenzano et al., 2006), and this behaviour is significantly increased in regions of high collagen density. The realignment of fibronectin fibrils has also been associated with increased local tumour invasion (Erdogan et al., 2017) enabling a smooth invasion of the cancer cells. On the other hand, collagen type I has been shown to down-regulate E-cadherin gene expression in pancreatic cancer cell lines which leads to a reduction in cell-cell adhesion and increased proliferation and cell migration (Menke et al., 2001). Hence, to combine and demonstrate these behaviours in our model we assume that a secondary cell sub-population exhibiting a decrease in cell-cell adhesion and an increase in migratory activity will arise in places of high matrix density.

Thus, the presence of this secondary cancer cell sub-population has implications for cancer dynamics at both macro- and micro- scales, and to address all these, in this chapter we will develop and adapt the modelling approach introduced initially in Chapter 3, and fully defined in Shuttleworth and Trucu (2019c), to the new context created by the two cancer cell sub-populations. The content of this chapter has been fully explored in the article Shuttleworth and Trucu (2019b).

4.2 The mathematical model

Using here the same terminology as in Chapter 2 for a heterotypic cell populations consisting of two cell sub-populations, we denote the support of the invading tumour region by $\Omega(t)$, and assume this evolves in the maximal reference tissue cube $Y \in \mathbb{R}^N$

with $N = 2, 3$, centred at the origin of the space. At any spatio-temporal node $(x, t) \in \Omega(t) \times [0, T]$ we consider the tumour to be a mixture of cancer cells $c_n(x, t)$, $n = 1, 2$, with their combined vector denoted $\mathbf{c}(x, t) = [c_1(x, t), c_2(x, t)]$, integrated within a multiphase distribution of ECM, $v(x, t)$, whose components will be defined in the next section.

4.2.1 Multiscale fibre structure and their dynamic contribution in tumour progression

Adopting the approach and terminology introduced in Shuttleworth and Trucu (2019c), to capture the dynamics of the two sub-populations of cancer cells in the presence of a two component heterogeneous extra-cellular matrix (consisting of a fibre and non-fibre phase), we proceed as follows. As derived in Chapter 3 and detailed in Shuttleworth and Trucu (2019c), at any macroscale point $x \in \Omega(t)$, the ECM-fibre phase is represented through a macro-scale vector field $\theta_{_f}(x, t)$. This vector field captures and represents at tissue-scale not only the amount of fibres distributed at (x, t) but also their naturally arising macroscopic fibres orientation induced by the revolving barycentral orientation $\theta_{_{f,\delta Y(x)}}(x, t)$ generated by the microscopic mass distribution of microfibres $f(\cdot, t)$ within the micro-domain $\delta Y(x) := \delta Y + x$. An example of a mass distribution of ECM micro-fibres $f(z, t)$, $z \in \delta Y(x)$, is illustrated in Fig. 4.1 below and is defined in Appendix D.1.

In brief, while referring the reader to its full derivation presented in Chapter 3 and Shuttleworth and Trucu (2019c), the naturally generated revolving barycentral orientation $\theta_{_{f,\delta Y(x)}}(x, t)$ associated with $\delta Y(x)$ is given by the *Bochner-mean-value* of the position vectors function $\delta Y(x) \ni z \mapsto z - x \in \mathbb{R}^N$ with respect to the density measure $f(x, t)\lambda(\cdot)$, where $\lambda(\cdot)$ is the usual Lebesgue measure (see Yosida (1980)),

and so this is expressed mathematically as:

$$\theta_{f,\delta Y(x)}(x,t) = \frac{\int\limits_{\delta Y(x)} f(z,t)(z-x)dz}{\int\limits_{\delta Y(x)} f(z,t)dz}. \tag{4.1}$$

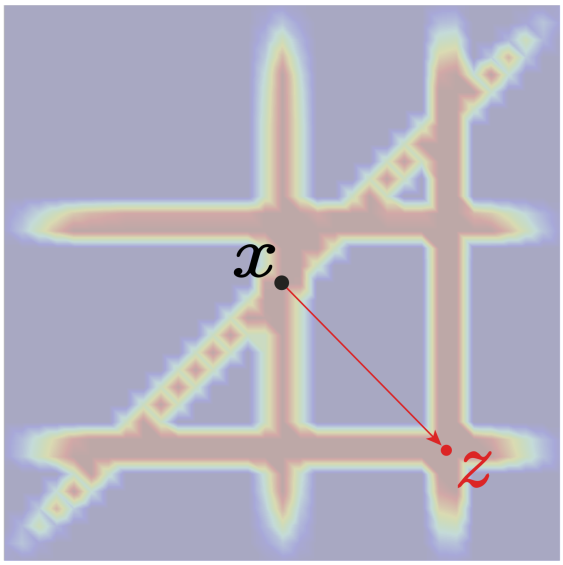

Figure 4.1: A 2D contour plot of the micro-fibres distribution on the micro-domain $\delta Y(x)$, centred at x, with the barycentral position vector $\overrightarrow{x\,z} := z - x$ pointing towards an arbitrary micro-location $z \in \delta Y(x)$ illustrated by the red arrow.

Following on, at any spatio-temporal node (x,t), the macroscopic fibre oriented is defined as

$$\theta_{f}(x,t) = \frac{1}{\lambda(\delta Y(x))} \int_{\delta Y(x)} f(z,t)\ dz \cdot \frac{\theta_{f,\delta Y(x)}(x,t)}{||\theta_{f,\delta Y(x)}(x,t)||_2} \tag{4.2}$$

where $\lambda(\cdot)$ is the usual Lebesgue measure. The macroscopic mean-value fibre representation at any (x,t) is then given by the Euclidean magnitude of $\theta_{f}(x,t)$, namely,

$$F(x,t) := ||\theta_{f}(x,t)||_2. \tag{4.3}$$

Finally, concerning the *non-fibre soluble phase* of the ECM, we consider that this

includes all the other non-fibre components of the ECM, i.e., elastin, laminins, fibroblasts, etc. Thus, denoting the spatial distribution of the non-fibre ECM phase distribution $l(x,t)$, the total ECM distributed at any spatio-temporal node (x,t) is therefore given by $v(x,t) = l(x,t) + F(x,t)$.

4.2.2 Macro-scale dynamics

To explore the dynamics of a heterotypic cancer cell population with two sub-populations consisting of a primary and a mutated cell population, within the modelling framework, let's revisit the macro-dynamics presented in Chapter 2 and adopting the same approach as in Andasari et al. (2011) and Shuttleworth and Trucu (2018), focusing first on the heterotypic cancer cell population, the dynamics of the two cell sub-populations are much similar. Under the presence of a logistic proliferation law, per unit time, the spatial movement of the primary tumour cells $c_1(x,t)$ is described by a combination of local Brownian movement (approximated here by diffusion) and cell-adhesion. They experience a loss of cells through mutation towards a second, more aggressive population $c_2(x,t)$. Similar to population $c_1(x,t)$, once mutations have begun, per unit time, sub-population $c_2(x,t)$ exercises spatial movement through a local Brownian movement and a perturbed cell-adhesion under the presence of logistic proliferation law. Hence, mathematically, the dynamics of these cell populations can be represented as

$$\frac{\partial c_1}{\partial t} = \nabla \cdot [D_1 \nabla c_1 - c_1 \mathcal{A}_1(x,t,\mathbf{u}(\cdot,t),\theta_f(\cdot,t))] + \mu_1 c_1 (1-\rho(\mathbf{u}))^+ - M_c(\mathbf{u},t)c_1, \tag{4.4}$$

$$\frac{\partial c_2}{\partial t} = \nabla \cdot [D_2 \nabla c_2 - c_2 \mathcal{A}_2(x,t,\mathbf{u}(\cdot,t),\theta_f(\cdot,t))] + \mu_2 c_2 (1-\rho(\mathbf{u}))^+ + M_c(\mathbf{u},t)c_1, \tag{4.5}$$

where: D_n and μ_n, $n = 1, 2$ are the non-negative diffusion and proliferation coefficients of sub-populations $c_1(x,t)$ and $c_2(x,t)$ respectively, M_c describes the conversion from population $c_1(x,t)$ to $c_2(x,t)$ and finally, the non-local flux $\mathcal{A}_n(x,t,\mathbf{u}(\cdot,t),\theta_f(\cdot,t))$ accounts for the cellular adhesion processes which directly influence the spatial movement of the tumour cell population c_n, $n = 1, 2$. Embracing the modelling concept proposed in Chapter 3 and Shuttleworth and Trucu (2019c), the cells will not only interact with other cells, i.e., cell-cell adhesion, but also with the surrounding multiphase ECM, that in this instance constitutes of both cell-fibre and cell-ECM-non-fibre adhesion. Hence, within a sensing radius R at time t, the non-local adhesive flux can be expressed as:

$$\mathcal{A}_n(x,t,\mathbf{u}(\cdot,t),\theta_{_f}(\cdot,t)) = \frac{1}{R}\int_{\mathbf{B}(0,R)} \mathcal{K}(\|\,y\,\|_2)\big(n(y)(\mathbf{S}_{_{cc}}\mathbf{c}(x+y,t) + \mathbf{S}_{_{cl}}l(x+y,t)) + \hat{n}(y)\ \mathbf{S}_{_{cF}}F(x+y,t)\big)(1-\rho(\mathbf{u}))^+ \tag{4.6}$$

Whilst we consider the adhesive activities of the cells to become less influential as the distance r from x increases, and account for this through the radial kernel $\mathcal{K}(\cdot)$ defined in Appendix C.2. We explore the strength of the adhesion bonds created between the cancer cells distributed at x and the cells or the non-fibre phase of the ECM distributed at y in the direction of the unit vector pointing from x to $x+y$ given by

$$n(y) := \begin{cases} y/||y||_2 & \text{if} \quad y \in \mathbf{B}((0,0),R) \setminus \{(0,0)\}, \\ (0,0) & \text{otherwise} \end{cases} \tag{4.7}$$

and let us denote the cell-cell and cell-non-fibre-ECM adhesive strengths by $\mathbf{S}_{_{cc}}$ and $\mathbf{S}_{_{cl}}$, respectively. Furthermore, proceeding as in Chapter 3 and Shuttleworth and Trucu (2019c), we consider $\mathbf{S}_{_{cl}}$ to be constant whilst the coefficient representing cell-cell adhesion $\mathbf{S}_{_{cc}}$ is monotonically dependent on the level of extracellular Ca^{2+}

ions enabling strong adhesive bonds between cells (Gu et al., 2014; Hofer et al., 2000). Hence we assume that cell-cell adhesion is dependent on the density of the underlying non-fibre ECM phase, ranging from 0 to a Ca^{2+}-saturation level denoted S_{max}, and is taken as

$$\mathbf{S}_{cc}(x,t) := S_{max} e^{\left(1-\frac{1}{1-(1-l(x,t))^2}\right)}. \tag{4.8}$$

The final term in (4.6) describes the adhesive behaviour between the cancer cells and the fibres distributed on $\mathbf{B}(x,R)$. Within this term we account for the role of the fibres in two ways. On one hand, we account for the influence of the macroscopic fibres magnitude $F(x+y,t)$ has over the adhesion that the cells distributed at the spatial location x exercise with adhesion strength $\mathbf{S}_{cF}$ upon the fibres distributed at $x+y$. On the other hand, their full macroscopic orientation $\theta_f(x,t)$ (induced by their micro-scale mass distribution of microfibres), biases the cell-matrix adhesion in the direction of the resultant vector

$$\hat{n}(y) := \begin{cases} \frac{y+\theta_f(x+y)}{||y+\theta_f(x+y)||_2} & \text{if } (y+\theta_f(x+y)) \neq (0,0) \\ (0,0) \in \mathbb{R}^2 & \text{otherwise.} \end{cases} \tag{4.9}$$

The last important aspect that we consider here concerns mutations that enable cells from primary tumour cell sub-population c_1 to undergo genetic conversions and become secondary cancer cells c_2, process that is explored here through the mutation term $M_c(\mathbf{u},t)$, which captures the direct correlation between the presence of significant ECM levels, as detailed in the following. Indeed, as cellular adhesion is controlled by the binding of the calcium dependent adhesion molecules, *E-cadherins*, with the intra-cellular proteins, *catenins*, it is significant to note that collagens present in the ECM (in particular collagen type I) down-regulate the gene expression of E-cadherins, resulting this way in a loss of cell-cell adhesion (Menke et al., 2001). This loss of adhesion is accompanied by an increase in proliferation and migratory

activity, and so, to reflect this behaviour, the mutation term $M_c(\mathbf{u}, t)$ is dependent on the underlying ECM density levels and is taken to be

$$M_c(x,t) := \begin{cases} \frac{\exp\left(\frac{-1}{\kappa^2-(1-v(x,t))^2}\right)}{\exp\left(\frac{1}{\kappa^2}\right)} \cdot H(t-t_m) & \text{if } 1-\kappa < v(x,t) < 1, \\ 0 \qquad \text{otherwise,} \end{cases} \tag{4.10}$$

where $\kappa > 0$ is a certain level of ECM beyond which mutations can occur and $H(\cdot)$ is the usual Heaviside function, with t_m being the time at which mutations begin.

Finally, we describe the dynamics of the ECM, considering the individual constituents of the matrix, namely the fibre and non-fibre component. Both constituents of the matrix are simply degraded by the cancer cells, and so their macroscopic dynamics can be mathematically written as

$$\frac{dF}{dt} = -\gamma_1 c F \tag{4.11}$$

$$\frac{dl}{dt} = -\gamma_2 c l + \mu_3 (1-\rho(\mathbf{u}))^+ \tag{4.12}$$

where γ_1 and γ_2 are the degradation rates of the fibre and non-fibre components respectively, and μ_3 describes the rate of non-fibre ECM remodelling. Furthermore, the matrix remodelling, which is important both in the development and in progression of cancer, contributing to processes such as metastasis and tumour cell invasion (Cox and Erler, 2011), is controlled here by the volume filling factor $(1-\rho(\mathbf{u}))^+$.

4.2.3 Microscopic fibre rearrangement

As explored and modelled in Chapter 3 and Shuttleworth and Trucu (2019c), during their invasion, the cancer cells push the surrounding fibres in accordance with the emerging cell-flux direction and rearrange their micro-fibre mass distribution managing this way to reorient the macro-scale fibres. Indeed, in addition to their

macroscopic degradation described in (4.11), the fibres go through a microscopic rearrangement process induced by the macro-dynamics of the cancer cells. Specifically, at time t and at any spatial location $x \in Y$, the cancer cells will realign the micro-fibres through a microscopic rearrangement process in each micro-domain $\delta Y(x)$ that is induced by the combined macro-scale spatial flux of both cancer cell sub-populations

$$\mathcal{F}(x,t) := \mathcal{F}_1(x,t) + \mathcal{F}_2(x,t),$$

where

$$\mathcal{F}_1(x,t) := D_1 \nabla c_1(x,t) - c_1(x,t)\mathcal{A}_1(x,t,\mathbf{u}(\cdot,t),\theta_f(\cdot,t)),$$
$$\mathcal{F}_2(x,t) := D_2 \nabla c_2(x,t) - c_2(x,t)\mathcal{A}_2(x,t,\mathbf{u}(\cdot,t),\theta_f(\cdot,t)).$$

The combined flux acts upon the micro-scale distribution $f(z,t)$, $\forall z \in \delta Y(x)$ in accordance to the magnitude that the total mass of cancer cells has relative to the combined mass of cells and fibres at (x,t), which is given by the weight

$$\omega(x,t) = \frac{\bar{c}(x,t)}{\bar{c}(x,t) + F(x,t)}.$$

At the same time, the spatial flux of cancer cells $\mathcal{F}(x,t)$ is balanced in a weighted manner by the orientation $\theta_f(x,t)$ of the existing distribution of fibres at (x,t) that is appropriately magnified by a weight that accounts for the magnitude of fibres versus the combine mass of cells and fibres at (x,t) and is given by $(1-\omega(x,t))$. As a consequence, the micro-scale distribution of micro-fibres $f(z,t)$, $\forall z \in \delta Y(x)$ is therefore acted upon uniformly by the resultant force given by the following macro-scale vector-valued function

$$r(\delta Y(x),t) := \omega(x,t)\mathcal{F}(x,t) + (1-\omega(x,t))\theta_f(x,t). \tag{4.13}$$

As detailed in Chapter 3 and Shuttleworth and Trucu (2019c), under the uniform incidence of the resultant force $r(\delta Y(x), t)$ upon the mass of micro-fibres distributed at any $z \in \delta Y(x)$, an *on-the-fly spatial* microscopic rearrangement of this micro-fibres mass takes place. Specifically, under the influence of $r(\delta Y(x), t)$, an appropriate level of micro-fibres mass $f(z, t)$ will undergo a spatial transport towards a new position

$$z^* := z + \nu_{\delta Y(x)}(z, t),$$

where the relocation direction and magnitude is given by

$$\nu_{\delta Y(x)}(z, t) = (x_{\text{dir}}(z) + r(\delta Y(x), t)) \cdot \frac{f(z, t)(f_{\max} - f(z, t))}{f^* + ||r(\delta Y(x)) - x_{\text{dir}}(z)||_2} \cdot \chi_{\{f(\cdot, t) > 0\}}(z), \tag{4.14}$$

Here we have $x_{\text{dir}}(z) = \overrightarrow{x\,z}$ representing the barycentric position vector pointing to z in $\delta Y(x)$, which enables us also the quantification of the *position defect* of z with respect to $r(\delta Y(x), t)$ namely

$$||r(\delta Y(x)) - x_{\text{dir}}(z)||_2,$$

which affects the spatial relocation of micro-fibres mass. Furthermore, $f_{\max}$ represents a level of micro-fibres that can be distributed at $z \in \delta Y(x)$, with the micro-fibres mass relocation in the direction of $(x_{\text{dir}}(z) + r(\delta Y(x), t))$ being enabled provided that their level is below $f_{\max}$. Finally, alongside the *position defect* of z with respect to $r(\delta Y(x), t)$, another aspect that affects the micro-fibres relocation is the level of micro-fibres distributed at location z, which is accounted for in (4.14) through the micro-fibres saturation fraction

$$f^* = \frac{f(z, t)}{f_{\max}}.$$

Thus, a micro-fibres mass transport from z to the location z^* is exercised provided that micro-fibres level at z are not at their maximum level $f_{\max}$, while lower levels of micro-fibres saturations at z together with a better position alignment given by a smaller position defect lead to a relocation of the micro-fibres mass in direction $(x_{\text{dir}}(z) + r(\delta Y(x), t))$ at a greater distance, resulting in reaching a position z^* that is further away from z. Finally, this micro-fibres transport is also regulated by the capacity available at the new position z^*, which is explored here through a movement probability

$$p_{move} := \max\big(0, \frac{f_{\max} - f(z^*, t)}{f_{\max}}\big),$$

that enables only an amount of $p_{move} f(z, t)$ of micro-fibres to be transported to position z^*, while the rest of $(1 - p_{move}) f(z, t)$ remain at z.

4.2.4 The multiscale moving boundary approach

Let us now briefly revisit the novel multiscale moving boundary framework initially introduced in Trucu et al. (2013) and later evolved to consider two cancer cell sub-populations in Shuttleworth and Trucu (2018), which explores the cell-scale proteolytic activity of MDEs along the invasive edge of the tumour that is non-locally induced by the tissue-scale cancer cell population dynamics and that degrades the peritumoural ECM determining this way the direction and associated displacement for tumour boundary progression. As detailed in Trucu et al. (2013), the link between the tumour macro-dynamics (3.14), (4.5), (4.11) and (4.12) and the proteolytic enzyme micro-dynamics is captured via a double feedback loop that is realised by a *top-down* link describing the source of MDEs induced at cell-scale by the spatial distribution of cancer cells at tissue-scale, and a *bottom-up* link describing the translation of the resulting boundary relocation to the tissue-scale.

Top-down link As previously discussed in Chapter 2 and readdressed here for readability, cancer invasion is a multiscale process in which the MDEs secreted by tumour cells from the outer proliferating ring undergo a cell-scale spatial transport in the neighbourhood of the invasive edge of the tumour and are responsible for the degradation of the surrounding ECM. It is this breakdown of peritumoural ECM that enables the tumour opportunities to expand and proceed with its local invasion. Continuing with the terminology of the framework introduced in Trucu et al. (2013), during a time interval $[t_0, t_0 + \Delta t]$, the MDEs micro-dynamics is explored on the invasive leading edge of the tumour $\partial\Omega(t)$ enclosed by a complete cover of ϵ-size half-way shifted overlapping micro-domains $\{\epsilon Y\}_{\epsilon Y \in \mathcal{P}}$. Furthermore, the specific topological requirements detailed in full in Trucu et al. (2013) that enable the construction of the covering bundle of micro-domains $\{\epsilon Y\}_{\epsilon Y \in \mathcal{P}}$, allow us to capture the cell-scale MDEs activity in a neighbourhood of $\partial\Omega(t)$, exploring this molecular dynamics in both the overlapping inner regions $\epsilon Y \cap \Omega(t)$ and the peritumoural outside regions $\epsilon Y \cap \backslash\Omega(t)$ where the MDEs get transported and degrade the ECM.

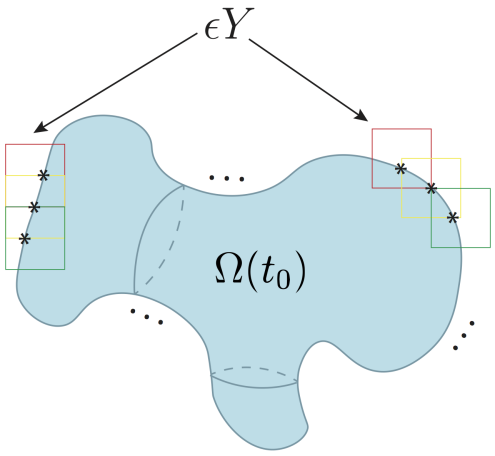

Figure 4.2: Schematic of the bundle of ϵY micro-cubes covering boundary of the tumour $\partial\Omega(t_0)$, including the half-way shifted overlapping ϵY cubes. Dots illustrate continuation of boundary coverage by ϵY cubes.

At each $y \in \epsilon Y \cap \Omega(t)$ a source of MDEs is induced as a collective contribution

of both cancer cell sub-populations that arrive during their dynamics in the outer proliferating rim within a maximal distance $\gamma > 0$ with respect to y (given by the maximal thickness of the outer proliferating rim), and so this can be mathematically given by

$$\begin{aligned} &1. \quad g_{\epsilon Y}(y,\tau) = \frac{\int\limits_{\mathbf{B}(z,\gamma)\cap\Omega(t_0)} \alpha_1 c_1(x,t_0+\tau) + \alpha_2 c_2(x,t_0+\tau)\, dx}{\lambda(\mathbf{B}(y,\gamma)\cap\Omega(t_0))}, \quad y \in \epsilon Y \cap \Omega(t_0), \\ &2. \quad g_{\epsilon Y}(y,\tau) = 0, \quad y \in \epsilon Y \setminus \big(\Omega(t_0) + \{y \in Y |\ ||z||_2 < \gamma\}\big), \end{aligned} \tag{4.15}$$

where $\mathbf{B}(y,\gamma) := \{\xi \in Y \mid \parallel y - \xi \parallel_\infty \leq \gamma\}$; α_i, $i = 1,2$, are the MDE secretion rates for the two cancer cell sub-populations, $\lambda(\cdot)$ is the standard Lebesgue measure on $\mathbb{R}^2$; and γ is a small distance between the zero source level from outside $\Omega(t_0)$ and the non-zero source levels on $\epsilon Y \cap \Omega(t_0)$ where via *Urysohn Lemma* (Yosida, 1980) we ensure a continuous transition. Once secreted by the cancer cells, the MDEs molecular distribution denoted here by $m(y,\tau)$ exercise a cell-scale cross interface spatio-temporal transport which in the simplest context of a generic MDEs is considered as being given by a local diffusion. Thus, given the topological properties of the covering bundle of overlapping micro-domains $\{\epsilon Y\}_{\epsilon Y \in \mathcal{P}}$ detailed in Trucu et al. (2013), this enable us to decompose this cross-interface diffusion process (into a corresponding bundle of micro-processes) and to explore this per each individual ϵY, where this micro-dynamics is given as

$$\frac{\partial m}{\partial \tau} = D_m \Delta m + g_{\epsilon Y}(y,\tau), \quad y \in \epsilon Y,\ \tau \in [0, \Delta t]. \tag{4.16}$$

Bottom-up link During the micro-dynamics, the MDEs present in the peritumoural region interact with the ECM distribution captured within each ϵY micro-

domain. The local degradation of ECM is dependent on the advancing spatial distribution of MDEs in $\epsilon Y \backslash \Omega(t)$ secreted by the cancer cells. This pattern of degradation gives rise to a movement direction, $\eta_{\epsilon Y}$, and a displacement magnitude, $\xi_{\epsilon Y}$ (briefly addressed in Chapter 2 and fully detailed in Trucu et al. (2013)), that ultimately dictate the movement of the boundary midpoint $x^*_{\epsilon Y}$ to a new position $\widetilde{x^*_{\epsilon Y}}$. This process is the catalyst behind the expansion of the macroscopic tumour boundary. Thus, the *bottom-up* link of the model between the molecular activities of MDEs on the tumour invasive edge and the macroscopic boundary $\Omega(t_0)$, is realised through the macro-scale boundary movement effectuated by the micro-dynamics of the proteolytic enzymes, resulting in an expanded tumour domain, $\Omega(t_0 + \Delta t)$, on which the invasion process continues.

4.2.5 Summary of model

As stated previously, the two-part multiscale model is comprised of two interconnected multiscale systems that share the same macro-scale whilst having their own distinct micro-scale dynamics, as schematically summarised in Chapter 3, Figure 3.6. The macro-scale dynamics governs the spatial distribution of cancer cells and both the fibre and non-fibre components of the ECM. The first multiscale system controls the dynamic redistribution of micro-fibres, weighted according to the cancer cell and macroscopic fibre distributions and triggers a micro-scale spatial rearrangement of micro-fibres via the combined spatial flux of the two cancer cell sub-populations. The second multiscale system reacts to a source of MDEs induced on the boundary by the spatial distribution of cancer cells. The microscopic distribution of MDEs instigates degradation of the peritumoural ECM and it is from this pattern of degradation that the position of the tumour boundary is changed. The microscopic change in the boundary is translated back to the tissue-level and the macro-dynamics con-

tinue leading to a newly expanded tumour region, where the cancer invasion process continues its dynamics.

4.3 Numerical approaches and initial conditions for computations

Building on the multiscale moving boundary computational framework introduced in Trucu et al. (2013) combined with its very recent novel extension introduced in Chapter 3 and Shuttleworth and Trucu (2019c) to address the multiscale fibres dynamics in the bulk of the tumour, we developed a new computational approach to explore the complex multiscale evolution of a heterotypic tumour with two cancer cell sub-populations within a fibrous environment. We consider a uniform spatial mesh of size $h = 0.03125$ to solve the macro-scale computations on the expanding tumour domain, whilst using an off-grid approach for the calculation of the macroscopic adhesion term that decomposes the cell-sensing region to approximate the adhesive flux at each spatio-temporal node. To complete the tumour macro-dynamics we use a novel predictor-corrector scheme developed in Chapter 3 and Shuttleworth and Trucu (2019c) that accounts for the complexity of the cancer dynamics. Further, to obtain the microscopic boundary relocation, we explore the *top-down* and *bottom-up* links as well as solve the micro-dynamics via finite element approximation as detailed in Trucu et al. (2013).

In the following sections we consider the initial cancer cell population c_1 to occupy the region $\Omega(0) = \mathbf{B}((2,2), 0.5)$ positioned in the centre of Y, Figure 4.3,

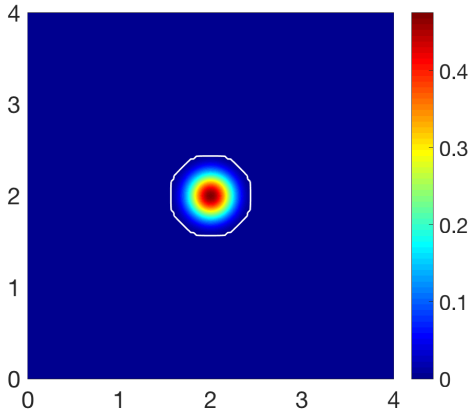

Figure 4.3: Initial condition for cancer cell population c_1.

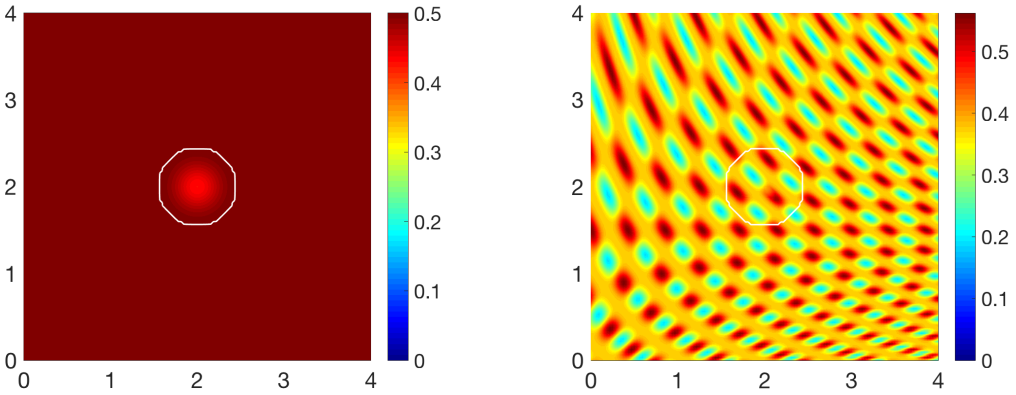

(a) Homogeneous non-fibre ECM **(b)** Heterogeneous non-fibre ECM

Figure 4.4: Initial conditions for non-fibre ECM phase: (a) homogeneous (a); and (b) heterogeneous

whilst the distribution of cell population c_2 is initially zero, i.e.,

$$c_1(x,0) = 0.5\left(\exp\left(-\frac{||x-(2,2)||_2^2}{0.03}\right) - \exp(-28.125)\right)\left(\chi_{\mathbf{B}((2,2),0.5-\gamma)} * \psi_\gamma\right), \tag{4.17}$$

$$c_2(x,0) = 0, \tag{4.18}$$

where ψ_γ is the standard mollifier detailed in Appendix C.1 that acts within a radius $\gamma << \frac{\Delta x}{3}$ from $\partial\mathbf{B}((2,2),0.5-\gamma)$ to smooth out the characteristic function $\chi_{\mathbf{B}((2,2),0.5-\gamma)}$. Furthermore, for the non-fibre ECM phase, we consider both a homogeneous and heterogeneous initial conditions, with the homogeneous initial conditions illustrated in Figure 4.4a and given by

$$l(x,0) = \min\{0.5, 1-c_1(x,0)\}, \tag{4.19}$$

and heterogeneous initial condition shown in Figure 4.4b and given by

$$l(x,0) = \min\left\{h(x_1,x_2), 1-c(x,0)\right\}, \tag{4.20}$$

where

$$\begin{aligned} h(x_1,x_2) &= \frac{1}{2} + \frac{1}{4}\sin(\zeta x_1 x_2)^3 \cdot \sin(\zeta\frac{x_2}{x_1}), \\ (x_1,x_2) &= \frac{1}{3}(x+1.5) \ \in [0,1]^2 \text{ for } x \in Y, \quad \zeta = 7\pi. \end{aligned}$$

these being previously used also in Chapter 3 and Shuttleworth and Trucu (2019c).

For the initial distribution of the ECM fibre phase, we assume a distribution of five pre-assigned micro-fibre distributions of the five different micro-fibre patterns generated along the family of path-networks $\{P_i^1\}_{i=1..5}$ and assigned randomly onto

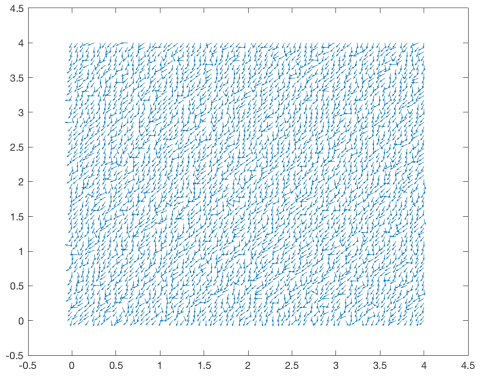

(a) Homogeneous 2D velocity plot

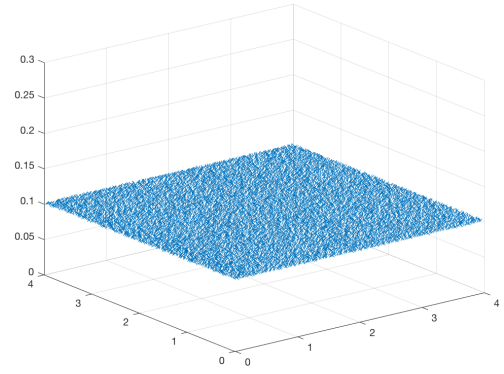

(b) Homogeneous magnitude in a 3D plot

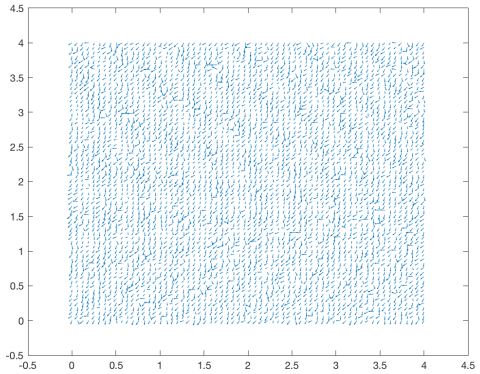

(c) Heterogeneous 2D velocity plot

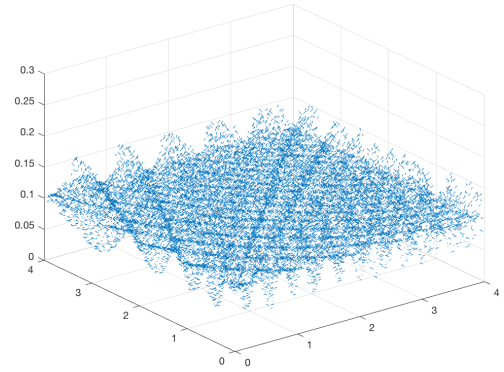

(d) Heterogeneous magnitude in a 3D plot

Figure 4.5: Initial conditions for ECM fibres phase $\theta_f(x, 0)$: (a) shows oriented fibres of homogeneous magnitude while (b) shows their corresponding 3D plot; (c) shows oriented fibres of heterogeneous magnitude while (d) shows their corresponding 3D plot.

$\delta Y(x) := x + \delta Y$ (as detailed in Appendix D.1). To represent a homogeneous distribution of fibres, we calibrate the maximal height of the microfibres to be uniform across all micro-domains, resulting in a macroscopic fibre distribution $F(\cdot, t)$ that represents a percentage p of the mean density of the non-fibrous homogeneous ECM phase (4.19), illustrated in Figure 4.5a-4.5b. On the other hand, a heterogeneous distribution of fibres is achieved by allowing the maximal height of the microfibres to be determined by a heterogeneous pattern, for example, the initial condition for a heterogeneous ECM non-fibre phase (4.20), Figure 4.5c-4.5d. We set the maximal height of the micro-fibres in each $\delta Y(x)$, centred at x, to correspond to the distribution $l(x, 0)$ for all $x \in Y$, resulting in the macroscopic fibre magnitude spatial distribution $F(\cdot, t)$ to represent again a percentage p of the heterogeneous non-fibre ECM phase.

The following simulations use the parameters detailed in parameter set Σ_2, Table 4.1.

4.4 Computational simulation results

4.4.1 Homogeneous non-fibre ECM component

Homogeneous non-fibre ECM component

In the first instance, the initial condition for the non-fibre ECM component will be taken as the homogeneous distribution, namely as $l(x, 0) = \min\{0.5, 1 - c_1(x, 0)\}$. The initial condition for both cancer cell populations is given in (4.17), (4.18), and the fibres take an initial macroscopic distribution of 15%, the non-fibre phase, with the combined ECM density $v(x, 0) = l(x, 0) + F(x, 0)$. Using the parameter set Σ_2, we show the computational results for the evolution of both individual cancer cell populations in subfigures 4.6a, 4.6b, their combined population in subfigure 4.6c, the

Table 4.1: *The parameters in* Σ_2

Parameter	Value	Description	Reference
D_1	3.5×10^{-4}	diffusion coeff. for cell population c_1	Domschke et al. (2014)
D_2	7×10^{-4}	diffusion coeff. for cell population c_2	Domschke et al. (2014)
D_m	10^{-3}	diffusion coeff. for MDEs	Estimated
μ_1	0.25	proliferation coeff. for cell population c_1	Domschke et al. (2014)
μ_2	0.25	proliferation coeff. for cell population c_2	Domschke et al. (2014)
γ_1	2	non-fibrous ECM degradation coeff.	Shuttleworth and Trucu (2019c)
γ_2	1.5	macroscopic fibre degradation coeff.	Peng et al. (2017)
μ_3	0-0.02	non-fibrous ECM remodelling coeff.	Domschke et al. (2014)
α_1	1	MDE secretion rate of c_1	Estimated
α_2	1.5	MDE secretion rate of c_2	Estimated
$\mathbf{S}_{max}$	$\begin{pmatrix} 0.5 & 0 \\ 0 & 0.3 \end{pmatrix}$	cell-cell adhesion coeff. matrix	Domschke et al. (2014)
$\mathbf{S}_{cF}$	$\begin{pmatrix} 0.1 & 0 \\ 0 & 0.2 \end{pmatrix}$	cell-fibre adhesion coeff.	Estimated
$\mathbf{S}_{cl}$	$\begin{pmatrix} 0.05 & 0 \\ 0 & 0.05 \end{pmatrix}$	cell-matrix adhesion coeff.	Estimated
R	0.15	sensing radius	Shuttleworth and Trucu (2019c)
r	0.0016	width of micro-fibres	Shuttleworth and Trucu (2019c)
$f_{\max}$	0.6360	max. micro-density of fibres	Shuttleworth and Trucu (2019c)
p	0.15-0.2	percentage of non-fibrous ECM	Estimated
h	0.03125	macro-scale spatial discretisation size	Trucu et al. (2013)
ϵ	0.0625	size of micro-domain ϵY	Trucu et al. (2013)
δ	0.03125	size of micro-domain δY	Shuttleworth and Trucu (2019c)

non-fibre ECM phase and fibre ECM phase in subfigures 4.6d and 4.6e respectively, presented with the full ECM density in subfigure 4.6f. Additionally, we display the vector field of oriented fibres at two different resolutions, namely, coarsened twice, 4.7a, and coarsened four times, 4.7b, and a 3D plot of the macroscopic oriented fibres 4.7c.

Figures 4.6-4.7 display computations at final stage $75\Delta t$, during which time mutations from population c_1 to c_2 have begun, starting at stage $5\Delta t$. Previously it was observed that in the presence of a homogeneous ECM, the tumour was limited

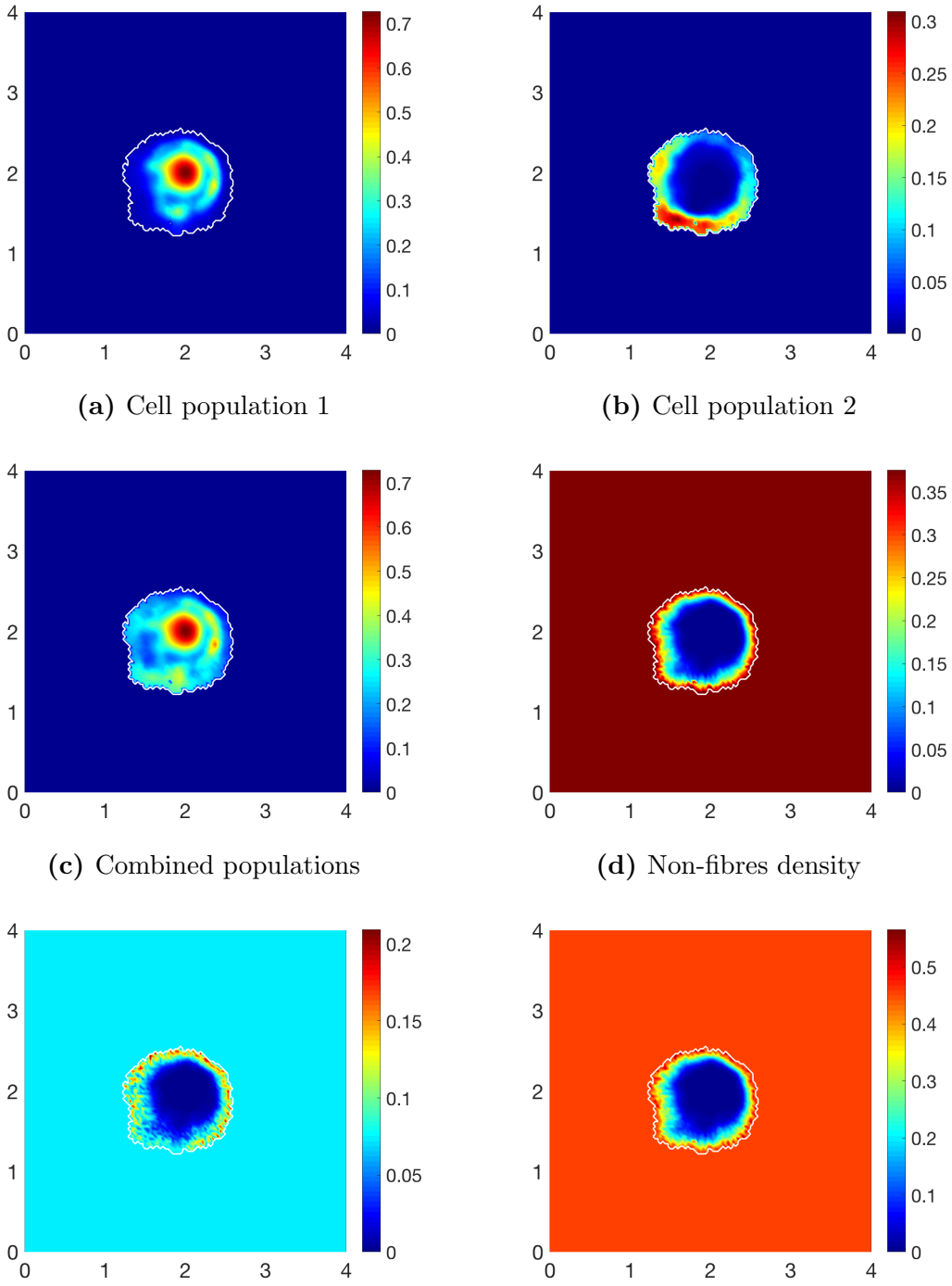

(a) Cell population 1

(b) Cell population 2

(c) Combined populations

(d) Non-fibres density

(e) Fibre density

(f) Combined ECM

Figure 4.6: Simulations at stage $75\Delta t$ with a homogeneous distribution of non-fibres and a random initial 15% homogeneous distribution of fibres with parameter set Σ_2.

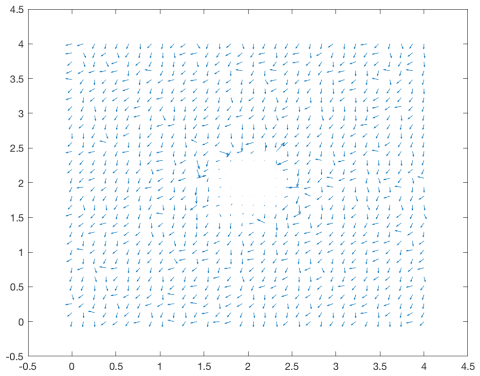

(a) 2D fibre plot

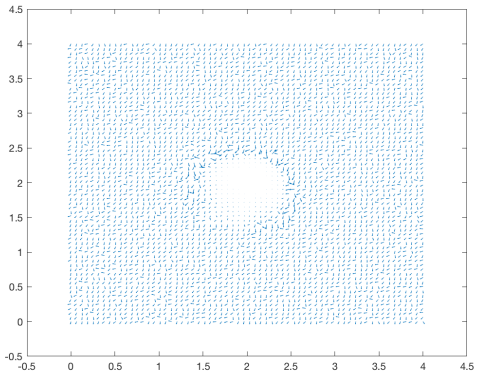

(b) 2D fibre plot

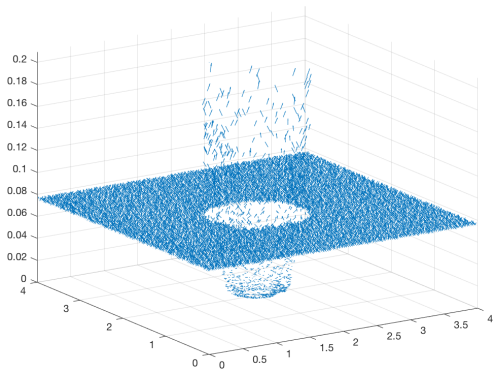

(c) 3D fibre plot

Figure 4.7: Simulations at stage $75\Delta t$ with a homogeneous distribution of non-fibres and a random initial 15% homogeneous distribution of fibres.

to a symmetric pattern of invasion, Figure 2.13(a) in Chapter 2, however with the addition of an initially homogeneous fibre distribution we witness a different pattern of invasion in 4.6c. Throughout the simulations, the ECM is degraded by the cancer cells, most notable by the large low density region in 4.6c, with the highest levels of degradation relative to the regions of highest cell distribution. The primary cell population c_1, 4.6a, has been manipulated and reshaped by the underlying fibre network. Although the fibre phase of the ECM begins as a macroscopically homogeneous distribution, once fibre rearrangement occurs, higher density regions of fibres are formed, 4.6e, and these areas become increasing influential on the direction of invasion. Since mutations have begun, we see the emergence of cells in population c_2, 4.6b. The pattern of cells in population c_2 is correspondent to the fibre orientations displayed in 4.7a-4.7b, where the general direction of fibres are aiming roughly towards the origin $(0, 0)$. Thus, the distribution of cells c_2 present in Figure 4.6b are more prominent in this direction. This behaviour is attributable to population c_2 retaining a higher affinity for cell-fibre adhesion than population c_1. We conclude from our computations that the underlying fibre network strongly influences the direction of invasion. It is clear from the computational results presented in Figure 4.7 that the tumour boundary has expanded in the general macroscopic fibre direction.

To further examine the effects of an underlying fibre distribution, we increase the initial homogeneous fibre distribution to 20% of the non-fibre ECM phase. Continuing with the same initial conditions for the non-fibre ECM phase and cancer distributions, we present the computations at final stage $70\Delta t$, Figure 4.8. Comparing with Figure 4.8, cells of population c_1 are exhibiting limited migration within the tumour boundary due to their high self-adhesion rate, 4.8a, whilst cells of population c_2, 4.8b, have migrated in a direction consistent with the macroscopic fibre

orientations in 4.9a-4.9b. The mutated cell population c_2 congregates around the cells of population c_1, this time showing more regions of high distribution, suggesting the increased fibre distribution enables faster migration of cells in population c_2. The entire ECM (both the fibre and non-fibre phase) presented in subfigures 4.8d-4.8e has been degraded in the centre of the domain where the cancer cells are most dense.

Consistent with the previous simulations, the micro-fibres have been pushed outwards towards the boundary, however this time the macroscopic representation of the fibres appears as a region of very low fibre density surrounded in a speckled pattern of fibre densities, Figure 4.8e. This behaviour occurs because of two reasons; firstly, the tumour boundary is progressing faster than the fibres are being rearranged, and because the rearrangement of fibres is restricted to neighbouring domains only, the fibre distributions will never be found to build up explicitly at the rapidly expanding tumour boundary. Secondly, as the degradation of fibres is kept within the bounds of the tumour and dependent on the cancer cell distribution, out-with the dense main body of cancer cells, we see little degradation of the fibres. The increased size of spread of the tumour indicates that the ratio of the underlying fibre network to the non-fibre ECM phase plays a key role in the success of local tumour invasion.

We can investigate a similar scenario to that presented previously whereby we now explore tumour invasion on an initially heterogeneous fibre network. The initial condition for the macroscopic fibre distributions will be taken as 15% of the heterogeneous distribution defined in (4.20) whilst the non-fibre ECM phase will be kept as a homogeneous distribution. Figure 4.10 displays computations at final stage $75\Delta t$. Comparing to Figure 4.6, the boundary of the tumour has formed lobules, specifically towards low density regions of the fibre network, most notable in subfig-

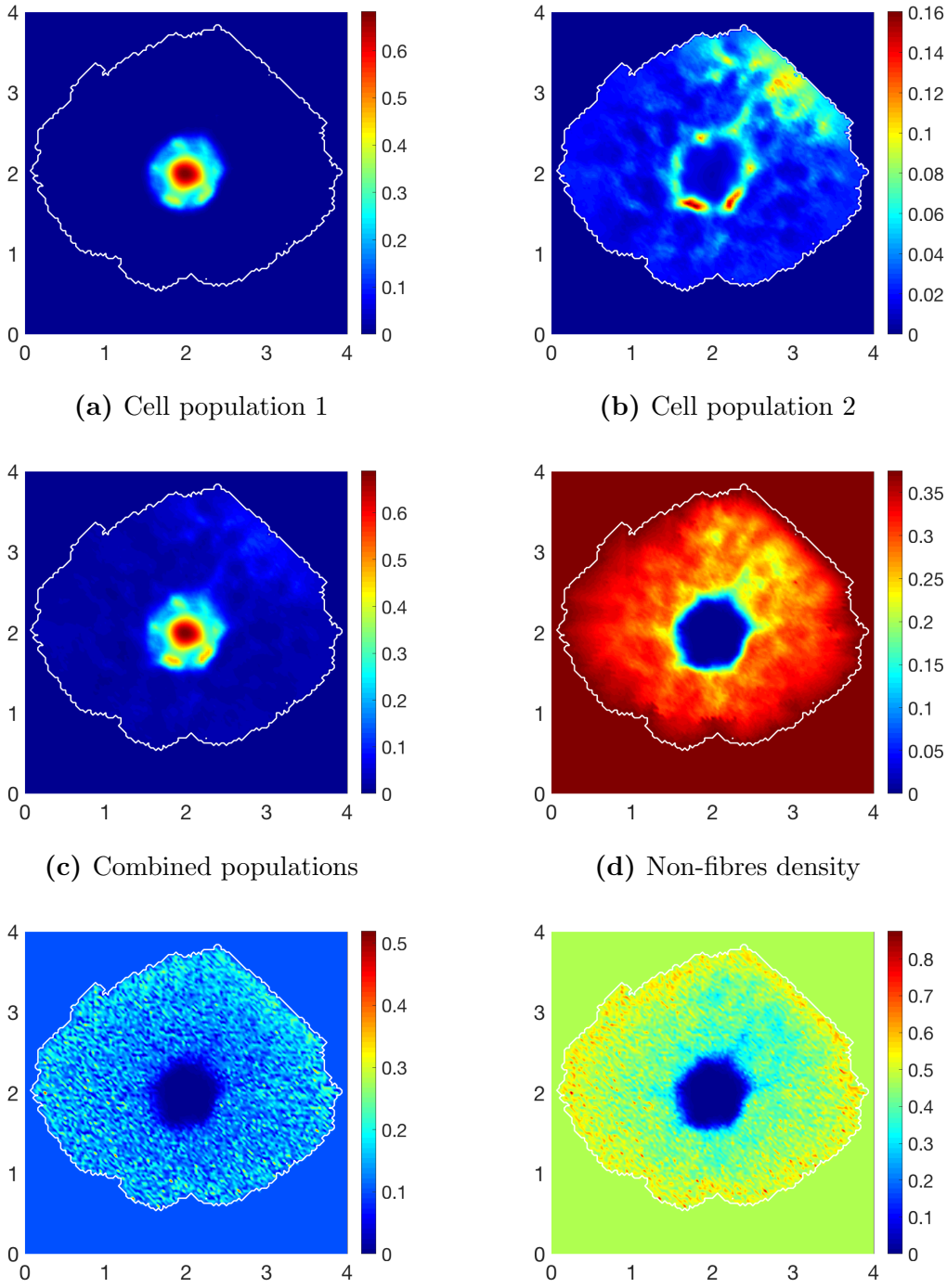

(a) Cell population 1

(b) Cell population 2

(c) Combined populations

(d) Non-fibres density

(e) Fibre density

(f) Combined ECM

Figure 4.8: Simulations at stage $70\Delta t$ with a homogeneous distribution of non-fibres and a random initial 20% homogeneous distribution of fibres with parameter set Σ_2.

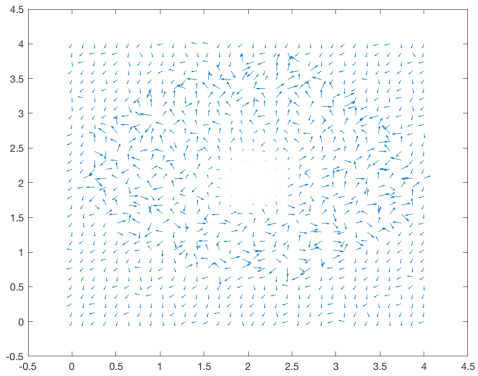

(a) 2D fibre plot

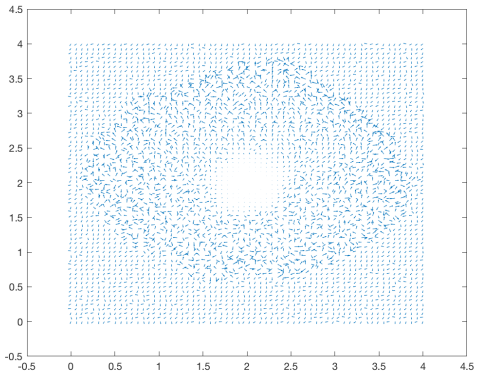

(b) 2D fibre plot

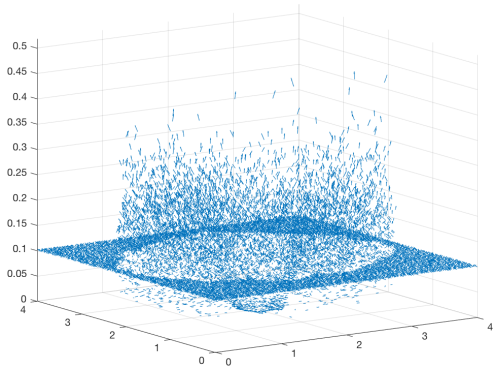

(c) 3D fibre plot

Figure 4.9: Simulations at stage $70\Delta t$ with a homogeneous distribution of non-fibres and a random initial 20% homogeneous distribution of fibres.

ure 4.10e. A different pattern of mutations from population c_1 to c_2 is adopted due to the heterogeneity of the fibre network and thus high distribution regions of cells are formed in 4.10b that differ to that when in the presence of a homogeneous fibre phase.

The macroscopic mean value of fibres has had a substantial impact on the overall invasion of cancer. The boundary of the tumour has grown many lobules, first reaching to the lower density areas of fibres in 4.10e before engulfing the higher density regions as invasion progresses. The high distributions of cells in population c_2 are reminiscent of Figure 4.10b in that they are building according to the general orientation of the fibre network in 4.11a-4.11b. Under the presence of a heterogenous fibre network, tumour invasion is halted at regions of high macroscopic fibre density, whilst in a homogeneous environment there are no barriers during invasion, evidenced in Figure 4.6. Here the tumour experiences a lobular expansion as it invades the surrounding ECM whilst the high macroscopic fibre distributions coupled with the higher cell-fibre adhesion rate that population c_2 carries allows the cells more migratory freedom within the tumour boundary.

We consider the same previous initial conditions considering a homogeneous non-fibre phase and heterogeneous fibre ECM phase, but we now introduce matrix remodelling to the non-fibre ECM phase, namely, increasing μ_3 from 0 to 0.02. Initially the computational results are very similar to that of the previous section, however, as tumour invasion progresses, Figures 4.12-4.13 show that both the boundary of the tumour and the main body of cells looks very different. Although the density of tumour cells is not as high as in Figure 4.10c, there is a definite increase in cell distribution within the boundary of the tumour, Figure 4.12c with almost the entire tumour containing a visible amount of cells. This behaviour is as a consequence of matrix remodelling only occurring under the presence of cancer cells, hence, the

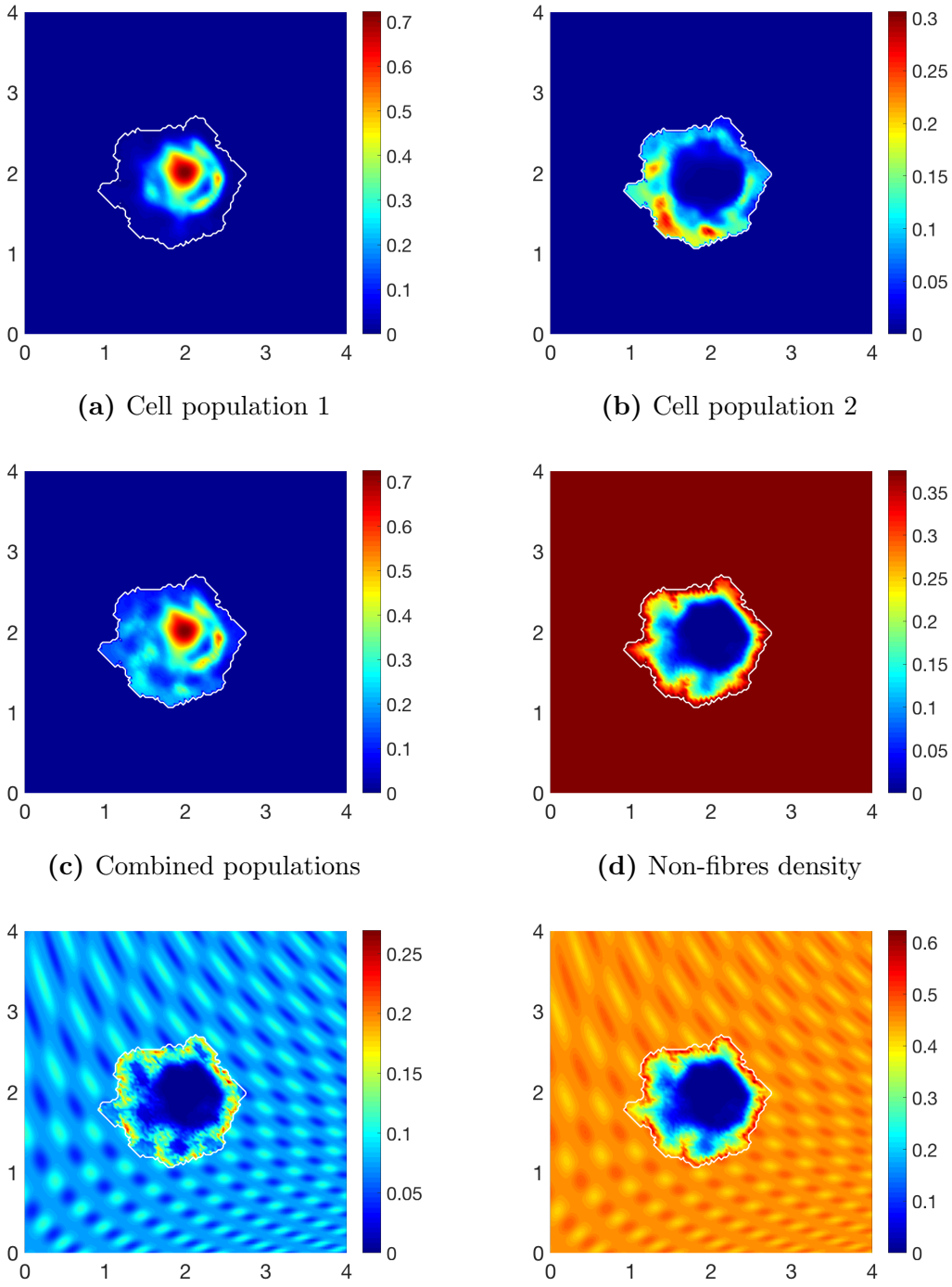

(a) Cell population 1

(b) Cell population 2

(c) Combined populations

(d) Non-fibres density

(e) Fibre density

(f) Combined ECM

Figure 4.10: Simulations at stage $75\Delta t$ with a homogeneous distribution of non-fibres and a random initial 15% heterogeneous distribution of fibres with parameter set Σ_2.

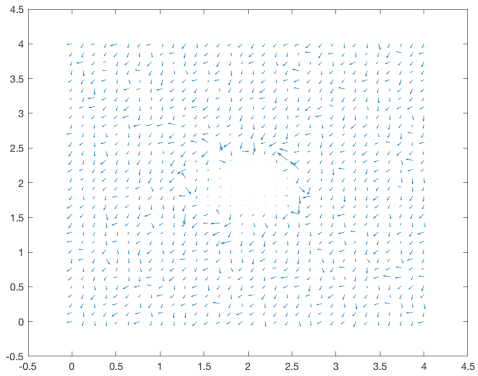

(a) 2D fibre plot

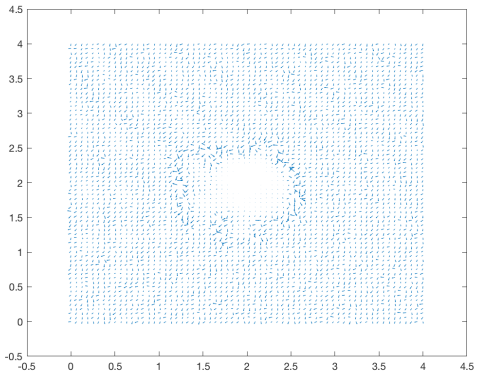

(b) 2D fibre plot

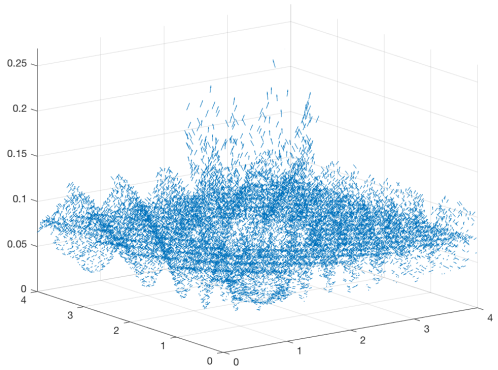

(c) 3D fibre plot

Figure 4.11: Simulations at stage $75\Delta t$ with a homogeneous distribution of non-fibres and a random initial 15% heterogeneous distribution of fibres.

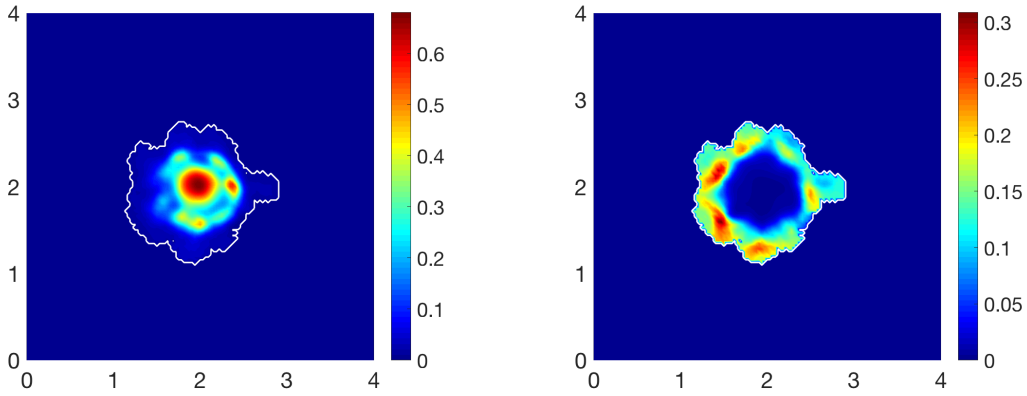

(a) Cell population 1

(b) Cell population 2

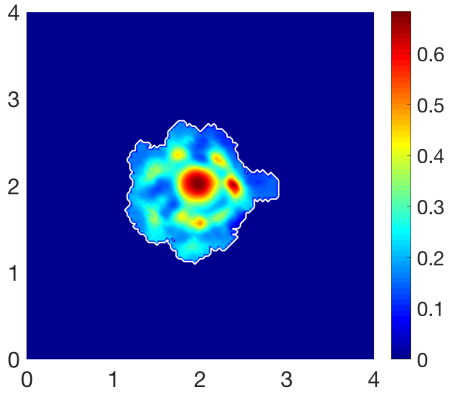

(c) Combined populations

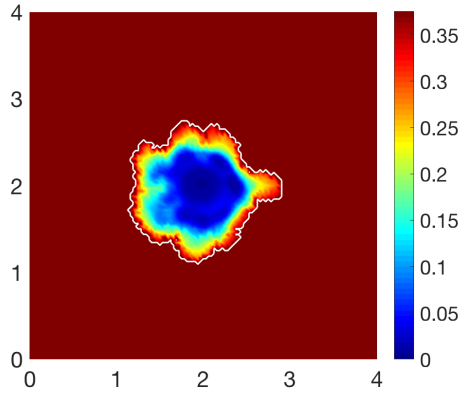

(d) Non-fibres density

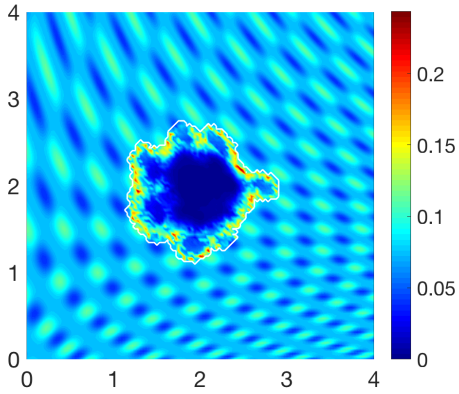

(e) Fibre density

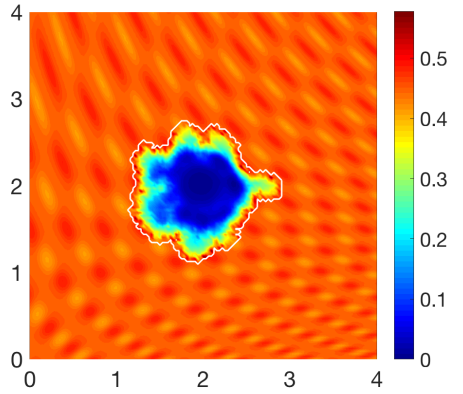

(f) Combined ECM

Figure 4.12: Simulations at stage $75\Delta t$ with a homogeneous distribution of the non-fibres with matrix remodelling, $\mu_3 = 0.02$, and a random initial 15% heterogeneous distribution of fibres with parameter set Σ_2.

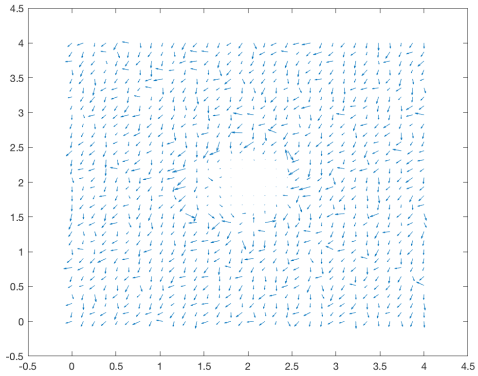

(a) 2D fibre plot

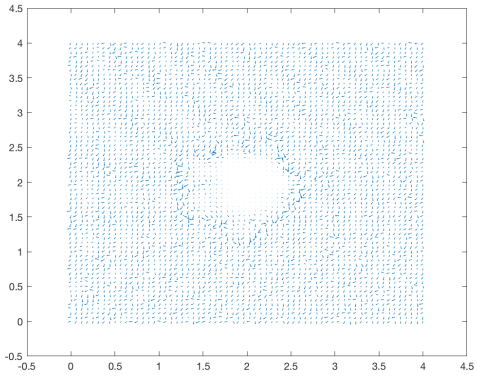

(b) 2D fibre plot

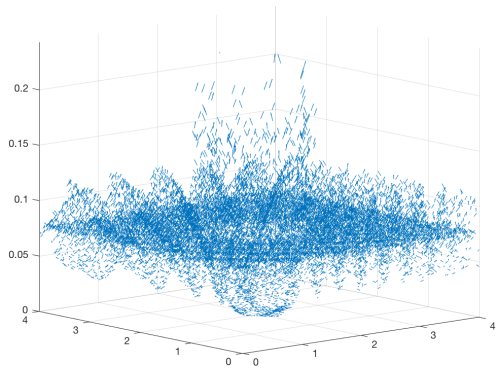

(c) 3D fibre plot

Figure 4.13: Simulations at stage $75\Delta t$ with a homogeneous distribution of the non-fibres with matrix remodelling and a random initial 15% heterogeneous distribution of fibres.

increased density of matrix within the boundary of the tumour gives more opportunity for cell adhesion and opens more pathways in which the cells can invade. Due to the heterogeneity of the fibre ECM phase, the tumour again exhibits a lobular route of invasion, first enveloping the low density regions where space is available for the cells to freely invade, and consequently overrunning the high density regions in their path, Figure 4.12d-4.12f.

4.4.2 Heterogeneous non-fibre ECM component

Investigating the effects of different initial fibre distributions present in a homogeneous non-fibre ECM domain is effective in showing the influence of fibres on tumour invasion, however, is it crucial to examine these varying fibre distributions under a heterogeneous non-fibre ECM phase. We express heterogeneity of the non-fibre ECM phase using the initial condition (4.20) and we assume an initial 15% homogeneous fibre distribution. Although the cell-non-fibre-ECM adhesion coefficients are kept low, we see the tumour of the boundary developing a lobular pattern, witnessed in subfigure 4.14c, encroaching on the lower density regions of matrix. By first advancing on the low density regions of the matrix, the cancer cells proceed by engulfing the high density regions in their path and thus the tumour region becomes larger. The tumour continues to progress in this manner with small islands appearing over the regions of high matrix density. These islands arise when the cancer cells have failed to fully overrun areas within the ECM. This behaviour can occur when there are not yet enough cells to fill the area, or because the matrix density is simply too high and the cells must first degrade part of the matrix in order to make space available. Population c_2 is sparse in its spread 4.14b, with only a few regions of cells visible, having gathered into pockets of the matrix where density of both fibre and non-fibre ECM is low, subfigures 4.14d-4.14e. Comparing to the simulations in

Figure 4.10, where initially the non-fibre ECM phase is homogeneous and the fibre phase is heterogeneous, we see a much larger overall spread of the tumour when the non-fibre ECM phase is taken as an initially heterogeneous distribution. This comparison implies that the non-fibre ECM phase plays a key role in the local invasion of cancer and is largely responsible for the progression of the tumour.

Continuing to explore invasion in a heterogeneous non-fibre ECM phase, we increase the initial homogeneous fibre distribution to 20% of the non-fibre phase. Figures 4.16-4.17 give simulations at the final stage $75\Delta t$. The tumour boundary is larger and more advanced when compared with the simulations in Figure 4.14, which have a lower initial fibre distribution. The increased fibres distributions within the ECM presents the cells with more opportunities for adhesion and as a result the cells spread at an increased rate into the surrounding matrix. Cell population c_2 has progressed outwards towards areas of the leading edge and formed small masses of cells in 4.16b. The direction of migration is similar to that in Figure 4.8, implying that even though they are subject to a rearrangement process, the initial fibre micro-domains influence the direction of migration of cells. It should also be noted that the density of cells in population c_2 is lower than that to previous simulations, this occurs as the cells have increased migration due to the increased fibre distributions, thus the cells do not build up in any one space, Figure 4.16b. Cells of population c_1 are surrounded by the more aggressive cells of population c_2, hence their invasion of the tissue is restricted and they have created denser regions of cells through proliferation, Figure 4.16a.

4.4.3 New family of pre-determined micro-fibre domains

Currently, we have explored the local invasion of a tumour under the presence of randomly placed micro-domains, allocated from a family of five pre-determined micro-

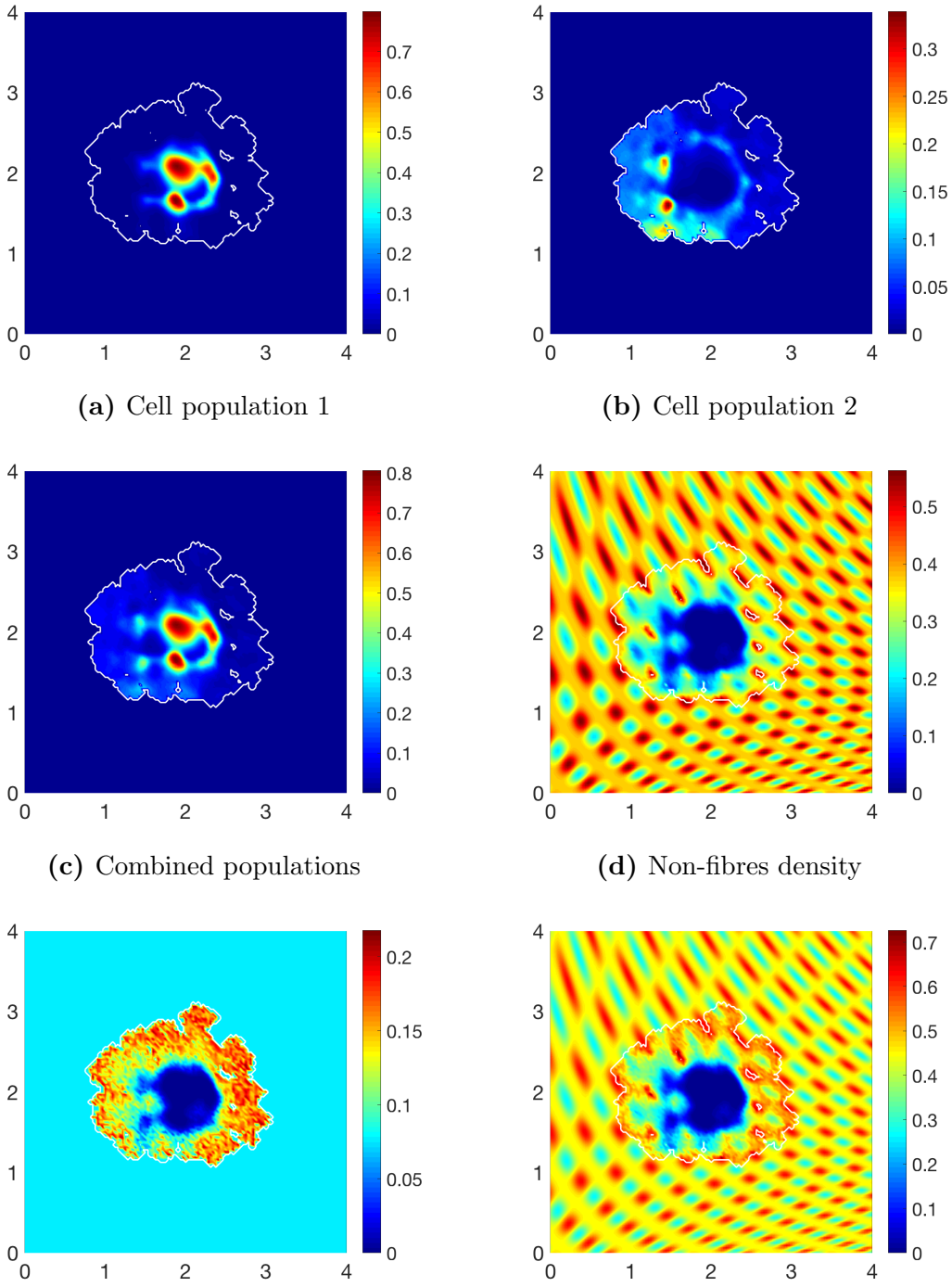

(a) Cell population 1

(b) Cell population 2

(c) Combined populations

(d) Non-fibres density

(e) Fibre density

(f) Combined ECM

Figure 4.14: Simulations at stage $75\Delta t$ with a heterogeneous distribution of non-fibres and a random initial 15% homogeneous distribution of fibres with parameter set Σ_2.

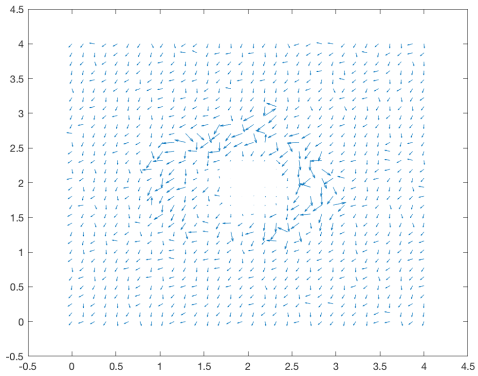

(a) 2D fibre plot

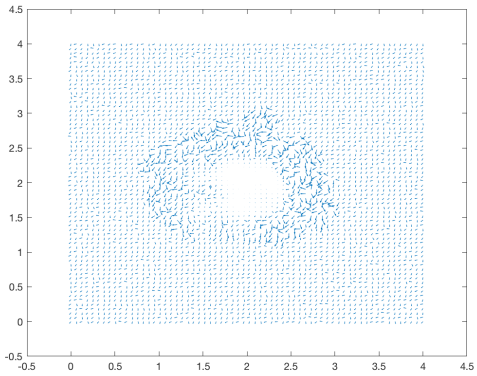

(b) 2D fibre plot

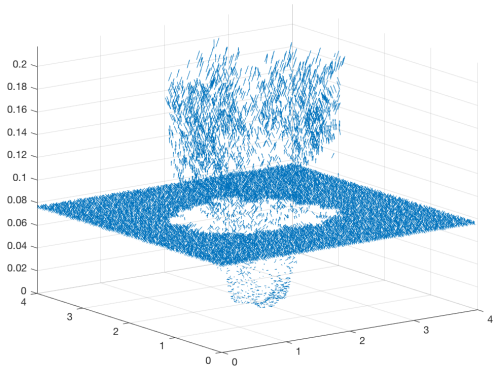

(c) 3D fibre plot

Figure 4.15: Simulations at stage $75\Delta t$ with a heterogeneous distribution of non-fibres and a random initial 15% homogeneous distribution of fibres.

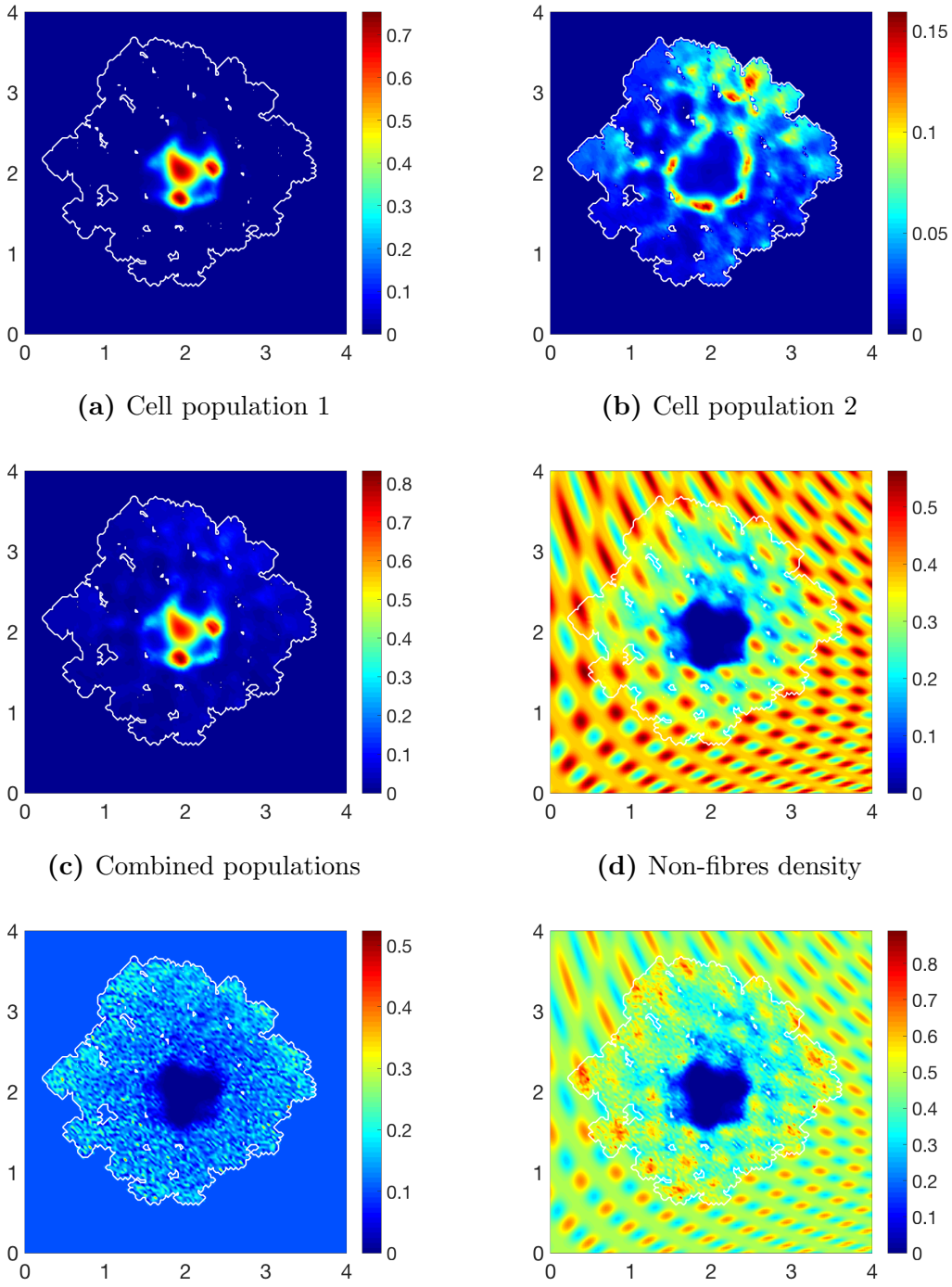

(a) Cell population 1

(b) Cell population 2

(c) Combined populations

(d) Non-fibres density

(e) Fibre density

(f) Combined ECM

Figure 4.16: Simulations at stage $75\Delta t$ with a heterogeneous distribution of non-fibres and a random initial 20% homogeneous distribution of fibres with parameter set Σ_2.

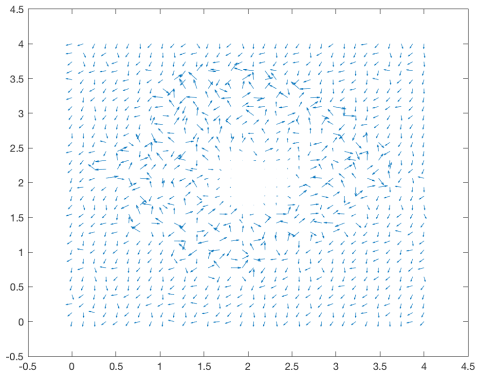

(a) 2D fibre plot

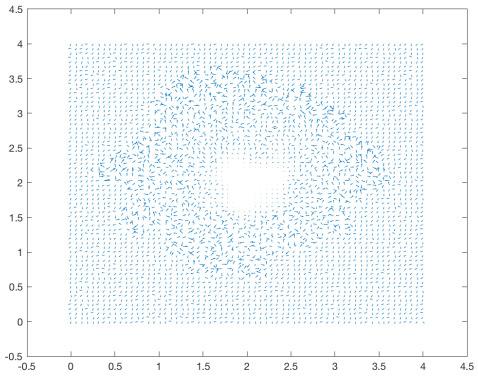

(b) 2D fibre plot

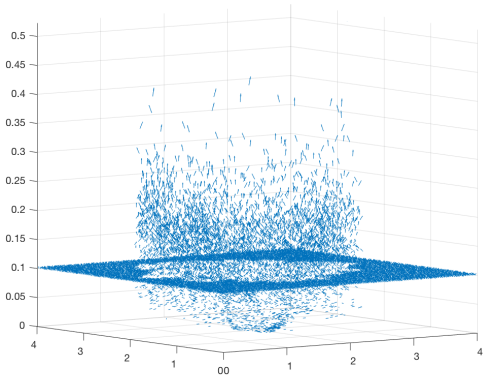

(c) 3D fibre plot

Figure 4.17: Simulations at stage $75\Delta t$ with a heterogeneous distribution of non-fibres and a random initial 20% homogeneous distribution of fibres.

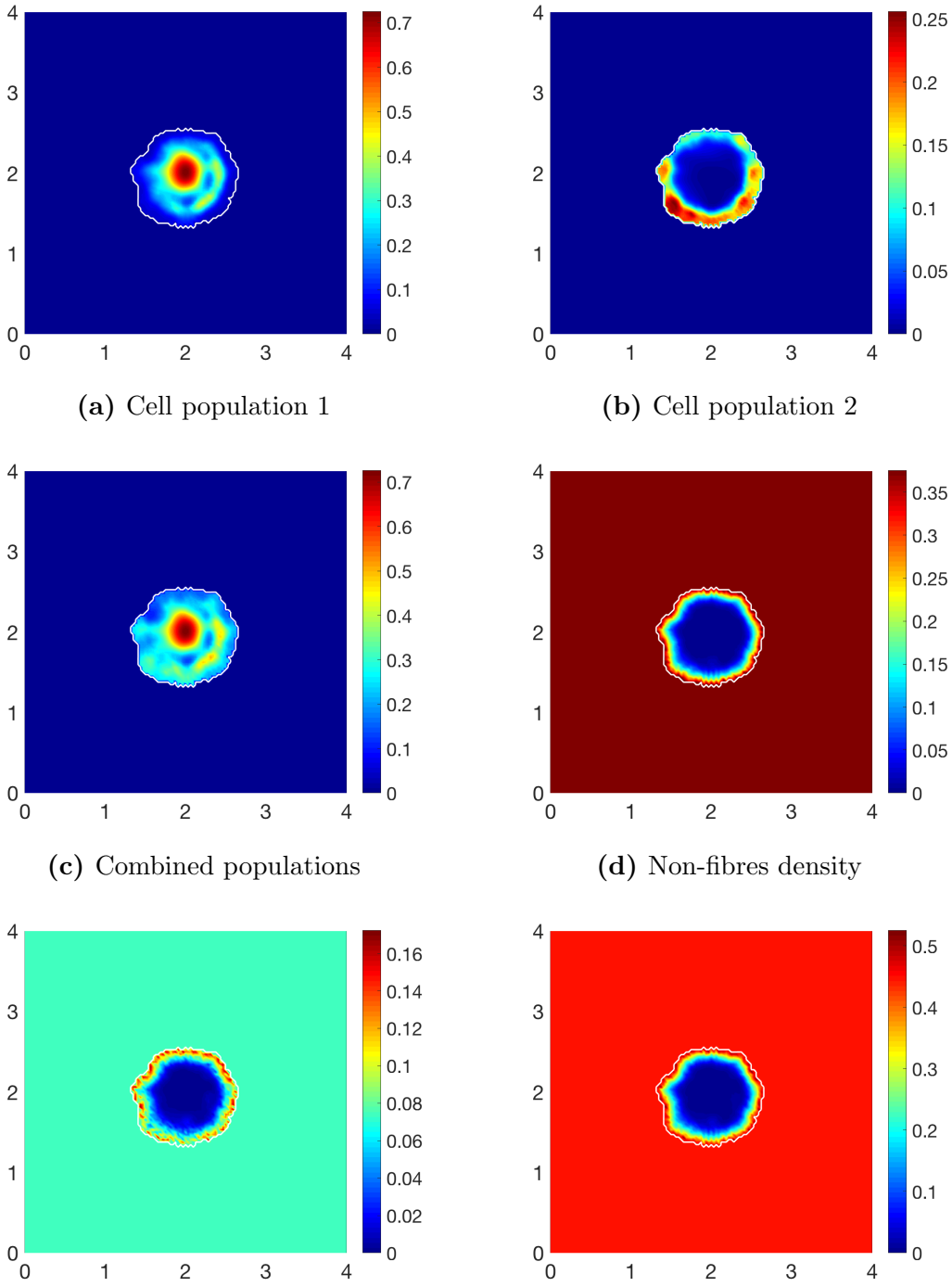

(a) Cell population 1

(b) Cell population 2

(c) Combined populations

(d) Non-fibres density

(e) Fibre density

(f) Combined ECM

Figure 4.18: Simulations at stage $75\Delta t$ with a homogeneous distribution of non-fibres and a random initial 15% homogeneous distribution of fibres from the family of fibre paths P^2 with parameter set Σ_2.

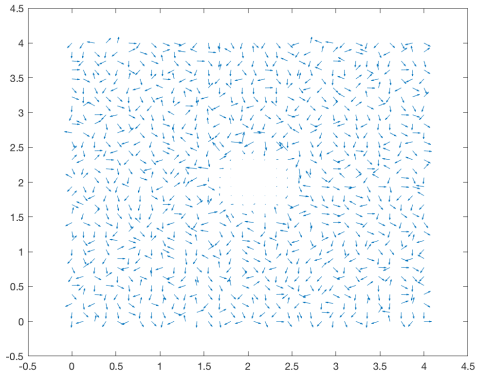

(a) 2D fibre plot

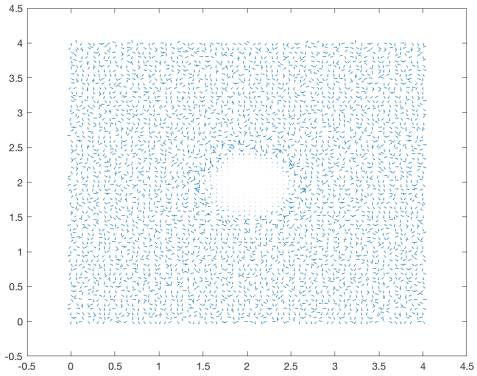

(b) 2D fibre plot

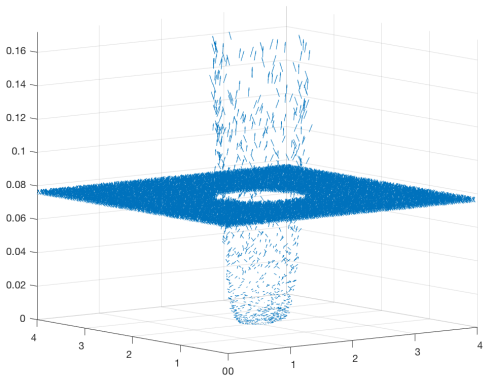

(c) 3D fibre plot

Figure 4.19: Simulations at stage $75\Delta t$ with a homogeneous distribution of non-fibres and a different random initial 15% homogeneous distribution of fibres from the family of fibre paths P^2.

domains. Now we consider the impact changing two of these micro-domains to contain a different pattern of micro-fibres, (i.e., those given by the second family of paths $\{P_i^2\}_{i=1..5}$ defined in Appendix D.1) will have on the overall invasion of cancer. Using the same initial condition as before for the cell populations (4.17), (4.18) and a homogeneous initial condition for the non-fibre ECM phase along with a 15% fibre phase, we obtain the computational results in Figures 4.18-4.19 at final stage $75\Delta t$. Comparing with the results using the previous family of micro-domains, Figure 4.6, the simulations appear similar, with only slight differences in the shape of the tumour boundary and the composition of the cells within each subpopulation. Cells in population c_2 have formed an increased number of high density regions in 4.18b, particularly at the lower part of the tumour boundary. The degradation of ECM is consistent to that of the previous results, showing regions of high degradation where the cells are of highest distribution, observed in subfigures 4.18d-4.18e.

To complete our comparison of the pre-determined fibre micro-domains, we explore cancer invasion within a heterogeneous 15% fibre component and a homogeneous non-fibre ECM component. Figures 4.20-4.21 display simulations at final stage $75\Delta t$, and when compared to Figure 4.10 there are definite changes in the migration of cells in population c_2, Figure 4.20b, with pools of high cell distributions forming in different regions to that of Figure 4.10b. Here, the tumour boundary is remaining closer to the main body of cells, with degradation of the ECM occurring explicitly within the boundary, subfigures 4.20d-4.20e. The boundary of the tumour has expanded in a pattern consistent with the heterogeneity of the fibre phase 4.20e. Population c_1 has developed in a similar fashion to that in Figure 4.10, however cells in population c_2 have formed regions of high cell distributions around the entire boundary 4.20b. From these simulations we cannot strictly conclude which family and arrangement of fibre micro-domains gives the more aggressive spread of

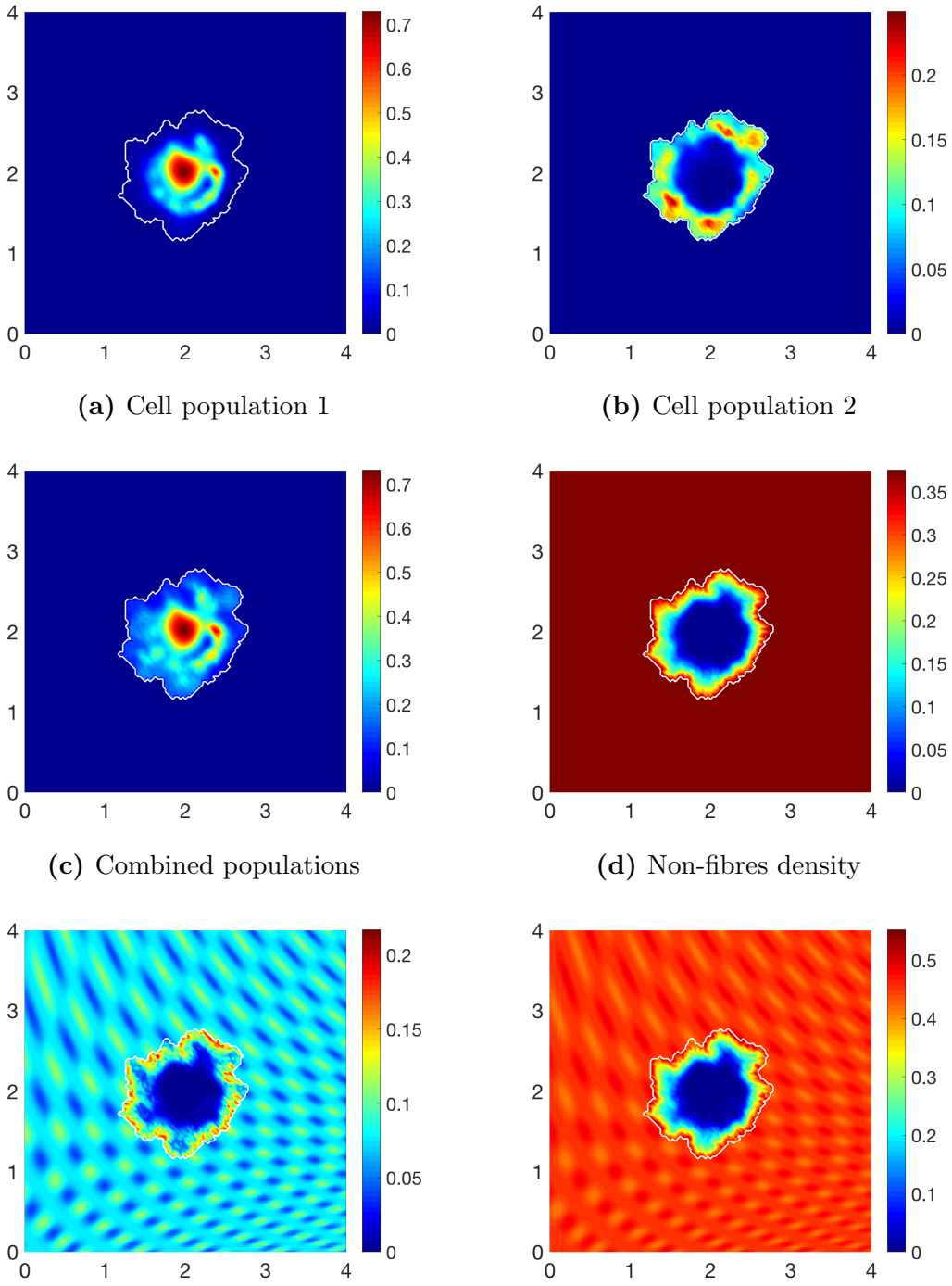

(a) Cell population 1

(b) Cell population 2

(c) Combined populations

(d) Non-fibres density

(e) Fibre density

(f) Combined ECM

Figure 4.20: Simulations at stage $50\Delta t$ with a homogeneous distribution of non-fibres and a random initial 15% heterogeneous distribution of fibres from the family of fibre paths P^2 with parameter set Σ_2.

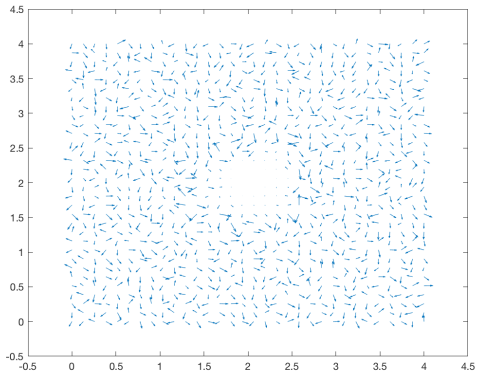

(a) 2D fibre plot

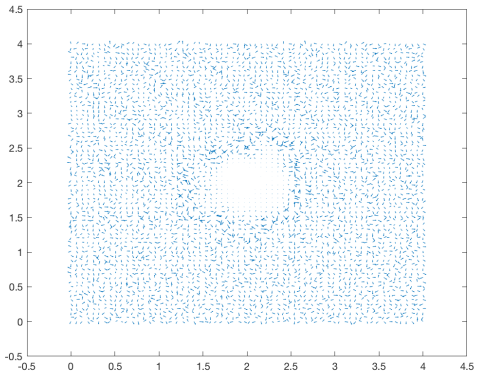

(b) 2D fibre plot

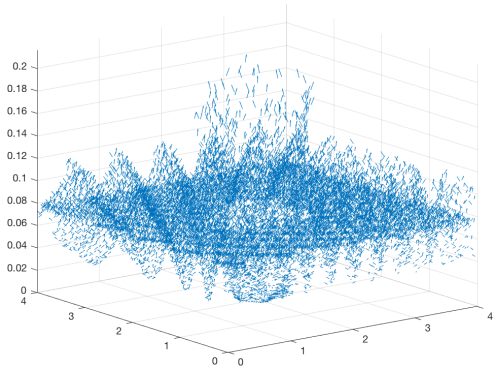

(c) 3D fibre plot

Figure 4.21: Simulations at stage $75\Delta t$ with a homogeneous distribution of the non-fibres and a different random initial 15% heterogeneous distribution of fibres.

cancer, however we can deduce that the initial placement of fibre micro-domains has a strong influence on the overall invasion of cancer, owing to the initial orientation of the fibres.

4.4.4 Heterogeneous two-phase ECM

We consider here a fully heterogeneous ECM, with the fibre phase taking 15% of the heterogeneous non-fibre phase, defined in (4.20). Figures 4.22-4.23 show simulations at final stage $70\Delta t$. Cell population c_1 continues to be confined to the centre of the domain showing little outward movement whilst exhibiting the highest distribution of cells noted throughout all previous simulations. Cell population c_2 has formed patches of high distributions of cells with these established in areas of very low to no ECM density, suggesting the abundance of physical space in these regions provides the easiest route of invasion. We again see the formation of small islands in the boundary over the lower density regions of ECM, similar to simulations in Figure 4.14. Overall the spread is larger than that when in the presence of a homogeneous component of ECM with 15% fibres, however it is smaller than when in the presence of 20% fibres, Figure 4.16. The tumour boundary is notable more lobular and consistent in its pattern with the pattern of the ECM, attributable to the heterogeneity of the entire matrix.

4.5 Discussion

We have presented a novel multiscale moving boundary model with dynamic fibre redistribution, first introduced in Chapter 3, which now includes a heterotypic cancer cell population, with two sub-populations, c_1 and c_2. This model was developed to explore both the random disposition of microscopic fibre distributions and the

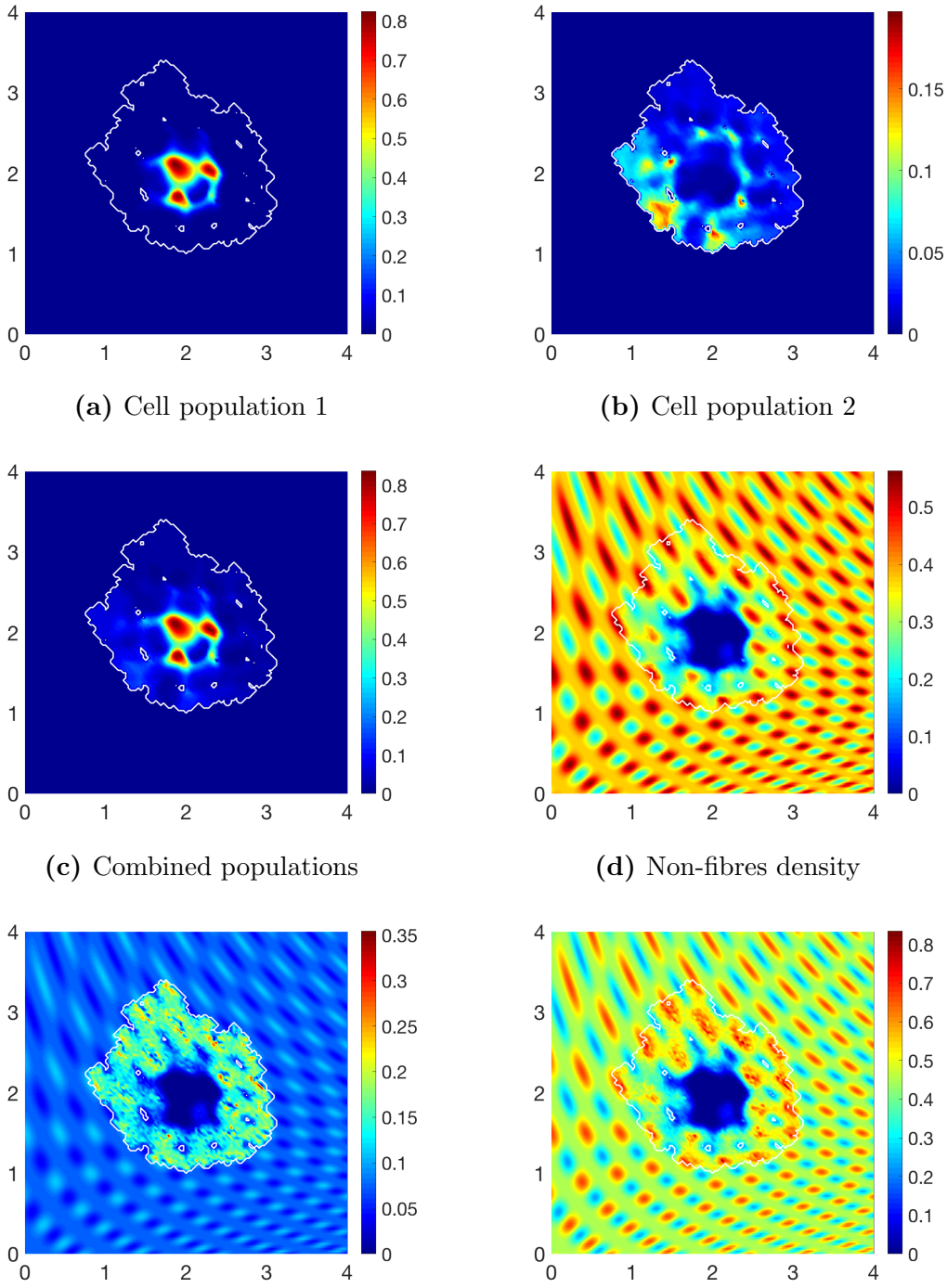

(a) Cell population 1

(b) Cell population 2

(c) Combined populations

(d) Non-fibres density

(e) Fibre density

(f) Combined ECM

Figure 4.22: Simulations at stage $70\Delta t$ with a heterogeneous distribution of non-fibres and a random initial 15% heterogeneous distribution of fibres with parameter set Σ_2.

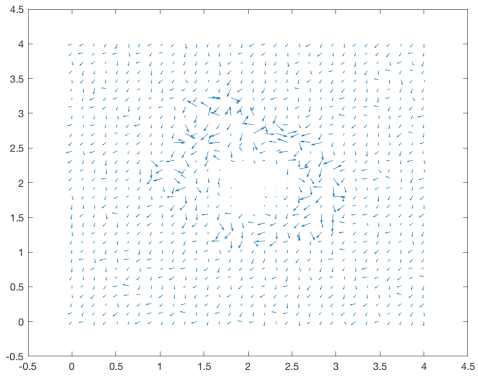

(a) 2D fibre plot

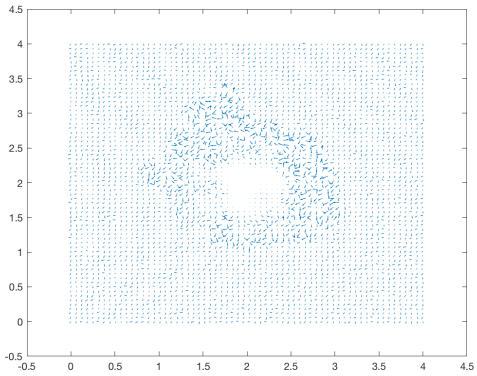

(b) 2D fibre plot

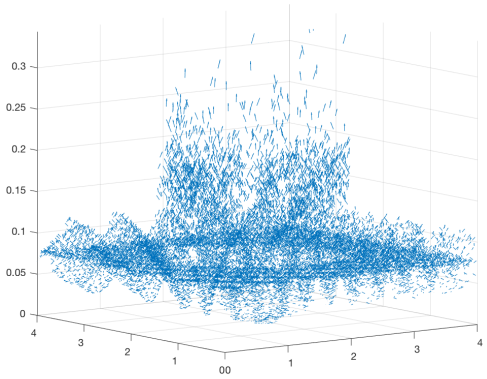

(c) 3D fibre plot

Figure 4.23: Simulations at stage $70\Delta t$ with a heterogeneous distribution of non-fibres and a random initial 15% heterogeneous distribution of fibres.

inclusion of a heterogeneous cancer cell population and their combined effects on the overall invasion pattern during tumour growth and local invasion of tissue. Paying attention in the first instance to the heterogeneous cell population, we introduced a secondary cell sub-population, mutated from the primary cell population, which holds a lower cell-cell adhesion rate and a higher affinity for cell-fibre adhesion. Mutations from the primary to secondary sub-population were irreversible, explored through a mutation rate dependent on the underlying ECM density. Focussing next on the fibre component of the ECM, we explored several scenarios; a homogeneous and heterogeneous macroscopic distribution of fibres, varying the initial ratio of macroscopic fibre distributions in relation to the non-fibre ECM phase, and finally the exploration of randomly allocated fibre micro-domains. The multiscale dynamics of the underlying fibre network were explored and modelled within a two-part multiscale model, where the micro-scale dynamics are connected to the macro-scale through a double feedback loop. We considered the macroscopic representations of the micro-fibres and their resulting effects on the macro-scale dynamics, in particular cellular adhesion, whilst at the same time allowing the distribution of both cancer cell sub-populations to cause macroscopic fibre degradation. In addition, through their spatial flux the cancer cells were able to influence the direction of microscopic fibre rearrangement. Finally, we include to this model the previously developed multiscale moving boundary framework developed in Chapter 2 that considers the effects of a heterogeneous cancer cell population and its combined contribution to the leading edge proteolytic MDE dynamics. Thus, the model proposed here combines two multiscale systems that contribute to the same tissue- (macro-) scale dynamics whilst having separate cell- (micro-) scale processes that are simultaneously connected via two double feedback loops. As in Chapter 3, the first multiscale model gives the cell-scale fibre rearrangement process within the tumour region, and the

second multi-scale system describes the MDE proteolytic activity within a cell-scale neighbourhood of the tumour boundary.

To accommodate a heterogeneous cancer cell population, we adapt the macro-scale dynamics introduced in Chapter 3 to include a similar set of dynamics for a second cell sub-population which has been mutated from the primary cell population. In doing so, we adjust the term for cellular adhesion to include both cell sub-populations allowing for different parameters for each population (Domschke et al., 2014), implementing a weaker self-adhesion coefficient and a higher rate of cell-fibre adhesion for the mutated population to promote migration and thus promote the overall invasive capabilities of the tumour. The heterogeneous cancer cell population is then incorporated within the micro-scale dynamics of both multi-scale systems. Firstly, it has influence in determining the source term for MDEs within each cell-scale neighbourhood, with the mutated population inducing a higher amount of MDEs than the primary cell population. Secondly, the distribution and spatial flux of cancer cells that determines the direction of micro-fibre redistribution is now taken as the combined cancer cell distributions and the addition of the spatial fluxes of both populations. Finally, we use the combined cell distributions to contribute equally to the degradation of both the fibre and non-fibre components of the ECM.

Comparing with results from the previous framework developed in Chapter 3 that describes the local invasion of a single population of tumour cells in the presence of a macroscopically homogeneous fibre network, we witness some similarities with our simulations. In the presence of a heterogeneous component of the ECM (fibre or non-fibre phase) we observe a fingering, lobular pattern of invasion, where the cells first flood the low density cavities and proceed to engulf the higher density regions on their route of invasion. In the presence of a homogeneous non-fibre ECM phase and an initially homogeneous fibre phase, we see the boundary of the

tumour stray from the symmetric invasion witnessed in Chapter 2, implying that the underlying fibre network indeed plays a role in tumour invasion. Increasing the initial macroscopic fibre density by only 5% from 15% to 20% of the non-fibre ECM phase results in a very fast growing tumour that almost takes over the entire domain. This solidifies the reasoning that the fibre network plays a key role in the local invasion of cancer. Additionally, we have explored this model with two sets of randomly placed micro-fibre domains. Comparing the simulations of each family of micro-domains, particularly under the presence of both components of the ECM being initially homogeneous, the pattern of the sub-populations of cancer cells is affected. The initial orientation of the fibres has influenced the migration of the cells, most obviously observed within population c_2, where the cell-fibre adhesion rate is higher. As expected, this concludes that the orientation of the fibres is key during tumour growth and development, particularly at the initial stage of invasion.

Looking forward, this modelling framework allows for the opportunity to deeper integrate both multi-scale models; incorporating the micro-scale fibre network within the MDE micro-scale neighbourhoods by investigating the cell-scale effects of MDEs on the fibres, i.e., the degradation/slicing of the fibres by the matrix metalloproteinases (MMPs) such as the freely moving MMP-2 and the membrane-bound MT1-MMP molecules. The exploration of TACS (tumour associated collagen signatures) could provide important information of the severity of the tumour. Biological experiments have shown that TACS-3, which is characterised by bundles of straightened and aligned collagen fibres that are orientated perpendicular to the tumour cells provide the poorest prognosis for patients (Provenzano et al., 2008), whilst tumours in a TACS-2 environment, where the angle between cells and the fibres are between $0^\circ - 30^\circ$, have been shown to provide an environment in which tumour progression is slower (Conklin et al., 2011).

Chapter 5

Cell-scale degradation of peritumoural extracellular matrix fibre network and its role within tissue-scale cancer invasion

Aims and novelty: In this Chapter we explore the interaction between the MDE boundary micro-dynamics and the peritumoural mass distribution of micro-fibres. To that end we investigate the link between underlying fibre distributions and the source and diffusion of MDEs at the tumour's leading edge, while also considering the resulting peritumoural degradation of micro-fibres by the MDEs. This Chapter proposes a novel extension to the model introduced in Chapter 3 to consider firstly, a homogeneous cancer cell population and secondly a heterogeneous cancer cell population as described in Chapter 4.

5.1 Introduction

The local invasion of cancer is, in the first instance, stimulated by the secretion of matrix-degrading enzymes (MDEs) that degrade the surrounding extracellular matrix. In particular, the subfamily of proteolytic enzymes, MMPs, are responsible for the degradation and remodelling of the main constituent of the ECM, the structural cross-linked collagen type I. The degradation of these dense fibres creates paths through which the cancer cells can migrate and thus promote tumour progression. During the MMP degradation cascade, the membrane tethered MMP, MT1-MMP, is the first proteolytic enzyme to interact with the ECM. This MMP exhibits strong collagenolytic capabilities in which they are able to cleave the cross-linked collagen type I fibres and break them into shorter, soluble fibres. Additionally, MT1-MMPs have the ability to cleave proMMP-2 molecules into active MMP-2 molecules which are unbounded from the cell membrane allowing for proteolytic activity outside the tumour region. This freely diffusible MMP displays weak collagenolytic yet strong gelatinolytic capabilities (Tam et al., 2004). Therefore MMP-2 molecules are able to degrade the un-cross-linked variants of collagen type I, thus they are restricted to only acting on the cleaved fibrils and cannot degrade cross-linked fibres. There are some advantages and disadvantages to both types of MMPs. MT1-MMP molecules can overcome high density regions of collagen type I, particularly the cross-linked fibres, however it does not degrade the collagen, rather cleaving the fibres into smaller fibrils. On the other hand, MMP-2 cannot degrade the dense cross-linked fibres, but can degrade the smaller, soluble fibrils within the peritumoural region (Van Doren, 2015). Consequently, these two MMPs work in harmony with one another for successful invasion of tissue.

Previously, we have considered the microscopic fibres to have influence over the direction of migration by the introduction of a cell-fibre adhesion term, with the

fibres subject to macroscopic degradation at a rate correlating to the distribution of cancer cells. We now aim to include the microscopic fibre distributions within the MDE moving boundary micro-dynamics by incorporating the behaviour and action of the MMP molecules, MT1-MMP and MMP-2, with respect to the peritumoural fibres. Since MT1-MMP are attached to the cell membrane, they do not diffuse into the surrounding environment but instead travel in the direction of the cancer cells. The level of MT1-MMP molecules present on the cell membrane is dependent on both the distribution of cancer cells and the underlying collagen density (Zigrino et al., 2001). This is turn gives the level of MMP-2 molecules present in the ECM, and it is the dynamics of these molecules we are interested in. Thus, we can consider the effects of fibre rearrangement to be the activity of the membrane bound molecule MT1-MMP, whilst the degradation of fibres occurs due to the travelling front of the distribution of freely moving MMP-2 molecules.

In this chapter, we focus on the dynamics of the MMPs and their interaction with the fibres at the tumour interface, firstly by considering the relationship between the distribution of fibres and MMP migration and the resulting effects on boundary relocation within the moving boundary multiscale system, and secondly by incorporating the dynamics of matrix-degrading enzymes at the tumour boundary into the microscopic degradation of fibres.

The content of this chapter has been fully explored in the article Shuttleworth and Trucu (2019a).

5.2 The mathematical model

Here we will build upon the two-part multiscale model introduced and developed in Chapter 3 that investigates cancer invasion within a heterogeneous ECM. We will revisit the multi-component structure of the ECM and macroscopic tumour

dynamics for one cancer cell population whilst adapting the model to include full integration between both the MDE and fibre micro-scales.

Using the same terminology as in previous Chapters, let us denote the support of the invading tumour region as $\Omega(t_0)$, and assume this evolves in the maximal reference tissue cube $Y \in \mathbb{R}^N$ for $N = 2, 3$, centred at the origin of the space. At any spatio-temporal node $(x, t) \in \Omega(t_0) \times [0, T]$, we consider the tumour to be comprised of a cancer cell population $c(x, t)$, integrated within a multiphase ECM density, $v(x, t) = l(x, t) + F(x, t)$. Furthermore, since this chapter builds on the modelling developed in Shuttleworth and Trucu (2019c) and Chapter 3, let us start this section by recalling the key details of the framework terminology that we introduced there. Specifically, the heterogeneous ECM is regarded as comprising of a *fibres* component and *non-fibres* soluble component. We consider the *non-fibres* ECM phase to include all non-fibre components of the ECM, i.e., elastin, laminins, fibroblasts, etc., whilst the *fibres* ECM phase concerns all fibrous proteins such as collagen and fibronectin within the matrix. For completion, the ECM multiscale structure and functionality alongside the involved macro-dynamics will be detailed in the following two subsections.

5.2.1 The heterogeneous ECM and its contribution to the tissue dynamics

At any macro-position $x \in \Omega(t_0)$, the ECM-fibre phase can be represented through a macro-scale vector field $\theta_f(x, t)$ that captures not only the macroscopic distribution of fibres $F(x, t)$, but also their naturally arising macroscopic orientation that is induced by their mass distribution of micro-fibres $f(z, t)$, previously defined in Chapter 3, (3.4), distributed on the microscale domain $Y(x)$ centred at the given macroscopic point x. An example of the pattern of micro-fibres $f(z, t),\ \forall z \in \delta Y(x)$

is shown schematically in Figure 5.1 and defined in Appendix D.1.

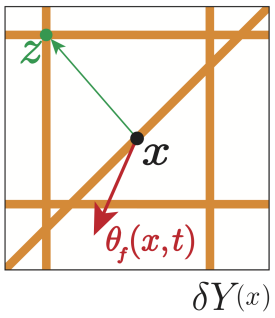

Figure 5.1: Schematic of the micro-fibres distribution on the micro-domain $\delta Y(x)$, centred at x, with the barycentral position vector $\overrightarrow{x\,z} := z - x$ pointing towards an arbitrary micro-location $z \in \delta Y(x)$ illustrated by the green arrow and the naturally arising macroscopic fibre orientation $\theta_f(x,t)$ is highlighted by the red arrow.

In brief, while referring to its full derivation presented in Chapter 3, the naturally generated revolving barycentral orientation $\theta_{f,\delta Y(x)}(x,t)$ associated with $\delta Y(x)$ is given by the *Bochner-mean-value* of the position vectors function $\delta Y(x) \ni z \mapsto z - x \in \mathbb{R}^N$ with respect to the density measure $f(z,t)\lambda(\cdot)$, where $\lambda(\cdot)$ is the usual Lebesgue measure (see Yosida (1980)), and so this is expressed mathematically as:

$$\theta_{f,\delta Y(x)}(x,t) = \frac{\int\limits_{\delta Y(x)} f(z,t)(z-x)dz}{\int\limits_{\delta Y(x)} f(z,t)dz}. \tag{5.1}$$

Following on, at any spatio-temporal node (x,t), this revolving barycentral orientation $\theta_{f,\delta Y(x)}(x,t)$ induces the naturally arising macroscopic fibre orientation vector field representation that is defined as

$$\theta_f(x,t) = \frac{1}{\lambda(\delta Y(x))} \int_{\delta Y(x)} f(z,t)\; dz \cdot \frac{\theta_{f,\delta Y(x)}(x,t)}{||\theta_{f,\delta Y(x)}(x,t)||_2}. \tag{5.2}$$

in which macroscopic mean-value fibre representation at any (x,t) is given by the

Euclidean magnitude of $\theta_f(x,t)$, namely,

$$F(x,t) := ||\theta_f(x,t)||_2. \tag{5.3}$$

Thus, denoting the spatial distribution of the non-fibre ECM phase distribution $l(x,t)$, the total ECM distributed at any spatio-temporal node (x,t) is therefore given by $v(x,t) = l(x,t) + F(x,t)$.

5.2.2 Macro-scale dynamics

As in Chapter 3, we focus first on one cancer cell population. Thus, using the precise terminology introduced in Chapter 3, let us recall here the mathematical model for dynamics of the cancer cell population (3.14), the macroscopic fibres phase (3.20), and the non-fibres phase (3.21), namely:

$$\frac{\partial c}{\partial t} = \underbrace{\nabla \cdot D_1 \nabla c}_{\text{random motility}} \underbrace{- \nabla \cdot c\mathcal{A}(x,t,\mathbf{u}(\cdot,t),\theta_f(\cdot,t))}_{\text{cell adhesion}} + \underbrace{\mu_1 c(1-\rho(\mathbf{u}))^+}_{\text{proliferation}} \tag{5.4}$$

$$\frac{dF}{dt} = \underbrace{-\gamma_1 cF}_{\text{degradation}}, \tag{5.5}$$

$$\frac{dl}{dt} = \underbrace{-\gamma_2 cl}_{\text{degradation}}, \tag{5.6}$$

which, besides the other usual terms, involves the non-local flux $\mathcal{A}(x,t,\mathbf{u}(\cdot,t),\theta_f(\cdot,t))$ describing the influence of the adhesion processes accounting for both cell-cell and cell-matrix adhesion (with cell-matrix adhesion accounting for both cell-fibre and cell-non-fibre adhesion) upon the spatial movement of the cancer cells defined in (3.15).

5.3 Microscopic fibre rearrangement on the topological closure of the invading tumour

During the macro-dynamics, as the cancer cells invade the surrounding tissue they have the ability to push the fibres in the direction of invasion and rearrange the micro-fibre mass distributions, thereby reorienting the macro-fibres direction, a process that was introduced in Chapter 3 and will be briefly revisited here. In this context, as described in full details in Chapter 3, under the influence of the rearrangement vector force $r(\delta Y(x), t)$ induced by the cancer cell population spatial flux, and given by (3.23), an appropriate level of micro-fibres mass $f(z, t)$, given by (3.4), distributed at any arbitrary point $z \in \delta Y(x)$ will undergo a spatial movement towards a new position

$$z^* := z + \nu_{_{\delta Y(x)}}(z, t),$$

where the relocation direction and magnitude is given by (3.26) and recalled here,

$$\nu_{_{\delta Y(x)}}(z, t) = (x_{\text{dir}}(z) + r(\delta Y(x), t)) \cdot \frac{f(z, t)(f_{\max} - f(z, t))}{f^* + ||r(\delta Y(x)) - x_{\text{dir}}(z)||_2} \cdot \chi_{_{\{f(\cdot,t)>0\}}}, \quad (5.7)$$

Thus, the macroscopic cancer cell population flux causes significant changes in the micro-structure distribution of the fibres, leading to *on-the-fly* changes to its spatial distribution and orientation on the topological closure of the invading tumour, and this way causing changes in their contribution to the macro-dynamics. However, it is important to recall that, whether in the bulk of the tumour or at the leading edge, a key part in the complex interactions of the cancer cells with the surrounding fibre network is played by the cell-scale action of the MMP molecules that remain attached to the surface of the cells. These membrane-tethered MMPs, MT1-MMPs, are actually the ones that are responsible for the cleaving of type I

collagen, splitting the collagen fibres into smaller, soluble fibrils (Wolf et al., 2013) in an effort to free space and create better paths of invasion for the cancer cells, an aspect that has been so far implicitly captured in Chapters 3 and 4 only through the macroscopic degradation of macro-scale fibre magnitudes formalised in equations (3.20) and (4.11) on the bulk of the invading tumour $\Omega(t)$. In the following we will complement this approach by addressing explicitly at micro-scale this complicated cell-scale action of MMPs on the peritumoural fibres at the leading edge of the tumour.

5.4 The micro-scale boundary dynamics and its double feedback link to macro-dynamics

To incorporate the dynamics of peritumoural micro-scale fibres with the MDE micro-dynamics at the tumour invasive edge, let us start by exploring the influence of the macro-fibre distributions on the emergence of a cell-scale molecular source of MDEs at the tumour interface. This will effectively enhance the *top-down* macro-micro link derived and introduced in Trucu et al. (2013) (and which we considered so far in all the previous Chapters) for the boundary micro-dynamics and in return will influence the *bottom-up* feedback link to macro-dynamics.

The top-down link As discussed previously, the expansion of the tumour boundary is dependent on the peritumoural degradation of ECM by the matrix-degrading enzymes (MDEs). However, the secretion of MDEs induced by the distribution of cancer cells in the outer proliferating rim is dependent upon the structure of the ECM and in particular upon the fibre distribution. Indeed, in the presence of a high distribution of ECM fibres, the cancer cells exhibit a strong rate of MT1-MMP se-

cretion, which in turn leads to an increase in the activation of proMMP-2 molecules (Thomson et al., 1994; Ruangpanit et al., 2001; Zigrino et al., 2001). Thus, since in this emerging MT1-MMP/MMP-2 cascade, the secretion rate of MT1-MMP correlates directly to the amount of MMP-2 molecules, we obtain therefore that the presence of the ECM fibres enhances the production of the MMP-2 molecules that are then released at the tumour boundary.

Thus, the MMPs source at each $y \in \epsilon Y \cap \Omega(t_0)$ arises as a collective contribution of the cancer cells within the outer proliferating rim which are further enhanced by the presence of ECM fibres, and therefore this can be mathematically expressed as

$$\begin{aligned} &1. \quad g_{\epsilon Y}(y,\tau) = \frac{\int\limits_{\mathbf{B}(y,\gamma)\cap\Omega(t_0)} \alpha c(x,t_0+\tau)\ \widetilde{F}(x,t_0+\tau)\ dx}{\widetilde{F}\cdot\lambda(\mathbf{B}(y,\gamma)\cap\Omega(t_0))}, \quad y \in \epsilon Y \cap \Omega(t_0), \\ &2. \quad g_{\epsilon Y}(y,\tau) = 0, \quad y \in \epsilon Y \setminus \big(\Omega(t_0) + \{y \in Y |\ ||y||_2 < \gamma\}\big), \end{aligned} \tag{5.8}$$

where γ represents the maximum thickness of the outer proliferating rim, $\mathbf{B}(y,\gamma) := \{\xi \in Y |\ \parallel y-\xi \parallel_\infty \leq \gamma\}$ and α is an MMP secretion rate for the cancer cell population. Furthermore, the function $\widetilde{F}(x,t+\tau) := 1 + F(x,t)$, $\forall\, t > 0$ explores the spatially distributed enhancement of the source of MMPs produced by the cancer cells that is enabled through the presence of fibres (Zigrino et al., 2001) (i.e., a higher distribution of fibres inducing a greater number of MMP-2 molecules). Finally, $\widetilde{F}\cdot\lambda$ represents the underlying fibre density measure that is defined by

$$\widetilde{F}\cdot\lambda(G) := \int\limits_G \widetilde{F}(x,t_0+\tau)\ dx, \quad G \in \Sigma(Y),$$

where λ is the standard Lebesgue measure on $\mathbb{R}^2$, and G is a nonempty Borel subset set of Y, i.e., $G \in \Sigma(Y)$, with $\Sigma(Y)$ representing the Borel σ-algebra on Y.

In the presence of this source, on any micro-domain ϵY, a cross-interface MMP-2 diffusive transport takes place, and as the MMP-2 find it easier to exercise their random movement in regions of lower micro-fibres density, the diffusion rate is micro-fibre density dependent, and therefore this spatio-temporal micro-dynamics can be mathematically formulated as

$$\frac{\partial m}{\partial \tau} = \underbrace{\nabla \cdot (D_m(f) \nabla m)}_{\text{diffusion}} + \underbrace{g_{\epsilon Y}(y, \tau)}_{\text{source term}}, \quad y \in \epsilon Y, \quad \tau \in [0, \Delta t] \tag{5.9}$$

with the fibre-dependent diffusion coefficient

$$D_m(f) = \frac{D}{1 + \alpha_m \tilde{f}(y, t_0 + \tau)},$$

where D is the baseline diffusion rate and α_m being a *"slowing down" constant factor* induced by the presence of the micro-fibres density $\tilde{f}(y, t_0 + \tau)$, which is defined as follows. Considering first the micro-scale set-valued mapping that surveys the number of points z corresponding to up to four fibres micro-domains $\delta Y(x)$ that represent the same micro-position y, namely

$$\epsilon Y \ni y \longmapsto z(y) \in \bigcup_{x \in Y} \delta Y(x)$$

is given by:

$z(y)$ is the set of the micro-spatial points within up to four $\delta Y(x)(y)$
where
each selected $\delta Y(x)(y)$ is a micro-cube within $\bigcup_{x \in Y} \delta Y(x)$
with the property that this contains $y \in \epsilon Y$
(please see Figure 5.2 for an illustration of this situation). (5.10)

we have that

$$\tilde{f}(y, t_0+\tau) := \begin{cases} f(z(y), t_0+\tau) & if \quad card(z(y)) = 1; \\ \frac{1}{card(z(y))} \sum\limits_{\zeta \in z(y)} f(\zeta, t_0+\tau) & if \quad card(z(y)) > 1. \end{cases} \tag{5.11}$$

The bottom-up link During their micro-dynamics, the MMPs diffuse into the surrounding ECM and it is the pattern of their advancing spatial distribution that control the degradation of the peritumoural ECM captured within each micro-domain ϵY. This degradation ultimately leads to the movement of the tumour boundary, whereby a movement direction $\eta_{\epsilon Y}$ and displacement magnitude $\xi_{\epsilon Y}$, as detailed in Chapter 2 are derived from the pattern of ECM degradation in each micro-cube ϵY (and for full derivation we refer the reader to Trucu et al. (2013)). The microscopic movement of the boundary is represented at the macro-scale through the movement from the boundary midpoint $x^*_{\epsilon Y}$ to a new spatial position $\widetilde{x^*_{\epsilon Y}}$. Thus, although the *bottom-up* link of the model is much akin to previous Chapters, the specific context in which the presence of micro-fibres distribution enables on one hand an enhanced source of MMPs and on the other hand acts as an impediment for their random motility, the MMP micro-dynamics within the peritumoural region of the tumour domain $\Omega(t_0)$ incorporates now these important aspects, ultimately resulting in an improved estimate for the macroscopic boundary movement characteristics (i.e., encapsulated by the movement direction $\eta_{\epsilon Y}$ and displacement magnitude $\xi_{\epsilon Y}$). This crucial micro-scale-induced boundary relocation is then translated back to the macro-scale, resulting in an expanded tumour domain $\Omega(t_0 + \Delta t)$ on which the multiscale dynamics is continued (as detailed in Chapter 2 and in Trucu et al. (2013)).

5.4.1 Microscopic fibre degradation

Given the proteolytic properties of the MMPs, the cell-scale cross-interface MMP-2 micro-dynamics will result in a direct peritumoural ECM degradation, whose pattern not only depends on the amount of MMP-2 transported at a given location y within a given micro-domain ϵY, but also on the existing ECM micro-fibres spatial distribution at y. To address this micro-scales interaction that takes place between the MMP-2 cross-interface transport and micro-fibres within any given micro-domain ϵY, we consider that the spatial patterns of micro-fibres distributions that are aligned with the MMP-2 flux $\nabla m(\cdot, t_0+\tau)$ suffer less degradation than those that are positioned orthogonal to it. Thus, for any fibre micro-domain $\delta Y(x)$ that has non-empty intersection with ϵY, by denoting $\Phi_{fm}(\cdot,\cdot) : \delta Y(x) \times [0, \Delta t] \to [0, \pi]$ the function that explores these emerging angles, given by

$$\Phi_{fm}(z,\tau)=\begin{cases} \arccos\left(\frac{<\nabla m(z,\tau),\nabla f(z,t_0+\tau)>}{||\nabla m(z,\tau)||_2 ||\nabla f(z,t_0+\tau)||_2}\right) \chi_{\delta Y(x)\cap\epsilon Y}(z), & if \quad \|\nabla f(z,t_0+\tau)\|_2 > 0, \\ \frac{\pi}{2}\chi_{\delta Y(x)\cap\epsilon Y}(z), & if \quad \|\nabla f(z,t_0+\tau)\|_2 = 0. \end{cases} \tag{5.12}$$

where $\chi_{\delta Y(x)\cap\epsilon Y}(\cdot)$ is the usual characteristic function of $\delta Y(x) \cap \epsilon Y$.

The strength of the micro-fibre degradation rate is influenced by their degree of alignment with the flux of the MMPs, which is explored by the angle $\Phi_{fm}(z,\tau)$ at which the flux of the MMP-2 molecules act upon the mass distribution of micro-fibres $f(z, t_0 + \tau)$ at each micro-position z, and so this can therefore be mathematically formalised as

$$D_g(z,\tau) := d_f \cdot \exp\left(1 - \frac{1}{1-(1-\Phi(z,\tau))^2}\right). \tag{5.13}$$

where d_f is a non-negative degradation constant, and the function $\Phi(\cdot,\cdot)$

$$\Phi(z,\tau) = \left|\frac{\Phi_{fm}(z,\tau)}{\Phi_{\max}}\right|,$$

represents the influence of the collision angle relative to the maximum angle $\Phi_{\max} := \frac{\pi}{2}$ where the highest rate of degradation will occur (i.e., when the flux of MMPs is perpendicular upon the micro-fibres mass). Thus, the micro-fibre dynamics at location z in the δ-sized micro-scale can be mathematically represented as

$$\frac{\partial f}{\partial \tau} = -D_g(z,\tau)\cdot f(z,t_0{+}\tau), \qquad z \in \delta Y,\ \tau \in [0,\Delta t]. \tag{5.14}$$

5.5 Summary of model

The tissue- and cell–scale dynamics of the new multiscale moving-boundary model proposed here, can therefore be summarised as:

Macro-scale dynamics:

$$\begin{aligned}
\frac{\partial c}{\partial t} &= \nabla\cdot[D_1\nabla c - c\mathcal{A}(t,x,\mathbf{u}(\cdot,t),\theta_f(\cdot,t))] + \mu_1 c(1-\rho(\mathbf{u}))^+,\\
\frac{dF}{dt} &= -\gamma_1 cF,\\
\frac{dl}{dt} &= -\gamma_2 cl,
\end{aligned} \tag{5.15a}$$

Micro-scale boundary MMP-2-dynamics interacting with peritumoural micro-fibres:

$$\begin{aligned}
\frac{\partial m}{\partial \tau} &= \nabla\cdot(D_m(f)\nabla m) + g_{\epsilon Y}(y,\tau), \quad y \in \epsilon Y,\ \tau \in [0,\Delta t],\\
\frac{\partial f}{\partial \tau} &= -D_g(z,\tau)\cdot f(z,t_0{+}\tau), \quad z \in \delta Y,\ \tau \in [0,\Delta t].
\end{aligned} \tag{5.15b}$$

The macro- and micro-dynamics summarised in (5.15) aggregates two interconnected multiscale frameworks that describe the interactions between two independent micro-scale systems and share the same macro-scale tissue level dynamics (summarised in (5.15a)) that is linked to the two micro-dynamics through two double

feedback loops, as established and detailed in Chapter 3.

While the macro-scale tissue dynamics describe the evolution of the spatial distribution of cancer cells and both the non-fibres and macro-fibres ECM phase, the micro-scale part of the first multiscale system governs the dynamic rearrangement of fibres. Specifically, the rearrangement of the fibres emerges as a consequence of the acting macro-scale flux of the cancer cells upon the mass distribution of micro-fibres distributed within micro-domains $\delta Y(x)$ which are centred at any given macroscopic point $x \in Y$. The redistributed micro-fibres naturally yield a new macroscopic vector field representation of the newly oriented fibres that will have a cascade influence upon adhesion processes the cancer cell population tissue-scale dynamics biasing their migration, as detailed in Chapter 3 and Shuttleworth and Trucu (2019c).

The second multiscale system involved in this modelling brings into the picture contribution of the micro-scale proteolytic dynamics occurring in a cell-scale neighbourhood of the tumour interface. Here we take forward the multiscale moving boundary approach initially introduced in Trucu et al. (2013) and recapitulated in Chapter 3, by considering the influence that the oriented macro-scale ECM fibres has upon the emergence of the micro-scale MMP-2 source and at the same time exploring the explicit cell-sale interaction that takes place between the MMP-2 spatial flux and the mass distribution of micro-fibres at micro-scale which results in fibre degradation, summarised in (5.15b), notably triggering changes in the macroscopic fibres orientation. Consequently, these leading edge MMPs dynamics instigate a change in the position of the tissue-scale tumour boundary that corresponds to the pattern of peritumoural ECM degradation, this way allowing the macro-dynamics to continue on the newly enlarged tumour region and thus the invasion process continues.

5.6 Numerical approaches and initial conditions for computations

Expanding on the multiscale moving boundary framework developed in Chapter 3, building on the model initially introduced in Trucu et al. (2013), we developed a new modelling and computational approach to address specifically the cell-scale peritumoural interaction between the MDE and the micro-fibres mass distributions at micro-scale. Specifically, we explore the link between fibre distribution and MMP density at the tumour interface, in addition to the MMP induced micro-fibre degradation at the cell-scale.

5.6.1 Brief description of the numerical approach

To address the tumour macro-dynamics, we use the novel predictor-corrector method developed in Chapter 3, and fully defined in Shuttleworth and Trucu (2019c), that accounts for the complexity of the cancer dynamics. For this, we consider a uniform spatial mesh of size $h = 0.03125$, and we use a combination of central differences and mid-point methods to discretise the local spatial operators, while involving an off-grid approach (introduced and detailed in Chapter 3) for the calculation of the non-local adhesion terms (that enable the adhesive flux) at each spatio-temporal node.

Furthermore, to obtain the microscopic boundary relocation described in Chapter 2, we explore the *top-down* and *bottom-up* link, using a new finite difference approach for computing the MMP micro-dynamics occurring on the bundle of boundary micro-domains $\{\epsilon Y\}_{\epsilon Y \in \mathcal{P}}$ over the time interval $[\tau_0 + \Delta t]$. Hence, while considering a time discretisation into p uniformly distributed time steps, i.e., $\delta t = \frac{\Delta t}{p}$, each micro-cube ϵY is also discretised uniformly, using a spatial mesh of size h_ϵ,

i.e., $\Delta x_\epsilon = \Delta y_\epsilon = h_\epsilon$. Therefore, to discretise the reaction-diffusion equation (5.9), we start by addressing the spatially discretised source term induced by the cancer cell and fibre distribution (5.8) in the way it was described in Trucu et al. (2013). Then, to solve the spatio-temporal dynamics in (5.9), we develop a similar predictor-corrector method using trapezoidal corrector for the time marching, while for the spatial operators involved we use again a combination of mid-points and central differences, which in this context are given by

$$\begin{aligned} \nabla \cdot [\nabla m]^n_{i,j} &= \mathrm{div}[\nabla m]^n_{i,j} \\ &\simeq \frac{[m_x]^n_{i+\frac{1}{2},j} - [m_x]^n_{i-\frac{1}{2},j}}{\Delta x_\epsilon} + \frac{[m_y]^n_{i,j+\frac{1}{2}} - [m_y]^n_{i,j-\frac{1}{2}}}{\Delta y_\epsilon} \end{aligned} \tag{5.16}$$

where

$$\begin{cases} [m_y]^n_{i,j+\frac{1}{2}} := \frac{m^n_{i,j+1} - m^n_{i,j}}{\Delta y_\epsilon} \\ [m_y]^n_{i,j-\frac{1}{2}} := \frac{m^n_{i,j} - m^n_{i,j-1}}{\Delta y_\epsilon} \\ [m_x]^n_{i+\frac{1}{2},j} := \frac{m^n_{i+1,j} - m^n_{i,j}}{\Delta x_\epsilon} \\ [m_x]^n_{i-\frac{1}{2},j} := \frac{m^n_{i,j} - m^n_{i-1,j}}{\Delta x_\epsilon} \end{cases}$$

with $n = 0, \ldots, p$ and $i = 1, \ldots, q$, $j = 1, \ldots, q$ representing the indices for the y- and x-directions, respectively. Finally, important for capturing the degradation of the mass distribution of peritumoural micro-fibres at micro-scale, we use bilinear shape functions on square elements (Hughes, 1987) to appropriately interpolate the solutions and the associated fluxes of the MMP-2 micro-dynamics in the eventually overlapping regions of their ϵYs boundary micro-domains. This way the appropriate MMP-2 flux information is obtained at any micro-position z in any given intersecting $\delta Y(x)$ fibres micro-domains, i.e., within those fibres micro-domains $\delta Y(x)$ in the

peritumoural region for which

$$\text{there exists an } \epsilon Y \text{ micro-domain such that } \delta Y(x) \cap \epsilon Y \neq \emptyset.$$

as illustrated in Figure 5.2.

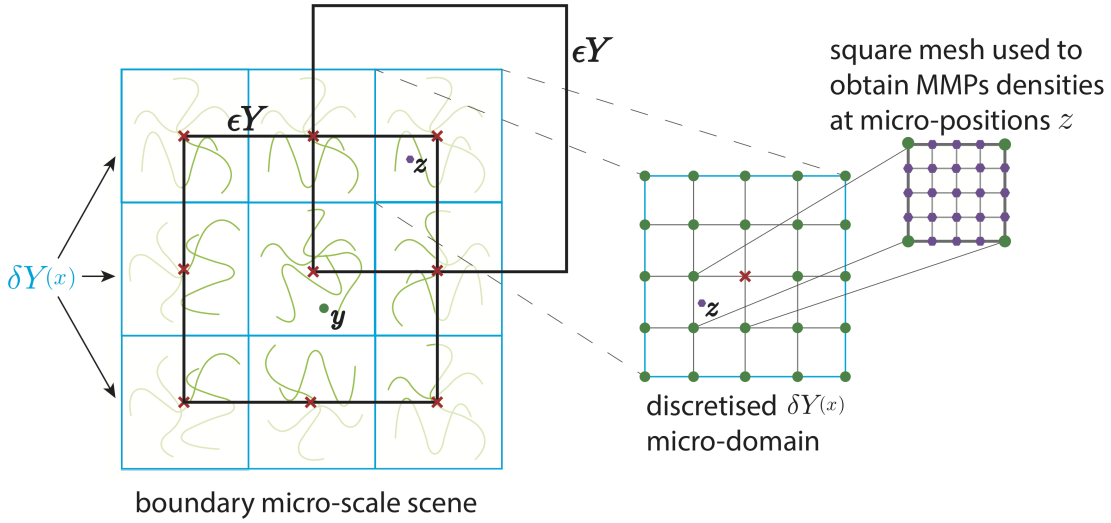

Symbol	Position	Density at position
⬢	fibre micro-position z	MMP-2 density found using bilinear shape functions in eventually overlapping regions of neighbouring ϵY micro-domains
●	MMP micro-position y	MMP-2 density
✖	tissue-scale position x (barycentral to fibre micro-domains $\delta Y(x)$)	cancer cell distribution

Figure 5.2: *Schematic illustrating the boundary micro-scales computational setting where the micro-dynamics is explored.*

All of the following simulations of the model have been performed on MATLAB.

5.6.2 Initial conditions used in computational simulations

We consider the same initial conditions as in Chapter 3, whereby we consider the initial cancer cell population $c(x,0)$ to occupy the region $\Omega(0) = \mathbf{B}((2,2),0.5)$ po-

sitioned in the centre of the tissue cube Y, given by (3.45) and shown in Figure 5.3. Moreover, we consider two different compositions of the non-fibres ECM phase, namely, a homogeneous distribution given by

$$l(x,0) = \min\{0.5, 1 - c(x,0)\} \tag{5.17}$$

and a heterogeneous distribution previously explored and detailed in Chapter 3,

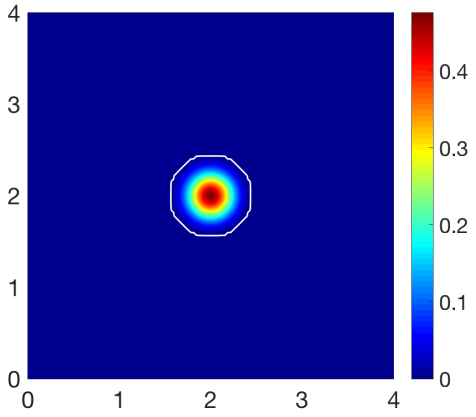

Figure 5.3: Initial condition for the cancer cell population $c(x,0)$, illustrating the tumour boundary by the white contour.

given by (4.20). These initial conditions are shown in Figure 5.4.

Finally, the fibres ECM phase will be initialised with both a homogeneous and heterogeneous macro-scale distribution. To this end, we first assume a random distribution of five pre-assigned micro-distributions containing patterns of five different micro-fibres (introduced in Chapter 4 and detailed in Appendix D.1) that are then randomly assigned onto $\delta Y(x) := x + \delta Y$. To calibrate the macro-fibre distributions, we use the initial conditions for the non-fibres ECM phase, for either a homogeneous or heterogeneous distribution, (5.17) and (4.20), respectively, taking a percentage p of the density of the non-fibres ECM at each spatio-temporal position x. This allows for the control of the maximal height of the micro-fibres in each $\delta Y(x)$, centred at

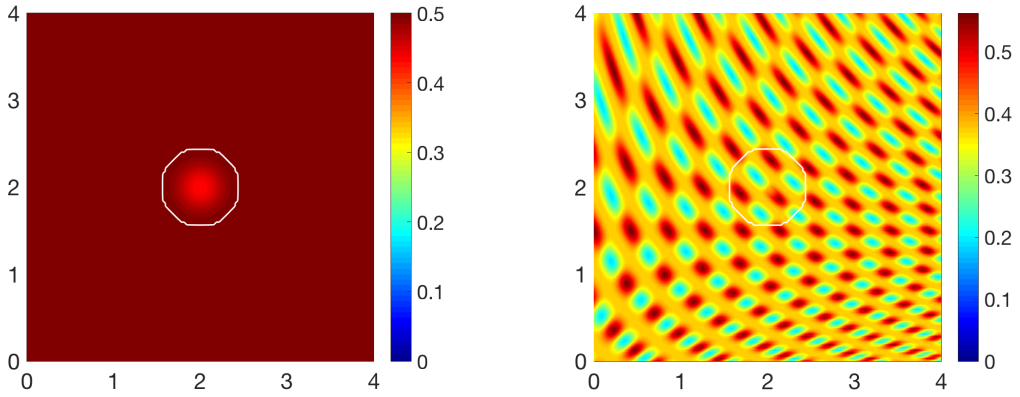

(a) initial cancer distribution **(b)** Initial ECM density

Figure 5.4: Initial conditions for the non-fibres ECM phase $l(x, 0)$, illustrating both a homogeneous (a) and heterogeneous (b) distribution.

macro-position x, so that the resulting macro-fibre distribution $F(x, 0)$ represents the percentage p, which here will be 15%, $p = 0.15$ or 20%, $p = 0.2$, with the latter representing a denser collagen structure.

5.7 Results

We first explore tumour invasion in the presence of a homogeneous ECM, where the non-fibres phase is the homogeneous distribution (5.17) with the fibres phase taking the percentage $p = 0.15$ of $l(x, 0)$. Using the parameter set Σ_1, Table 3.1, and the microscopic fibre degradation rate $d_f = 1$, we investigate the effects of micro-fibres degradation on tumour invasion. Figures 5.5, 5.6 and 5.7 display the evolution of the tumour at stages $\Delta 25t$, $\Delta 50t$ and $\Delta 75t$, respectively. Each figure contains the subfigures: (a) cancer cell population; (b) non-fibres ECM density; (c) macroscopic fibre distribution; vector fields of fibre orientations at two different resolutions, namely: (d) coarsened two-fold; and (f) coarsened four fold; and finally in (e) a 3D plot of the orientation of the complete ECM distribution $v(x, t) =$

$F(x,t) + l(x,t)$.

After $25\Delta t$ macro-stages, Figure 5.5, the boundary of the tumour has remained largely unchanged, subfigure 5.5a. Both the non-fibres and fibres ECM phase undergo degradation where the cancer cell distribution is highest, subfigures 5.5b, 5.5c, whilst minor degradation of the fibres has also occurred at the tumour boundary. The masses of micro-fibres have been rearranged such that the macroscopic orientation of fibres remains in line with the general fibre direction, subfigures 5.5d, 5.5f which points towards the origin of the space. However, there are some irregularities, particularly visible in subfigure 5.5f which has been magnified 4-fold, where the orientation of the fibres is mixed with some fibres realigned to near perpendicular of their original orientation. The cancer cells are pushing and rearranging the fibres in a direction opposite that of the initial fibre orientation, subfigure 5.5c, where a build up of fibre distributions occurs on the top right of the tumour region, situated close to the bulk of the tumour mass. As the tumour expands in size, the fibres are subsequently degraded during each stage of evolution, Figures 5.6 and 5.7, illustrating the simulations after $50\Delta t$ and $75\Delta t$, respectively. At stage $50\Delta t$, some cells have detached and formed a region encircling the initial bulk of tumour cells, subfigure 5.6a. The boundary of the tumour is expanding into the surrounding tissue, subfigure 5.6b, exhibiting a "rippling" effect along the proliferating edge caused by the fibre mediated movement of the boundary. The macroscopic fibre distribution becomes depressed as the cancer cells increase in distribution and thus increase in their degradative behaviour, subfigure 5.6c. Moving on to final stage $75\Delta t$, the tumour has largely increased in size and there are dense regions of cell distribution, subfigure 5.7a. The cells are gathering at the tumour interface, pulled in this direction by cell-fibre adhesion, following the direction of the fibres observed at the previous interval in subfigures 5.6d, 5.6f. The source of MMPs induced by the cancer

cells are very high in these dense areas, therefore the degradation of fibres is higher, subfigure 5.7c, witnessed here by the absence of macroscopic fibre distribution.

To investigate the effects of fibre distribution, whilst keeping the non-fibre ECM phase initially homogeneous (5.17), we initialise the fibre distribution $F(x, 0)$ with 15%, or $p = 0.15$, of the heterogeneous distribution (4.20). The simulations at stage $25\Delta t$, Figure 5.8, indicates that the initial pattern of fibres distribution is significant during the evolution of a tumour. The primary bulk of cancer cells have dispersed within the boundary into regions of high cell distribution, subfigure 5.8a, these coinciding with low density regions of the fibres ECM phase. The boundary of the tumour is remaining circular with small defects in the direction of the fibre orientation, subfigure 5.5f. The fibre magnitude density in subfigure 5.8c has small regions of high fibre distributions, again pushed outwards towards the proliferating edge. The fibre orientations are subject to an increased degree of realignment, subfigures 5.8d, 5.8f, attributed to the initially different levels of density at each macro-spatial position. Moreover, the fibres are realigned towards the higher density regions, where "frenzied" groups of fibre orientations can be observed. Moving on to simulations at stage $50\Delta t$, Figure 5.9, many of the behaviours previously observed at stage $25\Delta t$ are magnified. The cancer bundle has increased in size and notably spread further into the areas of initially low fibre density, subfigure 5.9a with the tumour boundary also increasing in size and irregularity. The fibres have been rearranged and pushed further out towards the tumour boundary, subfigure 5.9c, whilst simultaneously undergoing macroscopic degradation at the tissue scale (5.5), thus resulting is areas of very low to no fibre density. Finally, the simulations in Figure 5.10 show the evolution of the tumour at stage $75\Delta t$. The cancer cells have formed patterns within the tumour boundary, subfigure 5.10a, in the areas of low ECM density, where the cells have migrated towards the tumour boundary

collecting in high distribution bundles that more rapidly degrade the surrounding ECM. Furthermore, the cells are flooding areas where there is very low to no fibre density, subfigure 5.10c, and forming dense bundles of cells. This behaviour is in accordance with the conclusions presented in Chapter 3 that cancer cells can more freely invade areas of no ECM density and will progress upon these areas first before engulfing the higher density regions.

5.7.1 Increased collagen density

We proceed by exploring the cancer dynamics within an initial 20% homogeneous fibre distribution, taken as $p = 0.2$ of the non-fibres ECM phase $l(x, 0)$, and in the presence of the micro-fibre degradation rate $d_f = 0.5$. At stage $25\Delta t$, Figure 5.11, the non-fibres ECM phase has been degraded by the cancer cells, subfigure 5.11b, with the highest degradation occurring in the regions of highest cell distribution. The tumour boundary at this stage is larger than in previous simulations, this correlating with results in Chapters 3 and 4 where an initially higher density fibre ECM phase resulted in an accelerated spread of the tumour. Additionally, the macroscopic fibre density, subfigure 5.11c, also exhibits different behaviour than in previous simulations, where a similar pattern of fibres was noted in Chapter 3, subfigure 3.20d. This pattern of fibres is witnessed because the tumour boundary is expanding faster than the micro-fibres are being rearranged, thus the distributions are not found to build on the proliferating edge. Moving on to stage $50\Delta t$, the cancer cell distribution is increasing and spreading within the tumour region, subfigure 5.12a. There is significant non-fibres ECM degradation stretching the entire area of the tumour, subfigure 5.12b, with this only becoming more pronounced at later stages, subfigure 5.13b. The macroscopic fibre orientations, subfigures 5.12d, 5.12f, display high levels of reorientation with a similar "frenzied" appearance to figures in

Chapter 4. At the final stage $75\Delta t$, Figure 5.13, the cancer cells are dispersed further into the matrix, subfigure 5.13a and noticeably in the pattern of degradation of the non-fibres ECM phase, subfigure 5.13b. Overall, we conclude that in the presence of a homogeneous ECM, with a high initial homogeneous fibre distribution, the cancer cells have increased opportunity for adhesion and thus they are able to easier invade the surrounding matrix, resulting in a larger tumour region and a higher level of ECM degradation.

We continue our investigation of cancer invasion within a collagen dense environment by exploring the multiscale model within an initially 20% heterogeneous fibre ECM phase embedded in a homogeneous non-fibres ECM phase. Figures 5.14-5.16 display simulation results at stages $25\Delta t$, $50\Delta t$ and final stage $75\Delta t$. When comparing with the results in Figures 5.11-5.13, the significant differences between cancer invasion within a homogeneous or heterogeneous fibre environment is the shape and density of the main tumour bulk and the pattern of the proliferating boundary. The tumour boundary in Figure 5.14 is spreading first to the low density regions of fibres, this behaviour consistent with results in Chapter 4, where the cancer cells can more easily migrate to close-by areas of low fibre density due to the physical space available, thus the boundary of the tumour becomes lobular as the cells migrate outwards, subfigure 5.14c. The main bulk of tumour cells are also exhibiting this behaviour as they have formed a high distribution region of cells in the area of lowest fibre density, subfigure 5.14a. The macroscopic fibre orientations have been rearranged to direct the movement of the tumour boundary, witnessed in Figure 5.15 at the next time stage interval $50\Delta t$. The main body of the tumour has distributed the cells into several small high distribution bundles, subfigure 5.15a particularly in the low density regions of fibres, subfigure 5.15c. The microscopic fibres are continuously rearranged and due to a higher rate of fibres degradation

where the cancer cell distribution is highest, we observe a very low central region of fibre density with them being both degraded and pushed outwards from the central region of the tumour, subfigures 5.15d, 5.15f. The orientation of the fibres become increasingly erratic in areas of higher fibre density, witnessed in the protrusions of the tumour boundary, whereby they are orientated in opposing directions. This trait is exaggerated at final stage $75\Delta t$, Figure 5.16, where the tumour has spread further into the ECM and the protrusions have increased in size. Furthermore, the bulk of cancer cells have become separated and formed distinct regions within the tumour boundary. When comparing the cancer cell distribution and the macro-fibres density, subfigures 5.16a and 5.16c respectively, it can be noted that the cancer cells have bypassed the higher regions of fibres and formed bundles of cells around these areas. This behaviour can also be seen in the homogeneous case, however it is a more prominent feature when in the presence of a heterogeneous fibre ECM phase. In conclusion, in the presence of an initially high fibre ECM density, tumour progression is accelerated and encourages a more aggressively spreading tumour, in both the case of either a homogeneous or heterogeneous fibre distribution. Additionally, when the initial fibre density is high, the boundary of the tumour spreads further away from the main body of the tumour at a rate which the cells cannot maintain. Hence, the main body of the tumour stays centralised, compared to a lower initial fibre density, whereby the cancer cells spread at a consistent rate within the tumour region and stay close to the boundary.

5.7.2 Invasion patterns of a heterotypic cancer cell population

To conclude our exploration of cancer invasion within a two-phase microenvironment, we consider now the invasion patterns of a heterotypic cell population using

the two cell sub-populations macro-dynamics first introduced in Chapter 2 and expanded upon in Chapter 4. Restated here for completeness, the macro-dynamics of the two cell sub-populations can be mathematically expressed as

$$\frac{\partial c_1}{\partial t} = \underbrace{\nabla \cdot D_1 \nabla c_1}_{\text{random motility}} - \underbrace{\nabla \cdot c_1 \mathcal{A}_1(x,t,\mathbf{u}(t,\cdot),\theta_f(\cdot,t))}_{\text{cell adhesion}} + \underbrace{\mu_1 c_1 (1-\rho(\mathbf{u}))^+}_{\text{proliferation}} - \underbrace{M_c(\mathbf{u},t)c_1}_{\text{mutation}}, \tag{5.18}$$

$$\frac{\partial c_2}{\partial t} = \underbrace{\nabla \cdot D_2 \nabla c_2}_{\text{random motility}} - \underbrace{\nabla \cdot c_2 \mathcal{A}_2(x,t,\mathbf{u}(t,\cdot),\theta_f(\cdot,t))}_{\text{cell adhesion}} + \underbrace{\mu_2 c_2 (1-\rho(\mathbf{u}))^+}_{\text{proliferation}} + \underbrace{M_c(\mathbf{u},t)c_1}_{\text{mutation}}, \tag{5.19}$$

where the terms in these equations retain the exact definitions as laid out in Section 4.2.2, Chapter 4. We consider both cancer cells sub-populations to contribute to the source of MMPs on the tumour boundary, hence the microscopic source term (5.8) will be readdressed as

$$1. \quad g_{\epsilon Y}(y,\tau) = \frac{\int\limits_{\mathbf{B}(y,\gamma)\cap\Omega(t_0)} (\alpha_1 c_1(x,t_0+\tau) + \alpha_2 c_2(x,t_0+\tau))\ \widetilde{F}(x,t_0+\tau)\ dx}{\widetilde{F}\cdot\lambda(\mathbf{B}(y,\gamma)\cap\Omega(t_0))},$$

$$y \in \epsilon Y \cap \Omega(t_0),$$

$$2. \quad g_{\epsilon Y}(y,\tau) = 0, \quad y \in \epsilon Y \setminus \big(\Omega(t_0) + \{y \in Y |\ ||y||_2 < \gamma\}\big), \tag{5.20}$$

where α_1, α_2 are the MMP secretion rates for cell sub-populations c_1 and c_2, respectively, $\widetilde{F}(x,t_0+\tau) := 1 + F(x,t)$ and $\widetilde{F}\cdot\lambda$ are defined as in Section 5.4.

Using parameter set Σ_2, Table 4.1 and the micro-fibre degradation rate $d_f = 1$, in following Figures 5.17 - 5.22 we present the computational results for the evolution of: (a) the primary cancer cell sub-population; (b) the secondary cell sub-population;

(c) the fibre magnitude density; (d) the non-fibres ECM distribution; and of the vector field of orientated fibres at two different resolutions, namely: (e) coarsened twice; and (f) coarsened fourfold. Considering an initially homogeneous fibre ECM phase, when comparing these results directly with the results in Chapter 4, we observe no differences between simulations performed in the absence of micro-fibre degradation at the tumour interface at the first interval $25\Delta t$, Figure 5.17, with the fibre orientations in subfigures 5.17e and 5.17f consistent between the results presented in Chapter 4. Proceeding to later stages, $50\Delta t$ and $75\Delta t$, Figures 5.18 and 5.19, respectively, we begin to witness changes, whereby the boundary of the tumour is visibly smaller than in previous results, thus implying a slower progression of the tumour. The macroscopic fibre orientations are aligned differently in subfigures 5.18e, 5.18f, where the fibres are directed inwards to the centre of the tumour, confining the tumour to the centre of the domain, subfigure 5.17a. Moving on to the final stage, Figure 5.19, the tumour region is smaller than in previous results, Chapter 4, Figure 4.7. The bulk of the cancer cells stick closely to the tumour boundary and both the fibre and non-fibre ECM phase have undergone a higher level of degradation within the tumour region.

Finally, to further our understanding of the effects of micro-fibre degradation at the tumour interface, we explore the evolution of a heterotypic cell population within a heterogeneous fibre ECM phase, whilst the non-fibre ECM phase remains homogeneous, Figures 5.20-5.19. As with an initially homogeneous fibre density, at stage $25\Delta t$, Figure 5.20, there is very little difference when compared to simulations presented in Chapter 4. Moving on to later stages it is obvious that the process of boundary micro-fibre degradation causes a slower rate of tumour progression. The tumour region is considerably smaller in Figures 5.21 and 5.22 when compared with previous results in Figure 4.10. The bulk of tumour cells display a similar pattern,

however much closer to the tumour boundary, particularly cancer cell population c_2 where the cells have formed high distribution bundles at the leading edge. Much like in the presence of a homogeneous fibre density, both the fibre and non-fibre ECM phase has been subject to a higher level of degradation in the tumour region. This is attributed to the micro-fibre degradation at the tumour boundary, as degradation continuously occurs as the boundary expands we witness a lower fibre density as the tumour evolves. It can be concluded from these simulations and comparisons with previous results that the process of micro-fibre degradation at the tumour interface is disadvantageous to tumour progression, inhibiting the full invasive capabilities of the tumour. This is due to the lower levels of fibre density at the tumour interface, as degradation of the micro-fibres occurs both inside and within the peritumoural region of the tumour, the cell-fibre adhesion rate is reduced in line with low fibre levels, therefore the cancer cells do not have the same opportunities for adhesion and thus their migration is greatly reduced.

5.8 Discussion

In this chapter we have presented an integrated two-part multiscale model of cancer invasion, which builds on the approach introduced in Chapter 3 and Shuttleworth and Trucu (2019c) and extends that to capture explicitly the dynamic cell-scale interaction between the MDE boundary micro-dynamics and the peritumoural mass distribution of micro-fibres.

Structured largely similar to the modelling framework introduced in Chapter 3 and Shuttleworth and Trucu (2019c), the model proposed here combines two multiscale systems that share the same tissue (macro-) scale dynamics while having separate cell- (micro-) scale processes that are simultaneously connected via two double feedback loops. Specifically, while this new modelling framework inherits

completely the multiscale dynamics of naturally oriented ECM fibres (induced by the mass distribution of micro-fibres) occurring on the topological closure of the invading tumour (and including the dynamic rearrangement of fibres under the incidence of the macro-scale flux of cancer cells), this shares its macro-dynamics with a significantly extended multiscale moving-boundary modelling for the proteolytic dynamics at the tumour invasive edge that explicitly consider the interaction with the peritumoural fibres.

This model expands and takes forward both the initial multiscale moving-boundary framework introduced in Trucu et al. (2013) and its further development into the two-part multiscale modelling introduced in Shuttleworth and Trucu (2019c) by bringing in and exploring the cell-scale interaction between the cross-interface diffusion of MMPs and the micro-fibre distributions in the peritumoural region, with direct impact upon microscopic peritumoural degradation of micro-fibres that results in return in a continuously altered macroscopic vector field of oriented ECM fibres at the tumour boundary. Moreover, these altered peritumoural ECM fibres have major relevance within the macroscopic dynamics of the cancer cells as this affects the cell-fibres adhesion properties at the leading edge of the tumour, impacting this way not only the tumour mechanics close to the tumour interface but the entire tissue-scale dynamics of the tumour.

To that end, we first explore mathematically the positive feedback that of the macroscopic distribution of ECM fibres close to the tumour interface has upon the emerging cell-scale source of MMP-2 for the cross-interface micro-dynamics that MMP-2 exercise at the invading edge of the tumour. Specifically, in this new formulation we are able to capture the enhanced sources of MMP-2 in a relevant cell-scale neighbourhood which are enabled non-locally by the presence of elevated distributions of ECM fibres within neighbouring active regions from within the outer pro-

liferating rim of the tumour where cancer cells arrive during their macro-dynamics and produce MMPs.

Further, in the presence of the cell-scale MMP-2 source induced by the macro-dynamics, a cross-interface diffusion of MMP-2 occurs at the invasive edge of the tumour. However, as the MMP-2 find it easier to diverge along their gradient directions in regions with lower micro-fibres levels, by accounting for the presence micro-scale mass distribution, we finally obtain that the diffusion rate of this diffusive molecular transport process of MMP-2 naturally depend on the micro-fibres density. Thus, this cell-scale MMP-2 dynamics focuses the cross-interface molecular transport towards the regions of lower mass-distributions of micro-fibres, taking *on-the-fly* advantage on the potential "micro-fibres valleys" created by the multiscale dynamic rearrangement of fibres induced by the macro-scale flux of cancer cells, which was derived and explored with full details in Chapter 3 and Shuttleworth and Trucu (2019c). To accommodate this new fibre-dependent diffusion of MMPs, their micro-dynamics were computed using a finite difference scheme, similar to the method used in Chapter 2 for the spatial and time discretisation for the cancer macro-dynamics, as described in Section 2.3.1.

Since the MMP-2 cross-interface molecular transport leads to peritumoural micro-fibres degradation takes at the micro-scale, we explored this degradation explicitly at the cell-scale, remarking here at the same time that this complements the previous modelling framework introduced and discussed in Chapter 3 and Shuttleworth and Trucu (2019c) were the fibres degradation was only considered on the bulk of the tumour at the macro-scale. To that end, we considered the correlation between the micro-fibres degradation and the incidence angle that the MMP-2 molecular flux makes with the regions of significant levels of micro-fibres distributed with any given ϵY from the covering bundle of $\{\epsilon Y\}_{\epsilon Y \in \mathcal{P}}$ boundary micro-domains. This en-

abled us to derive mathematically a micro-fibres degradation law occurring on each fibre micro-domain $\delta Y(x)$ that has non-empty intersection with at least one of the boundary micro-domains ϵY, in which maximum fibre degradation occurs when the angle between the fibres and MMPs flux is perpendicular, while the degradation decreases with increasing alignment of the fibres with the direction of the MMP-2 molecular flux. This suggests that the highly aligned collagen fibrils will act as a pathway for invasion rather than a barrier against it, this being consistent with the biological evidence presented in Provenzano et al. (2006). Finally, this degradation of peritumoural mass distribution micro-fibres at the cell-scale is continuously in time translated back at macro-scale, having a natural and major impact upon *on-the-fly* changes in the orientation and magnitudes of macro-scale ECM fibres from the peritumoural region.

This new modelling framework has been explored in several scenarios, within both a homogeneous and heterogeneous initial distribution of fibres, and varying the initial ratio of macroscopic fibre distribution in relation to the non-fibres ECM phase. The non-fibres ECM phase was kept as a homogeneous density throughout the Chapter for the purpose of exploring only the influence of ECM fibres during cancer invasion. These scenarios were explored through randomly allocated distributions of micro-fibres over the fibres micro-domain, as considered already in Chapter 4 and defined in Appendix D.1.

We explored the differences between a homogeneous and heterogeneous initial distribution of fibres where we varied the initial percentage of fibres density from 15% to 20%, as well as investigating the morphology of a heterotypic cancer cell population whose macroscopic dynamics were developed in Chapter 4. We conclude from these simulations that a heterogeneous distribution of fibres induces a more lobular, fingering pattern of the tumour boundary, and an increase in initial fibre

density promotes a more aggressive tumour spreading further into the surrounding tissue, a behaviour which is mirrored in the biological experiments performed in Provenzano et al. (2008). These remarks are in line with previous Chapters where the same conclusions are drawn regarding the initial condition of the fibres ECM phase. The simulations performed in this Chapter exhibit an overall larger tumour spread than the simulations in Chapter 3, implying that the degradation of fibres at the tumour interface promotes tumour invasion. The final simulations, which consider the invasive behaviour of a heterotypic cell population, suggest that although the cancer cells migrate more easily into low density regions of ECM, at the tumour interface a lack of fibre density is detrimental to the progression of the tumour. The low levels of fibre density inhibit the migration of cancer cells and thus the movement of the tumour boundary by reducing the opportunities for cell-fibre adhesion. In general, we conclude that the invasion of a heterotypic cancer cell population is accelerated in the presence of a high fibres ECM density, however within a low fibres ECM the tumour undergoes slower progression and the bulk of the cancer cells remain closer to the gradually expanding tumour boundary.

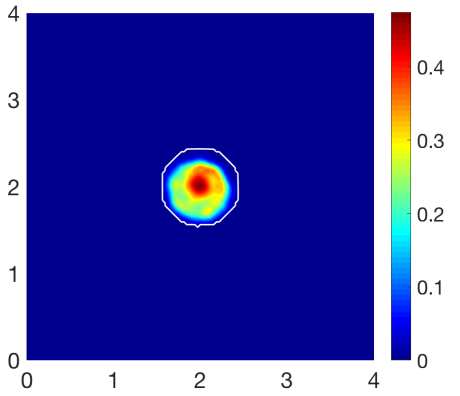

(a) Cancer cell population

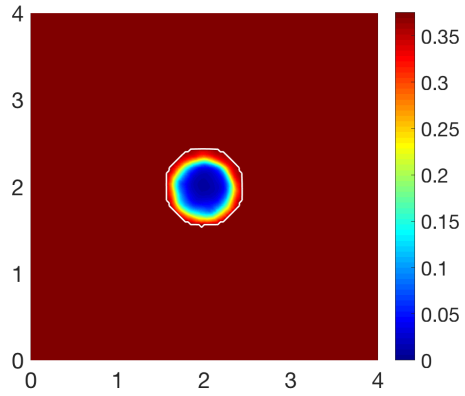

(b) Non-fibres ECM distribution

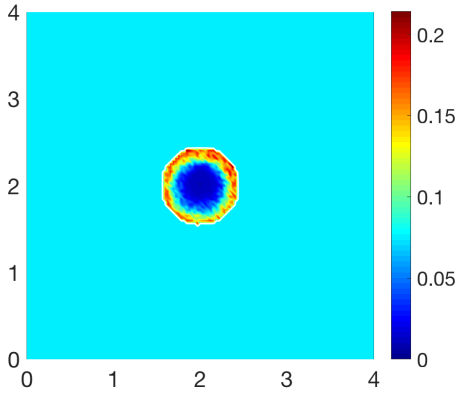

(c) Fibre magnitude density

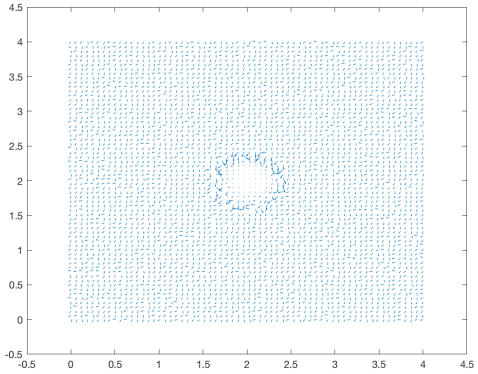

(d) Fibre vector field - coarsened 2 fold

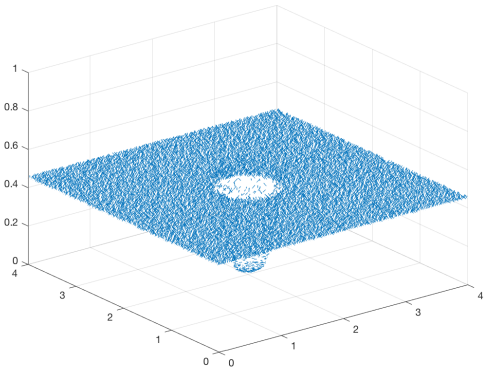

(e) 3D ECM vector field

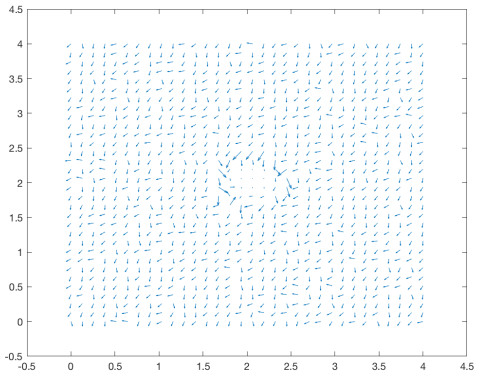

(f) Fibre vector field - coarsened 4 fold

Figure 5.5: Simulations at stage $25\Delta t$ with a homogeneous distribution of the non-fibrous and fibres phase of the ECM and a micro-fibres degradation rate of $d_f = 1$.

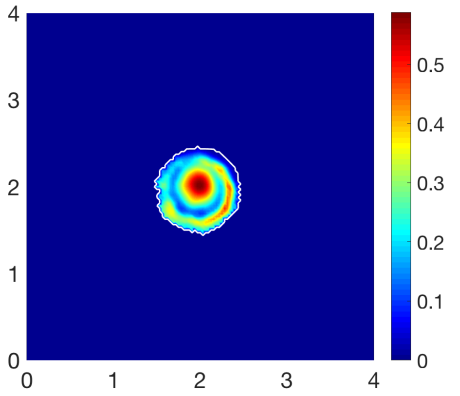

(a) Cancer cell population

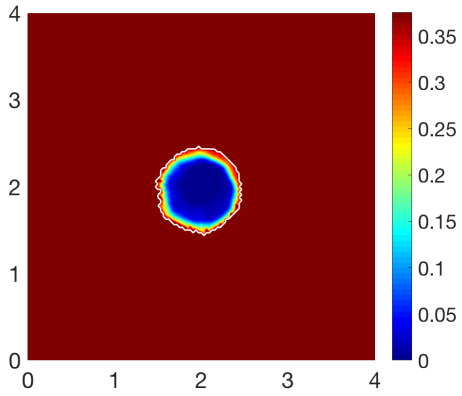

(b) Non-fibres ECM distribution

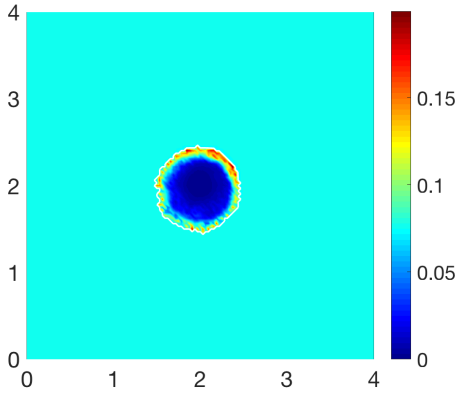

(c) Fibre magnitude density

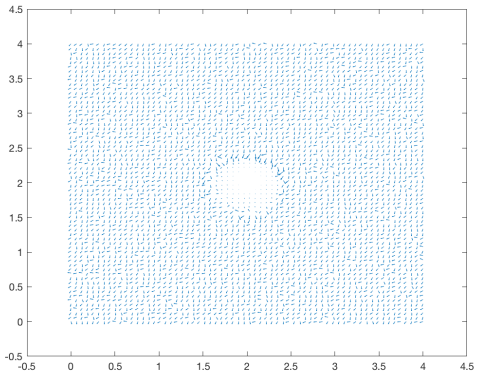

(d) Fibre vector field - coarsened 2 fold

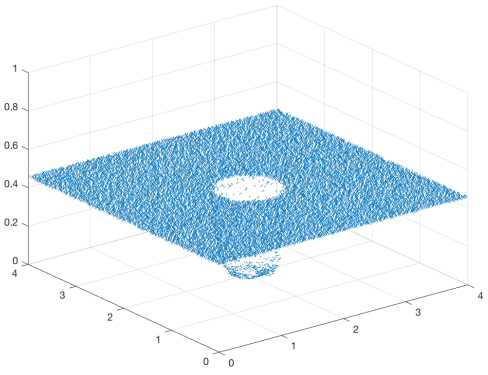

(e) 3D ECM vector field

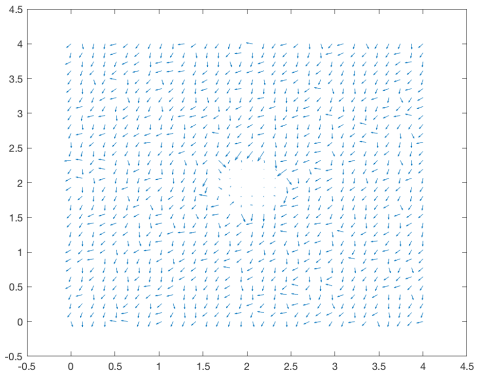

(f) Fibre vector field - coarsened 4 fold

Figure 5.6: Simulations at stage $50\Delta t$ with a homogeneous distribution of the non-fibrous and fibres phase of the ECM and a micro-fibres degradation rate of $d_f = 1$.

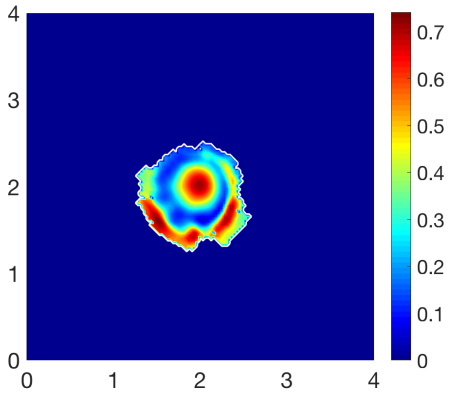

(a) Cancer cell population

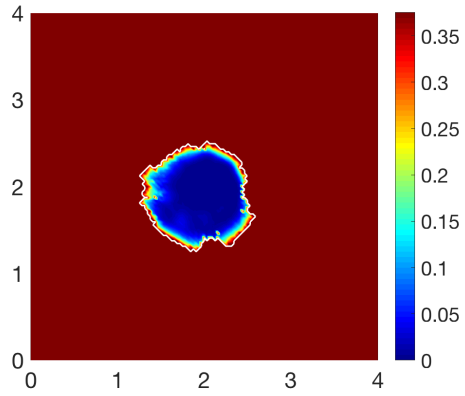

(b) Non-fibres ECM distribution

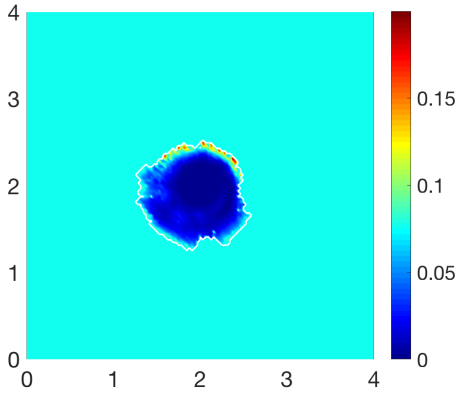

(c) Fibre magnitude density

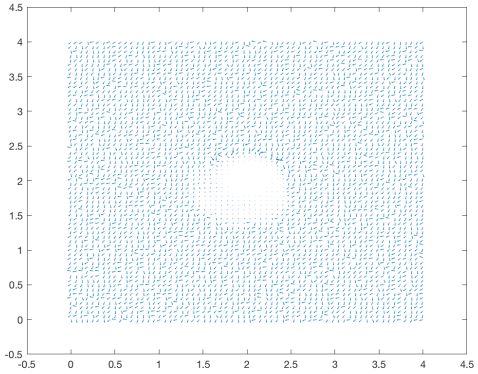

(d) Fibre vector field - coarsened 2 fold

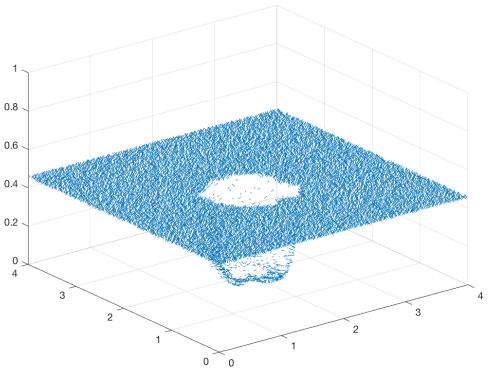

(e) 3D ECM vector field

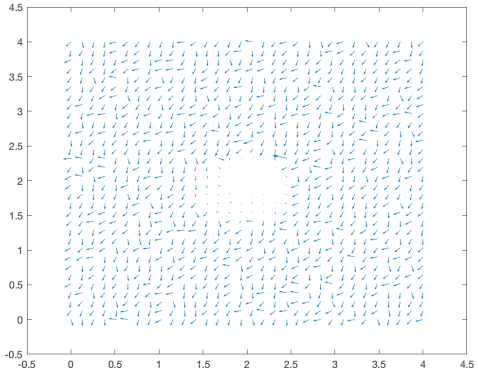

(f) Fibre vector field - coarsened 4 fold

Figure 5.7: Simulations at stage $75\Delta t$ with a homogeneous distribution of the non-fibrous and fibres phase of the ECM and a micro-fibres degradation rate of $d_f = 1$.

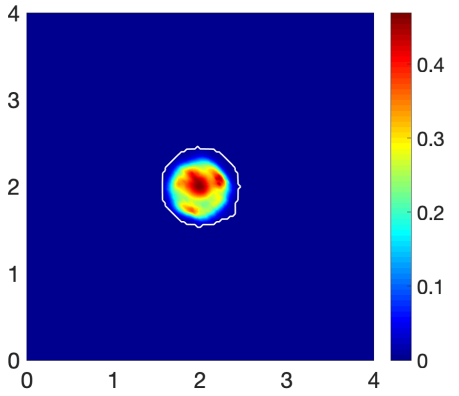

(a) Cancer cell population

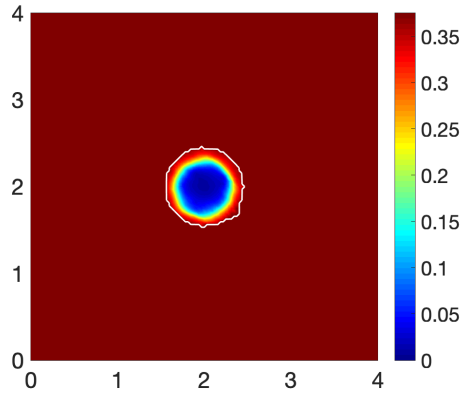

(b) Non-fibres ECM distribution

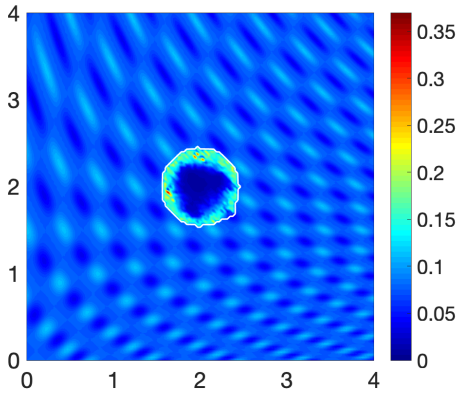

(c) Fibre magnitude density

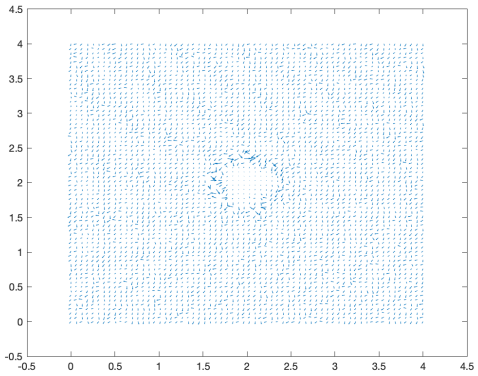

(d) Fibre vector field - coarsened 2 fold

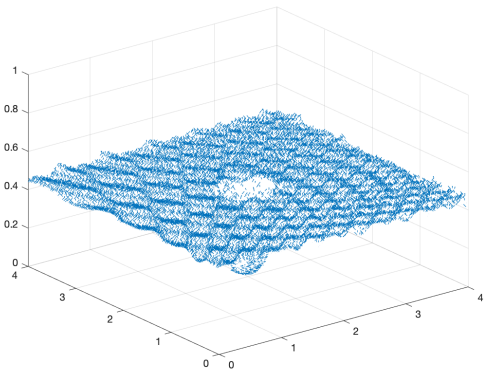

(e) 3D ECM vector field

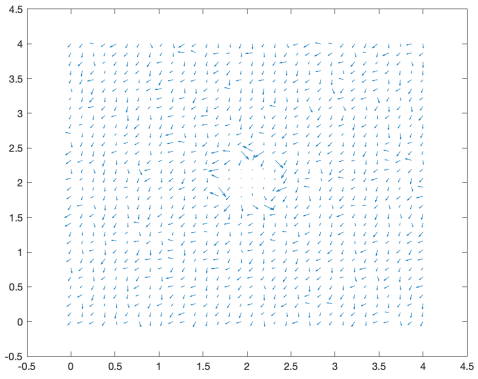

(f) Fibre vector field - coarsened 4 fold

Figure 5.8: Simulations at stage $25\Delta t$ with a homogeneous distribution of the non-fibrous phase and 15% heterogeneous fibres phase of the ECM with a micro-fibres degradation rate of $d_f = 1$.

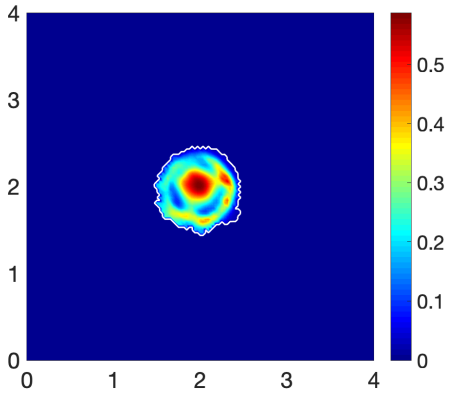

(a) Cancer cell population

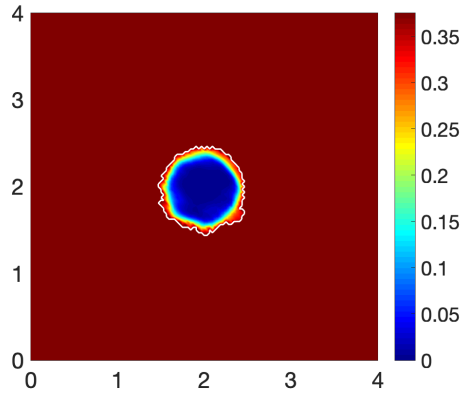

(b) Non-fibres ECM distribution

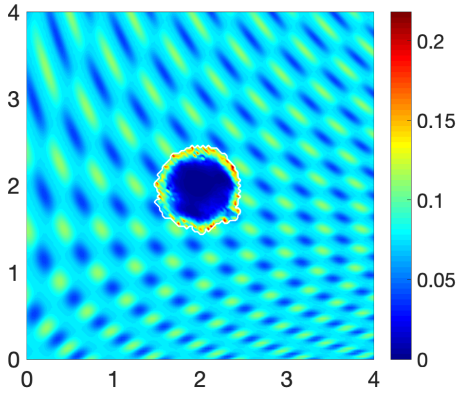

(c) Fibre magnitude density

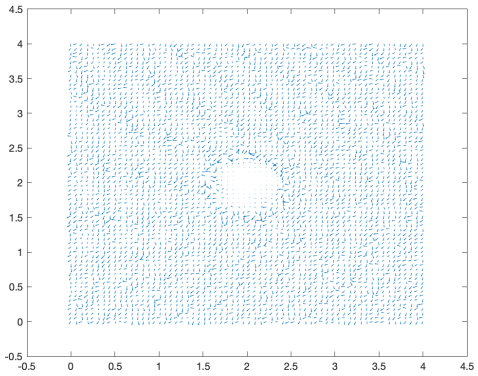

(d) Fibre vector field - coarsened 2 fold

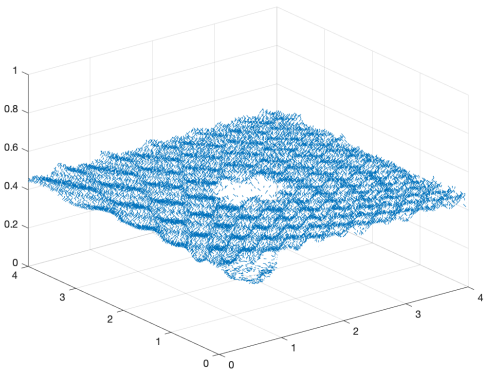

(e) 3D ECM vector field

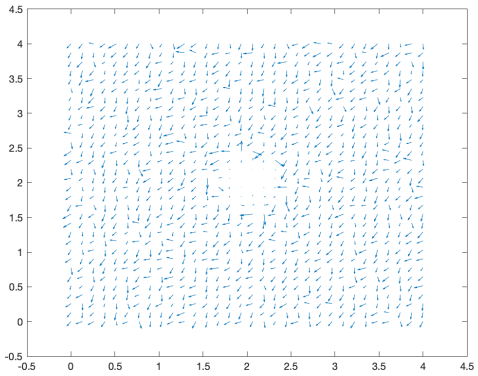

(f) Fibre vector field - coarsened 4 fold

Figure 5.9: Simulations at stage $50\Delta t$ with a homogeneous distribution of the non-fibrous phase and 15% heterogeneous fibres phase of the ECM with a micro-fibres degradation rate of $d_f = 1$.

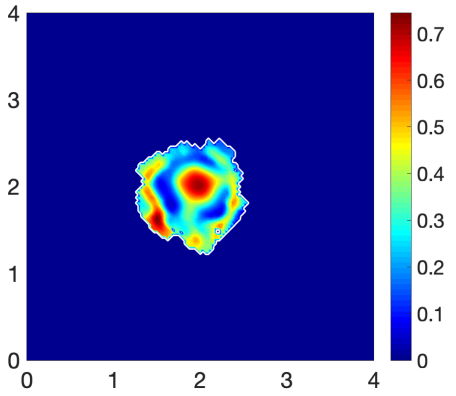

(a) Cancer cell population

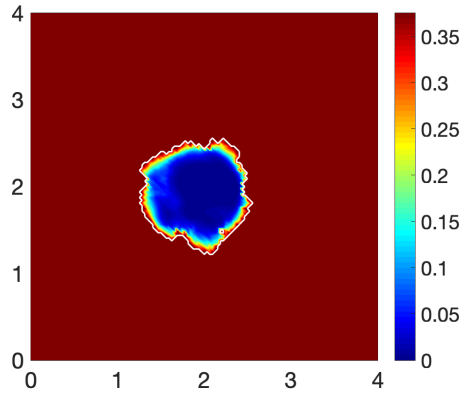

(b) Non-fibres ECM distribution

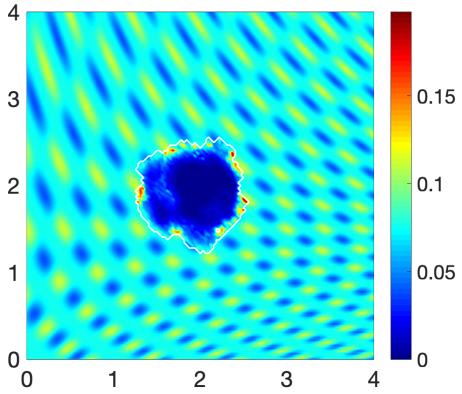

(c) Fibre magnitude density

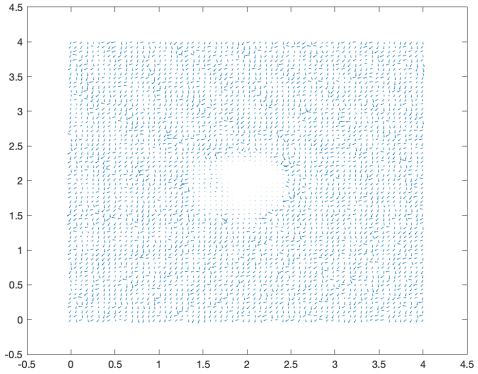

(d) Fibre vector field - coarsened 2 fold

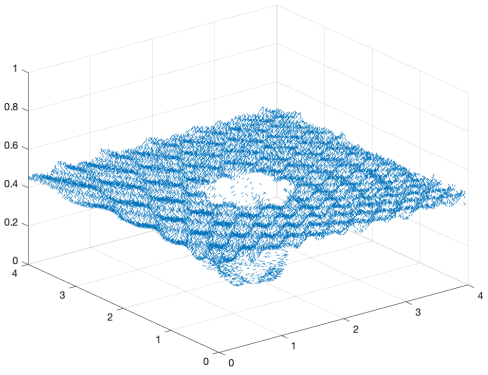

(e) 3D ECM vector field

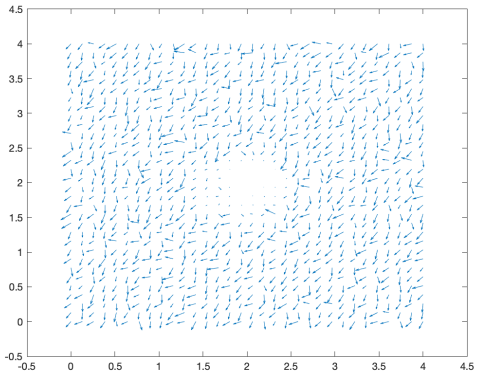

(f) Fibre vector field - coarsened 4 fold

Figure 5.10: Simulations at stage $75\Delta t$ with a homogeneous distribution of the non-fibrous phase and 15% heterogeneous fibres phase of the ECM with a micro-fibres degradation rate of $d_f = 1$.

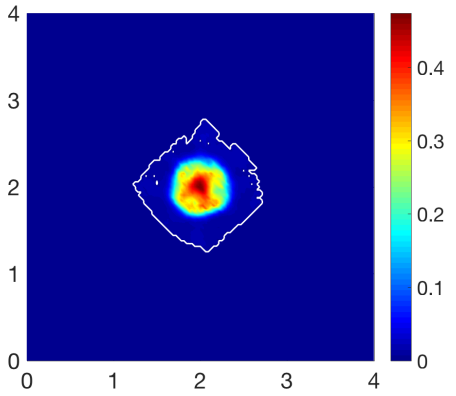

(a) Cancer cell population

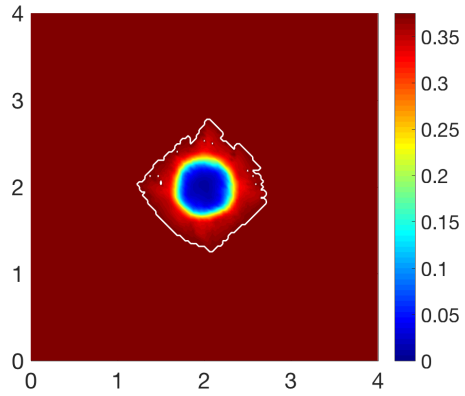

(b) Non-fibres ECM distribution

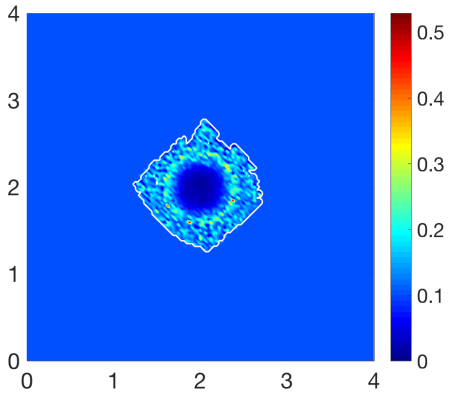

(c) Fibre magnitude density

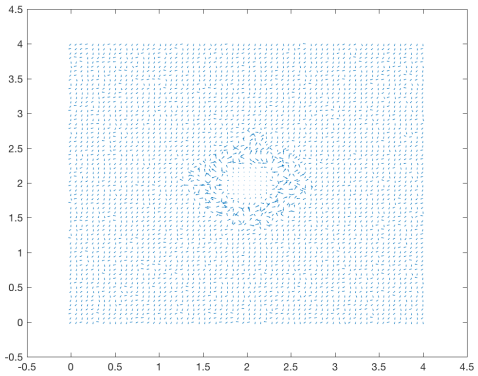

(d) Fibre vector field - coarsened 2 fold

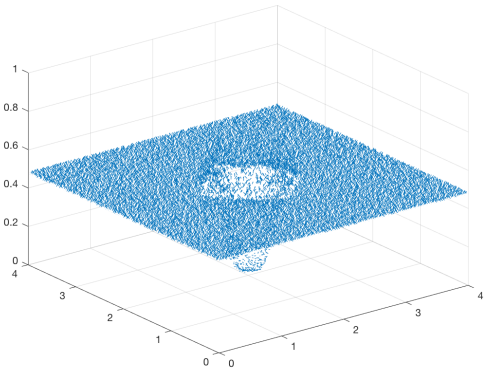

(e) 3D ECM vector field

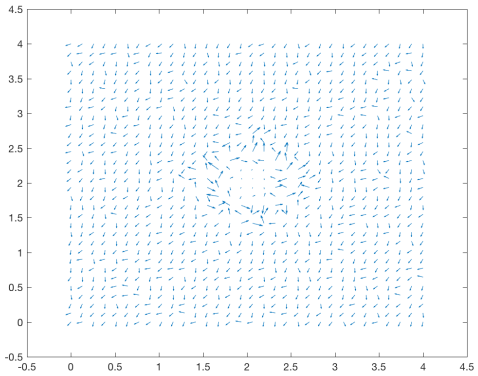

(f) Fibre vector field - coarsened 4 fold

Figure 5.11: Simulations at stage $25\Delta t$ with a homogeneous distribution of the non-fibrous phase and 20% homogeneous fibres phase of the ECM with a micro-fibres degradation rate of $d_f = 0.5$.

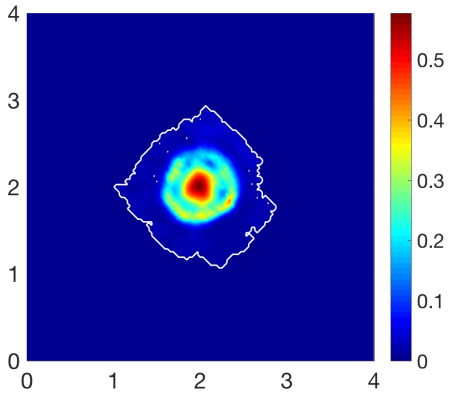

(a) Cancer cell population

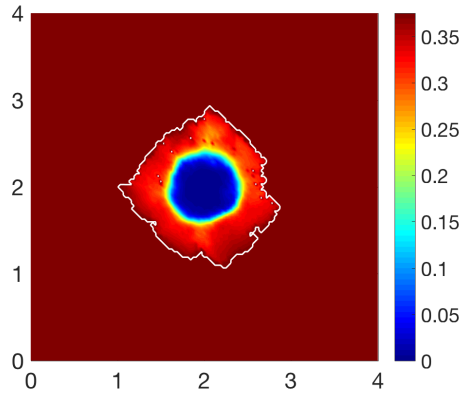

(b) Non-fibres ECM distribution

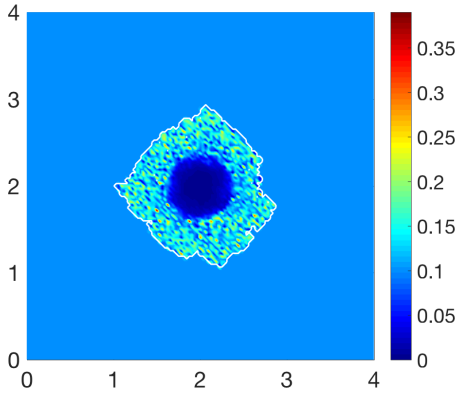

(c) Fibre magnitude density

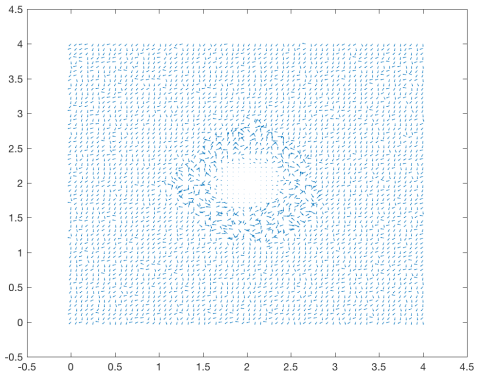

(d) Fibre vector field - coarsened 2 fold

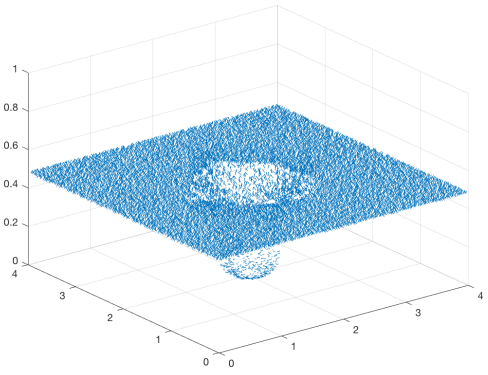

(e) 3D ECM vector field

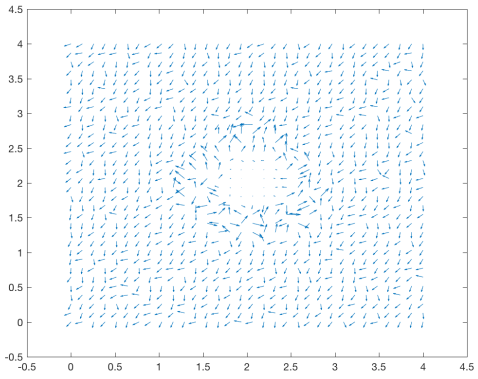

(f) Fibre vector field - coarsened 4 fold

Figure 5.12: Simulations at stage $50\Delta t$ with a homogeneous distribution of the non-fibrous phase and 20% homogeneous fibres phase of the ECM with a micro-fibres degradation rate of $d_f = 0.5$.

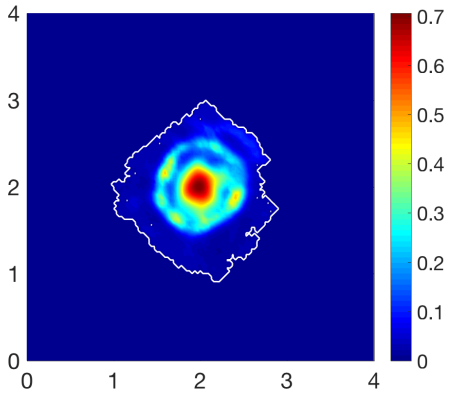

(a) Cancer cell population

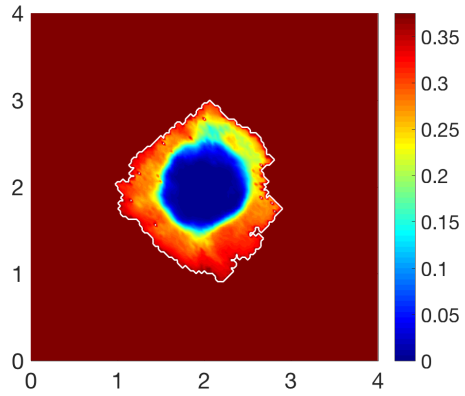

(b) Non-fibres ECM distribution

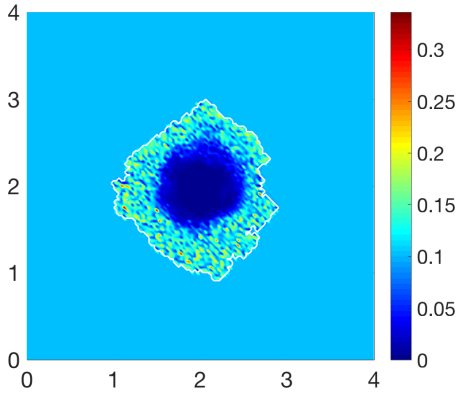

(c) Fibre magnitude density

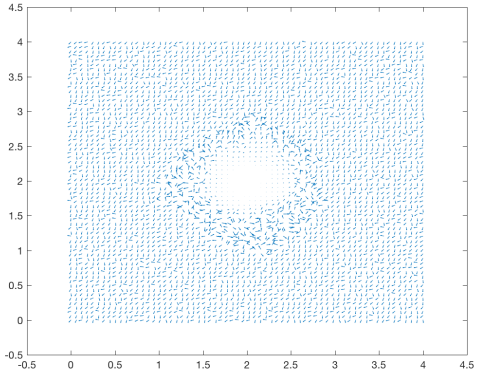

(d) Fibre vector field - coarsened 2 fold

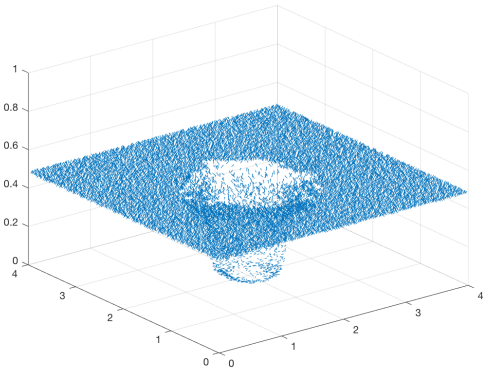

(e) 3D ECM vector field

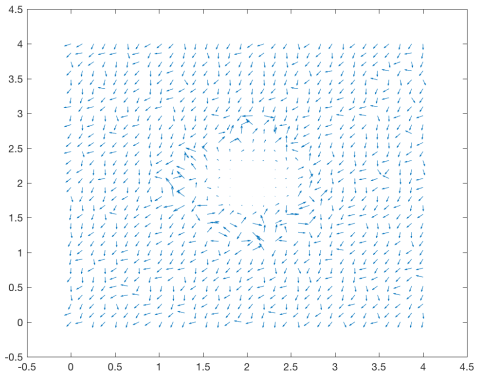

(f) Fibre vector field - coarsened 4 fold

Figure 5.13: Simulations at stage $75\Delta t$ with a homogeneous distribution of the non-fibrous phase and 20% homogeneous fibres phase of the ECM with a micro-fibres degradation rate of $d_f = 0.5$.

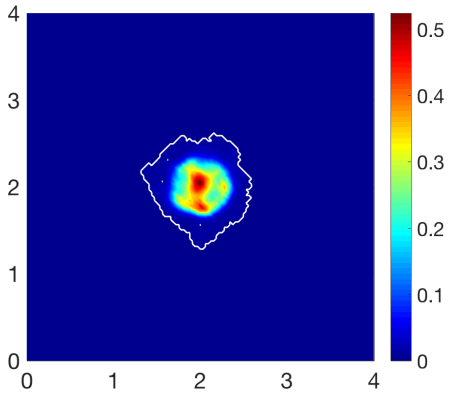

(a) Cancer cell population

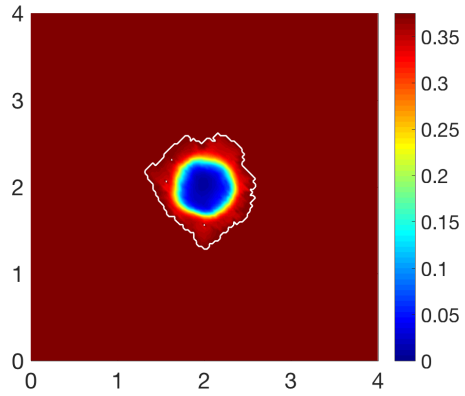

(b) Non-fibres ECM distribution

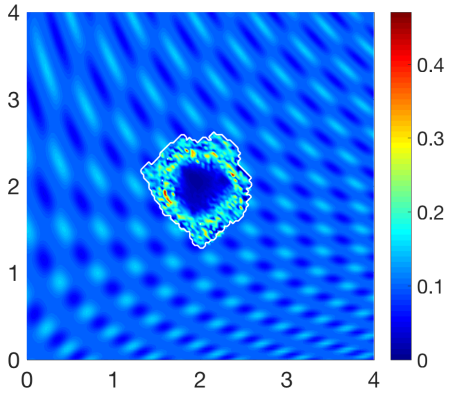

(c) Fibre magnitude density

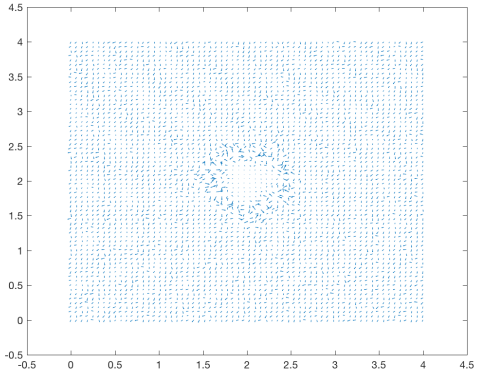

(d) Fibre vector field - coarsened 2 fold

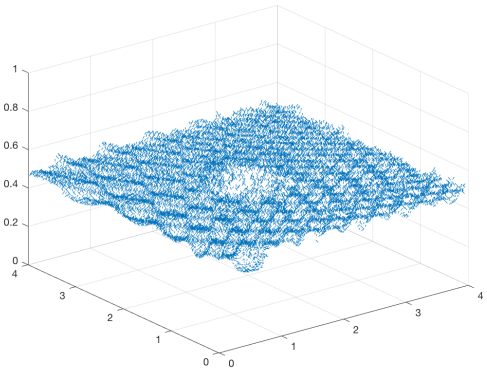

(e) 3D ECM vector field

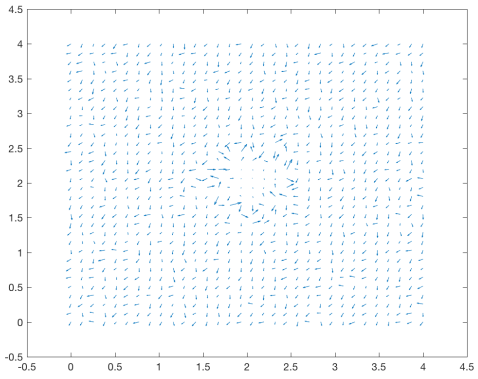

(f) Fibre vector field - coarsened 4 fold

Figure 5.14: Simulations at stage $25\Delta t$ with a homogeneous distribution of the non-fibrous phase and 20% homogeneous fibres phase of the ECM with a micro-fibres degradation rate of $d_f = 0.5$.

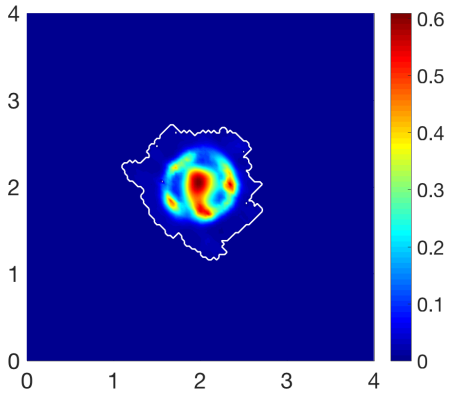

(a) Cancer cell population

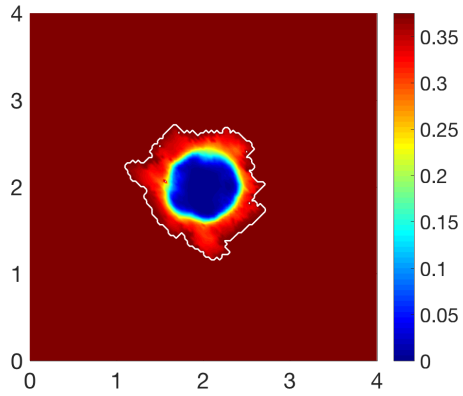

(b) Non-fibres ECM distribution

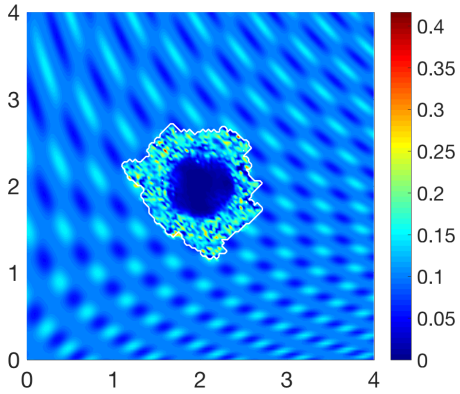

(c) Fibre magnitude density

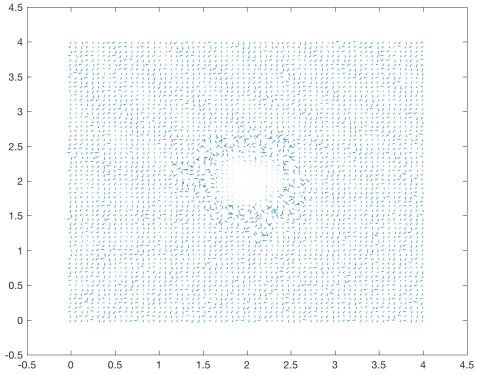

(d) Fibre vector field - coarsened 2 fold

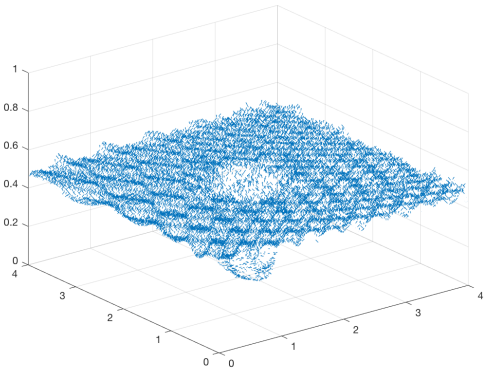

(e) 3D ECM vector field

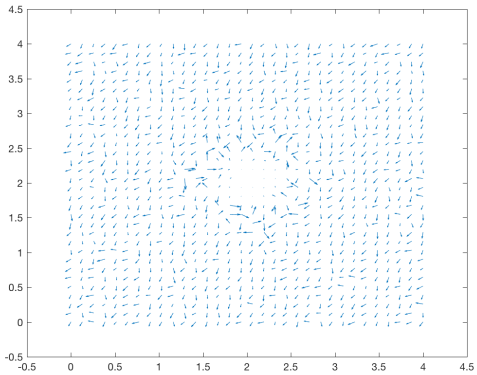

(f) Fibre vector field - coarsened 4 fold

Figure 5.15: Simulations at stage $50\Delta t$ with a homogeneous distribution of the non-fibrous phase and 20% homogeneous fibres phase of the ECM with a micro-fibres degradation rate of $d_f = 0.5$.

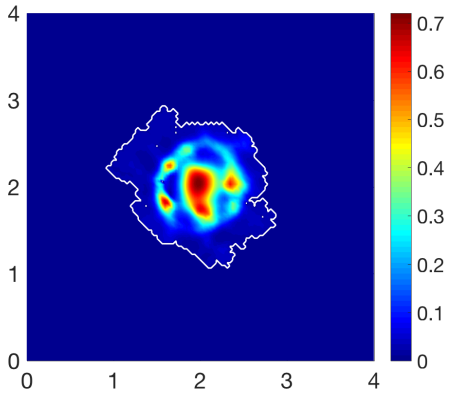

(a) Cancer cell population

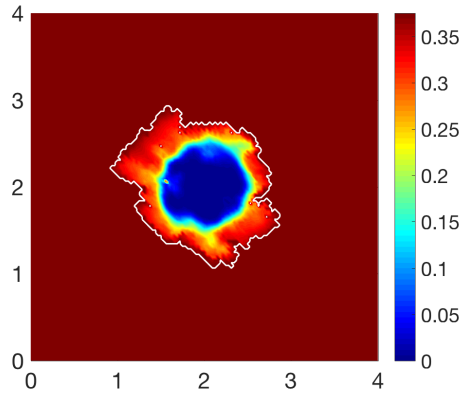

(b) Non-fibres ECM distribution

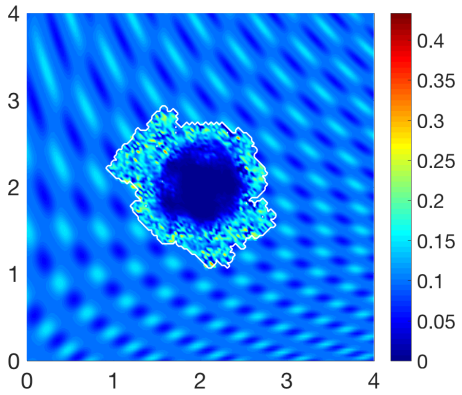

(c) Fibre magnitude density

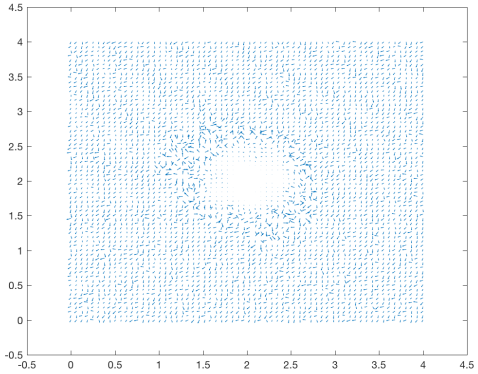

(d) Fibre vector field - coarsened 2 fold

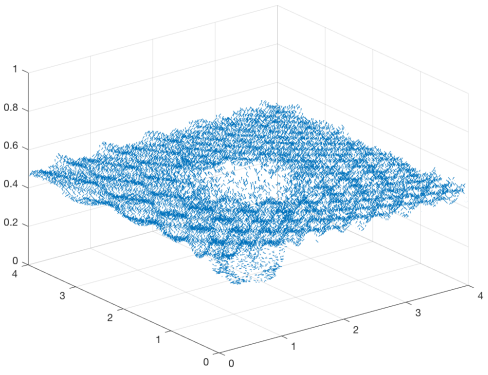

(e) 3D ECM vector field

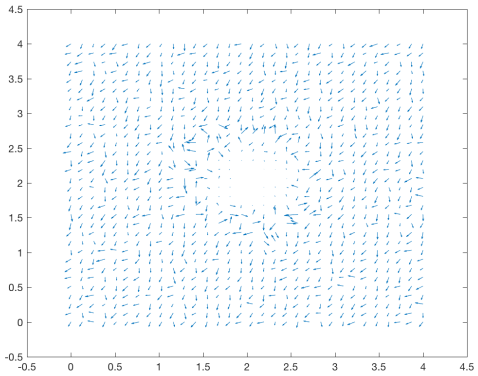

(f) Fibre vector field - coarsened 4 fold

Figure 5.16: Simulations at stage $75\Delta t$ with a homogeneous distribution of the non-fibrous phase and 20% homogeneous fibres phase of the ECM with a micro-fibres degradation rate of $d_f = 0.5$.

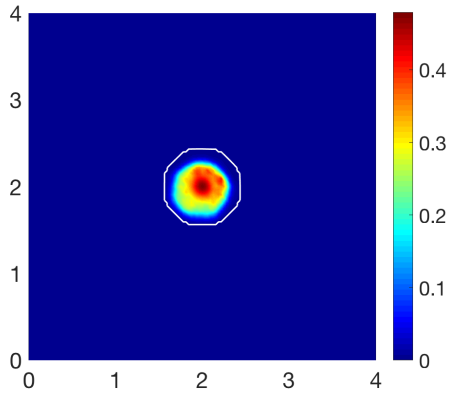

(a) Cancer cell population 1

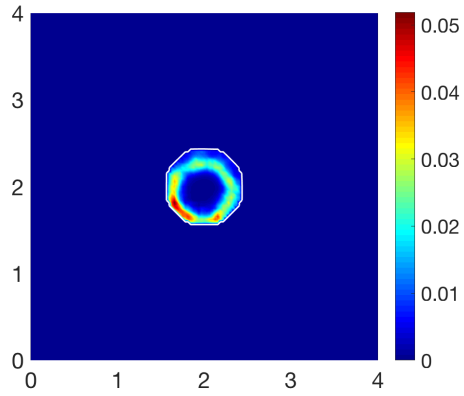

(b) Cancer cell population 2

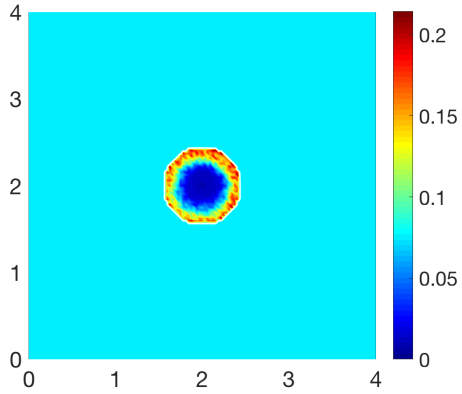

(c) Fibre magnitude density

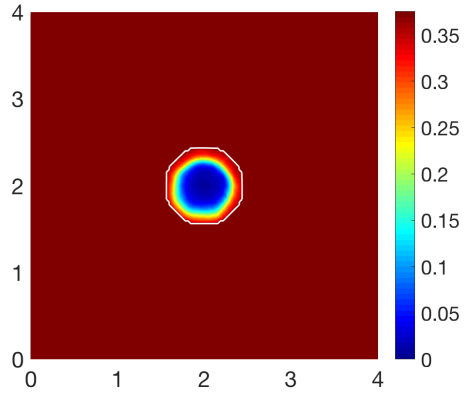

(d) Non-fibres ECM distribution

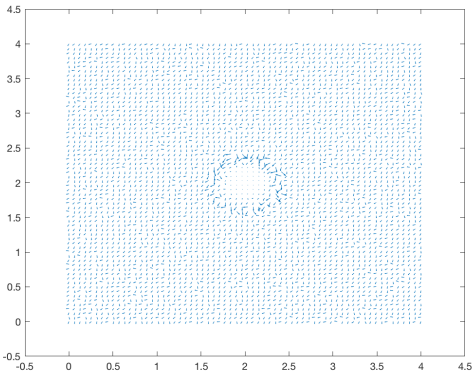

(e) Fibre vector field - coarsened 2 fold

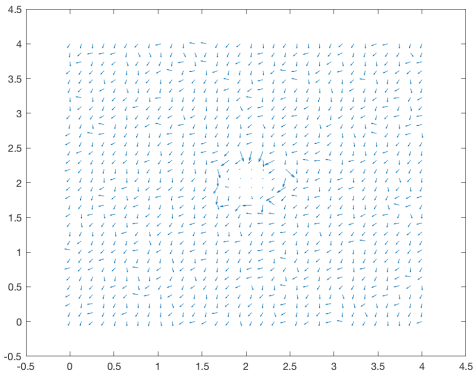

(f) Fibre vector field - coarsened 4 fold

Figure 5.17: Simulations at stage $25\Delta t$ with a homogeneous distribution of the non-fibrous phase and 15% homogeneous fibres phase of the ECM with a micro-fibres degradation rate of $d_f = 1$.

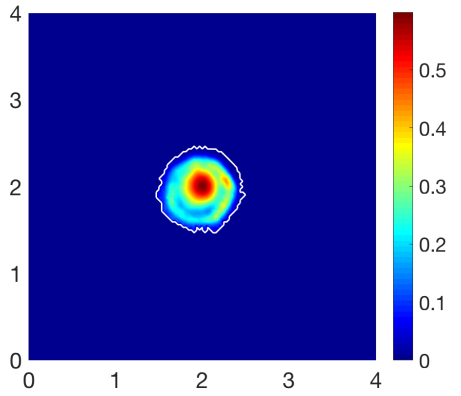

(a) Cancer cell population

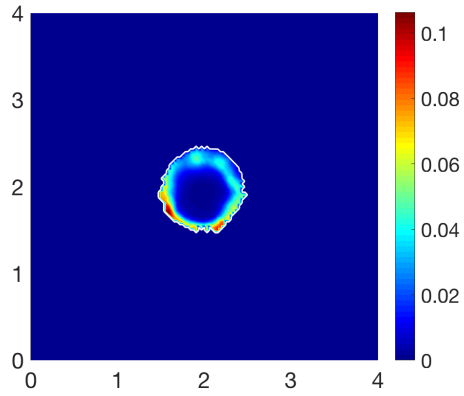

(b) Cancer cell population 2

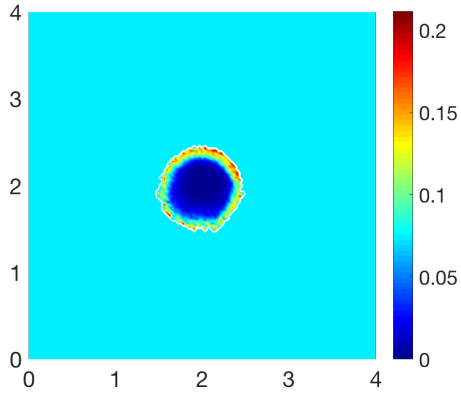

(c) Fibre magnitude density

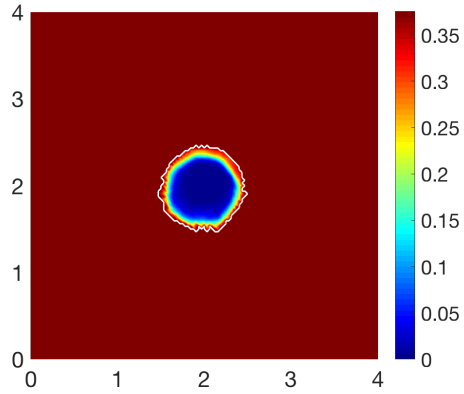

(d) Non-fibres ECM distribution

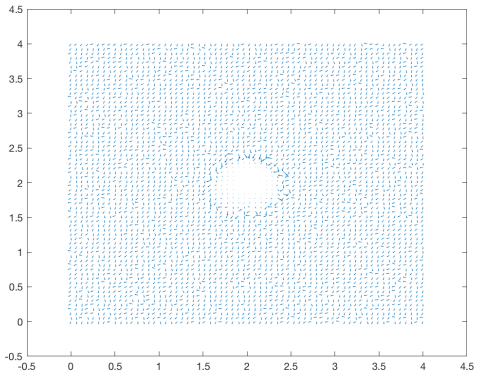

(e) Fibre vector field - coarsened 2 fold

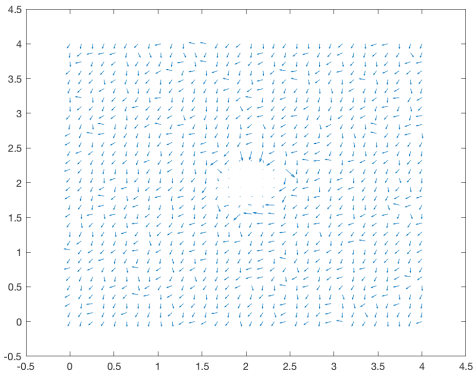

(f) Fibre vector field - coarsened 4 fold

Figure 5.18: Simulations at stage $50\Delta t$ with a homogeneous distribution of the non-fibrous phase and 15% homogeneous fibres phase of the ECM with a micro-fibres degradation rate of $d_f = 1$.

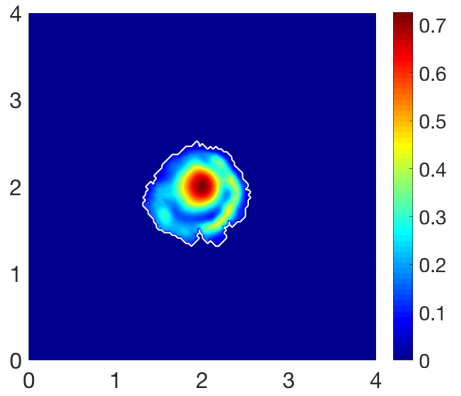

(a) Cancer cell population

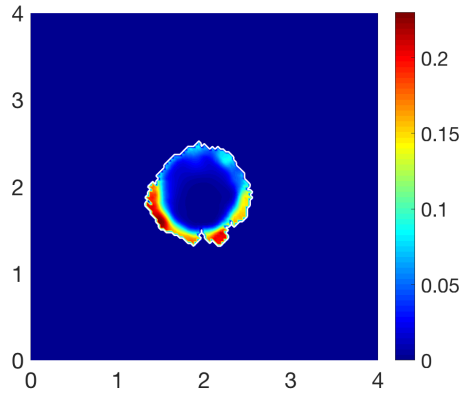

(b) cancer cell population 2

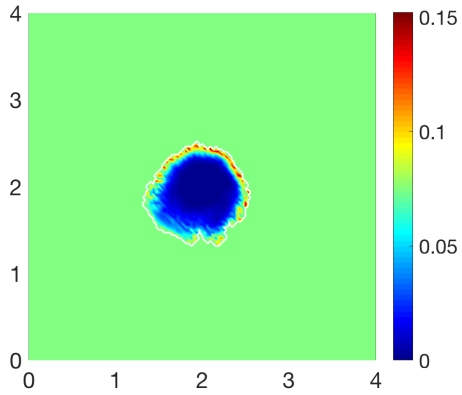

(c) Fibre magnitude density

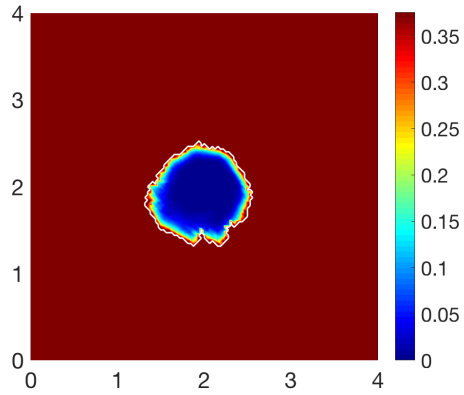

(d) Non-fibres ECM distribution

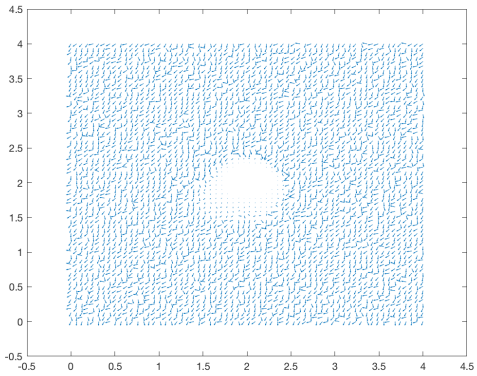

(e) Fibre vector field - coarsened 2 fold

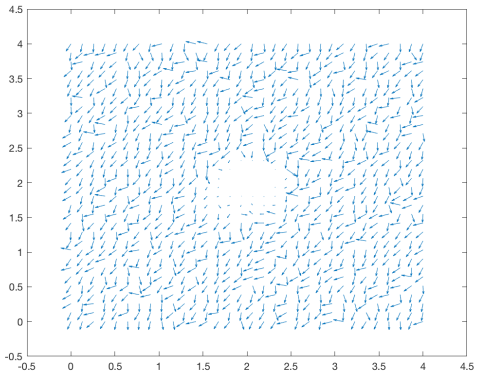

(f) Fibre vector field - coarsened 4 fold

Figure 5.19: Simulations at stage $75\Delta t$ with a homogeneous distribution of the non-fibrous phase and 15% homogeneous fibres phase of the ECM with a micro-fibres degradation rate of $d_f = 1$.

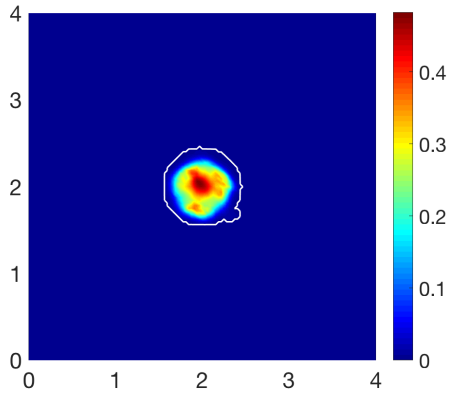

(a) Cancer cell population

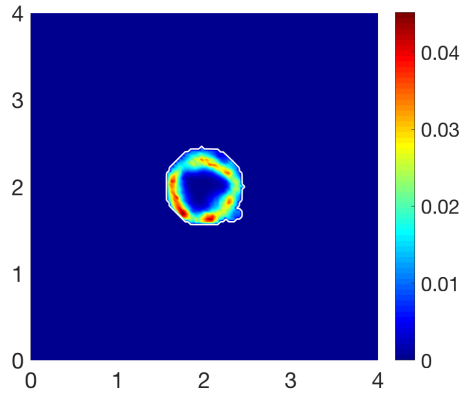

(b) Cancer cell population 2

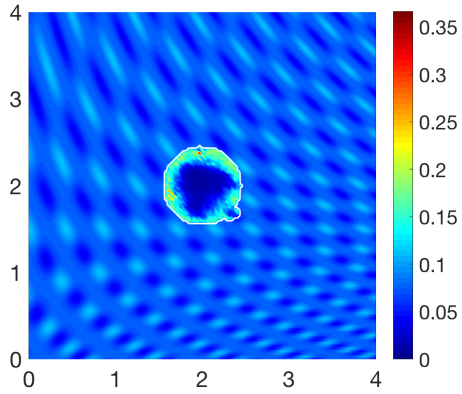

(c) Fibre magnitude density

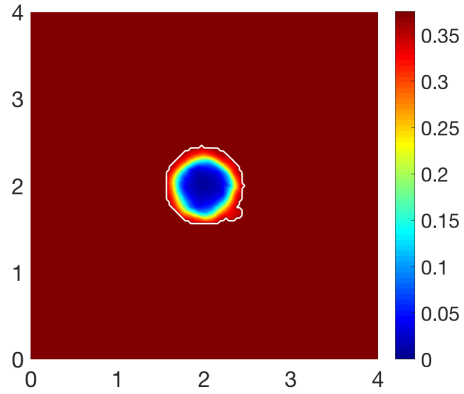

(d) Non-fibres ECM distribution

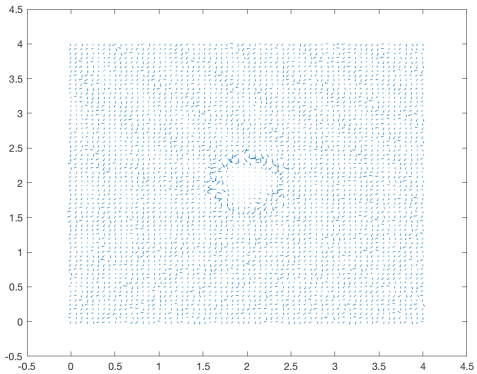

(e) Fibre vector field - coarsened 2 fold

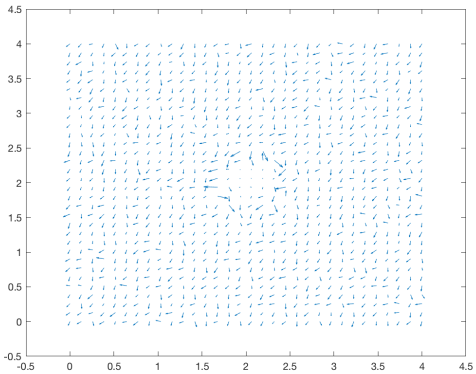

(f) Fibre vector field - coarsened 4 fold

Figure 5.20: Simulations at stage $25\Delta t$ with a homogeneous distribution of the non-fibrous phase and 15% heterogeneous fibres phase of the ECM with a micro-fibres degradation rate of $d_f = 1$.

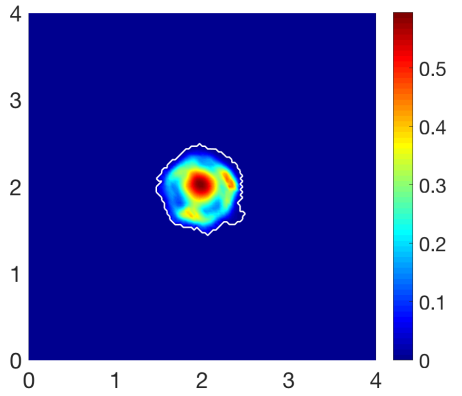

(a) Cancer cell population

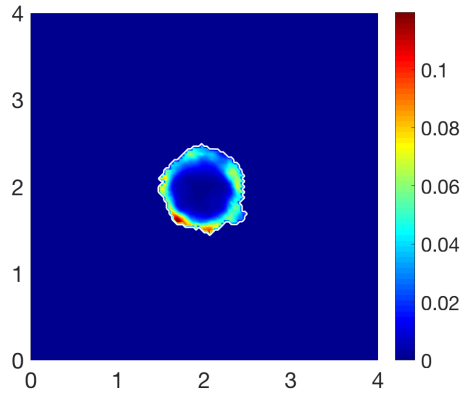

(b) Cancer cell population 2

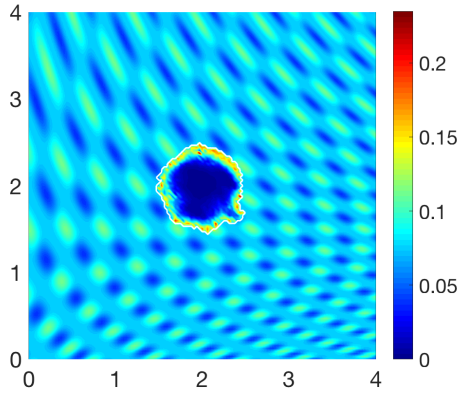

(c) Fibre magnitude density

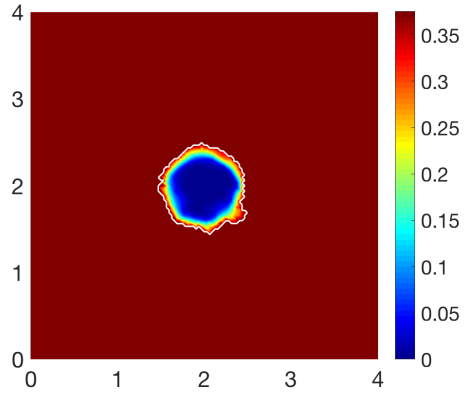

(d) Non-fibres ECM distribution

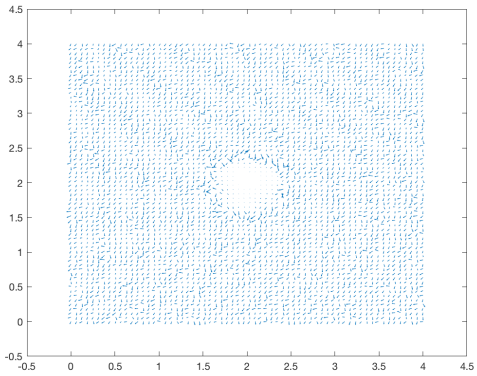

(e) Fibre vector field - coarsened 2 fold

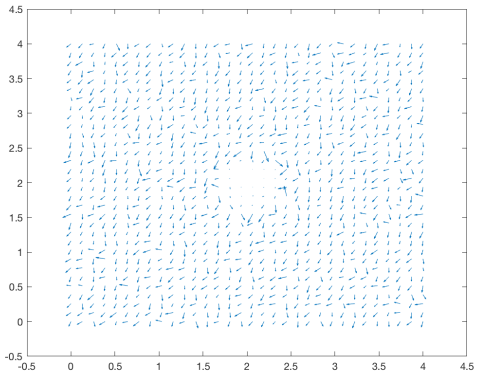

(f) Fibre vector field - coarsened 4 fold

Figure 5.21: Simulations at stage $50\Delta t$ with a homogeneous distribution of the non-fibrous phase and 15% heterogeneous fibres phase of the ECM with a micro-fibres degradation rate of $d_f = 1$.

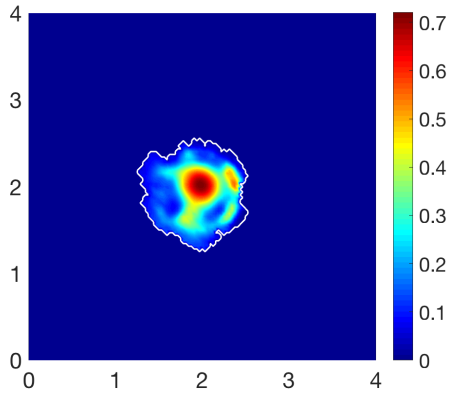

(a) Cancer cell population

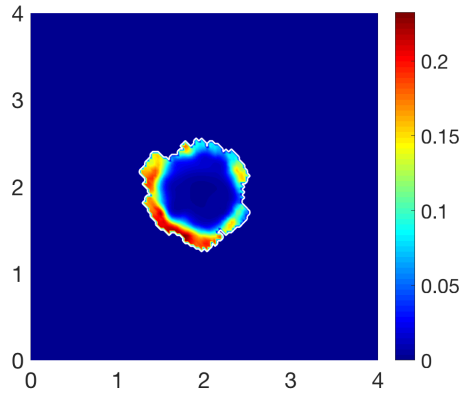

(b) Cancer cell population 2

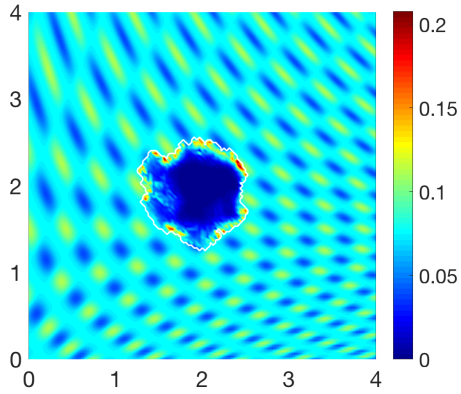

(c) Fibre magnitude density

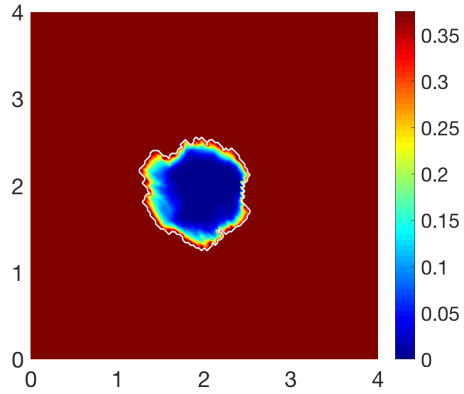

(d) Non-fibres ECM distribution

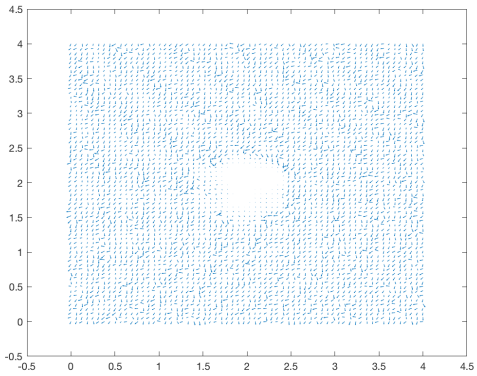

(e) Fibre vector field - coarsened 2 fold

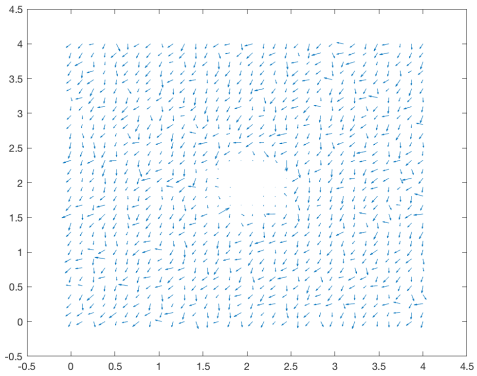

(f) Fibre vector field - coarsened 4 fold

Figure 5.22: Simulations at stage $75\Delta t$ with a homogeneous distribution of the non-fibrous phase and 15% heterogeneous fibres phase of the ECM with a micro-fibres degradation rate of $d_f = 1$.

Chapter 6

Conclusions and Discussion

In this thesis we have presented a comprehensive mathematical modelling approach for exploring cancer invasion. This considered several interlinked tissue- and cell-scale processes, which are critically involved within cancer invasion, and addressed them through a gradual development of the multiscale moving-boundary framework first introduced in Trucu et al. (2013), which was advanced here to consider the fibrous structure of the surrounding microenvironment and its role within the invasion process of both a single and heterotypic cell population. We investigated the local invasion of a tumour within a multi-phase ECM and explored the contribution of a dynamic cancer cell-mediated fibre rearrangement process coupled with interactions between matrix degrading enzymes, secreted by the cancer cells, and the peritumoural fibres network.

For the multiscale model considered in Chapter 2 we built upon the multiscale moving boundary framework introduced in Trucu et al. (2013) by exploring the adhesive dynamics between a heterotypic cancer cell population and the surrounding environment. To that end, we considered the dynamics of a tumour consisting of two cell populations, with the second sub-population arising through cellular

mutations from the primary cell population, and their influence on the micro-scale MDEs boundary dynamics occurring at the cell-scale along the invasive edge of the tumour. This macro-micro *"top-down"* link is given via the source of MDEs that are secreted by the cancer cells from both cell sub-populations arriving within the outer proliferating rim of the tumour. In turn, the MDEs micro-dynamics occurring on the cell-scale enables a micro-macro feedback in the form of a *"bottom-up"* link by providing the movement direction and displacement magnitude of the tumour boundary.

During the macro-scale tumour dynamics, we investigated the effects of cell adhesion, in particular cell-cell and cell-matrix adhesion, and how these influenced the movement of the cancer cells. For that, we considered a non-local adhesion term that accounted for these interactions occurring within a certain radius from the macro-mesh point and thus evaluated the adhesive qualities at each point within the tumour region. The addition of cell adhesion and a secondary cell sub-population enhanced the invasiveness of the tumour when compared to previous results in Trucu et al. (2013), exhibiting increased movement of both the main bulk of cancer cells and the tumour boundary. Furthermore, when sensitivity to the initial conditions of the extracellular matrix were explored, it was noted that as heterogeneity of the ECM was increased, the tumour boundary became increasingly lobular and fingering in its pattern of invasion.

Building on the framework proposed in Chapter 2 and Trucu et al. (2013), in Chapter 3 we proposed a novel two-part multiscale model to explore the adhesive dynamics of a cancer cell population within a two-phase heterogeneous ECM and its impact on the overall pattern of tumour invasion. The ECM was considered here to be a mixture of densities of fibres and non-fibre phases, with the fibres representing all the fibrous proteins such as collagen or fibronectin, and the non-fibres phase

standing for the rest of the ECM constituents (including soluble components such as calcium ions and other classes of ECM molecules such as laminin and elastin).

A special attention was paid to the ECM fibres phase, which was considered and explored through its own multiscale dynamics integrated within the multiscale moving boundary framework initially introduced in Trucu et al. (2013). This gave rise to a second multiscale system acting within the bulk of the tumour which was sharing the macro-dynamics with the underlying multiscale moving boundary system, while having its own specific micro-dynamics addressing the rearrangement of fibres instigated by the macroscopic cell population flux, which established a new *top-down* link between the macro-dynamics and now the fibres micro-dynamics. Notably here, the rearrangement of the micro-structure of the ECM fibres, regarded here as mass distribution of micro-fibres, yields a new naturally induced orientation for the macro-fibres that will have critical influence within the tumour macro-dynamics. This establishes a *bottom-up* link between now the fibre micro-dynamics and the macro-scale, closing this way a double feedback loop that connects the macro- and micro-dynamics in this new fibre focussed multiscale system.

Specifically, within the fibre focussed multiscale system, we developed a model which on one hand explored the way the fibre micro-dynamics are up-taken *on-the-fly* into the tissue-level tumour dynamics by providing at tissue-scale a spatially-distributed macroscopic vector field of oriented ECM fibres (whose orientations are naturally induced by the mass distribution of micro-fibres at micro-scale), these having direct influence within the tumour progression thereby influencing cell migration through their input within cell adhesion, and on the other hand, the way in which the macro-scale cancer cell population dynamics influences both the macroscopic degradation and the microscopic rearrangement of the fibres. Furthermore, mediated by their macro-scale input, the role played by the fibres also have an influence

on the proteolytic leading edge micro-dynamics of the MDEs which are part of the moving boundary multiscale system that was initially formulated in Chapter 2 and Trucu et al. (2013).

In order to integrate the fibre micro-scale into the macro-scale dynamics, we explored the influence of the orientated ECM fibres within cell adhesion while accounting for the continuous (in time) changes in fibres magnitudes and orientations enabled by the fibres micro-dynamics. This enhances and takes further the cell adhesion term introduced in Gerisch and Chaplain (2008); Domschke et al. (2014) and explored in Chapter 2, where besides the cell-cell and cell-ECM-non-fibres adhesion, we now account explicitly for the cell-fibres adhesion. The new type of adhesion, cell-fibres adhesion, brings in the influence of the fibres macroscopic orientation and magnitudes distribution, this way biasing the direction of cell adhesion within the macro-dynamics.

Further, while the cancer cells degrade both the ECM fibres and non-fibres phases at macro-scale, it is the flux of the cancer cells that cause the rearrangement of the micro-fibres at macro-scale. To that end, the cancer cells redistribute and rearrange the micro-fibres in a relocation direction obtained as the contribution of the macroscopic cancer cell flux weighted in accordance with the amount of cancer cells transported at the macro-position and the magnitude of micro-fibres they come into contact with. Finally, this micro-fibres relocation was enabled through a movement probability dependent on the level of micro-fibres at the new position.

Alongside the newly developed two-part multiscale model, we extended the computational framework to address the complex cancer dynamics by formulating a novel non-local predictor-corrector numerical scheme to address the challenging macro-scale computational conditions created through the presence of a multi-phase ECM. We accompanied the new two-part multiscale model with simulation results

which have some similarities to previous work in Chapter 2 and Trucu et al. (2013) where there is a generally fingering, lobular pattern of tumour progression, which is here exacerbated as the cell-fibre adhesion rate is increased. These results suggest that the fibres do indeed play a key role during cancer invasion when compared to previous results in Trucu et al. (2013) where cell adhesion and the role of a fibrous network within the ECM are not considered. We conclude from these results that a fibres-ECM component embedded within a heterogeneous non-fibre ECM phase facilitates a more significant tumour progression than in the case when this is embeded within a homogeneous non-fibre ECM distribution and the rearrangement of the underlying micro-fibres allows the cancer cells to influence their own direction of migration.

An extension to the two-part multiscale model described in Chapter 3 was presented in Chapter 4 to explore the invasion of a heterotypic cancer cell population, consisting of two cell sub-populations, within a two-phase ECM. The behaviour of the secondary cell sub-population is similar to the cancer cell macro-dynamics presented in Chapter 2, however here the mutated population held more aggressive invasion qualities, i.e., a lower cell-cell adhesion rate and a higher affinity for cell-fibre adhesion. Additionally, the secondary cell sub-population arose through mutations from the primary cell population that were conditional on the underlying combined ECM density.

Focussing next on the fibre ECM phase, having previously explored cancer invasion on a network of identical initial distributions of micro-fibres among the micro-domains, to create a *"non-aligned"* fibre ECM phase, in this Chapter we introduced two families consisting each of five different micro-fibre distributions that were randomly allocated to the all the fibres micro-domains (centred at the macro-mesh positions). This form of the ECM fibres phase portrayed a different example of

human tissue when compared to the highly aligned fibre ECM phase modelled in Chapter 3. We again considered the macroscopic representations of the micro-fibres and their resulting effects on the macro-scale dynamics, as introduced in Chapter 3, while, at the same time, allowing the distribution of both cancer cell sub-populations to cause macroscopic fibre degradation. The results presented in Chapter 4 convey much the same conclusions as previous results, namely that tumour progression is enhanced as the heterogeneity of the ECM is increased. Additionally, as the initial fibre density is increased, the spread of the tumour area is largely increased. These results suggest that the cancer cells are more invasive when in the presence of a high fibre ECM phase, in line with biological experiments performed in Provenzano et al. (2008), with this behaviour due to the increased opportunity for cell-fibre adhesion which drives the migration of the cells. Comparing these results with the simulations in Chapter 2, the cells in sub-population c_2 exhibit much greater movement towards the tumour boundary, and the boundary of the tumour is much more irregular due to the heterogeneity of the ECM and the arrangement of the underlying micro-fibres.

Lastly, the model proposed in Chapter 5 expands upon the model developed in Chapter 3 by extending the exploration of the proteolytic dynamics at the tumour invasive edge to the more natural context where this MDEs boundary micro-dynamics takes place in direct interaction with the underlying fibre network. In particular, this model focussed on the peritumoural processes of the freely diffusing matrix degrading enzyme MMP-2, which are sourced from the macro-scale cancer cell population arriving during their migration within the outer proliferation rim within a given sensing distance to the tumour boundary. A particularly important aspect in this context is the enhancement enabled by the underlying macroscopic ECM fibre magnitudes upon the source of MMPs secreted by the macro-scale cancer

cell distributions, whereby a higher source of MMPs is secreted within dense fibres regions. Finally, in the presence of this source, a cross-interface fibre-dependent diffusion of the MMP-2 takes place within the peritumoural boundary micro-domains, which takes advantage of the potential "fibre valleys" created by the micro-fibres rearrangements (instigated by the macro-scale cell-population flux), exploring these as preferred transport routes at the expense of dense micro-fibres regions.

The model proposed here incorporated the biological activities of two particular MMPs, namely the membrane-tethered MT1-MMPs and the MMP-2. On one hand, the membrane-tethered MT1-MMPs indirectly play a role within the topological closure of the tumour, being responsible for cleaving and breaking down the strong collagen fibres, thus bringing its contribution to facilitating appropriate cell-scale conditions for the dynamic rearrangement of micro-fibres, a process that was already addressed starting with Chapter 3. On the other hand, the membrane-tethered MT1-MMPs also plays an important role in activating MMP-2, and this way, again indirectly, contributing to the cell-scale MMP-2 boundary micro-dynamics that ultimately leads to peritumoural ECM fibres degradation. The degradation of micro-fibres, captured here within each boundary micro-domain ϵY, accounts for the angle at which the flux of the MMPs collides with the micro-fibres mass at each micro-spatial position. Indeed, maximum fibre degradation occurrs when the angle between the fibres and MMPs flux is $\pi/2$, while increased alignment of the micro-fibres masses with the direction of the MMP-2 molecular flux leads to a decrease in the fibres degradation rate. Finally, this degradation of peritumoural mass distribution micro-fibres at the cell-scale is continuously in time translated back at macro-scale, having a natural and major impact upon *on-the-fly* changes in the orientations and magnitudes of macro-scale ECM fibres from the peritumoural region.

This model was accompanied by a new computational framework whereby a

finite difference approach was developed to compute the MMPs micro-dynamics, using a trapezoidal predictor-corrector method for time integration. Simulation results from this model were performed to explore this new multiscale framework under varying densities of homogeneous and heterogeneous initial fibres ECM phases. When considering a single cell population, the process of micro-fibre degradation at the boundary was found to promote tumour progression and resulted in larger, denser tumours than previous results in Chapter 3. However when we considered a heterotypic cell population, the micro-fibre degradation at the tumour interface was found to be detrimental to cancer invasion and slowed the progression of the tumour when compared to results from Chapter 4.

Looking forward, this model would benefit from biological experiments specifically tailored to explore the relevance of both the composition of the ECM and the peritumoural MDE processes during tumour invasion, this way providing more accurate parameter values and giving a more comprehensive characterisation of the micro-structures and processes that can then be conveyed into the mathematical model. Although some of the results in this thesis are already implied and correlate to current biological findings, for example, experiments performed by Provenzano et al. (2008) influenced the development of the fibres dynamics and our simulations corroborate these experimental results, more efforts should be made to increase the biological relevance of these models and enable the validation of the simulation results.

The main aim of this thesis was to understand the process of cancer invasion within a multi-component extracellular matrix and explore the crucial interactions between cancer cells and their environment to better predict tumour morphology. Due to deficiencies in current imaging techniques, which only capture between 65% and 90% of the true size of a tumour, it is crucial to develop new models to predict

the true extent of a tumour. Our model simulations suggest that for an aggressive cancer, while having the bulk of cancer cells localised to the central region of the tumour, the tumour itself will in fact be much larger with the boundary expanding far into the surrounding tissue. Thus, information about the true boundary would be invaluable to surgeons during the resection of a tumour to ensure the entire mass was removed, including the regions that are not visible with the current imaging techniques. The results obtained in this thesis are significant, however the model would benefit from biological validation through the use of clinical data and experiments and through the appropriate model development to allow for the modelling of any type of cancer.

Appendix A

Appendix

A.1 Derivation of adhesive flux term

The motion of the cells due to adhesion occurs as a result of the forces produced when adhesion bonds are both produced and broken. The derivation of this term can be seen when the adhesive flux is written as

$$J_a = \frac{\phi}{R} uF,$$

where ϕ is a constant of proportionality related to viscosity of ECM, R is the sensing radius and F is the total force acting on all cells, (Armstrong et al., 2006). Thus, F can be expressed as the sum of all forces on f, created by cells at position x with cells a distance y away. The magnitude of local forces will depend on the local cell density whilst the direction of local forces will depend on the position of the cells at y with respect to x. Hence

$$f = \alpha g(u(x+y)) \cdot \mathcal{K}(y),$$

where $g(u(x+y))$ describes the forces and their dependence on the local cell density, $\mathcal{K}(y)$ is the kernel describing how the direction and magnitude of the force alters and α is a positive parameter reflecting the strength of adhesive force between the cells. The total force F is then

$$F = \int_{-R}^{R} \alpha g(u(x+y)) \cdot \mathcal{K}(y)\ dy,$$

and when substituting this in to our previous equation for the adhesive flux we have

$$J_a = \frac{\phi}{R} u \int_{-R}^{R} \alpha g(u(x+y)) \cdot \mathcal{K}(y)\ dy.$$

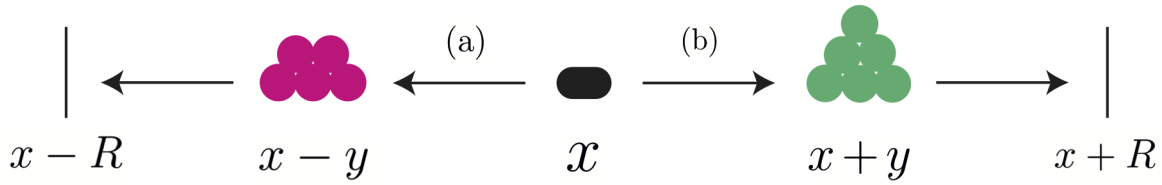

Figure A.1: Schematic describing the force of cells with respect to a point x. The sign of y will determine the direction of force. Here, (a) gives the force exerted by cells at $x-y$ and (b) gives the force exerted by cells at $x+y$. On either side is $x-R$ and $x+R$ (the sensing radius) which is the maximum distance from x that we can evaluate force.

Appendix B

Appendix

B.1 The computational microscopic scheme and its relation to the macro-scale

We describe here the computational scheme for the microscale dynamics first introduced in Trucu et al. (2013) and its relation to the macroscopic level. We begin by recalling the ϵ-sized cubes, $\epsilon Y \in \mathcal{P}$, covering the entire boundary $\partial\Omega(t_0)$ and described in section 2.2.2. The uniform mesh size $h = \frac{\epsilon}{2}$ is used to discretise the entire macro-domain with each micro-domain ϵY centred at a boundary point from the macroscopic mesh. Thus, because the ϵ-cubes are half-way shifted copies on the entire boundary, the neighbouring ϵ-cubes start from the centre of the current one, with the centre of the micro-domains corresponds to the midpoint $x^*_{\epsilon Y}$ induced by ϵY on $[\partial\Omega(t_0)]_{\epsilon Y}$.

To compute the integrals in the source term (2.7), Trucu et al. (2013) proposed a specially developed midpoint rule that approximates the integral of a function f over a generic element domain K, with K being in a finite subdivision with either triangular or square elements of a given region $A \subset \mathbb{R}^2$, as the product between the

value of f at the center of mass K, K_{center}, and the Lebesgue measure of K denoted

$$\int_K f \;=\; f(K_{center})\lambda(K).$$

For an arbitrarily chosen $\epsilon Y \in \mathcal{P}$, we consider a finite element approach involving triangular elements on a uniform micro-mesh which is maintained with identical structure for all the micro-domains. We consider the time constant approximation $\tilde{f}_{\epsilon Y}$ of $f_{\epsilon Y}$ on the time interval $[0, \Delta t]$. Using the final-time computed values of both cell populations $c_1(\cdot, t_0 + \Delta t),\ c_2(\cdot, t_0 + \Delta t)$ at the micro-mesh points, $x_1, x_2, ...x_{p_\epsilon} \in \epsilon Y \cap \Omega(t_0)$, we take

$$\tilde{f}_{\epsilon Y} = \frac{1}{\lambda(\mathbf{B}(x_s, \delta) \cap \Omega(t_0))} \int_{\mathbf{B}(x_s,\delta)\cap\Omega(t_0)} \alpha_1 c_1(x_s, t_0 + \tau) + \alpha_2 c_2(x_s, t_0 + \tau)\ dx$$

where $s = 1, ..., p_\epsilon$ and the integrals are computed using the midpoint rule (Trucu et al., 2013). For the remaining points $y \in \epsilon Y$, the values of $\tilde{f}_{\epsilon Y}$ are calculated via the set of finite element basis functions considered at the contact points $\{\phi_s | s = 1, ..., p_\epsilon\}$. We consider two scenarios for any micro-mesh point $y \in \epsilon Y$:

Case 1: If there exists three overlapping points $x_{i_1}, x_{i_2}, x_{i_3} \in \{x_1, x_2, ...x_{p_\epsilon}\}$, which belongs to the same connected component of $\partial\Omega(t_0) \cap \epsilon Y$ such that y belongs to the convex closure of the set $y \in \text{Conv}\{x_{i_1}, x_{i_2}, x_{i_3}\}$, then the finite element approximation of $\tilde{f}_{\epsilon Y}$ at y is

$$\tilde{f}_{\epsilon Y}(y) = \tilde{f}_{\epsilon Y}(x_{i_1})\phi_{x_{i_1}}(y) + \tilde{f}_{\epsilon Y}(x_{i_2})\phi_{x_{i_2}}(y) + \tilde{f}_{\epsilon Y}(x_{i_3})\phi_{x_{i_3}}(y)$$

Case 2: If y does not satisfy Case 1, then

$$\tilde{f}_{\epsilon Y}(y) = 0.$$

On each micro-domain $\epsilon Y \in \mathcal{P}$, under the presence of zero Neumann boundary conditions and using the computed source terms $\tilde{f}_{\epsilon Y}$, we use the finite element method to solve the reaction-diffusion equation (2.8) over the time interval $[0, \Delta t]$. We then use bilinear elements on a square mesh to obtain the numerical scheme for the MDE micro-processes occurring within each boundary micro-domain ϵY using a trapezoidal predictor-corrector method for the time integration (Trucu et al., 2013).

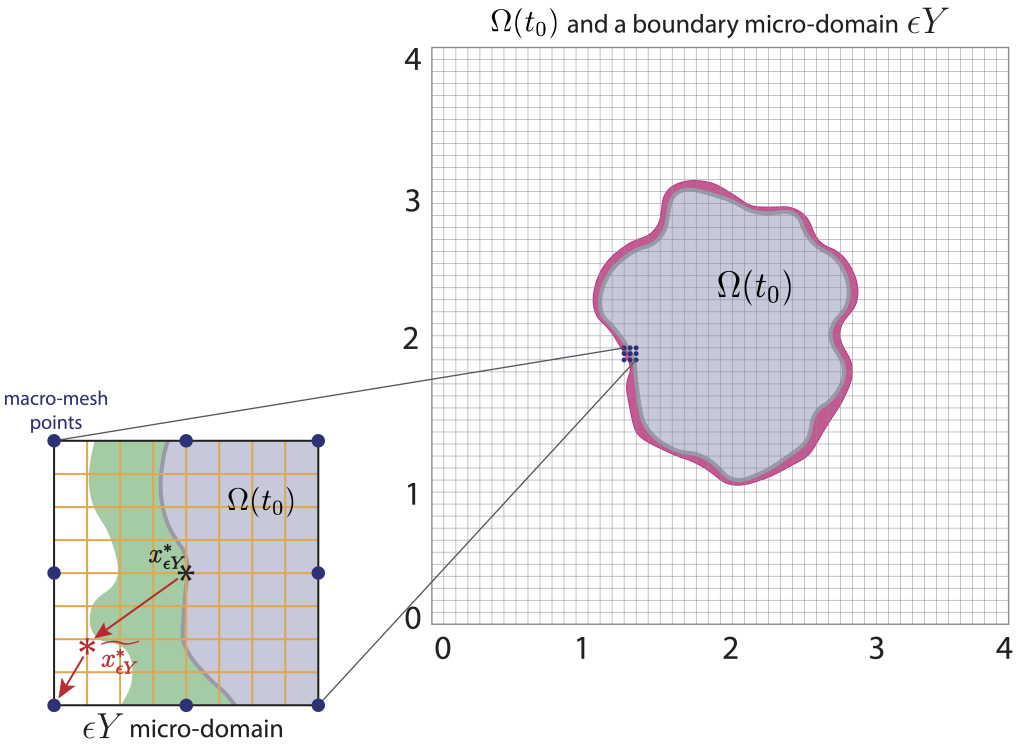

Figure B.1: Plots showing the macro- and micro-domains used in the numerical scheme. The right figure shows the macro-domain with the cancer region $\Omega(t_0)$ in purple, with the expanded tumour region $\Omega(t_0 + \Delta t)$ shown in pink. The left figure is an example of an $\epsilon Y(x)$ boundary micro-domain, with the central boundary point $x^*_{\epsilon Y}$. The pattern of the MDE invading front is illustrated in green, whilst the new boundary position $\widetilde{x^*_{\epsilon Y}}$ and its closest macro-mesh position (shown here in dark blue) in Euclidean distance are both highlighted in red with appropriately pointing arrows.

For each $\epsilon Y \in \mathcal{P}$, we use the midpoint rule to find the transitional probability q^*_ϵ described in Section 2.2.2, and fully defined in Trucu et al. (2013). Thus, pro-

vided that the transitional probability exceeds a certain threshold $\omega_{\epsilon Y} \in (0,1)$, the boundary mesh point $x^*_{\epsilon Y}$ will be moved in direction $\eta_{\epsilon Y}$ from the macro-mesh point from the $\partial\Omega(t_0) \setminus [\Omega(t_0)]_{\epsilon Y}$ to the closest (in Euclidean distance) to $\widetilde{x^*_{\epsilon Y}}$, Figure B.1. If the threshold is not satisfied, then $x^*_{\epsilon Y}$ will remain at the same spatial position. Therefore, the new boundary $\partial\Omega(t_0 + \Delta t)$ is an interpolation of the set of points that have been moved and the set of points that have remained in the same spatial position, namely,

$$\{x^*_{\epsilon Y} | \epsilon Y \in \mathcal{P} \text{ and } q^*_\epsilon(x^*_{\epsilon Y}) < \omega_{\epsilon Y}\} \cap \{\widetilde{x^*_{\epsilon Y}} | \epsilon Y \in \mathcal{P} \text{ and } q^*_\epsilon(x^*_{\epsilon Y}) \geq \omega_{\epsilon Y}\},$$

and the computational process continues on the new domain $\Omega(t_0 + \Delta t)$, using a discretised version of (2.9) and hence a new initial condition for the macroscopic stage, i.e.,

$$v^{new}(x_{i,j}, t_0 + \Delta t) = v^k_{i,j},$$

$$c^{new}_n(x_{i,j}, t_0 + \Delta t) = \begin{cases} c^k_{n_{i,j}}, & x_{i,j} \in \overline{\Omega(t_0)}, \\ \frac{1}{8}(c^k_{n_{i,j+1}} + c^k_{n_{i+1,j+1}} + c^k_{n_{i+1,j}} + c^k_{n_{i+1,j-1}} & x_{i,j} \in \overline{\mathbf{B}(\overline{\Omega(t_0)}, h)} \setminus \overline{\Omega(t_0)}, \\ \quad + c^k_{n_{i,j-1}} + c^k_{n_{i-1,j-1}} + c^k_{n_{i-1,j}} + c^k_{n_{i-1,j+1}}), & \\ 0, & x_{i,j} \notin \overline{\mathbf{B}(\overline{\Omega(t_0)}, h)}, \end{cases}$$

where $\{x_{i,j}, i,j = 1, ..., q\}$ are the macro-mesh points in Y, k is the final time-step index and as defined in Trucu et al. (2013), $\overline{\Omega(t_0)}$ is the topological closure of the tumour region $\Omega(t_0)$ and $\overline{\mathbf{B}(\overline{\Omega(t_0)}, h)}$ is the topological closure of the h-bundle of $\overline{\Omega(t_0)}$, i.e.,

$$\overline{\mathbf{B}(\overline{\Omega(t_0)}, h)} := \{x \in Y | \exists z_x \in \overline{\Omega(t_0)} \text{ such that } ||x - z_x||_2 \leq h\}.$$

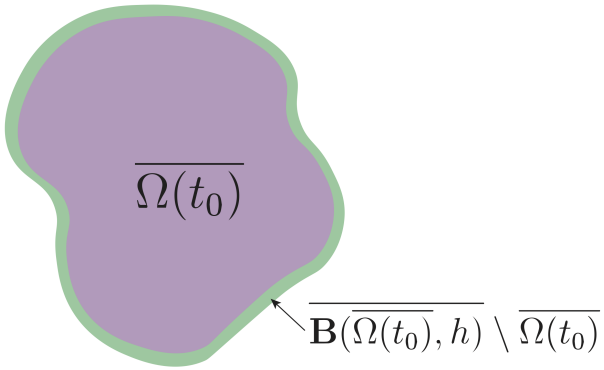

Figure B.2: Schematic representation of the new initial condition for the tumour domain. The purple region represents the topologically closed tumour region $\overline{\Omega(t_0)}$, with the green region representing the interpolation of tumour boundary positions within $\overline{\mathbf{B}(\overline{\Omega(t_0)}, h)} \setminus \overline{\Omega(t_0)}$.

Appendix C

Appendix

C.1 The mollifier ψ_γ

The standard mollifier $\psi_\gamma : \mathbb{R}^N \to \mathbb{R}_+$ (which was used also in Trucu et al. (2013)) is defined as usual, namely

$$\psi_\gamma(x) := \frac{1}{\gamma^N}\psi\big(\frac{x}{\gamma}\big),$$

where ψ is the smooth compact support function given by

$$\psi(x) := \begin{cases} \frac{exp\frac{1}{\|x\|_2^2-1}}{\int\limits_{\mathbf{B}(0,1)} exp\frac{1}{\|z\|_2^2-1}dz}, & if \quad x \in \mathbf{B}(0,1), \\ 0, & if \quad x \notin \mathbf{B}(0,1) \end{cases}$$

C.2 The radial kernel $\mathcal{K}(\cdot)$

To explore the influence on adhesion-driven migration decreases as the distance from $x+y$ to x within the sensing region $B(x,r)$ increases, the expression of the radial dependent spatial kernel $\mathcal{K}(\cdot)$ appearing in (4.6) is taken here to be:

$$\mathcal{K}(r) := \frac{2\pi R^2}{3}\left(1 - \frac{r}{2R}\right).$$

Appendix D

Appendix

D.1 Microscopic fibre domains

For the fibres initial conditions in Chapter 4, on the micro-domains $\delta Y(x)$, we consider two families of five distinctive micro-fibres patterns, $\{P_i^1\}_{i\in J}$ and $\{P_i^2\}_{i=1..5}$, which are defined by the union of paths $P_i^l = \bigcup_{j=1..5} h_{i,j}^l$, $l = 1, 2$, which are given as follows.

For the first family of fibre paths P^1, we have:

$$h_{1,1}^1 : z_1 = z_2; \quad h_{1,2}^1 : z_1 = \frac{1}{2}; \quad h_{1,3}^1 : z_1 = \frac{1}{5}; \quad h_{1,4}^1 : z_2 = \frac{2}{5}; \quad h_{1,5}^1 : z_2 = \frac{4}{5}.$$

$$h_{2,1}^1 : z_1 = z_2; \quad h_{2,2}^1 : z_1 = \frac{1}{2}; \quad h_{2,3}^1 : z_1 = \frac{1}{5}; \quad h_{2,4}^1 : z_2 = \frac{2}{5}; \quad h_{2,5}^1 : z_2 = \frac{1}{10}.$$

$$h_{3,1}^1 : z_1 = z_2; \quad h_{3,2}^1 : z_1 = \frac{1}{10}; \quad h_{3,3}^1 : z_1 = \frac{9}{10}; \quad h_{3,4}^1 : z_2 = \frac{2}{5}; \quad h_{3,5}^1 : z_2 = \frac{1}{10}.$$

$$h^1_{4,1} : z_1 = z_2; \quad h^1_{4,2} : z_1 = \frac{1}{10}; \quad h^1_{4,3} : z_1 = \frac{3}{10}; \quad h^1_{4,4} : z_2 = \frac{2}{5}; \quad h^1_{4,5} : z_2 = \frac{1}{10}.$$

$$h^1_{5,1} : z_1 = z_2; \quad h^1_{5,2} : z_1 = \frac{4}{5}; \quad h^1_{5,3} : z_1 = \frac{3}{10}; \quad h^1_{5,4} : z_2 = \frac{1}{10}; \quad h^1_{5,5} : z_2 = \frac{7}{10}.$$

For the second family of fibre paths P^2, we have:

$$h^2_{1,1} : z_1 = z_2; \quad h^2_{1,2} : z_1 = \frac{1}{2}; \quad h^2_{1,3} : z_1 = \frac{1}{5}; \quad h^2_{1,4} : z_2 = \frac{2}{5}; \quad h^2_{1,5} : z_2 = \frac{4}{5}.$$

$$h^2_{2,1} : z_1 = z_2; \quad h^2_{2,2} : z_1 = \frac{1}{2}; \quad h^2_{2,3} : z_1 = \frac{1}{5}; \quad h^2_{2,4} : z_2 = \frac{2}{5}; \quad h^2_{2,5} : z_2 = \frac{1}{10}.$$

$$h^2_{3,1} : z_1 = z_2; \quad h^2_{3,2} : z_1 = \frac{1}{10}; \quad h^2_{3,3} : z_1 = \frac{9}{10}; \quad h^2_{3,4} : z_2 = \frac{2}{5}; \quad h^2_{3,5} : z_2 = \frac{1}{10}.$$

$$h^2_{4,1} : z_1 = z_2; \quad h^2_{4,2} : z_1 = \frac{4}{5}; \quad h^2_{4,3} : z_1 = \frac{3}{5}; \quad h^2_{4,4} : z_2 = \frac{4}{5}; \quad h^2_{4,5} : z_2 = \frac{3}{5}.$$

$$h^2_{5,1} : z_1 = z_2; \quad h^2_{5,2} : z_1 = \frac{4}{5}; \quad h^2_{5,3} : z_1 = \frac{3}{5}; \quad h^2_{5,4} : z_2 = \frac{4}{5}; \quad h^2_{5,5} : z_2 = \frac{1}{10}.$$

For each of these families of fibre paths P^l, $l = 1, 2$, as described in Shuttleworth and Trucu (2019c), the micro-scale fibres pattern within each micro-domain $\delta Y(x)$ is given as

$$f(z,t) := \sum_{j=1}^{5} \psi_{h^l_{i,j}}(z)(\chi_{(\delta-2\gamma_0)Y(x)} * \psi_{\gamma_0})(z) \tag{D.1}$$

where $\{\psi_{h^l_{i,j}}\}_{i,j=1..5}$ are smooth compact support functions of the form

$$\psi_{h_j} : \delta Y(x) \to \mathbb{R}$$

defined as follows:

$Case\,1$: if $h^l_{i,j}$ is not parallel to z_1-axis
(i.e., $h^l_{i,j}$ is identified as the graph of a function of z_2)

we have:

$$\psi_{h^l_{i,j}}(z_1,z_2) := \begin{cases} C_{h^l_{i,j}} e^{-\frac{1}{r^2-(h_j(z_2)-z_1)^2}}, & \text{if } z_1 \in [h^l_{i,j}(z_2)-r, h^l_{i,j}(z_2)+r], \\ \\ 0, & \text{if } z_1 \notin [h^l_{i,j}(z_2)-r, h^l_{i,j}(z_2)+r]; \end{cases}$$

$Case\,2$: if $h^l_{i,j}$ is parallel to z_1-axis
(i.e., $h^l_{i,j}$ is identified as the graph of a constant function of z_1)

we have:

$$\psi_{h^l_{i,j}}(z_1,z_2) := \begin{cases} C_{h^l_{i,j}} e^{-\frac{1}{r^2-(h^l_{i,j}(z_1)-z_2)^2}}, & \text{if } z_2 \in [h^l_{i,j}(z_1)-r, h^l_{i,j}(z_1)+r], \\ \\ 0, & \text{if } z_2 \notin [h^l_{i,j}(z_1)-r, h^l_{i,j}(z_1)+r]. \end{cases} \tag{D.2}$$

Here $r > 0$ is the width of the micro-fibres and $C_{h^l_{i,j}}$ are constants that determine the maximum height of $\psi_{h^l_{i,j}}$ along the smooth paths $\{h^l_{i,j}\}_{i,j=1..5}$ in $\delta Y(x)$. Finally, ψ_γ is the standard mollifier defined in Appendix C.1, with $\gamma_0 = h/16$.

Finally, the initial spatial configuration of the pattern of macroscopic ECM fibre phase is selected according to a randomly generated matrix of labels $A = (a_{i,j})_{i,j=1..n}$ corresponding to the entire $n \times n$ grid discretising Y, in which the entries $a_{i,j}$ are allocated values randomly selected from the set of configuration labels $\{1,2,3,4,5\}$

that will dictate the choice of micro-fibres pattern among those described above that will be assigned to the micro-domains $\delta Y(j\Delta x, i\Delta y)$, for all $i, j = 1..n$.

Bibliography

Andasari, V., Gerisch, A., Lolas, G., South, A., Chaplain, M.A.J., 2011. Mathematical modeling of cancer cell invasion of tissue: biological insight from mathematical analysis and computational simulation. *J. Math. Biol.* **63**(1), 141–171. doi:10.1007/s00285-010-0369-1.

Anderson, A.R.A., 2005. A hybrid mathematical model of solid tumour invasion: the importance of cell adhesion. *Math. Medic. Biol.* **22**(2), 163–186. doi:10.1093/imammb/dqi005.

Anderson, A.R.A., Chaplain, M.A.J., Newman, E.L., Steele, R.J.C., Thompson, A.M., 2000. Mathematical modelling of tumour invasion and metastasis. *J. Theor. Medic.* **2**(2), 129–154.

Anderson, A.R.A., Rejniak, K.A., Gerlee, P., Quaranta, V., 2007. Modelling of cancer growth, evolution and invasion: Bridging scales and models. *Math. Model. Nat. Phenom.* **2**(3), 1–29.

Armstrong, N.J., Painter, K.J., Sherratt, J.A., 2006. A continuum approach to modelling cell-cell adhesion. *J. Theor. Biol.* **243**(1), 98–113.

Behrens, J., Mareel, M.M., Van Roy, F.M., Birchmeier, W., 1989. Dissecting tumor cell invasion: Epithelial cells acquire invasive properties after the loss

of uvomorulin-mediated cell-cell adhesion. *J. Cell. Biol.* **108**(6), 2435–2447. doi:10.1083/jcb.108.6.2435.

Bellamo, N., Chaplain, M.A.J., de Angelis, E., 2008. Selected Topics in Cancer Modeling: genesis, evolution, immune competition, and therapy. Modeling and Simulation in Science, Engineering and Technology, Birkhauser.

Berrier, A.L., Yamada, K.M., 2007. Cell-matrix adhesion. *J. Cell. Physiol* **213**(3), 565–573. doi:10.1002/jcp.21237.

Bhagavathula, N., Hanosh, A.W., Nerusu, K.C., Appelman, H., Chakrabarty, S., Varani, J., 2007. Regulation of e-cadherin and β-catenin by Ca^{2+} in colon carcinoma is dependent on calcium-sensing receptor expression and function. *Int. J. Cancer* **121**, 1455–1462. doi:10.1002/ijc.22858.

Bitsouni, V., Chaplain, M.A.J., Eftimie, R., 2017. Mathematical modelling of cancer invasion: The multiple roles of tgf-β pathway on tumour proliferation and cell adhesion. *Math. Model. Meth. Appl. Sci.* **27**(10), 1929–1962.

Brinckerhoff, C.E., Matrisian, L.M., 2002. Matrix metalloproteinases: a tail of a frog that became a prince. *Nat. Rev. Mol. Cel. Biol.* **3**(3), 207–214. doi:10.1038/nrm763.

Cavallaro, U., Christofori, G., 2001. Cell adhesion in tumor invasion and metastasis: loss of the glue is not enough. *Biochim. Biophys. Acta.* **1552**(1), 39–45. doi:10.1016/S0304-419X(01)00038-5.

Chaplain, M.A.J., Lachowicz, M., Szymańska, Z., Wrzosek, D., 2011. Mathematical modelling of cancer invasion: The importance of cell-cell adhesion and cell-matrix adhesion. *Math. Model. Meth. Appl. Sci.* **21**(4), 719–743.

Chaplain, M.A.J., Lolas, G., 2005. Mathematical modelling of cancer cell invasion of tissue: The role of the urokinase plasminogen activation system. *Math. Model. Meth. Appl. Sci.* **15**, 1685–1734. doi:10.1142/S0218202505000947.

Chaplain, M.A.J., McDougall, S.R., Anderson, A.R.A., 2006. Mathematical modelling of tumor-induced angiogenesis. *Annu. Rev. Biomed. Eng.* **8**, 233–257. doi:10.1146/annurev.bioeng.8.061505.095807.

Chauviere, A., Hillen, T., Preziosi, L., 2007. Modeling cell movement in anisotropic and heterogeneous network tissues. *Netw. Heterog. Media.* **2**(2), 333–357.

Cirri, P., Chiarugi, P., 2011. Cancer associated fibroblasts: the dark side of the coin. *Americ. J. Cancer Res.* **1**(4), 482–497.

Conklin, M.W., Eickhoff, J.C., Riching, K.M., Pehlke, C.A., Eliceiri, K.W., Provenzano, P.P., Friedl, A., Keely, P.J., 2011. Aligned collagen is a prognostic signature for survival in human breast carcinoma. *Americ. J. Pathol.* **178**(3), 1221–1232. doi:10.1016/j.ajpath.2010.11.076.

Cox, T.R., Erler, J.T., 2011. Remodeling and homeostasis of the extracellular matrix: implications for fibrotic diseases and cancer. *Dis. Model. & Mech* **4**(2), 165–178.

Dalberg, K., Eriksson, E., Enberg, U., Kjellman, M., Backdahl, M., 2000. Gelatinase a, membrane type 1 matrix metalloproteinase, and extracellular matrix metalloproteinase inducer mrna expression: correlation with invasive growth of breast cancer. *World. J. Surg.* **24**(3), 334–340.

Deakin, N.E., Chaplain, M.A.J., 2013. Mathematical modelling of cancer cell invasion: the role of membrane-bound matrix metalloproteinases. *Front. Oncol.* **3**(70), 1–9.

Deisboeck, T.S., Wang, Z., Macklin, P., Cristini, V., 2011. Multiscale cancer modeling. *Annu. Rev. Biomed. Eng.* **13**, 127–155.

Delon, I., Brown, N.H., 2007. Integrins and the actin cytoskeleton. *Curr. Opin. Cell. Biol.* **19**, 43–50. doi:10.1016/j.ceb.2006.12.013.

Domschke, P., Trucu, D., Gerisch, A., Chaplain, M.A.J., 2014. Mathematical modelling of cancer invasion: Implications of cell adhesion variability for tumour infiltrative growth patterns. *J. Theor. Biol.* **361**, 41–60.

Erdogan, B., Ao, M., White, L.M., Means, A.L., Brewer, B.M., Yang, L., Washington, M.K., Shi, C., Franco, O.E., Weaver, A.M., Hayward, S.W., Li, D., Webb, D.J., 2017. Cancer-associated fibroblasts promote directional cancer cell migration by aligning fibronectin. *J. Cell. Biol.* **216**(11), 3799–3816. doi:10.1083/jcb.201704053.

Fang, M., Yuan, J., Peng, C., Li, Y., 2014. Collagen as a double-edged sword in tumor progression. *Tumour Biol.* **35**(4), 2871–2882. doi:10.1007/s13277-013-1511-7.

Gerisch, A., Chaplain, M.A.J., 2008. Mathematical modelling of cancer cell invasion of tissue: Local and non-local models and the effect of adhesion. *J. Theor. Biol.* **250**(4), 684–704. doi:10.1016/j.jtbi.2007.10.026.

Gopal, S., Veracini, L., Grall, D., Butoru, C., Schaub, S., Audebert, S., Camoin, L., Baudelet, E., Radwanska, A., Divonne, S.B.F., Violette, S.M., Weinreb, P.H., Rekima, S., Ilie, M., Sudaka, A., Hofman, P., Obberghen-Schilling, E.V., 2017. Fibronectin-guided migration of carcinoma collectives. *Nat. Commun.* **8**. doi:10.1038/ncomms14105.

Gu, Z., Liu, F., Tonkova, E.A., Lee, S.Y., Tschumperlin, D.J., Brenner, M.B., Ginsberg, M.H., 2014. Soft matrix is a natural stimulator for cellular invasiveness. *Mol. Biol. Cell.* **25**(4), 457–469. doi:10.1091/mbc.e13-05-0260.

Hanahan, D., Weinberg, R.A., 2000. The hallmarks of cancer. *Cell* **100**, 57–70. doi:10.1016/S0092-8674(00)81683-9.

Hanahan, D., Weinberg, R.A., 2011. The hallmarks of cancer: The next generation. *Cell* **144**, 646–674.

He, X., Lee, B., Jiang, Y., 2016. Cell-ECM Interactions in Tumor Invasion. Springer International Publishing. pp. 73–91. doi:10.1007/978-3-319-42023-3_4.

Hillen, T., 2006. M5 mesoscopic and macroscopic models for mesenchymal motion. *J. Math. Biol.* **53**(4), 585–616. doi:10.1007/s00285-006-0017-y.

Hillen, T., Hinow, P., Wang, Z., 2010. Mathematical analysis of a kinetic model for cell movement in network tissues. *Discr. Contin. Dyn. Sys.* **14**(3), 1055–1080.

Hills, C.E., Younis, M.Y.G., Bennett, J., Siamantouras, E., Liu, K.K., Squires, P.E., 2012. Calcium-sensing receptor activation increases cell-cell adhesion and β-cell function. *Cell. Physiol. Biochem.* **30**(3), 575–586. doi:10.1159/000341439.

Hofer, A.M., Curci, S., Doble, M.A., Brown, E.M., Soybel, D.I., 2000. Intercellular communication mediated by the extracellular calcium-sensing receptor. *Nat. Cell. Biol.* **2**(7), 392–398. doi:10.1038/35017020.

Hughes, T.J.R., 1987. The Finite Element Method: Linear static and dynamic finite element analysis. Prentice-Hall.

Humphries, J.D., Byron, A., Humphries, M.J., 2006. Integrin ligands at a glance. *J. Cell. Sci.* **119**, 3901–3903. doi:10.1242/jcs.03098.

Ioachim, E., Charchanti, A., Briasoulis, E., Karavasilis, V., Tsanou, H., Arvanitis, D.L., Agnantis, N.J., Pavlidis, N., 2002. Immunohistochemical expression of extracellular matrix components tenascin, fibronectin, collagen type iv and laminin in breast cancer: their prognostic value and role in tumour invasion and progression. *Euro. J. Cancer* **38**, 2362–2370.

Jolly, L.A., Novitskiy, S., Owens, P., Massoll, N., Cheng, N., Fang, W., Moses, H.L., Franco, A.T., 2016. Fibroblast-mediated collagen remodeling within the tumour microenvironent facilitates progression of thyroid cancers driven by braf^{V600E} and Pten loss. *Cancer Res.* **76**, 1804–1813. doi:10.1158/0008-5472.CAN-15-2351.

Kalluri, R., 2016. The biology and function of fibroblasts in cancer. *Nat. Rev. Cancer* **16**, 582–598. doi:doi:10.1038/nrc.2016.73.

Katt, M.E., Placone, A.L., Wong, A.D., Xu, Z.S., Searson, P.C., 2016. In vitro tumor models: Advantages, disadvantages, variables, and selecting the right platform. *Front. Bioeng. Biotech.* **4**(12).

Kawanishi, J., Kato, J., Sasaki, K., Fujii, S., Watanabe, N., Niitsu, Y., 1995. Loss of e-cadherin-dependent cell-cell adhesion due to mutation of the beta-catenin gene in a human cancer cell line, hsc-39. *Mol. Cell. Biol.* **15**(3), 1175–1181.

Ko, K.S., Arora, P.D., Bhide, V., Chen, A., McCulloch, C.A.G., 2001. Cell-cell adhesion in human fibroblasts requires calcium signalling. *J. Cell. Sci.* **114**(6), 1155–1167.

Krakhmal, N.V., Zavyalova, M.V., Denisov, E.V., Vtorushin, S.V., Perelmuter, V.M., 2015. Cancer invasion: Patterns and mechanisms. *Acta. Naturae.* **7**(2), 17–28.

Kristensen, J.H., Karsdal, M.A., 2016. Biochemistry of Collagens, Laminins and Elastin. Academic Press. chapter 30 - Elastin. pp. 197–201. doi:10.1016/B978-0-12-809847-9.00030-1.

LeVeque, R.J., 2007. Finite Difference Methods for Ordinary and Partial Differential Equations: Steady-State and Time-Dependent Problmes. SIAM.

Lodish, H., Berk, A., Zipursky, S.L., 2000. Molecular Cell Biology. 4th ed., W.H.Freeman.

Loeb, K.R., Loeb, L.A., 2000. Significance of multiple mutations in cancer. *Carcinogenesis* **21**(3), 379–385. doi:10.1093/carcin/21.3.379.

Lu, P., Takai, K., Weaver, V.M., Werb, Z., 2011. Extracellular matrix degradation and remodeling in development and disease. *Cold Spring Harb Perspect Biol.* **3**(12). doi:10.1101/cshperspect.a005058.

MATLAB, 2017. version 9.3.0.713579 (2017b). The Mathworks, Inc., Natick, Massachusetts.

Menke, A., Philippi, C., Vogelmann, R., Seidel, B., Lutz, M.P., Adler, G., Wedlich, D., 2001. Down-regulation of e-cadherin gene expression by collagen type i and type iii in pancreatic cancer cell lines. *Cancer Res.* **61**(8), 3508–3517.

Moissoglu, K., Schwartz, M.A., 2006. Integrin signalling in directed cell migration. *Biol. Cell.* **98**(9), 547–555. doi:10.1042/BC20060025.

Nabeshima, K., Inoue, T., Shimao, Y., Sameshima, T., 2002. Matrix metalloproteinases in tumor invasion: Role for cell migration. *Path. Int.* **52**(4), 255–264.

Painter, K.J., 2008. Modelling cell migration strategies in the extracellular matrix. *J. Math. Biol.* **58**(4), 511. doi:10.1007/s00285-008-0217-8.

Painter, K.J., Armstrong, N.J., Sherratt, J.A., 2010. The impact of adhesion on cellular invasion processes in cancer and development. *J. Theor. Biol.* **264**, 1057–1067. doi:10.1016/j.jtbi.2010.03.033.

Parsons, S.L., Watson, S.A., Brown, P.D., Collins, H.M., Steele, R.J., 1997. Matrix metalloproteinases. *Brit. J. Surg.* **84**(2), 160–166. doi:10.1046/j.1365-2168.1997.02719.x.

Peng, L., Trucu, D., Lin, P., Thompson, A., Chaplain, M.A.J., 2017. A multiscale mathematical model of tumour invasive growth. *Bull. Math. Biol.* **79**(3), 389–429.

Perumpanani, A.J., Simmons, D.L., Gearing, A.J.H., Miller, K.M., Ward, G., Norbury, J., Schneemann, M., Sherratt, J.A., 1998. Extracellular matrix-mediated chemotaxis can impede cell migration. *Proc. Biol. Sci.* **265**(1413), 2347–2352.

Pinner, S., Sahai, E., 2008. Imaging amoeboid cancer cell motility in vivo. *J. Microsc.* **231**(3), 441–445.

Provenzano, P.P., Eliceiri, K.W., Campbell, J.M., Inman, D.R., White, J.G., Keely, P.J., 2006. Collagen reorganization at the tumor-stromal interface facilitates local invasion. *BMC Med.* **4**(38). doi:10.1186/1741-7015-4-38.

Provenzano, P.P., Inman, D.R., Eliceiri, K.W., Knittel, J.G., Yan, L., Rueden, C.T., White, J.G., Keely, P.J., 2008. Collagen density promotes mammary tumour initiation and progression. *BMC Med.* **6**(11). doi:10.1186/1741-7015-6-11.

Ramis-Conde, I., Chaplain, M.A.J., Anderson, A.R.A., 2008. Mathematical modelling of tumour invasion and metastasis. *Math. Comput. Model.* **47**(5-6), 533–545.

Rozario, T., DeSimone, D.W., 2010. The extracellular matrix in development and morphogenesis: A dynamic view. *Develop. Biol.* **341**(1), 126–140. doi:10.1016/j.ydbio.2009.10.026.

Ruangpanit, N., Chan, D., Holmbeck, K., Birkedal-Hansen, H., Polarek, J., Yang, C., Bateman, J.F., Thompson, E.W., 2001. Gelatinase a (mmp-2) activation by skin fibroblasts: dependence on mt1-mmp expression and fibrillar collagen form. *Matrix Biol.* **20**(3), 193–203. doi:10.1016/S0945-053X(01)00135-4.

Scianna, M., Preziosi, L., 2012. A hybrid model describing different morphologies of tumor invasion fronts. *Math. Model. Nat. Phenom.* **7**(1), 78–104.

Shiga, K., Hara, M., Nagasaki, T., Sata, T., Takahashi, H., Takeyama, H., 2015. Cancer-associated fibroblasts: Their characteristics and their roles in tumor growth. *Cancers* **7**(4), 2443–2458. doi:10.3390/cancers7040902.

Shuttleworth, R., Trucu, D., 2018. Cell Movement Modelling and Applications. Springer. chapter Two-scale Moving Boundary Dynamics of Cancer Invasion: Heterotypic Cell Populations Evolution in Heterogeneous ECM. pp. 1–26. doi:10.1007/978-3-319-96842-1.

Shuttleworth, R., Trucu, D., 2019a. Cell-scale degradation of peritumoural extracellular matrix fibre network and its role within tissue-scale cancer invasion. *submitted to Bull. Math. Bio., arXiv:submit/2753201* .

Shuttleworth, R., Trucu, D., 2019b. Multiscale dynamics of a hetertypic cancer cell population within a fibrous extracellular matrix. *submitted to J. Theor. Bio., arXiv:1907.01092* .

Shuttleworth, R., Trucu, D., 2019c. Multiscale modelling of fibres dynamics and cell adhesion within moving boundary cancer invasion. *Bull. Math. Biol.* doi:10.1007/s11538-019-00598-w.

Sporn, M.B., 1996. The war on cancer. *Lancet* **347**, 1377–1381.

Szymańska, Z., Morales-Rodrigo, C., Lachowicz, M., Chaplain, M.A.J., 2009. Mathematical modelling of cancer invasion of tissue: the role and effect of nonlocal interactions. *Math. Model. Meth. Appl. Sci.* **19**(2), 257–281.

Tam, E.M., Moore, T.R., Butler, G.S., Overall, C.M., 2004. Characterization of the distint collagen binding, helicase and cleavage mechanisms of matrix metalloproteinases 2 and 14 (gelatinase a and mt1-mmp). *J. Biol. Chem.* **279**(41), 43336–43344.

Tao, L., Huang, G., Song, H., Chen, Y., Chen, L., 2017. Cancer associated fibroblasts: an essential role in the tumour microenvironment. *Oncol. Letters* **14**(3), 2611–2620. doi:10.3892/ol.2017.6497.

Thomson, E.W., Yu, M., Bueno, J., Jin, L., Maiti, S.N., Palao-Marco, F.L., Pulyaeva, H., Tamborlane, J.W., Tirgari, R., et al., I.W., 1994. Collagen induced mmp-2 activation in human breast cancer. *Breast Cancer Res. Treat.* **31**(2-3), 357–370.

Todd, J.R., Ryall, K.A., Vyse, S., Wong, J.P., Natrajan, R.C., Yuan, Y., Tan, A., Huang, P.H., 2016. Systematic analysis of tumour cell-extracellular matrix adhesion identifies independent prognostic factors in breast cancer. *Oncotarget* **7**(39), 62939–62953. doi:10.18632/oncotarget.11307.

Trucu, D., Lin, P., Chaplain, M.A.J., Wang, Y., 2013. A multiscale moving boundary model arising in cancer invasion. *Multiscale Model. Simul.* **11**(1), 309–335.

Turner, S., Sherratt, J.A., 2002. Intercellular adhesion and cancer invasion: A discrete simulation using the extended potts model. *J. Theorl. Biol.* **216**(1), 85–100. doi:10.1006/jtbi.2001.2522.

Van Doren, S.R., 2015. Matrix metallopreinase interactions with collagen and elastin. *Matrix Biol.* **44-46**, 224–231. doi:10.1016/j.matbio.2015.01.005.

Visse, R., Nagase, H., 2003. Matrix metalloproteinases and tissue inhibitors of metalloproteinases: structure function and biochemistry. *Circ. Res.* **92**, 827–839. doi:10.1161/01.RES.0000070112.80711.3D.

Wallace, D.I., Guo, X., 2013. Properties of tumour spheroid growth exhibited by simple mathematical models. *Front. Oncol.* **3**(51). doi:10.3389/fonc.2013.00051.

Wang, Z., Hillen, T., Li, M., 2008. Mesenchymal motion models in one dimension. *J. Appl. Math.* **69**(2), 375–397.

Wijnhoven, B.J., Dinjens, W.N., Pignatelli, M., 2000. E-cadherin-catenin cell-cell adhesion complex and human cancer. *Brit. J. Surg.* **87**(8), 992–1005.

Wolf, K., te Lindert, M., Krause, M., Alexander, S., te Riet, J., Willis, A.L., Hoffman, R.M., Figdor, C.G., Weiss, S.J., Friedl, P., 2013. Physical limits of cell migration: Control by ECM space and nuclear deformation and tuning by proteolysis and traction force. *J. Cell. Biol.* **201**(7), 1069–1084. doi:10.1083/jcb.201210152.

Xue, M., Jackson, C.J., 2015. Extracellular matrix reorganization during wound healing and its impact on abnormal scarring. *Adv. Wound Care* **4**(3), 119–136. doi:10.1089/wound.2013.0485.

Yamaguchi, H., Wyckoff, J., Condeelis, J., 2005. Cell migration in tumors. *Curr. Opin. Cell. Biol.* **17**(5), 559–564. doi:10.1016/j.ceb.2005.08.002.

Yosida, K., 1980. Functional Analysis. 6th ed., Springer-Verlag.

Zigrino, P., Drescher, C., Mauch, C., 2001. Collagen-induced proMMP-2 activation

by MT1-MMP in human dermal fibroblasts and the possible role of $\alpha 2\beta 1$ integrins. *Euro. J. Cell. Biol.* **80**, 68–77.